

ABSTRACT

Title of Dissertation: IN-SITU ADDITIVE MANUFACTURING OF METALS FOR EMBEDDING PARTS COMPATIBLE WITH LIQUID METALS TO ENHANCE THERMAL PERFORMANCE OF AVIONICS FOR SPACECRAFT

Jerald Armen
Doctor of Philosophy, 2020

Dissertation directed by: Professor Hugh A. Bruck
Department of Mechanical Engineering

With advances in micromachinery, the aggregation of sensors, and more powerful microcontroller platforms on satellites, the size of avionics for space missions are getting dramatically smaller with faster processing speeds. This has resulted in greater localized heat generation, requiring more reliable thermal management systems to enhance the thermal performance of the avionics. The emergence of advanced additive manufacturing (AM), such as selective laser melting (SLM) and engineering materials, such as low-melting eutectic liquid metal (LM) alloys and synthetic ceramics offer new opportunities for thermal cooling systems. Therefore, there has been an opportunity for adapting in-situ AM to overcome limitations of traditional manufacturing in thermal application, where improvements can be achieved through reducing thermal contact resistance of multi-layer interfaces. This dissertation investigates adapting in-situ AM technologies to embed LM compatible prefabricated components, such as ceramic tubes, inside of metals without the need for a parting surface, resulting in more intimate contact between the

metal and ceramic and a reduction in the interfacial thermal resistance. A focus was placed on using more ubiquitous powder bed AM technologies, where it was determined that the morphology of the prefabricated LM compatible ceramic tubes had to be optimized to prevent collision with the apparatus of powder bed based AM. Furthermore, to enhance the wettability of the ceramic tubes during laser fusion, the surfaces were electroplated, resulting in a 1.72X improvement in heat transfer compared to cold plates packaged by conventional assembly. Additionally, multiple AM technologies synergistically complement with cross platform tools such as magnetohydrodynamic (MHD) to solve the corrosion problem in the use of low melting eutectic alloy in geometrically complex patterns as an active cooling system with no moving parts. The MHD pumping system was designed using FEA and CFD simulations to approximate Maxwell and Navier-Stokes equations, were then validated using experiments with model heat exchanger to determine the tradeoff in performance with conventional pumping systems. The MHD cooling prototype was shown to reach volumetric flow rates of up to $650 \text{ mm}^3/\text{sec}$ and generated flow pressure due to Lorentz forces of up to 230 Pa, resulting in heat transfer improvement relative to passive prototype of 1.054.

Key words: Additive Manufacturing, Assembly Systems, Non-Traditional Joining Methods, Liquid Metal, Contact Resistance, Electrodeposition Metal Films, Cold Plate Heat Exchanger, Synthetic Ceramic, Magnetohydrodynamic Active Cooling, Engineering Simulation, Optimality

IN-SITU ADDITIVE MANUFACTURING OF METALS FOR EMBEDDING
PARTS COMPATIBLE WITH LIQUID METALS TO ENHANCE THERMAL
PERFORMANCE OF AVIONICS FOR SPACECRAFT

by

Jerald Armen

Dissertation submitted to the Faculty of the Graduate School of the
University of Maryland, College Park, in partial fulfillment
of the requirements for the degree of
Doctor of Philosophy
2020

Advisory Committee:

Professor Hugh Bruck, Chair

Professor Abhijit, Dasgupta

Professor David, Bigio

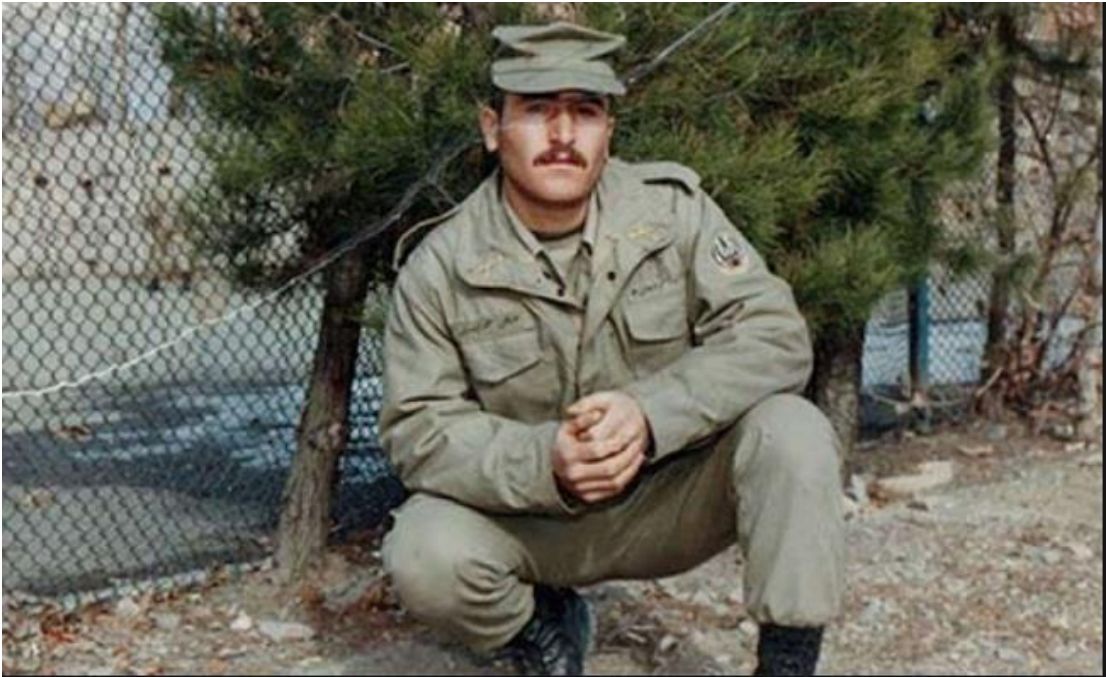
Professor Ryan, Sochol

Professor Kyu Yong, Choi (Dean's Representative)

© Copyright by
Jerald Armen
Doctor of Philosophy

Dedication

In Honor of My Beloved Uncle, **Vigen Garapedi**, Martyr of War



Acknowledgements

I would like to thank my advisor, Professor Hugh Bruck, whose diligence and direction have always inspired me to walk ahead on my research works while he caringly observed from behind. I have known Dr. Bruck since taking his advance composite materials course, a course that covers most key concepts of mechanics. His passion, knowledge and mannerism on how to apply governing principles in mechanical engineering have inspired me to select him as my PhD advisor and he played an important role in shaping my research style.

I am grateful to Professors Kyu Yong Choi, David Bigio, Abhijit Dasgupta and Ryan Sochol for serving on my dissertation committee. Their insightful feedbacks and constructive critics on my dissertation proposal have shown how caring they are to help students improving the quality of their research works. I would like to extend my gratitude to all my dissertation committee members and Professor SK Gupta, my previous co-advisor, for all his passionate guidance and assistance before joining USC Viterbi school of engineering. I also would like to thank Professor Shapour Azarm for sharing invaluable data on engineering optimization; the validation of my algorithms was not possible without his recommended approach.

My sincere thanks to Catherine Gridley VP of Northrop Grumman, Cessily Greene director of space programs, engineering manager Tracey Clay and Dr. John Lenard to facilitate the Northrop Grumman funding for my PhD work. Without Northrop Grumman support, this work was not possible. I also would like to thank my mentor Mr. Viguen Ter-Minassian, a brand name at NASA GSFC, who has treated me like his son in passing the torch to next generation.

I also would like to thank my motivator Dr. Vahe Petrosian from Stanford University, all my teachers and professors throughout my school years who inspired me and made me who I am today. Remarkably, master Gevorg Aboulian my middle school math teacher, scholar Samson Arakelian my Armenian/English teacher who has thought me inspirational poem “Menk” from “Gevorg Emin”. My undergraduate differential equations Professor, Dr. Banifatemi, Professor Richard Seltzer from GCC, computer compiler and programming Professor Claire Bono from USC and Professor James D. Lee from GWU who took my knowledge in continuum mechanics to next level.

I offer sincere respect to my great grandfather Ter Vartan, grandparents Serpoohi, Siran, Savoogh and Aghek, my uncles Vazgen, Bobken, Valod, Edik, Hovhannes and my aunt Maral and Khachik with families for continuous presence and support. Moreover, special thanks to my first cousin Norik Keshishian, a breath-taking road trip of California route one with him and listening to symphony No. 6 of Gustav Mahler, Loris Tjeknavorian, and Andy Madadian was quite fascinating and memorable.

I must admit that playing soccer has played an important role to enhance my concentration and better-developed problem solving skills, and I would like to thank all my FC Ararat of Tehran teammates for creating this joy lasting many years. I also thank my valuable friends Edward Grigorian, Carlo, Neshan, Vahe, Ara, Razmik Karimian. Heros, Allen, Albert Keshishian, Velvet Navasartian, Robert Shirvanian, Nejdeh Azizian Vanand Isajanian, Aris, Henrik Gorgi, Hovik, Dr. Zareh, Dr. George Mathai, Dr. Leyu Wang, Luan ,James Motta and in particular, Dr. Raymond Sarkissian that we have started searching for graduate programs together long time ago, without his inspiration I was not able to make it this far.

Lastly, words cannot express the feeling I have for my mother and father because of their genuine love and unconditional support, I deeply thank you for being amazing parents and my sincerest love to my brothers Zorik and Vazrik, my sister Arpi and her newborn for humbleness, encouragement, understanding and caring. Thank you all!

Table of Contents

Dedication	ii
Acknowledgements	iii
List of Tables	ix
List of Figures	x
Chapter 1: Motivation	1
1.1 Introduction	1
1.2 Brief Overview of Related Works	5
1.3 Overview of Research Methodology and Gaps in the State of Knowledge	7
1.4 Coherent Critical Thinking and Organization of the Dissertation Chapters	13
Chapter 2: Literature Review	17
2.1 Introduction	17
2.2 Material Selection	17
2.3 Manufacturability and Formability	24
2.3.1 Thermal Contact Resistance	25
2.3.2 Attributes of AM Technologies	27
2.4 Performance and Efficiency of MHD	39
2.5 Reliable Thermal Management for High Power Electronics	45
2.6 Conclusion	57
Chapter 3: Interfacial Thermal Resistance of HXs Packaged by Conventional Assembly Methods in Avionics	58
3.1 Introduction	58
3.2 Levels of Avionics Packaging	60
3.3 Interface Contact Resistance	62
3.4 Categorizes of Thermal Management Systems	68
3.5 Development of Metal-Ceramic HX Using Conventional Assembly and Active Cooling with Diaphragm Pump	73
3.5.1 Computational Fluid Dynamics of Active Thermal Cooling Prototype	83
3.5.2 Thermal Testing Setup and Data Acquisition Instruments	88
3.6 Conclusion	91
Chapter 4: Improving Interface Contact Resistance of LM Compatible HXs by In-Situ AM with Embedded Electroplated Ceramic Tubes	92
4.1 Introduction	92
4.1.1 Using LMs as A Class of Coolants for Thermal Control of High-Power Avionics	92
4.1.2 Creating Interfaces Between Ceramic and Metal	94
4.1.3 Manufacturing Metallic HX with Embedded Ceramics by AM	95
4.1.4 Highlighted Attributes of AM on Thermal Efficiency of HX	96
4.1.5 A Strategy to Augment Wettability of Thermal Interfaces	98
4.2 Manufacturability of Metal-Ceramic HXs	100
4.2.1 Iteration #1 (Series, Parallel, and Branched Out FDM Polymeric Tube Inserted in SLM Metallic Block of HX)	100
4.2.2 Iteration #2 (1D Straight Ceramic/Polymeric Tube Embedded in Metallic AM HX)	105
4.2.3 In-Situ SLM Operation to Insert Tubes	111

4.3 Assembly Model of In-situ AM Active Cooling Prototype.....	114
4.4 Thermal Test and Experimental Data	114
4.5 Conclusion	119
Chapter 5: MHD Thermal Management for Avionics Using LM Alloys in Geometrically Complex Structures Realized through AM	122
5.1 Introduction.....	122
5.2 Magnetization and Governing Laws in Electromagnetism.....	123
5.2.1 Biot-Savart Law	125
5.2.2 Ampere’s Circuital Law.....	126
5.2.3 Faraday’s Law of Induction.....	127
5.2.4. Lorentz Force	128
5.3 Development of MHD Cooling Prototype.....	129
5.3.1 MHD Pump Design.....	130
5.3.2 MHD Cold Plate	144
5.4 CAD Model of MHD Cooling Prototype and Boundary Condition.....	145
5.5 Ansys Maxwell Simulations of MHD Cooling Prototype	146
5.6 MHD Active Cooling Thermal Experiment	158
5.6.1 Experimental Setup and Instrumentations	159
5.6.2 Conducting Experiment and Analyzing Data	161
5.7 Conclusion	169
Chapter 6: Optimality of MHD Active Cooling System	172
6.1 Introduction.....	172
6.2 Standard Design of MHD Active Cooling Optimization Model	173
6.2.1 Formulation of Optimality Problem.....	175
6.2.2 Constraints	180
6.3 Surrogate Modeling and Approximation-Assisted Multiple Objective (AAMO) of MHD Cooling System.....	191
6.3.1 Simulation, Preliminary Experiment	193
6.3.2 Sampling Plan	195
6.3.3 Infill criteria and optimizing	196
6.3.4 Exploring and Exploiting.....	197
6.3.5 Convergence Criteria	198
6.3.6 Combining the Concepts for Optimum Latin Hypercube Sampling Process	198
6.4 Optimal Model Verification and Validation	200
6.5 Conclusion	205
Chapter 7: Mission Context and Assessing Impact of MHD Cooling Technology at Spacecraft System Level	206
7.1 Introduction.....	206
7.2 Thermal Management Alternatives Developed in This Dissertation.....	207
7.3 Multiple Criteria Decision Analysis	213
7.3.1 Step 1 of AHP Approach	214
7.3.2 Step 2 of AHP Approach	218
7.3.3 Step 3 of AHP Approach	219
7.4 Brief Overview of System Level Approach of MHD Cooling Technology for Spacecraft Avionics and Big Picture.....	221
7.4.1 Why the Big Picture Matters.....	222

7.4.2 Reuse of Electromagnetic Energy for MHD Thermal Cooling	223
7.4.3 Summary and Root Cause.....	225
7.5 Conclusion	227
Chapter 8: Dissertation Summary	229
8.1 Introduction.....	229
8.1.1 Using LMs for Improving Heat Transfer.....	231
8.1.2 Creating Efficient Thermal Interfaces Between Ceramic Tube and Metallic Block.....	232
8.1.3 In-Situ AM Technology to Embed LM Compatible Ceramic Tubular Insert	233
8.1.4 Driving LM Coolant Through Geometrically Complex Control Volume Using MHD	233
8.1.5 Optimality and Assessing Impact of MHD Cooling Technology at Spacecraft System Level.....	235
8.2 Scientific and Technical Contributions and Intellectual Merit	236
8.3 Conclusions.....	238
8.4 Future Work	243
Bibliography	246

List of Tables

Table 3.1	Thermocouple Readings of Cold Plate Made of SLM Aluminum Alloy with Different Inserted Tubes and Assembled by Conventional Sandwiched Structure.....	90
Table 4.1	Results of Thermal Test and Type T Thermocouple Readings to Evaluate the Thermal Performance of Cold Plate Made of SLM Aluminum Alloy with Different Inserted Tubes and Packaged by In-Situ AM or Conventional Sandwiched Structure	118
Table 5.1	Material Properties of MHD Cooling	149
Table 5.2	Thermal Test of the Prototypes, Showing Results of Passive (Conduction), Active Cooling With No Moving Parts (MHD), and With Moving Parts (Diaphragm Pump).....	164
Table 5.3	Measured Magnetic Field (Gauss) at the Tip of Geometrically Optimized C-Shaped Core Under Direct and Alternate Current Excitation for Two Different Materials: Soft-Magnet Hiperco50A and Stainless Steel 718....	169
Table 6.1	Characteristics of Gauge 22 Magnetic Copper Wire, Computed Based on 100% IACS Conductivity of 58.0 MS/m and at 68 °F	178
Table 6.2	Hydraulic Pressure Loss in Fittings	183
Table 7.1	The Performances of Four Thermal Management Alternatives Based on Three Attributes (Values Are Arbitrary and Solely Based on Decision Maker’s Judgment)	214
Table 7.2	Pairwise Comparison of Cooling Technologies Attribute #1	215
Table 7.3	MATLAB Program Output for Eigen Related Analysis Attribute #1	215
Table 7.4	Pairwise Comparison of Cooling Technologies Attribute #2	216
Table 7.5	MATLAB Program Output for Eigen Related Analysis Attribute #2	216
Table 7.6	Pairwise Comparison of Cooling Technologies Attribute #3	217
Table 7.7	MATLAB Program Output for Eigen Related Analysis Attribute #3	217
Table 7.8	Hypothetical Alternatives	218
Table 7.9	Pairwise Comparison of the Hypothetical Alternatives.....	218
Table 7.10	MATLAB Program Output Step 2.....	219
Table 7.11	AHP Total Scores for Attributes.....	220

List of Figures

Figure 1.1	Organization of the chapters of the dissertation and critical thinking of dissertation	14
Figure 2.1	A phase diagram and microstructure diagram of an alloy system with limited solubility of the components for a fictitious binary chemical mixture (with the two components denoted by A and B) used to depict the eutectic composition, temperature, and point.	18
Figure 2.2	Thermoplastic engineering materials as subclass of engineering plastics.....	21
Figure 2.3	Industrial revolutions and futuristic manufacturing system.....	27
Figure 2.4	Thermal loading of three layers in powder bed based fusion of AM process.....	29
Figure 2.5	Modeling of AM laser bed based fusion process, incremental physics fidelity, significantly alters the heat transfer (temperature range 4000°K to 293°K), melt pool depth and flow	31
Figure 2.6	Goldak's moving spot (left) compared to scaled Lined input (middle) and scaled elongated ellipse (right) power densities, unscaled peak values are less intense than Goldak's model and not visible.	33
Figure 2.7	Metal powder bed based laser process simulation showing In situ single bead thermal contour (°K) (top), b) Compressive longitudinal stress (MPa) by balancing force and momentum (bottom).....	35
Figure 2.8	AM Inconel 625, minimized support structure, specimen: heat sink with fins (3mmx10mmx18mm)	36
Figure 2.9	3DSIM AM simulation, Post processing Von Misses Stress "Pa" for orientation 26 degree relative to print bed, voxel .4 mm relaxation factor .8	37
Figure 2.10	Post processing results of FEA AM model cylindrical part	38
Figure 2.11	Developed velocity profile for MHD channel (HIMAG software)	41
Figure 2.12	MHD incompressible flow, pressure gradient K in a square duct as a function of the Hartmann number Ha.	42
Figure 2.13	Patrick Gelsinger, an Intel executive, predicted that unless something changed, computer chips would become hotter than nuclear reactors within a few years.	46
Figure 2.14	Schematic of electromagnetic pump, broken down into three subsections: the pump channel, the magnet and the electrode	49
Figure 2.15	Active cooling with LM showing cold pate temperature of LM cooling product and PCCooler- HP-1216V (copper/aluminum Heat pipe CPU Cooler)..	50
Figure 2.16	Temperature distribution in the computational domain with LM cooling and water-cooling, under discharge rate of 3C and inlet velocity of 0.1 m/s.....	52
Figure 2.17	Cell center temperature distribution under different discharge rate, with coolant flow velocity of 0.1 m/s	52
Figure 2.18	Average temperature of the four cells under different coolant velocity, with discharge rate of 3C.	53

Figure 2.19	Hot spot temperature measured by thermistor when energizing the microheater with different voltages ranging from 1 to 4.5 V.	54
Figure 2.20	Different geometries used in analysis: (a) V-type (b) A-type (c) rectangular. By Sharma et al.....	55
Figure 2.21	Temperature contour for rectangular and V-type cross section of the pipe.....	56
Figure 3.1	A plot of CPU transistor counts against dates of introduction.....	59
Figure 3.2	Levels of avionics packaging.....	61
Figure 3.3	1D Conduction in solid layers in series for assuming 100% contact.....	62
Figure 3.4	Thermal bottleneck creates a "contact" resistance to conducting heat across the interface.....	63
Figure 3.5	Application of thermal interface materials between two solids to fill the air gaps in order to improve the heat conduction.....	64
Figure 3.6	Range of thermal conductivity for various states of matter at normal temperature and pressure. (courtesy of GE crops).....	65
Figure 3.7	Temperature dependence of thermal conductivity for various selected solids.	65
Figure 3.8	Performance of compressible thermal interface materials changes with pressure	66
Figure 3.9	Effect of surface finish on contact conductance of Aluminum and Magnesium.....	67
Figure 3.10	Effect of surface finish on contact conductance of 304 Stainless Steel and Copper.	68
Figure 3.11	Categories of thermal management systems.....	69
Figure 3.12	Exploded view of single phase microchannel liquid cooled cold plate. Thermal Stack includes: branched out heat pipe, interface material, metal plate and clamping mechanism.....	71
Figure 3.13	Heat transfer coefficients depending on cooling technologies	72
Figure 3.14	CAD model of active cooling prototype including Peltier cooler, diaphragm pump, reservoir, sandwiched structure of conventionally assembled cold plate including embedded copper or silver plates and ceramic tubes	73
Figure 3.15	Basic physics of thermoelectric Peltier cooler with solid-state construction.....	74
Figure 3.16	Cooling performance graph of CP-121 Peltier cooler from tetech.com ...	75
Figure 3.17	Schematic of Diaphragm Pump, flow rate .3 L/min and maximum pressure head 14.5 PSIG.....	75
Figure 3.18	CADDOCK, MP9100 Series Power Film Resistors.....	76
Figure 3.19	Derating curve and specification of mounting resistors (heat source).....	76
Figure 3.20	Resistors parallel grid providing total electrical resistivity required to generate power to dissipate heat	77
Figure 3.21	Exploded CAD model of cold plate including BN pipes, gauge 20 copper plate (.8mm thick), encapsulated by conventional manufacturing of 3 piece SLM aluminum alloy block (final envelope size is 100x185x18 cubic mm)	78

Figure 3.22	Exploded view of conventionally assembled cold plate including FDMed Ultem tube, gauge 20 copper (top row) or silver (bottom row) off-the-shelf plate, fastened with #4-40 screws torqued to 4.7 IN-LB.	78
Figure 3.23	Exploded view of conventionally assembled cold plate including ceramic tube, gauge 20 silver (left) or copper (right) off-the-shelf plate and #4-40 stainless steel screws torqued to 4.7 IN-LB to 3- piece SLM aluminum metallic block.....	79
Figure 3.24	Galinstan, viscosity vs temperature curve	80
Figure 3.25	LM compatible Series 2000 variable area flow meter (flowmetrics inc) and its schematic view showing subassemblies and piece parts.....	81
Figure 3.26	Calibration worksheet for Galinstan, Dynamic viscosity= .0024 Pa.s and Density 6.44 g/cm ³	82
Figure 3.27	Flow meter is connected in series to flow line to measure the flow rate and removed for thermal testing	83
Figure 3.28	Ansys Fluent, preprocessing tetrahedron adaptive mesh of control volume and cold plate of active cooling prototype by diaphragm pumping	84
Figure 3.29	Characteristics curve of diaphragm pump, applied in CFD simulation for forced correlation-based convection couplings.....	84
Figure 3.30	Ansys Fluent, steady state converging solution for monitored points for parameters of interest i.e. velocity after several iterations	85
Figure 3.31	Ansys Fluent CFD post processing results of active cooling by diaphragm pump and circulating Galinstan LM coolant through cold plate to reservoir in closed loop	86
Figure 3.32	Ansys Fluent active cooling by diaphragm pump: post processing report.....	87
Figure 3.33	Active cooling with moving parts and conventionally packaged cold plate (3-piece cold plate, BN ceramic or FDMed Ultem tubes, and gauge 20 copper or silver plate).....	89
Figure 3.34	Polycode of cold plate types used on Table 3.1 (block material for all cases is AM aluminum alloy AlSi10Mg).....	90
Figure 4.1	Four candidates tubes consideration to eliminate support structure for overhang in AM process and maximizing surface area normal to heat load.....	101
Figure 4.2	Cross section of LM compatible polymeric (Ultem) tube with 1) irregular pentagon for outer profile 2) circular interior profile ID=4 mm and min wall thickness amenable for FDM is 1mm (iteration #1)	102
Figure 4.3	A). Isometric view of CAD models (185mmx100mmx18mm), B). Prefabricated channels for insertion in SLM process (ID 4mm), wall thickness 1mm, material: Ultem, C). Post processing of fabricated channels (.05mm thick copper plating and .012 mm nickel plating) D). Fabricated in-situ cold plate by SLM process (EOS290 machine) material aluminum alloy AlSi10Mg_200.	103
Figure 4.4	X-rays images normal to top surface of insitu DMLS cold plate (model: Go Terps I) at partial locations labeled A, B and C taken by GE Phoenix Nanome X (140kV, 50UA beam power), showing the damaged	

	copper/nickel plated Ultem pipe inserted in SLM aluminum alloy process.....	104
Figure 4.5	Simplified 1-D profile of LM tube with irregular pentagon as outer profile and circular inner profile feasible for CNC machining or FDM process of iteration #2.....	105
Figure 4.6	In-situ SLM process showing inserted bare solid BN ceramic tube in aluminum alloy block, when scanning the layer on top of the ceramic, the powder was unable to adhere causing the build to fail.	106
Figure 4.7	Copper electroplated (.8mm thickness) ceramic BN tubes in electrolytic solution during electrodeposition process, required surface of ceramic is metalized prior to deposition process.....	107
Figure 4.8	X-ray images from GE Phoenix Nanome X (140kV, 50UA beam power) of ceramic-metal in-situ AM cold plate.....	109
Figure 4.9	LM compatible tubes (plated vs nonplused) prepared for cold plate.....	110
Figure 4.10	Set of LM compatible tubes.....	111
Figure 4.11	Upper row (left to right) 1. Cultivation of CAD model for in-situ AM showing embedded tubes for subtraction 2. Finalized CAD model 3. Partially printed block ready for insetion. Lower row (left to right) 1. Inserted tubes inside channels of SLM block. 2. Finished in-situ AM cold plate (roller of AM SLM process is shown) 3. Removed cold plates from print bed by electrical discharged machining (EDM).....	113
Figure 4.12	(left to right) In-situ SLM (EOS AISI10Mg_200) cold plate including 1).Bare inserted ceramic tubes. The aluminum delaminated from the ceramic and failed to finish 3D 2). Bare BN ceramic tubes are glued and sprinkled aluminum powder on flat surfaces prior to insertion, failed to finish 3D 3). Silver plated Ultem inserted tubes 4). Copper plated Ultem inserted tubes 5). Copper plated solid BN inserted tubes 6). Silver plated solid BN inserted tubes (iterations 3 to 6, successfully finished SLM).	113
Figure 4.13	CAD model of active cooling prototype including 1) diaphragm pump, 2) Peltier cooler, 3) LM reservoir, 4) in-situ SLM cold plate with embedded copper plated ceramic tubes 5) MP9100 Caddock resistor (12x) 6) Nylon coupling 7) Polypropylene flex tube 8) #4-40 mounting hardware (4x).....	114
Figure 4.14	CAD model of in-situ SLM cold plate including two copper plated (0.8 mm) solid BN ceramic tubes (100 mm x 185 mm x 18 mm)	115
Figure 4.15	Exploded CAD model of cold plate including BN pipes, gauge 20 copper plate (0.8 mm thick), encapsulated by conventional manufacturing of three-piece SLM aluminum alloy block (final envelope size is 100 mm x 185 mm x 18 mm)	115
Figure 4.16	In-situ SLM cold plates including copper- or silver-plated BN ceramic pipes creating superior bonding by fusion of silver (or copper) with aluminum alloy AM powder (left) compared to conventionally assembled cold plates (right) including three-piece SLM aluminum alloy block, gauge 20 copper or silver off-the-shelf plate.	116

Figure 4.17	Assembly of active cooling prototype and location of thermocouples (TC#).....	117
Figure 4.18	Comparison of cold plates fabricated by in-situ SLM technique.	119
Figure 5.1	Technologies applied to development of MHD thermal management ..	123
Figure 5.2	Response of magnetic material represented by permeability under influence of the magnetic field strength H, which is generated by the current I flowing in the coil.	124
Figure 5.3	B-H curve, Hiperco50A and Iron- Induced Field vs Applied Field	124
Figure 5.4	Magnetic field lines of a long conductive wire carrying electrical current	125
Figure 5.5	Magnetic field inside a long solenoid with n turn and electrical current I	126
Figure 5.6	The circuital law used to determine the magnetic field strength (H) in a toroidal magnetic circle with n turns and electrical current I	127
Figure 5.7	Schematic of a DC generator (left), a transformer (middle) and eddy current (right)	128
Figure 5.8	The principle of measuring of the flux density B in a magnetic circuit .	128
Figure 5.9	Fleming's right hand rule showing direction of Lorentz force	129
Figure 5.10	Coercivity, saturation magnetization, and remanence of various magnetic materials	131
Figure 5.11	Electromagnet as a source of magnetic field with inefficient flat tips....	132
Figure 5.12	Flat and tapered poles of magnet or electromagnet i.e. D=250mm	133
Figure 5.13	Tapered pole of electromagnet.....	133
Figure 5.14	Morphology of electromagnet C-shaped core, 2D drawing for CNC machining of hiperco50A core.....	134
Figure 5.15	From left to right: granulized Hiperco50A block(5"x3.4"x5.2"), fixture for CNC machining, tooling for winding, C shape tapered hiperco50A magnetic core with magnetic wounds (2x650 turns AWG 22).....	135
Figure 5.16	MHD pump electromagnets with two magnetic materials for C-shaped core (hiperco50A vs magnetic stainless steel).....	136
Figure 5.17	Ferromagnetic material under magnetic field creates its own magnetic field (the magnetized sample operates as a magnet due to poles induced at its ends).	137
Figure 5.18	Dependence of the demagnetizing factor of ellipsoid on its shape factor c/a (length to diameter ratio).....	137
Figure 5.19	Demagnetizing factor along applied field for elliptic shape	138
Figure 5.20	Major and minor diameters of LM container in x-y plane.....	139
Figure 5.21	Isometric and projection views of ellipsoid LM container in MHD pumping, including inlet and outlet for LM, provision for insertion of copper electrodes generating electric field required for Lorenz force.	140
Figure 5.22	Magnetic curves, encompassed in ellipsoid container to reduce eddy current	140
Figure 5.23	Inserted tungsten plated copper electrodes of MHD pump (4.8mmx50mmx.8mm)	141
Figure 5.24	AM SLS Nylon 6,6 with wired electrodes elliptic coupling for AC and DC powering	142

Figure 5.25	Electric current flows through closed loop of control volume of LM, with major will take the path of least resistance that is shortest distance between electrodes and perpendicular to magnetic field	142
Figure 5.26	Copper electroplated with gold finish on SLS nylon 6,6 inside immersed in electrolyte solution during electrodeposition process.....	143
Figure 5.27	Fabricated elliptic coupling with AM SLS technology: (left to right) 1). Electroless .1” silver plated nylon 6,6 . 2) Electroforming .1” copper with gold finish nylon 6,6 and 3). Bare nylon 6,6. (lengths of coupling are 50,20 and 5mm along flow, electrode and magnetic flux directions respectively).....	144
Figure 5.28	Components (left) and assembly (right) of cold plate including: AM Aluminum alloy (AlSi10Mg_200) 3 piece block (total size: 185mmx100mmx18mm), embedded LM compatible thermally efficient solid BN tubes (internal diameter= 6.2mm),also heat source (12x15Ohms parallel resistors) and elliptic Nylon 6,6 SLS coupling with embedded electrodes ,#4-40 stainless steel fasteners torqued to 4.7 LB-IN.....	145
Figure 5.29	MHD cooling system: 1) hiperco50A CNC machined, 2) elliptic coupling SLS Nylon66 3) DMLS hybrid (AlSi10Mg_200) heatsink with embedded BN ceramic heat tube 4) gauge 22 AWG magnetic wire 5) tapered tip of core 6) Glass reservoir containing Galinstan7) tungsten plated copper electrode 8)MP9100 Caddock resistor 9)Nylon tube fitting 10)Polypropylene tube 11)Peltier cold plate P/N TE CP121 12) MHD pump bracket 13) reservoir holder 14) mounting hardware.....	146
Figure 5.30	Ansys Maxwell preprocessing, defining rectangular open region that best fits the MHD cooling prototype	149
Figure 5.31	ANSYS Maxwell preprocessing, assigning B-H curve for C-shaped hiperco50A.....	150
Figure 5.32	Preprocessing in Ansys Maxwell, showing adaptive tetrahedron meshing refinement applied to elements of the MHD pump to maximize accuracy of magnetic flux density, excitations (6 Amp-650turns) to two copper winding with AWG 22 magnetic wire.....	151
Figure 5.33	Ansys Maxwell, magnetic field contour of finite region, witnessing needs for EMI shielding.....	152
Figure 5.34	Post processing in Ansys Maxwell, showing projection views distribution of magnetic flux density by applying (650 turns 6 amp) to windings.....	152
Figure 5.35	ANSYS Fluent MHD module, for enabling application of Lorentz force to fluid by induced magnetic field to LM	153
Figure 5.36	ANSYS FLUENT Preprocessing with adaptive tetrahedron meshing, boundary condition (10°C boundary condition) in blue arrows for the Peltier cooler, heat source in red arrows, induced magnetic field in orange arrows and electrical current to electrodes in purple arrows.	154
Figure 5.37	Ansys Fluent MHD, converge solution of critical parameters	154

Figure 5.38	Ansys Fluent MHD, boundary condition : induced magnetic field applied to LM, generated from external magnetic field from C-shaped core in tesla	155
Figure 5.39	Ansys Fluent MHD, boundary condition : applied electrical field to electrodes in volts	155
Figure 5.40	MHD Fluent, post processing, pressure profile of control volume due to Lorentz force (left), scaled view of elliptic portion of control volume (right) in pascal	156
Figure 5.41	MHD Fluent, post processing, velocity profile of control volume due to Lorentz force (left), scaled view of elliptic portion of control volume (right) in meter per second.....	156
Figure 5.42	MHD Fluent, post processing, Temperature profile of heat sink block in active cooling system derived by MHD pump running Galinstan (top and bottom views), scaled view showing interfaces of tube inside the block (conjugate convective heat transfer) in °C.....	157
Figure 5.43	MHD active cooling test components, showing components of AC and DC power setup, Peltier cooler (B.C.) set to 10°C, and ambient temperature of 25°C.....	160
Figure 5.44	Prototype I: Active cooling with no moving parts (MHD pumping) and location of thermocouples (TC#) identical with diaphragm pumping....	162
Figure 5.45	Prototype II: Active cooling with moving parts (diaphragm pump), identical setup with MHD cooling including similar cold plate geometry and material, control volume, applied load ,boundary condition and location of thermocouples (TC#)	163
Figure 6.1	Roadmap of AAMO: screening design of experiments (DOE) meta-modeling, verification exploring and exploiting.....	173
Figure 6.2	Inlet of magnetic flow (area of coupling) vs area of pipe are shown	176
Figure 6.3	Geometric details of magnetic core	178
Figure 6.4	Electromagnet core including two coils, showing limits of design variables	180
Figure 6.5	Derating temperature for curve resistor MP9000 Series Kool-Pak from Caddock electronics Inc.....	184
Figure 6.6	Isometric view of geometrically optimized cold plate with embedded ceramic pipes, the gap between pipes is influenced by length of elliptic coupling defined by magnetization criterion for elliptic shape.	185
Figure 6.7	Demagnetizing factor along applied field for elliptic shape.....	186
Figure 6.8	Field generation in the gap of permanent magnet polar pieces with troncoconical pole tips.	187
Figure 6.9	Dependence of the demagnetizing factor of ellipsoid on its shape factor c/a (length to diameter ratio).....	188
Figure 6.10	Optimal shape for magnetic MHD pump coupling, to reduce demagnetization effect, $a=5\text{mm}$, $b=20\text{ mm}$, $c=lg=2.5\text{ mm}$, magnetic field is in line with ‘c’ dimension, perpendicular to ‘b’ and ‘a’	188
Figure 6.11	Constrained multi-objective optimization of the MHD cooling system using Approximation Assisted Approach	192

Figure 6.12	Extracted data from Ansys Fluent for first objective of optimization (generated gauge pressure) for d=6.2mm, I-1.7A and 650 turns for mag wire	193
Figure 6.13	Extracted data from Ansys Fluent for Second objective of optimization (maximum temperature of heat sink) for d=6.2mm, I-1.7A and 650 turns for mag wire.....	194
Figure 6.14	Space filling Latin Hypercube Morris-Mitchell optimum sampling plan of MHD cooling, A randomly generated Latin hypercube design (LHD) is structured for MHD cooling model.....	196
Figure 6.15	Pareto Frontier of MHD cooling extracted from approximation assisted optimization multi objective approach.....	199
Figure 6.16	Pareto frontier of MHD from Pareto points by 4th generation Bezier smoothing technique	200
Figure 6.17	Ansys Maxwell simulation for verification per optimal surrogate model (magnetic field) for 201 turns of magnetic wires and 3.39 Amp applied current.	201
Figure 6.18	Ansys Fluent MHD module simulation for verification per optimal surrogate model (temperature profile) for 201 turns of magnetic wires and 3.39 Amp applied current and 9 mm for internal diameter of ceramic pipe	202
Figure 6.19	Ansys Fluent MHD simulation for verification per optimal surrogate model (velocity profile) for 201 turns of magnetic wires and 3.39 Amp applied current and 9 mm for internal diameter of ceramic pipe.....	203
Figure 6.20	Ansys Fluent MHD simulation for verification per optimal surrogate model (pressure profile) for 201 turns of magnetic wires and 3.39 Amp applied current and 9 mm for internal diameter of ceramic pipe.....	203
Figure 6.21	Ansys Fluent MHD simulation for verification per optimal surrogate model (electrical potential) for 201 turns of magnetic wires and 3.39 Amp applied current and 9 mm for internal diameter of ceramic pipe...	204
Figure 6.22	Ansys Fluent MHD converged results from inputing optimized variables 201 turns of magnetic wires and 3.39 Amp applied current and 9 mm for internal diameter of ceramic pipe.....	204
Figure 7.1	Prototype #1: MHD active cooling system including 1) MHD HX including conventionally assembled aluminum alloy block, gauge 20 silver off-the-shelf plate and ceramic pipe 2) Peltier cooler 3) Data acquisition unit 4) Potentiometer 5) flowmeter 6) High voltage power supply 7) AC Signal generator 8) Amplifier 9) Temperature controller	208
Figure 7.2	Prototype #2: Active cooling prototype including LM compatible diaphragm pump and in-situ hybrid AM cold plate with embedded silver plated ceramic pipes.....	210
Figure 7.3	Prototype #3: Active cooling by diaphragm pump and conventionally assembled cold plate including 3-piece SLM aluminum alloy block, gauge 20 silver off-the-shelf plate.	212
Figure 7.4	Prototype #4: Passive cooling heat source mounted to conventionally assembled cold plate including 3-piece SLM aluminum alloy block, gauge 20 silver off-the-shelf plate, ceramic pipes with LM inside.....	213

Figure 7.5	Exploded view of NASA LCROSS Robotic Spacecraft including subsystems generating undesired electromagnetic energy	224
Figure 7.6	Root definition for MHD cooling technology at spacecraft system level.....	226
Figure 7.7	Conceptualized exploded view of spacecraft avionics including MHD cooling, magnetic field is generated from leaked undesired magnetic fields from electronics, sun's magnetic energy and magnetic pump.	227

Chapter 1: Motivation

1.1 Introduction

In this fast-approaching post-digital era marked by significant advancements in transistor technology, electronic systems are becoming lighter, more compact, and efficient. For space avionics, this has been achieved through micromachinery, aggregation of sensors, and more powerful microcontroller platforms. This has also resulted in more complex electronic systems that have smaller volumes and increased thermal density, which requires more effective thermal management solutions. The need for high reliability in space avionics requires very capable thermal management systems but must contend with limitations and costs in size and weight of the system needed to dissipate the generated heat. Therefore, creative solutions are needed using advanced manufacturing methods and use of exotic materials for future powerful rockets. Liquid metals as a class of coolant offer the advantage of high thermal conductivity and thermal capacity to transport the heat from the source to the heat sink. Additionally, their high electrical conductivities allow them to be circulated by an MHD with no moving parts, making it a superior coolant choice for reliable active cooling system. This dissertation presents a study of the use of LM as the coolant in an electronic thermal management system and describes solutions to the many problems involved.

The primary problem with LMs, such as gallium alloys, is they are highly corrosive to all metals except tungsten and tantalum. To combat the corrosion issue, LMs must be encapsulated in a compatible ceramic or polymeric container, which also needs to be thermally conductive to dissipate heat. One candidate is the ceramic Boron Nitride (BN), which is compatible with LM, machinable, and has a high thermal conductivity.

Engineering thermoplastics were also considered as the LM coolant container in a weighted tradeoff study, based on their structural and environmental performance, and compatibility with the LM. Thermally conductive thermoplastics, such as Ultem, have the ability to withstand long-term exposure to elevated temperature and are categorized as space qualified material due to their outgassing properties, but are thermally inefficient.

Solid boron nitride and thermally conductive thermoplastics are fragile and have wear resistance issue, causing reliability concerns. To guarantee structural integrity, the ceramic or thermoplastic tubes are embedded in a strong thermal structure such as a metallic block with the use of in-situ Additive Manufacturing (AM) techniques. Within the subassemblies of the thermal structure, there is also the requirement to transfer the heat efficiently through the interfaces with the constraint of material compatibility.

However, interfacial thermal resistance creates a bottleneck for heat transfer and negates the thermal transfer efficiency of each stack component. Heat transfer associated with interfaces in gas-solid, liquid-solid and solid-solid interactions are not well studied, and only a few studies have been conducted to understand the basic mechanism of inherent thermal boundary resistance.

Due to surface roughness and tolerance stack-up in an assembly, the actual contact area is significantly less than the apparent contact area of heat transfer systems manufactured by conventional techniques. Therefore, a conductive filler (thermal grease, pliant thermal gasket, or metallic thin foil) is often used to decrease interface thermal resistance, but these compliant materials most often have very poor thermal conductivity. Therefore, the superior thermal conductivity of individual elements that makes them excellent candidates for a hybrid heat spreader is reduced by interfacial resistance in the

assembly, drastically impacting the overall passive thermal conductivity. In-situ AM assembly, using powder bed-based melting such as Selective Laser Melting (SLM), can fabricate parts by printing metal on top of a plated LM compatible structure, which then produces a superior thermal interface.

However, there are technical challenges associated with in-situ AM processes. The first challenge is related to the feasibility of inserting foreign parts such as a tube in the metallic AM block and the possible collision of the embedded part with the powder coater and roller during the powder bed-based melting processes. The inserted part can collide with the roller and halt the SLM operation. A second issue is the melt pool depth and flow while printing the next layers in SLM process on top of the inserted part. This requires further investigation to understand the characteristics of the "processing-structure-property" relationship of the interface for the printed part. Additional challenges involve survivability of the insert of the in-print assembly from radiation of the laser beam, the wettability of the multi-material interface during laser fusion, as well as convection of melt pool, which has the potential for destroying delicate features of the embedded part.

Primarily, this dissertation addresses these challenges for embedding LM compatible parts using in-situ AM by investigating approaches for embedding the parts and enhancing interfacial contact. This involved the following: (1) determining appropriate morphologies for inserted parts compatible with the AM process and thermal performance, (2) enhancing the bonding of the major interfaces and seams through electroplating of embedded parts to reduce interfacial thermal resistance, (3) determining the intensity of laser penetration into the mixed interface layer affecting formation of the

interface, (4) determining the tolerance stack-up of mating parts for compatibility with the AM process, and (5) minimizing the coefficient of thermal expansion (CTE) mismatch for the embedded part through material selection. Therefore, this study revealed the potential of in-situ AM to overcome limitations of traditional manufacturing resulting in improvement of thermal contact resistance at interfaces of layered thermal structures, “a major advantage for heat transfer application”.

Furthermore, to realize the full potential of using LM for heat dissipation, this dissertation investigates using MHD as the driving force for active cooling. This results in the development of a prototype hybrid heat exchanger (HX), that can be optimized for significantly higher power dissipation through MHD modeling. This results in many benefits:

1. Geometric optimization of the MHD pump, which impacts the intensity of induced magnetic field and applied electric field to LM , and consequently affects the flow efficiency through Lorentzian force
2. No moving parts for the active cooling system results in greater reliability, since there is no wear caused by friction and movement of pump components.
3. Minimal maintenance, including functional checks, servicing, repairing, or replacing of necessary devices, making the system highly suitable for long mission space applications.
4. Short transient time, as the driving and control system does not have a inductor or a capacitor as energy storing elements and converges quickly to steady state.

5. Compatibility of applied cooling technology to space flight hardware.

The presented MHD cooling solution is based on applied governing principles in electromagnetic coupled with fluid dynamics to develop the concept. The concept is then transformed to suitable model for engineering simulation. The outcome of iterative simulations resulted in geometrically optimized models to overcome coercivity and demagnetization losses and yet compatible with corrosive LM. Geometrically optimized complex structures are amenable to AM and fabricated by adapting AM techniques. Finally MHD cooling is synthesized to perform experimental test to realize behavior of flow regime per MHD dimensionless parameters extracted from experiment and draw scientific conclusions. These are the significances distinguishing this new way of thermal management for avionics from previous endeavors.

1.2 Brief Overview of Related Works

A wealth of research has been conducted in avionics cooling. However, limited research exists on active cooling by LM realized through AM technologies. Chapter 2 of this dissertation is dedicated to literature review, investigating noteworthy evidence and limitations in previous efforts to justify this research. However, it is worth to briefly mention highlighted works related to avionics cooling by LM.

In this regard, eutectic gallium alloys have been shown to improve thermal conductivity of heat transfer structures using conductive MHD pumping for central processing units (CPUs), but rapidly fail due to corrosion (Deng et al, 2013). Tang et al demonstrated how a LM bead could drive flow of an ionic fluid (salt water) by applying square wave signal across it to create a pressure differential through the Lippman Effect (Tang et al, 2014). A novel technique is developed to suspend the powder in LM

composite fluid to enhance its magnetic properties for MHD pumping (Carle et al, 2017). LM can be pumped by pipetting 40 ul into a reservoir and applying square wave signal across it where the surface tension of the fluid is altered near the surface of the Galinstan drop due to the charge density and resulting difference in surface tension causes a pressure drop inversely proportional to the size of the Galinstan drop (Young-Laplace equation) (Zhu & Khoshmanesh, 2016). Jeff Didion at NASA GSFC had invented a single phase thermal control system using "small interdigitated plates" to characterize the operations of electrohydrodynamic techniques for flow management and heat transfer enhancement (Didion, 2001).

The UMD Advanced manufacturing lab, directed by professor Bruck have studied rheology and melt flow for in-mold assembly of pre-molded components in applications such as thermal management related to proposed heat exchange structures (Hall et al, 2012; Ananthanarayanan & Gupta & Bruck, 2010; Bejgerowski & Gupta & Bruck, 2009). To resolve some of these issues using LMs and AM processes, electrostatic and vacuum powder removals have been investigated for powder based AM which does not work for closed cavities (Rodriguez et al, 2015; Lappo et al, 2003). Support optimization for overhangs is also an active research for FDM which requires post processing to remove support structures (Kumar et al, 2012). FDM has been used to deposit Gallium-Indium via syringes but challenges have arisen due to oxidation, clogging of the nozzle, and poor bonding between drops due to surface roughness were found to be issues (Jacoby et al, 2016). Based on previous researches on conductive polymers with non-metallic fillers for tactile sensing, it is possible to create a multifunctional interface by encapsulating the LM with a conductive polymer that prevents corrosion while

conducting enough current for MHD and transporting enough heat for thermal performance (Barnett et al, 2017; Robinson et al, 2011; Bilger et al, 2017). Vader systems has patented the AM deposition methodology through manipulation of LM through magnetism, but oxidation and clogging of the nozzle are the challenges to face with (Vader, 2017 Sukhotskiy et al, 2017). Metal-doped gallium oxide based FDM is investigated at UTEP and bonding between drops and surface roughness are the manufacturing challenge (Rubio, 2016).

1.3 Overview of Research Methodology and Gaps in the State of Knowledge

The following steps demonstrates a coherent panoply of clarifications in place to argue and describe solutions to many concerning problems.

1. Problem: With the application of microcontroller on spacecraft, electronics get smaller and faster, resulting in greater localized heat generation, therefore; efficient thermal management systems are required for avionics packaging.
Solution: Increase the thermal efficiency of the thermal systems using LM alloys as a class of coolant. Their high electrical conductivities allow circulation by a simple, silent with short transient time electromagnetic pump. However, LMs are corrosive to metals and they have to be contained in thermally conductive ceramics or polymers for heat transfer application with consideration of wetting issue between ceramic and LM due to intermolecular interactions caused by balance between adhesive and cohesive forces for LM.
2. Problem: Selection of solid BN ceramic or thermally conductive polymer LM compatible containers are wise choices where corrosion resistance is more important than wear resistance for heat transfer. However, solid BN is a fragile

diffusion bonded ceramic with wear and tear issues and not strong enough to withstand the applied mechanical stresses. Alternatively, thermally conductive thermoplastics such as Polyetherimide, PEI (C₃₇H₂₄O₆N₂)_n commonly named (Ultem) has been used for space application because of its ability to withstand long-term exposure to elevated temperatures and low outgassing properties. However, they have thermal inefficacy, derating and wear and tear issues. Solution: To increase structural integrity and dimensional stability of thin wall LM compatible tubes, encapsulate them in metallic housing.

3. Problem: Contact resistance in solid interfaces that are inherently rough and actual contact area is significantly less than the apparent contact area is a thermal bottleneck for cold plates fabricated by conventional manufacturing techniques. Solution: There has been an opportunity for adapting in-situ AM to overcome limitations of traditional packaging techniques that can produce a superior bond at interfaces of layered thermal structures.
4. Problem: Complexity of insertion process of in-situ AM and wettability of ceramic and metal interfaces, solid BN will not fuse to metallic powder in powder bed-based melting and heat generated from laser will damage the inserted polymeric container. Solution: First, the material of the inserted part must have a high melting point to withstand the temperature of build chamber and prior insertion, the morphology of the prefabricated LM compatible tubes had to be optimized to prevent collision with roller or blade of powder bed based AM process. Additionally, the geometric gap due to tolerance stack up between the inserted part and the mating channel should be filled with powder

around the inserted part in powder bed based AM process, otherwise short feeding issues might occur. Furthermore in-situ placement of foreign part in SLM block with different material properties is another challenge (CTE mismatch between ceramic/polymeric tubes placed inside the aluminum channels). Moreover, deposition of metallic layer (plating) on ceramic or plastic part before placement in SLM AM process will enhance the wettability of the ceramic tubes during laser fusion, resulting in an order of magnitude improvement in heat transfer compared to cold plates packaged by conventional assembly. LM containers (tubes) can be silver or copper/nickel plated prior to the insertion process. (An electroless nickel process to get the ceramic (polymeric) tubes conductive, and then electrolytic copper and finally nickel to protect pure copper from corrosion).

5. Problem: Reliability issues of active cooling with moving parts and inefficiency of active cooling with MHD pump due to unsatisfactory structures fabricated by conventional manufacturing techniques resulting demagnetization issue retarding the flow rate. Solution: The flow of a low-melting point eutectic alloy encapsulated in channels is dramatically different from polar liquids because of the surface tension and conductivity, allowing for different pumping concepts such as MHD to be used in new heat exchanger concepts based on liquid metals. Moreover, fabricate the geometrically complex but optimal and compatible structures of MHD pump by AM techniques cost effectively. However, there are challenges related to implementation of MHD pumps:

- Electromagnetic saturation can put a practical limit on the maximum magnetic fields achievable in ferromagnetic electromagnetic core and consequently increases the size of the electromagnetic pump. Selection of appropriate core material i.e. Hiperco50A or powering by AC pulsed might improve efficiency and saturation issue.
- The forces of LM are "cohesive" rather than "adhesive" which is similar to water with ceramic or plastic tubes. Inverted meniscus increases the resistance to motion through tubes, meaning more pumping pressure (not to mention the extra pressure from the substantially higher inertial force of liquid metals). However, greater heat transfer ability of LM should offset the greater pumping power.
- The movement of an electrically conductive material in a magnetic field generates electric currents that induce forces on the medium known as Lorentz force and the induced magnetic flux is shape dependent. The shape dependent demagnetizing field opposes the magnetic field and deteriorates permeability of induced coolant. The fabrication of optimal coupling structures used in MHD pump is not amenable to conventional manufacturing techniques. There has been an opportunity for SLS AM to overcome these limitations to fabricate neat net shape (NNS) MHD structures cost effectively.
- To block the electromagnetic influence of magnetic field generated by electromagnet on electronics, a Faraday cage is required. The electromagnetic core shall be placed in a shielded enclosure and magnetic

fields would be blocked by ferromagnetic layer such as shielding film made from an amorphous cobalt alloy.

6. Problem: Multi-physics analyses and experimental testing of MHD cooling system is complex, computationally expensive, and time-consuming. Solution: Optimal solution with approximation-assisted multiple objective (AAMO) approach.

- Engineering simulation complements physical testing by reducing the total effort and cost required for experimentation and data acquisition.

However, we are encountered with computationally expensive and time-consuming nonlinear complex models. Moreover, we do not want to simplify the model, since simplification will affect the validity of the analysis.

- Recent developments in engineering optimization have led to surrogate models to gain insights that might approximate the solution and converge to optimal solution for MHD cooling system. However, optimization requires using simulation software applications i.e. computational fluid dynamics, electromagnetism to evaluate designs and rigorous mathematical effort of solving the optimization problem. Insufficient data for sensitivity analysis may be the primary challenge to find global optimized set.

7. Problem: At system level, there is a possibility of insufficient information to formulate an optimal MHD active cooling problem for spacecraft or there is no consensus on the objective functions. Solution: Develop system level model,

and implement a rigorous decision-making process for alternatives to gain insight about highlighted attributes for higher reliability instead of judgement solely based on efficiency of thermal management systems. Comparison of cooling systems for avionics by viewing decision making as optimality problem might be inappropriate, however; in situations when there is insufficient information to formulate. Therefore, the essence of engineering decision making to select from possible choices can be used to gain insight about assessing impact at the system level and selection of the most reliable alternative as optimal cooling system for the system. The challenges at system level model for HXs are:

- The operating temperature for eutectic system should be controlled to prevent solidification (freezing), subsequently cooling efficiency, and reliability issues. A Programmable Logic Controller (PLC) might be used for designing a temperature control simulation system with a field programmable gate array (FPGA) to control the temperature and operations of heaters if needed. The temperature control system includes temperature sensors, FPGA, heaters, electromagnet (EM) drive. This effort is out of the scope of this study and it is recommended for real application of the concept in space-like environment.
- To break down thermal management at system level of spacecraft into subsystems to analyze each subsystem to determine its performance and optimize parameters of subsystem to synthesize iteratively as a whole at

spacecraft system level required rigorous implementation and quite challenging task.

1.4 Coherent Critical Thinking and Organization of the Dissertation Chapters

The goals of this dissertation are as follows:

- To improve interface contact resistance and corrosion issues of LM compatible HX through effective and novel insertion method for fabrication realized by additively manufactured techniques.
- To improve efficiency of the MHD pump allowing significantly higher power dissipation and realizing them through multi AM techniques that permits use of what normally would be corrosive LM.
- Highlighted attributes for selection of a reliable thermal management system for spacecraft avionics.

The following chapters in this dissertation are coherently organized to investigate the problems for accomplishing these goals (see Fig. 1.1).

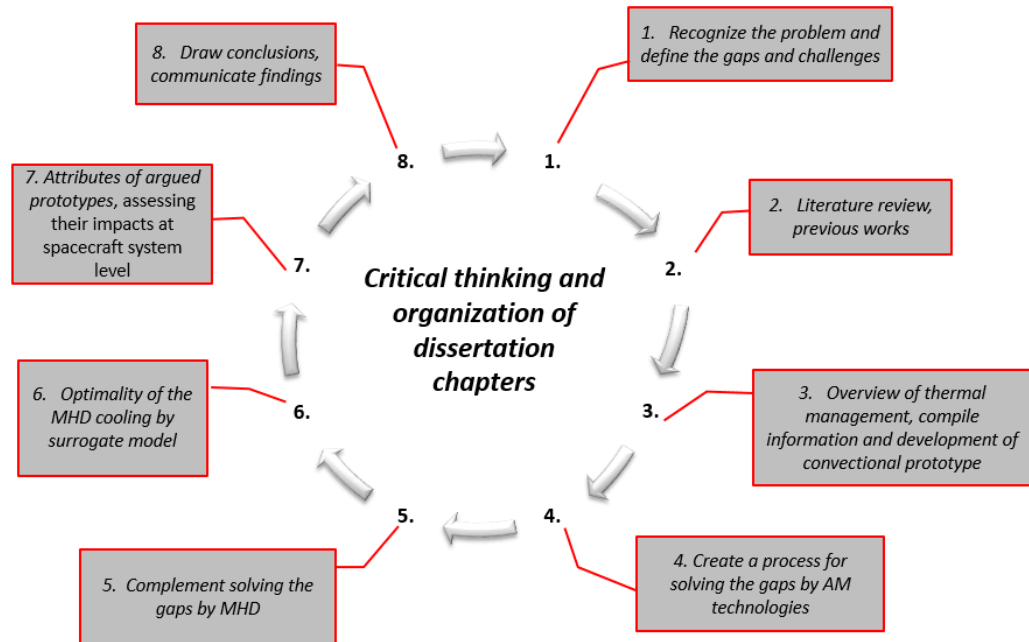


Figure 1.1: Organization of the chapters of the dissertation and critical thinking of dissertation

Chapter 1 is the motivation for the subject of this research study, which is the heat dissipation for control of high thermal density problem in avionics for spacecraft. It is discussed and then translated to the objectives of this research study by defining its limitations, determining the perspective for approaching the problem, and identifying what is needed to address the problem.

Chapter 2 is a literature review divided into 4 sections, similar to Aristotle’s four causes, but applied to engineering. The selected works for review are in accordance with four areas of MHD heat exchanger as follows: (1) material selection and compatibility for in-situ AM, (2) manufacturability and formability using in-situ AM, (3) performance and efficiency of a prototype design, and (4) the objective or final goal of achieving a reliable concept for a thermal management system that enhances performance of high power avionics in spacecraft applications.

Chapter 3 presents an in depth assessment of the thermal interface problem to define the gaps between "the engineering challenges" and the "need for fundamental characterization and knowledge" of the science behind active thermal management system manufactured and assembled by conventional techniques. In this chapter, the heat transfer in layered structures or stack up assemblies manufactured and assembled by conventional method (first prototype) with the emphasis on interfacial thermal resistance and governing equations of heat transfer are primary subjects.

Chapter 4 demonstrates how in-situ AM technologies can overcome critical limitations of traditional manufacturing processes to address the challenges defined in previous chapter and how it can improve heat transfer capability of hybrid ceramic/metal heat exchanger.

Chapter 5 focuses on the fundamentals of MHD and its application to avionics cooling, which is implement through the use of multiple AM technologies, such as DMLS, SLS, and FDM, that enable us to fabricate reliable cooling system with no moving parts. Rigorous CAD modeling of the complex structures needed for MHD is employed to achieve optimal structures, where nonlinear electromagnetic equations are approximated via ANSYS Maxwell finite element model (FEM), computational fluid dynamics (CFD) of MHD model via ANSYS Fluent, verification and validation of results via empirical data are highlighted topics in this chapter.

Chapter 6 discusses the optimality of the MHD cooling and a meta model (i.e., surrogate model) representation tailored to the MHD cooling system. Engineering simulation complements the physical testing for experimentation and data acquisition presented in the previous chapters. However, these analyses are quite computationally

expensive and time-consuming analyses, so rigorous surrogate modelling complemented by simulation and physical testing was determined to be the most suitable approach for this study.

Chapter 7 presents an overview of the attributes of active cooling for spacecraft avionics for long missions. Up to this point, the dissertation is rigorously involved with avionics cooling technology from the problem solving perspective or subsystems development of smaller scope (e.g., components, instruments, materials) without providing sufficient evidence of incorporation into a mission context. While innovative and exciting in and of itself, the impact of practical MHD cooling technology needs to be assessed at a system level to prove its benefits.

Finally, chapter 8 presents a summary of the overall objectives of this dissertation, where in-situ AM can be used to realize thermal managements systems employing LM alloys to improve thermal control of high-powered electronics. The chapter concludes with emphasis on the five major areas of scientific and technical contribution, as well as the associated intellectual merit, which resulted in two journal papers submitted for publication and enabled future work to be identified that can broaden the scope of the current contributions.

Chapter 2: Literature Review

2.1 Introduction

The practical introduction to recognize the problem of efficient thermal management for avionics in the first chapter is limited to a subclass of the plethora of techniques that have emerged. The importance of thermal management in a wide range of disciplines is reflected in the richness of the relevant literature. Most ideas that reform and reshape our lives, such as cooling systems, are not created from scratch, rather we step into an environment that already exists, and we learn to interact with it (Sproul, 2000). Reviewing existing works in any discipline are nets cast to catch the ideas, to rationalize, to explain, to master and to improve it. We endeavor to make the mesh even finer and finer by resolving existing gaps in pervious works (Heidegger et al, 1977). These attempts can be traced back to Aristotle's writing (from a translation by Hooker, 1993) on the four explanations of any "thing" as 1) material cause, 2) its formal cause or essence, 3) its efficient cause and 4) final cause or end (Cross, 2001 & Shirley et al, 2007). Therefore, literature review is organized in four sections according to Aristotle's four causes transformed to engineering problem as: 1) Applicable materials and tailoring material properties for thermal cooling (material selection). 2) In situ manufacturing and in mold assembly, geometric optimality and thermal interface bonding (formal cause) 3) MHD as driving force for active cooling (efficient cause) and 4) Thermal management techniques for avionics packaging (final cause).

2.2 Material Selection

Engineering materials fall into three classifications as metallic (ferrous, nonferrous, alloys etc.), ceramic (glasses, graphite, diamond etc.) and polymeric

(thermoplastic, thermoset, elastomer etc.), additionally, combination of different materials create a composite material (reinforced plastic, metal-matrix, ceramic-matrix, sandwich structure etc.) (Flinn et al, 1990). Inside a composite, the types of materials developing the composite preserve their particular unique qualities (Christensen, 2013). An alloy as subcategory of metallic material made by combining two or more metallic elements resulting in material properties that often differ from the constituents (Haynes, 2016). Liquid alloy or LM consists of alloys with very low melting points, which form a eutectic that is liquid at room temperature. Eutectic alloys have two or more materials and have a eutectic composition with single and sharp melting point (ASM handbook, Alloy phase diagram, 1992). A phase diagram determining the microstructure of alloy system is seen in Fig. 2.1 (courtesy of www.tec-science.com).

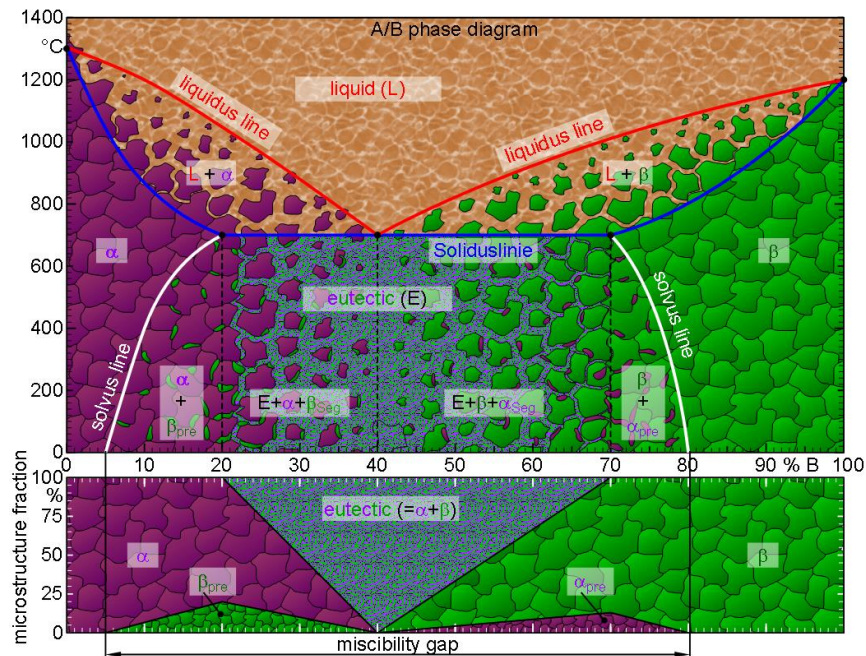


Figure 2.1: A phase diagram and microstructure diagram of an alloy system with limited solubility of the components for a fictitious binary chemical mixture (with the two components denoted by A and B) used to depict the eutectic composition, temperature, and point.

Another type of metal alloy relevant to this study is fusible alloy that is easily meltable at relatively low temperatures. Fusible alloys are commonly, but not necessarily, eutectic alloys. Stability under heating and relatively high thermal conductivity make the melted fusible alloys a wise choice as coolants, particularly with high thermally conductive constituents such as indium or sodium (Jacoby, 2016). Examples of fusible alloys are eutectic Galinstan (Gallium: 68.5%, Indium : 21.5% Tin: 10%), Gallium-Indium eutectic (Gallium: 75.5%, Indium 24.5% by weight), NaK (Sodium-potassium alloy) which is highly reactive with water (like its constituent elements) and may catch fire when exposed to air, Lipowitz's alloy (50% Bismuth, 26.7% Lead, 13.3% Tin, and 10% Cadmium by weight), Field's metal (32.5% Bismuth, 51% Indium, 16.5% Tin by weight) and Rose's metal (50% Bismuth, 25–28% Lead and 22–25% Tin).

Highlighted properties of Galinstan are as followings: 1). Thermal conductivity: 16.5 W/m^{°K} 2). 2) Electrical Conductivity: 3.46×10^6 S/m (room temperature) 3). Surface Tension: $s = 0.718$ N/m (room temperature) 4).Magnetic properties: None magnetic 5). Galinstan does not wet glass and boron nitride ceramic; a layer of oxidation is built and removable. 6). 2.1 times lighter than Mercury. 7). Nontoxic, Galinstan is also used as a replacement for Mercury and NaK because of its low toxicity. 8). Solubility: Insoluble in water and organic solvents and 8). Ability to withstand dramatic thermal expansion mismatch (Davis, 1998). Alloys containing gallium are corrosive to all metals except tungsten and tantalum, which have a high resistance to corrosion, more so than niobium, titanium and molybdenum. As temperature of gallium alloy increases, it becomes highly corrosive, additionally; gallium alloy is highly reactive to aluminum alloy including additive manufacturing aluminum alloy specifically at temperature above

500°C (Revie, 2011). LM is packed in polymeric container such as polyethylene bottles or ceramic container. To prevent corrosion, hydrochloric acid (HCl) solution is added to top of LM (Holcomb et al, 2016). Alternatively, replace the empty volume of the bottle containing LM with dry argon gas to minimize oxidation at the surface of corrosive LM (<http://www.chemistrylearner.com/Galinstan.html>). Lasance and Simons studied different approaches showing industrial potential for the cooling of high-power electronics and concluded that LM is a new frontier in the thermal management of computer systems with thermophysical properties superior to those of ordinary fluids (Lasance et al, 2005).

Reliability issues and the need to prevent corrosion caused by liquid metals require the use of plastic and ceramic materials. The choice to use engineering plastics is based on the specific material properties required by the application (Rubin, 1990). The thermoplastic engineering materials is seen Fig. 2.2 and extracted from <https://insights.globalspec.com>.

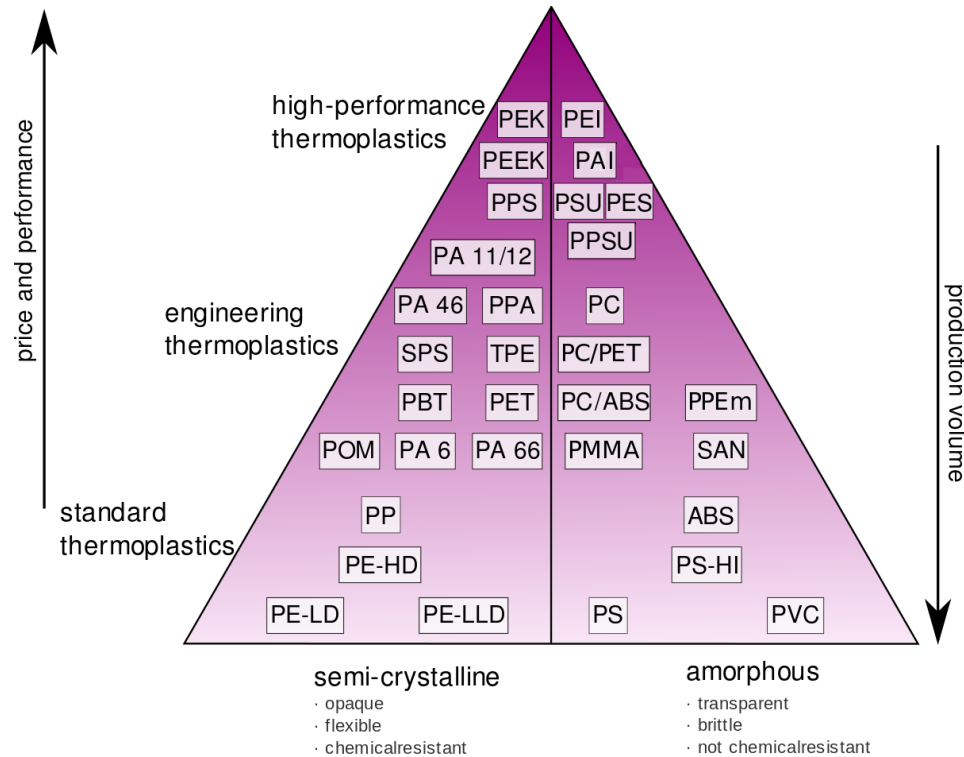


Figure 2.2: Thermoplastic engineering materials as subclass of engineering plastics

There are six basic divisions of the most common engineering polymers, but there are many more subdivisions. The common subdivisions are as following: 1). Polycarbonates (PC) 2). Polyesters 3). Polyethylene Terephthalate (PET) 4). Polybutylene Terephthalate (PBT) 5). Liquid Crystal Polymer (LCP) 6). Styrenic copolymers 7). Acrylonitrile Butadiene Styrene (ABS) 8). Styrene Acrylonitrile (SAN) 9). Styrene Maleic Anhydride (SMA) 10). Polyamides (Nylons) 11). Polymethylmethacrylate (PMMA or Acrylic) 12). Polyoxymethylene (Acetal or POM) 13). PEI (Polyetherimide) (Olabisi , 2015). We selected Ultem that is a family of PEI products for this study because of its thermal conductivity (0.22 W/m·°K) and manufacturability by FDM process. Heat resistance, solvent resistance, flame resistance, outgassing properties for space application, high ultraviolet light resistance, high FST (flame, smoke and toxicity) rating, superior flexural strength and fatigue are highlighted attributes of Ultem. The

glass transition temperature and melting temperature of Ultem is 217 °C and 330 °C respectively. In regards of additive manufacturing of Ultem following configuration is recommended for FDM process: extruder temperature: 330 °C, print bed temperature: 110 - 120°C, print speed of 1000mm/min. Also its amorphous density at 25 °C is 1.27 g/cm³. Plastics for long space missions encountered derating reliability issue therefore this leads us to another subset of candidate material as ceramics for long space missions. Crystallinity, orientation of the macromolecules, operational condition influence thermal conduction of polymers (Rossinsky, 2009).

Engineering ceramics are based primarily on pure borides, carbides, nitrides or oxides. Ceramics are used in avionics, electronic, computer and communication systems due to wide range of mechanical and physical properties but they are brittle materials and often contain flaws caused by processing and preparation. The thermal conductivity of ceramic materials plays an important role in this study. Example of thermally conductive ceramics used in engineering application are polycrystalline diamond (PCD) ceramics, boron nitride , aluminum nitride, beryllium oxide, silicon nitride, silicon carbide, Macor, Lava and Shapal which is a machinable composite ceramic made up of boron nitride and aluminum nitride. Synthetic boron nitride comes in different grades such as Grade A, AX05, HP, M & ZSBN. Solid boron nitride hexagonal grade AX05 is selected for this study because of following properties: 1) High thermal conductivity, minimal thermal expansion, thermal shock stability. 2) It is inert and do not wet to molten liquid metal. 3) It provides dielectric strength and high electrical resistivity with a low loss tangent and dielectric constant. These characteristics make it an excellent choice for MHD application

as LM container. 4) Ease of fabrication with subtractive manufacturing close to tight tolerances (Richerson et al, 2018).

Another challenge among application of multi material structures, specially thermal structures, is fusion of ceramic and metal interfaces to create superior bonding especially in power bed based in situ AM processes. Fundamentally, wetting of a metal on ceramic is difficult due to the unusually large difference between their melting temperature and surface tensions and is a bottleneck for making metal–ceramic fused structures. Like plastics, ceramics and glass offer beneficial compatibility, corrosive resistance advantages, making them a commonly plated structure for electronic components. Ceramics can withstand high temperatures, and when plated with a specific metal or alloy, gain strength and vital wettability for use in bonding interface of thermal transport application. Copper and silver are some of the most commonly used metals for plating ceramics because of their thermal and wettability properties, and are applied as a thin layer onto the ceramic surface of the interfaces. Conductive pretreatment of ceramic and plastic is required to the areas where electroplating will occur. Graphite, silver, brass or copper powders are used for the initial treatment, and then the part can be submersed in the solutions of dissolved metals for plating.

Additional highlighted attributes of plating are improving surface flatness, resistance to cracking, studying flow rate in electromagnetic application per Hartmann wall effect, enhancing strength and durability. Moreover, nickel plating with phosphorous contents has enhanced wettability of the content, as the phosphorous contents increased, the surface morphology of the Ni-P deposit was smoother and surface roughness of Ni-P became trivial (Lin, Duh & Chiou, 2006). To

achieve superior covalent bonds of aluminum particles on the CNT surface, two steps experiment demonstrated (i) electroplating of aluminum nanoparticles on multiwalled carbon nanotubes and (ii) aluminum powder is spread again on Al-electroplated CNTs, followed by high-temperature annealing to enhance wettability of the aluminum (So et al, 2011). Electroplating is used to improve the wetting characteristics of silicon-based materials with copper electrolyte by various surface treatments to achieve uniform and void free copper deposition in high aspect ratio. Due to its polar functional groups causing better wettability, silicon nitride was later used as an insulating layer instead of commonly used silicon oxide in the electroplating experiments (Dixit et al, 2007). In level zero and level one of avionics packaging, plating on chip and metallization of substrates have improved quality and durability of fabricated parts (Zandrini et al, 2017; Ikegami et al, 2012; Watanabe et al, 2001). Eichler and Lesniak went over the properties of a synthetic solid ceramic BN such as high heat capacity, outstanding thermal conductivity, excellent electrical insulating, and not being wet by most molten metals and LMs (Eichler, 2008).

2.3 Manufacturability and Formability

Mechanical issues influence the design of all elements in electronics instrument, which is known as microsystems packaging. These issues of electronic systems include materials selection, manufacturing and manufacturability, size and weight, power and thermal management, mechanical/thermomechanical stress management (shock, vibration, temperature cycling), reliability, maintainability and testability, economics and cost analysis (Jacobsen, 2000). This section focuses on literatures related to geometric optimality, compatibility and manufacturability. In summary what gives the components

their forms for thermal function of electronics packaging that provides a path for dissipating heat generated during operation.

2.3.1 Thermal Contact Resistance

Thermal contact conductance is an important factor in avionics, largely because microsystems packaging contain a mechanical combination of two materials and following factors influence contact conductance: contact pressure, surface flatness and roughness, surface cleanliness, interstitial materials and plastic deformation (Zhao et al, 2016). Compliant, thin, interstices to fill the gap between two touching surfaces with applied pressure reduces contact resistance. Furthermore, fillers added to interstitial materials can enhance thermal properties, reduce coefficient of thermal expansion. Carbon fiber fillers used for polymeric interstices are produced from either Polyacrylonitrile (PAN) or pitch (mainly pitch). The form of the Carbon fibers are either short i.e. 3-6 mm long or filament woven yarn (1-320k filaments and 1-12k used in plastics). The aramid fibers as heat-resistant and strong synthetics filler have two types: Kevlar and Nomex and greatly increase impact strength at elevates stress rates, aramid has also antiballistic and lubrication effects. Ceramic filler with high thermal conductivity such as boron nitride (Hu et al, 2017) and diamond (Kidalov, 2009) have been used to improve the thermal conductivity of composites.

Researchers also studied the factors influencing the thermal conductivity of graphene-polymer composites, such as amount of loading, guidance on the preparation of composites, orientation of graphene, surface modification, and the interface (Balandin, 2008 ; Geim, 2009; Yavari et al, 2011). The potential advantage with the use of CNTs to reduce weight and increase thermal conductivity and also layer delamination issues were

addressed by researchers (Moisala et al, 2006 ; Ramesh et al, 2010; Yang et al, 2010; Han et al, 2011). Thermal conductivity unequivocally increases with polygonal aluminum oxide (Al₂O₃) filler with different ratios of composition of hybrid composite system (Choi et al, 2013 ; Li et al 2017). Most failure mechanisms are accelerated by temperature stresses due to CTE mismatch, chemical corrosion, electromigration, oxide breakdown (Pecht et al, 1998). Thermal stresses affect efficiency of thermal interface materials (TIMs) in a variety of electronic applications. Vinh et al, used laser flash method to characterize the long-term performance of 3-layer structures in pad form, an adhesive and a gel under critical temperature and high humidity operating conditions and revealed delamination and cracking of putty specimen (Vinh, 2009). Dongmei et al conducted experimental investigation of the thermal contact resistance (TCR) between non-conforming rough surfaces of copper and stainless steel revealing effect of thermal conductivity on TCR, harmonic mean thermal conductivity of dissimilar contact materials and experimental measurement of TCR between thin films. The TCR of oxygen free coppers and the thermal conductivity exhibited an exponential relationship under low pressure conditions and a polynomial relationship when the external pressure ranged from 0.53 to 0.71 MPa. (Dongmei, 2020).

Phonons and electrons carry heat in material including dielectrics, and electron movement in metals causing heat transport and dominates thermal conductivity. Heat transport from one material to another is measured through interface thermal conductance. For example, thermal conductance of bismuth/hydrogen and diamond is $8.5 \frac{mW}{m^2 \cdot K}$. Due to different lattice parameters in these two materials, phonons are not linked across the interface, additionally bismuth is metallic, primary heat carriers are electron,

and diamond is electrical insulator but has high thermal conductivity. Moreover, the Debye temperature (temperature limit below which quantum effects may be observed) is low for bismuth but has many phonons at low frequencies and high for diamond and phonons carry heat at higher frequencies than bismuth (Costescu, 2003). Bahrami *et al.* calculated theoretical contact conductance of two rectangular solid rough surfaces as a function of applied pressure (between .035 and .35 MPa); however, it cannot be used when solid interstitial materials such as compounds are applied (Bahrami, 2005).

2.3.2 Attributes of AM Technologies

The disruptive AM technology is essential for futuristic manufacturing to increase efficiency, conserve resources and time management for new product and the latest industrial revolution, Industry 4.0, asserted its potential in an upcoming paradigm to open up new opportunities in design and production (Brettel et al, 2014). Futuristic manufacturing due to revolutionary manufacturing systems i.e. additive manufacturing is advancing as seen in Fig. 2.3 extracted from <https://news.heidelbergusa.com>

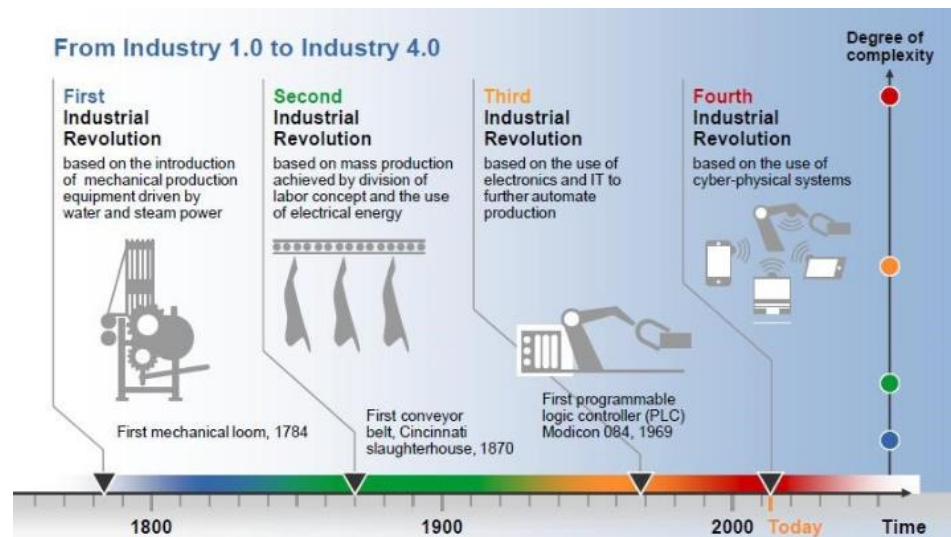


Figure 2.3: Industrial revolutions and futuristic manufacturing system

However, there are limitations for parts fabricated by AM technologies such as comparable low strength and near net shape linked to density, associated quality, coupled with a high cost of the printing machine system (Haleem & Javaid, 2019). Bruck's group have previously developed for pressureless sintering processes for Functionally Graded Materials (FGMs) (Pines & Bruck, 2006) and processing-structure-property models can be extended to design features for realizing the desired shape, surface finish, and properties for final machining of near net shape AM parts to employ a microthermomechanical FEA technique they developed to predict the thermal stress, and subsequent final shape and surface roughness (Shababa et al, 2007; Krufft et al, 2008, Joshua et al, 2019). Fabrication and evaluation of 3-D printed composite molds simplify the production of hollow and trapped-tool configurations, providing greater design freedom without the need for complex tooling (Abe, 2001). Integrating 3D printing and traditional subtractive manufacturing in single machine create endless benefits of both (hybrid manufacturing) (Du et al, 2016). Comparison of inert and open atmosphere laser metal deposition systems asserted that inert systems eliminates oxidation but open atmosphere system is more practical when metallurgy is acceptable. Inert is an air tight system that isolates internal gas from room air, it does not rely on shield gas since the entire chamber is argon, air lock to pass parts and tooling through and door system offers direct access and then chamber must be purged. Conversely, for open atmosphere laser metal deposition incorporates shield gas nozzle in open air, laser cladding (2D coatings) uses a similar shield gas method and shield gas to protect the melt pool (Conn, 2016). A research sponsored by Air Force lab generated a fast thermal model that can be integrated into optimization routines to minimize thermal distortion in DMLS including features

such as 1). Simulate layer-by-layer additive process 2). Generic to any parts by using STL files as model input. 3). Include part orientation and support structures into the thermal model (Hao et al, 2016). In Hao's research, thermo mechanical model of powder bed-based fusion as shown in Fig. 2.4, argued temperature history of three super layers, increased heat capacity due to latent heat through the built process decomposed into three thermal contraction processes. Each thermal contraction is quasi-static loading process and total thermal stress is superposition of thermal stresses in each thermal contraction process.

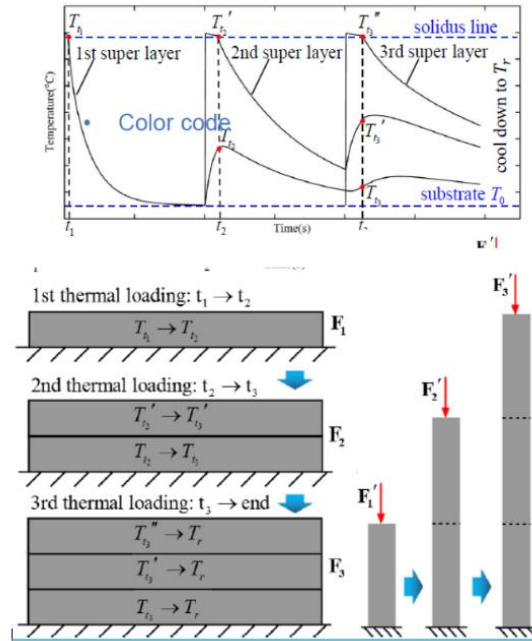


Figure 2.4: Thermal loading of three layers in powder bed based fusion of AM process

A wealth of researches also conducted on industrializing AM, additive and one process manufacturing, best practices in implementing a production unit for industrial AM parts and designing for AM at the intersection of materials, machine and process (Jyrki et al, 2020; Busachi et al, 2017; Caue et al, 2015; Huang et al, 2015). Oxidation is another issue in additive manufacturing and following common metallic powders

compared in terms of corrosive issue: 1) Titanium- Oxygen causes embrittlement of Titanium. With more oxygen, the material gets brittle and more susceptible to crack propagation, a failure that causes structural damage (Qian, 2015). Aluminum alloy powders show surface oxides quickly, which can create weld quality issues, they have very low viscosity when molten by laser and difficult metal to work with even in controlled atmosphere (Manfredi et al, 2014). Corrosion resistance of the AlSi10Mg and gravity cast aluminum alloys are relatively similar. However, due to significant differences between the microstructure and defect characteristics of AlSi10Mg, the corrosion fatigue endurance was relatively improved compared to cast alloy (Avi et al, 2016). Inconel 718 is high temperature corrosion resistant alloys with excellent mechanical strength, preferred material for aerospace engine components. This article compared additive manufacturing and forging to realize the process temperature effect on corrosion of IN-718 Ni-based superalloys. Inward growth prevailed in the additive manufactured IN-718 while the forged IN-718 grew oxide protrusions at the surface (Juillet et al, 2018).

Researchers also discuss the modeling technique, and physics related to AM processes. Khairallah et al have modeled, validated against the experiment and investigated the sensitivity of laser absorptivity for the Marangoni convection and recoil pressure in laser for powder bed based fusion of stainless steel for generated melt pool, material sparking and denudation zone. The melt track is divided into three sections: topological depression, transition and tail region revealing melt pool bottom and duration laser power ramp down (SA Khairallah et al, 2016).

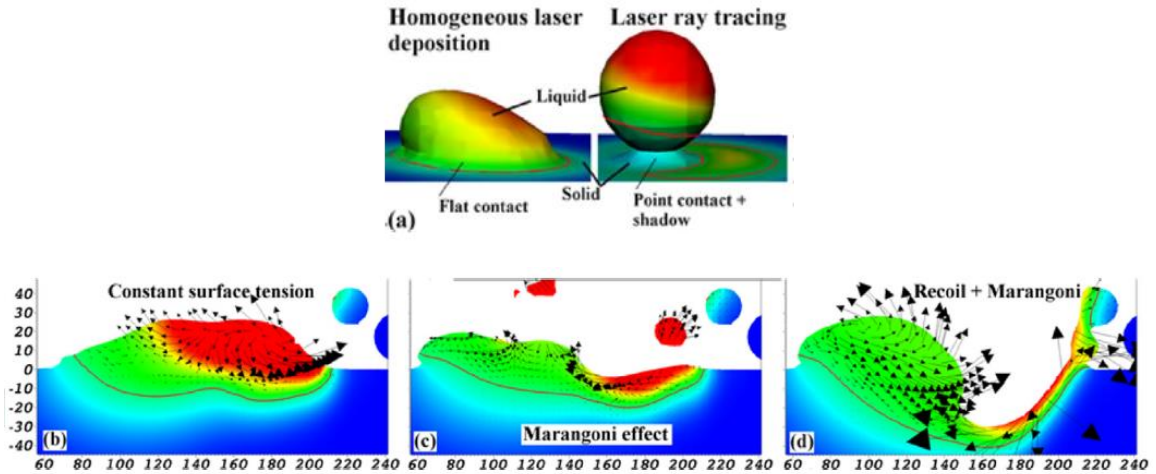


Figure 2.5: Modeling of AM laser bed based fusion process, incremental physics fidelity, significantly alters the heat transfer (temperature range 4000°K to 293°K), melt pool depth and flow. Model demonstrates 200 W laser moving to the right (scan speed 1.5 m/s) for 10 microseconds showing Marangoni effect and recoil pressure for stainless steel powder.

Autodesk Netfabb simulation software is used to predict the net shape part fabricated by metal additive manufacturing. This software is not advertised for low conductivity plastics and polymers, this software works based on multiscale modeling technique instead of time consuming moving heat source. In this software, deposited material in cubic form defines the fine-scale process parameter model (PRM) that represents the physics and resulting thermo-mechanical behavior for that material and processing parameters set. There is no importation of a cad file for this step and if one is imported, it is not used anywhere in the simulation. Importing a cad file is only possible for the subsequent part scale simulation based upon this earlier PRM generation step. New PRM is generated for a given material/process-parameter input including:

- (1) Material Parameters: K temperature dependent thermal conductivity, temperature dependent specific heat, temperature dependent elastic modulus, temperature dependent coefficient of thermal expansion, temperature dependent yield stress and density

(2) Process Parameters: laser power, laser scan speed, laser spot size, print layer thickness and hatch spacing and rotation. The small scale PRM model is mapped onto imported STL file with corresponding parameter/material combination.

Regarding the physics behind Netfabb software, this paper asserts the effect of material and dwell time on in situ distortion measurements, post-process distortion and residual stress. In conclusion, the addition of longer dwell times results on the consistent accumulation of distortion with increasing layers, also the elimination of dwell time during the laser deposition results in a decrease in distortion and much lower overall distortion levels in the built. Distortion of Inconel is twice of Ti-6Al-4V for same heat input and dwell time based on post processing data (Erik R. Denlinger et al, 2015). Using natural convection yields the most accurate temperature history and using a physically representative convection model applied to a continually evolving mesh surface captures the change of part geometry due to the addition of material during the laser cladding process (Gouge et al, 2015). The residual stress measurements and in situ deflection measurement show that the measurement-based convection model produces more accurate stress measurements for forced and free convection, additionally, out-of-plate distortion and resulting deflection measured using post-process measurement CMM techniques and the results demonstrate that the distortion experienced during laser cladding is more complex than that observed during equivalent welding process (Heigel et al, 2015). Application of heat to straighten a substrate or depositing additional material to balance the bending moment about the neutral axis of the work piece were argued (Denlinger, 2017). Heat transfer energy balance that governs transient thermal analysis is used for thermal modeling. For mechanical modeling, the response to the thermal history

is determined by performing a 3D quasi-static incremental analysis. The results show that the lower shielding flow rate of Argon, decreases the deflection and residual stress in Ti-6Al-4V, however the amount of change depends on geometry and dwell time (Michaleris et al, 2015). Goldak's model applies an assumed heat distribution (welding research) and the model is 60% of the laser diameter in the z direction, so one would get about 0.060 mm depth for a 0.100 mm spot size. For distortion simulations, it makes almost no effect what the depth is, as long as there is depth. This applies an artificially high thermal conductivity (typically 2-6x highest temperature value) at melting temperatures, to approximate the Maragoni convection in the melt pool, which tends to widen and deepen the melt pool. In Fig. 2.6, Goldak's model compared to the power distribution along the direction of the source's motion model and a computationally efficient line input (LI) model of powder bed processes more (Irwin et al, 2016).

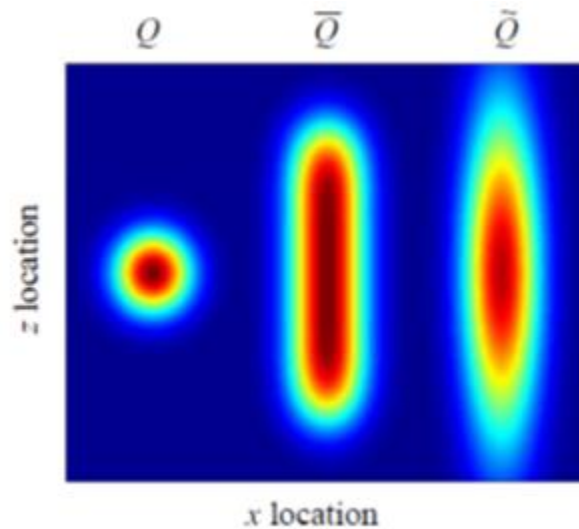


Figure 2.6: Goldak's moving spot (left) compared to scaled Lined input (middle) and scaled elongated ellipse (right) power densities, unscaled peak values are less intense than Goldak's model and not visible.

For overview and limitation of the software, the Netfabb simulation tool is investigated and it is primarily useful for the prediction of distortion of common AM

metals including Inconel 625 and 718, Ti-6Al-4V, AlSi10Mg, and CoCr. This software as of now cannot simulate low conductivity materials including plastics. The simulation tool produces only qualitative values for stress due to the multi-scale method used and cannot be used for accurate predictions of residual stress. The modeling method only replicates parallel scan strategies with an interlayer rotation. The modeling method does not take into account the difference in processing parameters between hatches, contours, upskin, downskin, etc. The model does not predict microstructure and anisotropic material properties. The simulation tool assumes constant density and neglects gravity. The simulation tool has been validated for continuous laser systems. Pulsed laser and electron beam systems have yet to be validated. During each iteration recoater tolerance varies, further research required. Support structure predictions are a beta feature with limited validation. The accuracy of this software is ~ %70 compare to validated model. Due to the roughness of the approximations used, even the distortion will only match in trend. Crack propagation cannot be determined, and only qualitative stress results, which can be used to determine areas of peak stress, might be helpful where cracking may occur.

Another simulation software reviewed in this study is 3DSIM developed for metal additive manufacturing acquired by Ansys. The backbone of this software is Deepankar Pal et al research work asserted a modeling technique by including the key aspects of a successful AM simulation toolset. The paper covers: a) optimization of materials and geometry and prediction of residual stress, warping, mechanical properties, b) closed loop control including optical sensors, recording layer-by-layer information such as temperature, geometry, distortion, porosity where on-the-fly compensation for out-of-spec thermal or microstructural defects can be achieved, c) prediction of mechanical

properties as a function of process parameters, materials and geometry, d) scan strategies and optimized support structure placement, leading to lower residual stresses and less postprocessing of the fabricated part. The melt pool, thermal contours, compressive nonlinear longitudinal stress (MPa) are seen in Fig. 2.7 (Pal Deepankar et al, 2014).

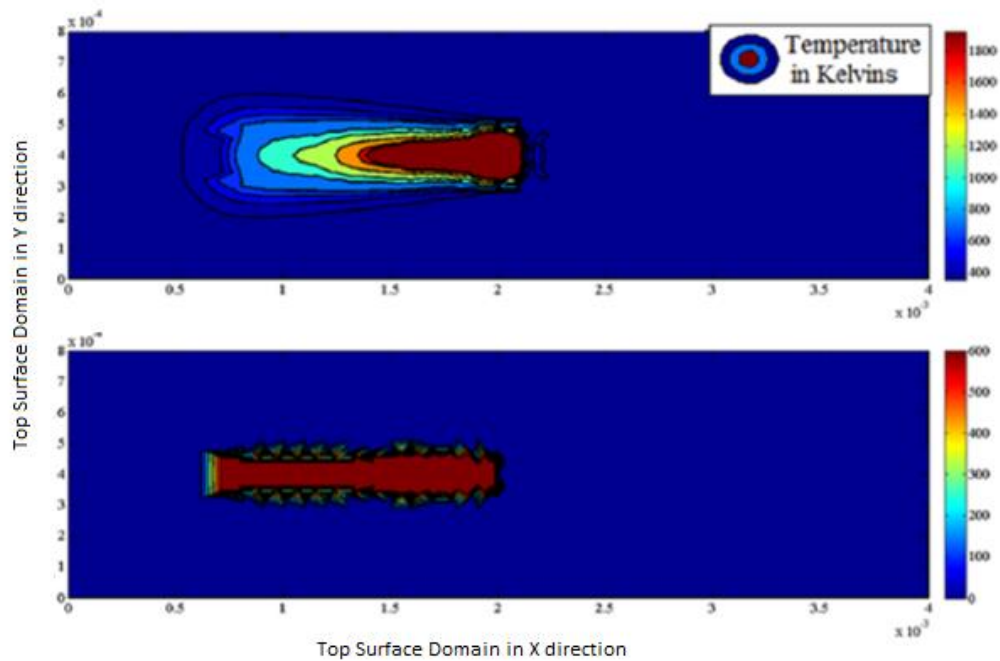


Figure 2.7: Metal powder bed based laser process simulation showing In situ single bead thermal contour ($^{\circ}K$) (top), b) Compressive longitudinal stress (MPa) by balancing force and momentum (bottom)

Geometrical standard elements and attributes of additively manufactured parts specify the design rules and appropriate AM process to meet the form, fit and functionality requirements of the part (Guido, 2015). Additionally, support structures are designed to reduce deformation due to residual stress for AM processes. Geometric attributes of support structures including wall thickness and interwall distance are experimentally optimized based on “trial and error” strategies introduced by machine manufacturer and/or user experience. In order to incorporate the effects of support structures for overhangs in thermomechanical behavior of AM structure, a study of

effective thermal conductivity for thermal residual stresses was undertaken (F. Calignano, 2014). Support structures enable the 3D printing of models with steep overhangs and cantilevered sections also are used to attach the 3D print part to the print bed. Support structures most often are required to fabricate overhanging designs to assure integrity and quality. Currently support structure design is done by rule of thumb and most 3D printing software will automatically place support structures based on the parameters you set. The common support structure is a grid pattern underneath of the cantilevered sections with optimized grid wall thickness and interwall parameters. The support is removed by EDM or any postprocessing techniques (Paramita Das et al, 2015). At UMD, based on our study of fabricated specimen by SLM process, pre-solidification powder necking/sagging leads to sudden change in thermal conductivity and density of the powder bed. Additionally, self-weight of the layers also causes the upper layers of the part to bend and sag and causing flatness and cracking issues seen in Fig. 2.8.

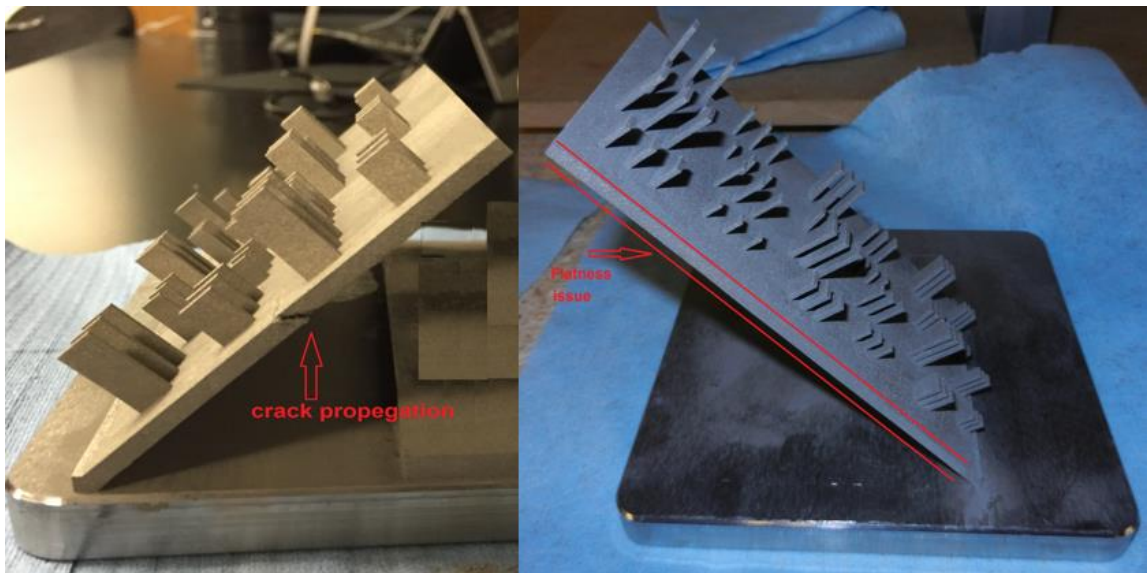


Figure 2.8: AM Inconel 625, minimized support structure, specimen: heat sink with fins (3mmx10mmx18mm). Design of experiment, (variables: height, thickness and angle of fin), part encountered flatness and crack propagation due to thermal stresses

In this study, the goal was to investigate the effect of minimized support structure to net or near net shape fabricated part while conserving material and reducing post processing effort. In addition, we have investigated the thermally motivated total shrinkage strain and predicted sagging for a given angle of the part relative to print bed, density, scan pattern, machine setting, and material type. The post processing results performed in 3DSIM Exasim metal AM simulation toolkit is seen in Fig. 2.9.

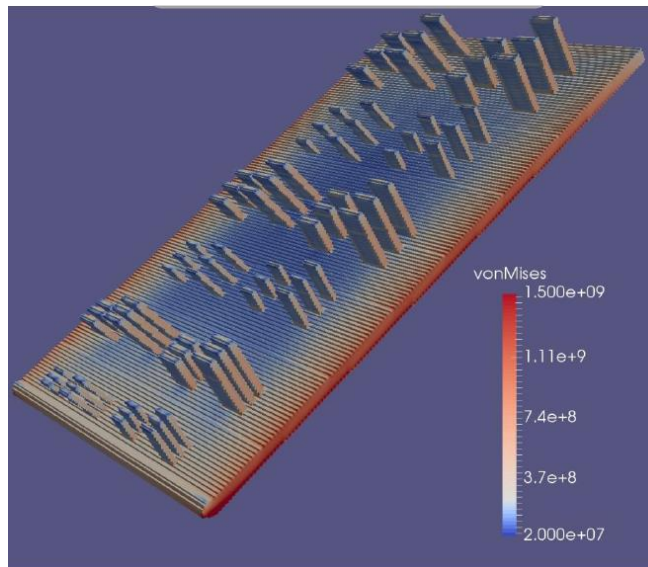


Figure 2.9: 3DSIM AM simulation, Post processing Von Misses Stress "Pa" for orientation 26 degree relative to print bed, voxel .4 mm relaxation factor .8

Paul et al also estimated the effect of thermal deformation on part geometric dimensioning and tolerancing (GD&T) error via a combined analytical, thermomechanical and geometry based model. During the generation of the layers in metal AM process, the metal powder 1) melted by the laser energy, 2) then LM cools and solidifies and 3) finally the solid metal cools to the ambient. During the first two stages, shrinkage in the metal volume is the dominant phenomenon. During the third stage, thermal stresses, due to nonuniform cooling, cause the part to distort and warp. Heat transfer occurs through conduction form the layers to the substrate. The substrate is

preheated and maintained at that temperature until all the layers have been printed, after completion of the fabrication process, the part and the substrate cooled down to the ambient temperature. Moreover, GD&T features including flatness, circularity, cylindricity, circular runout and total runout argued for AM metallic parts. The overall deformed shapes of a cylindrical specimen obtained from the thermo-mechanical model is shown in Fig. 2.10.

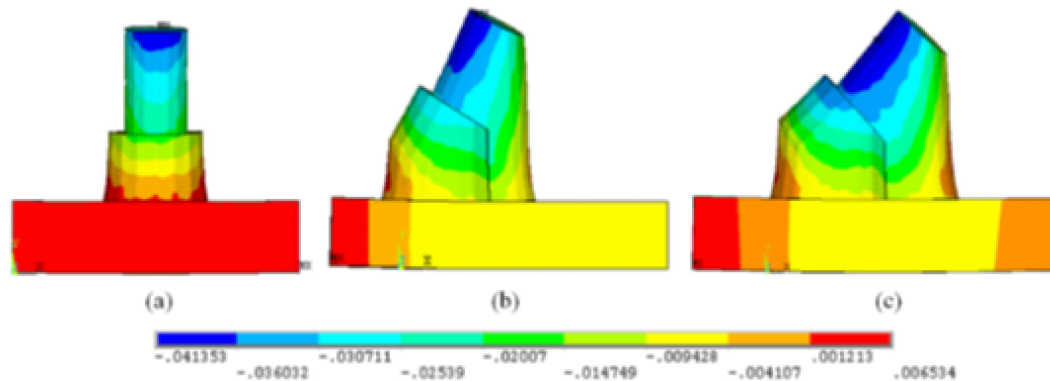


Figure 2.10: Post processing results of FEA AM model cylindrical part. Substrate shows vertical nodal displacement (mm) with a) 0° part orientation, b) 30° orientation, c) 45° orientation. Substrate is bent in a ball shape with the outer edges pointing upward, causing part to flex and deform in a bow like shape (material AISI 1015 steel).

The first built up layers in contact with the substrate have upward deflection, as the layers move away from the substrate, the upward deflection reduces ending with a concave downward deflection in the top layers. Additionally, since the initial built up layers are constrained to the substrate, they cannot shrink freely compared to upper layers, which leads to an overall tapered shape of the cylindrical part (Paul et al, 2014).

Metallization is one of the surface treatment processes used to alter the surface of an AM fabricated material or machined ceramic to a metal form either chemically or by other processes that depend on the applied process, constituents, parameters, and requirements (Naruskevicius et al, 2012; Fritz et al, 2012; Wang et al, 2006).

Electroforming is a very fascinating technique in metalsmithing and in particular to a ceramic module for power semiconductor integrated packaging (Tsai, 2017). Zhaohui et al filed two patents for preparing a ceramic package substrate with a copper-plated dam encompassing electrodes and also performing thin film metallization on a surface of a ceramic board (Zhaohui, 2019). Chemical bonding, chemical reaction, and the interfacial structure of metal/ceramic interfaces are influenced by temperature, time, pressure and alloying additions. Metal/ceramic interfaces wettability and work of adhesion can be predicted qualitatively from bonding models based on the elements of metal and ceramic and interfacial energy minimization dominates the atomic structure of metal/ceramic interfaces (Howe, 1993).

2.4 Performance and Efficiency of MHD

MHD is related to phenomena arising from the motion of electrically conducting fluids (such as plasmas) in the presence of electric and magnetic fields (Alfvén, 1942). In MHD, one must always be prepared to consider the complete electromagnetic field. The current and magnetic fluxes must have complete paths which may extend outside the region of fluid-mechanical interest into locations whose exact position may be crucial (Richard Baker, 1997). Basic scaling parameters and typical simplifications for MHD are as followings (Muller & Buhler, 2001).

$$Re = Reynolds\ number = \frac{Inertia\ forces}{Viscous\ forces} = \frac{U_0 L}{\nu}$$

$$Ha = Hartmann\ number = M = \left(\frac{Electromagnetic\ forces}{Viscous\ forces} \right)^{1/2} = B_0 L \sqrt{\frac{\sigma}{\nu \rho}}$$

$$\begin{aligned} Re_m = Magnetic\ Reynolds\ number &= \frac{Convection\ of\ B}{Diffusion\ of\ B} = \frac{Induced\ field}{Applied\ field} = \frac{U_0 L}{\nu_m} \\ &= \mu_0 \sigma U_0 L \end{aligned}$$

$$N = St = \text{Stuart number} = \frac{\text{Electromagnetic forces}}{\text{Inertia forces}} = \frac{Ha^2}{Re} = \frac{\sigma L B_0^2}{\rho U_0}$$

Where B_0 is magnetic field, U_0 is velocity, ν is kinematic viscosity, L is length scale, ρ is density, J is current density $\frac{A}{m^2}$, σ electrical conductivity $\frac{1}{\Omega m}$, E electric field V/m , μ_0 is magnetic permeability in newtons per ampere squared $(\frac{N}{A^2})$.

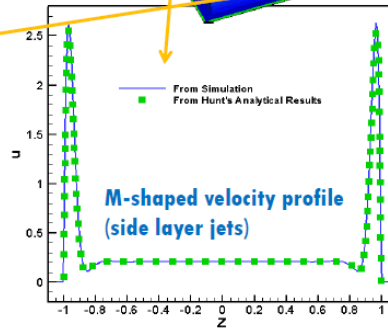
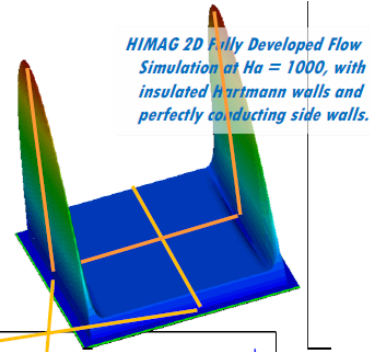
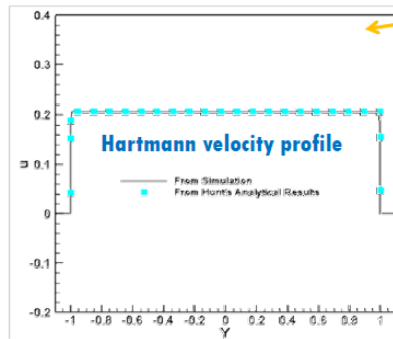
If magnetic Reynolds number is much less than one, then induced magnetic field is small compared to applied field B_a , electric field can be expressed as gradient of a potential, $\mathbf{E} = -\nabla\phi$. If ratio of Hartmann number over Reynolds number is greater than .005 then core flow is generally laminar. Navier-Stokes equation for incompressible MHD flow (velocity u) with dimensionless parameters is as followings:

$$\frac{1}{N} \left(\frac{\partial u}{\partial t} + (u \cdot \nabla) u \right) = -\nabla p + \frac{1}{Ha^2} (\nabla^2 u) + j \times B_a \quad (1)$$

In MHD channel flow, the distinctive feature is axial current loops, which are responsible for extra MHD pressure drop and M-shaped velocity profile and it is a hard problem for analytical studies (Neil b. Morley, 2006). HIMAG software simulates M-shaped velocity structure formation at expansion and at beginning of parallel channels, relaxation (diffusion) along field for MHD channels at high Ha and N . Center core behaves differently as shown in Fig. 2.11:

Viscous and inertial effects confined to thin layers

- Hartmann layer on all walls with a perpendicular component of B , thickness Ha^{-1}



- Side (Shercliff) layers on walls parallel to B , thickness scales like $Ha^{-1/2}$ and magnitude Ha^*cw

Figure 2.11: Developed velocity profile for MHD channel (HIMAG software)

Four behaviors observed from simulation of incompressible MHD flow in channel: 1) streamlines near the center proceed to center channel 2) streamlines between center and Hartmann wall proceed to side channel 3) streamlines near Hartmann wall are pulled back within side layer jet to the expansion wall and move vertically along it before proceeding to side channel 4) strange behavior in the center channel as exhibiting counter rotating current cells. Dragos (1975) analytically demonstrated the pressure gradient versus Hartmann number of MHD flow for the limiting cases with electrically insulating wall $c = 0$ and perfectly conducting walls (c to infinity) and also for $c_h = \infty, c_s = 0$. It is clearly seen that perfectly conducting walls result in significantly higher MHD pressure losses and insulating wall is the efficient choice.

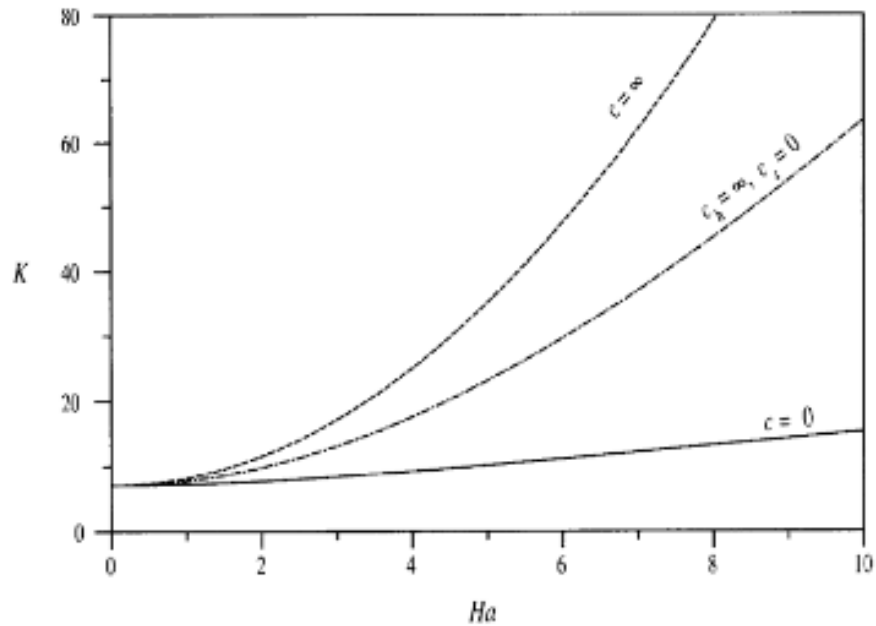


Figure 2.12: MHD incompressible flow, pressure gradient K in a square duct as a function of the Hartmann number Ha .

Electrical conductivity of wall material effects linear stability of MHD flow and it is mainly determined by the effective Hartmann wall conductance ratio cHa for Ha greater than 300 and wall conductance ratio c in the range of 0.01 to 1. Maximal destabilization of the flow occurs at $Ha = 30/c$ (Arlt et al, 2017). A nonlinear mechanism is observed for the situation of laminar-turbulent transition in magnetohydrodynamic duct, pipe, and channel flows with homogeneous magnetic field and electrically insulating walls, in particular via transient algebraic growth and breakdown of certain perturbations (Oleg Zikanov et al, 2014). A numerical finite model of homogeneous decaying turbulence in conductive MHD flow with a uniform magnetic field asserted that except for a short period of time when $N = 50$, the flow evolution is strongly influenced by nonlinearity and cannot be adequately described by any of the existing theoretical models. Further, the velocity components value depends on the strength of the magnetic field and the stage of the decay leading to Reynolds stress anisotropy ellipsoid (Burattini

et al, 2010). Localized velocity measurements on LM duct with Lorentz force flow meter (LFF) by implementing a permanent 1 cm cube magnet is capable of distinguishing obstacles in the flow and the resulting modified flow structures.

However, obtaining the full flow profile requires the solution of an inverse problem and further investigation is needed (Heinicke. 2013). Pipe flow of LM entering a region where walls are covered by a flow channel inserts is investigated experimentally under the influence of a strong constant magnetic field and demonstrated that flow channel inserts may reduce pressure drop by at least one order of magnitude but 3D effects at the entrance of inserts may reduce the efficiency of the insulating inserts by just some degree (Mistrangelo & Brinkmann, 2020). A novel MHD micropump using Silicon MEMS fabrication technology capable of actuating Galinstan with Linear velocity of up to 10 mm/s has been fabricated using strong permanent magnets, on 4-mm wide and 0.5-mm deep microchannels (Irshad et al, 2009). MHD pump in toroidal and rectangular loops conduits fabricated with low temperature co-fired ceramic tapes is demonstrated. Electrodes printed on the ceramic substrate along the conduits walls and applied magnetic field to mercury slugs, saline solution, and deionized water generates Lorentz force and results were in correlation with theoretical data (Zhong et al, 2002). The numerical simulations conducted with the explicit finite difference method to approximate steady state, incompressible and fully developed laminar MHD flow in micro fluidic system to characterize a MHD pump revealed that the channel dimensions and the induced Lorentz forces have significant influences on the flow velocity profile (Wang et al, 2004). Lemoff et al demonstrated a microfluidic MHD pump with a continuous (not pulsatile) flow by using an AC MHD propulsion system in which the Lorentz force is used to propel an

electrolytic solution along a microchannel etched in silicon (Lemoff et al, 2000). An incompressible and fully developed laminar MHD flow is formulated and characterized with different scalar dimensions in duct channel and then by converting the Lorentz forces which is cross product of electric current and magnetic flux into hydrostatic pressure gradient in the moment equations, the governing equations transformed into Poisson equation which makes the analytic solution possible (Ho, 2007).

Electromagnetic radiation (EMR) that takes the form of self-propagating waves in a vacuum among avionics can cause interference and malfunctioning of avionics such as command and data handling. Electromagnetic shielding is required through a conductive or magnetic enclosure known as a Faraday cage to isolate the electromagnetic fields propagated from MHD. The effect of earth's magnetohydrodynamic electromagnetic pulse (MHD-EMP) in electrical transmission and distribution systems is studied and argued MHD-EMP environment would have a marked effect on a power system by inducing up to several hundreds of amperes of quasi-dc current on power lines causing saturation which could result in excessive harmonic generation, voltage swings, and voltage suppression (Tesch, 1992). Rectangular MHD generator electric response is investigated based on the Faraday's principle of electromagnetism and fluid dynamics to improve its cyclic thermal efficiency. These results validate the measurement approach of the MHD generator with segmented electrodes and can be scaled for larger MHD (Ayeleso, 2018). Apertures on shielded faraday cage required for ventilation, optical displays or mechanical supports. Fortunately, apertures with maximum dimensions that are much smaller than a wavelength provide very little impedance to the flow of currents on a conducting surface. In addition, seams exist wherever two pieces of an enclosure

come together and causing a major breach in the shielding enclosure, application of overlapping seam, conductive gasket, increasing thickness of effective material i.e. (aluminum 60601 or copper) and adequate fasteners can resolve the leakage issue (Bogorad, 2008). Functionally graded materials (FGMs) provide a potential solution to overcome the electromagnetic shielding problem by gradient distribution of conductive/magnetic additive (Sugano, 2006). Another concern is the heat generated from MHD core and peripheral solenoids (ampere-turns). A numerical simulation of thermochemical nonequilibrium flow of the dipole and multipolar magnetic fields is implemented, results show that the five-magnet system, whose central polar orientation is the same with the peripheral ones have stronger work capability and better shock control and thermal protection performance. Moreover, compared with the dipole magnetic field, the stagnation non-catalytic heat fluxes are decreased by a factor of 47.5% and 34.0% respectively (Kai et al, 2017). In following section, the application of LM for active cooling of avionics with emphasis on MHD will be discussed.

2.5 Reliable Thermal Management for High Power Electronics

The invention of the transistor in 1947 and the subsequent of integrated circuits in 1958 sparked the unprecedented growth of information processing technology employing silicon devices. Moor's Law by Gordon Moore in 1965 predicts that the number of transistors on a chip doubles every 18 months. While such an exponential trend cannot continue indefinitely due to limitations governed by basic physics, such barriers have to date been overcome, by innovations that have enabled miniaturized fast circuits. As processors get faster, they also get hotter. Increasing thermal management demand driven by increasing performance of avionics has led to the development of a number of

innovative technologies in mesoscale and thermal management at electronics component level (Krishnan, 2007).

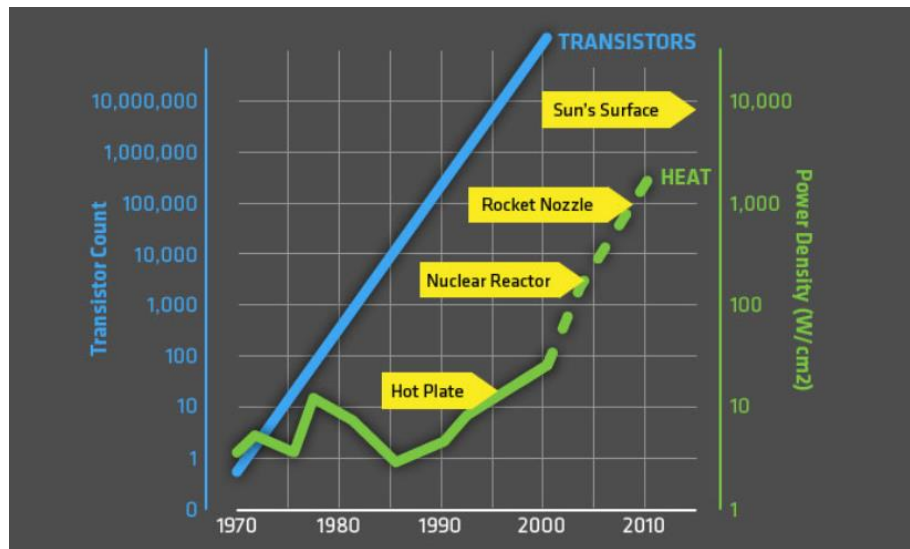


Figure 2.13: Patrick Gelsinger, an Intel executive, predicted that unless something changed, computer chips would become hotter than nuclear reactors within a few years.

Researchers are also exploring clever ways to beat the heat of avionics packaging. There have been some previous research efforts using low melting point eutectic alloys to justify the proposed research. An overall review on chip cooling using liquid metals or their alloys as coolant is conducted with emphasis on thermal properties of liquid metals with low melting points and principles of several typical pumping methods such as mechanical, electromagnetic or peristaltic or roller pumps. In latter pumping system, the fluid contacts only the inside surface of the tubing thereby negating concern for incompatibility and contamination of viscous and shear-sensitive and aggressive LM fluids, however; efficiency is limited by liquid viscosity since the flow is pulsed, particularly at low rotational speeds (Ma & Liu, 2007). The two principal advantages (superior thermophysical properties and ability to be pumped by MHD pump) of developing single phase cooling systems based on liquid metals by implementing a

closed loop gravity independent high performance pumping for cooling systems have shown heat transfer coefficients on the order of $10 \frac{W}{cm^2 K}$ and 8 KPa pumping pressure (Miner & Ghoshal, 2004). Active cooling by LM under thermosyphon effect without using external energy was demonstrated through driving LM by the buoyancy force induced by the waste dissipated heat. This self-driven electronic cooling approach is useful for future thermal management areas such as cooling LED lamp, power distribution unit by extracting heat from a confined space to a much larger area and no air flow occurs in the limited space, providing a dust-free and water-free environment for the normal operation of the electronic devices. The cooling performance of this method becomes better with increase of the heat load. However, solidification in an extremely low temperature environment of LM can cause reliability and risk concern. To address the freezing issue of LM, thin wire heater can be implanted into LM or attached to the tube wall to guarantee the flow of coolant (Li & Liu, 2011 ; Ma K Q et al, 2009).

Galinstan, which is a eutectic alloy, has been shown to be an effective coolant medium because of its low melting point, high boiling point, and its intrinsically high thermal conductivity properties. Fluid cooling using microchannels have gained significant attention owing their several advantages such as high heat transfer coefficient, higher surface area, direct integration on the substrate but contact resistance is a bottleneck (Lasance & Simons, 2005). A patent claims heat transfer chamber containing double circulations of a LM or a phase change material. First circulation coupled heat source (electronic component) to the heat transfer chamber and circulating the heated substance through the heat transfer chamber for mixing with the liquid coolant. Then a sub rack with second circulation of coolant with lower density coupled to the heat

transfer chamber and circulating the liquid coolant through the heat transfer chamber for mixing with the heated substance. This patent is about method of cooling an electronic component by way of a direct contact heat exchanger and pumping system (Dariavach & Engelhardt, 2019). A cooling adapter capable of being mounted to a pre-existing power module that can be located within the electronics chassis. The cooling manifold has a housing with an inlet plenum, an outlet plenum and a plurality of channels disposed between the inlet channel and the outlet channel for allowing the cooling fluid to move efficiently (Yang & Eddins & Grimes, 2019).

Thermal management of solid-state devices at micro level realized by micro heat pipes provides a passive and efficient way of spreading heat away from a heat source. Instead of alcohol or water, LM with superior thermal properties has been used in microscale heat pipes fabricated by indium cold welding of micromachined silicon structures, then evaluation asserted its performance to be superior compared to equivalent water-filled micro heat pipes (Dean et al, 2012). The thermal properties of ethyl carbamate modified Field's alloy nanoparticles and nanofluid were characterized by differential scanning calorimetry (DSC). Results show that the ethyl carbamate modified Field's alloy nanofluid displays improved thermal properties and excellent dispersion stability promising in future applications for thermal management of electric vehicles, electronics packaging and other energy transfer systems. In this study, native or ethyl carbamate modified Field's alloy nanoparticles were synthesized through a facile nanoemulsification method asserted excellent dispersion stability and good thermal stability in poly-alpha-olefin (PAO) oil (Huang et al, 2019). Tang et al demonstrated how a LM bead could drive flow of an ionic fluid (salt water) by applying square wave signal

across it to create a pressure differential through the Lippman Effect (Tang et al, 2014). LM Galinstan has been shown to improve thermal conductivity of thermal management structures using Lorentz Force MHD pumping for hi-performance CPUs, but rapidly fail due to corrosion. In this research, Deng et al presented the optimization of a LM CPU cooling product. The focus of this research was to optimize the critical parameters of the electromagnetic pump and the radiator fin with the use of LM coolant. To optimize the pump means to maximize the driving pressure while simultaneously decreasing the resistance of the flow. The parameters of the electromagnetic pump were broken down into three subsections: the pump channel, the magnet and the electrode as seen in Fig. 2.14.

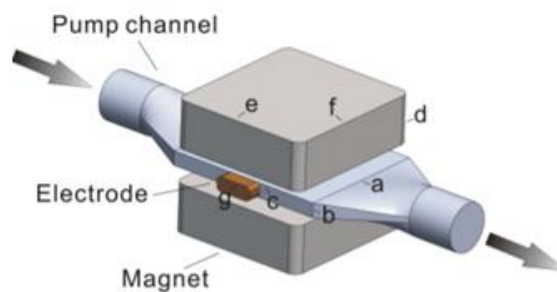


Figure 2.14: Schematic of electromagnetic pump, broken down into three subsections: the pump channel, the magnet and the electrode

The height of the channel of the electromagnetic pump affects the magnetic field, and the effect of width of the channel is trivial. The driving pressure of electromagnetic pump with rectangular cross section is $P_{EM_pump} = \frac{BI}{b}$, where B and I are magnetic field and electrical current respectively. Therefore, a width b was chosen to be equivalent to that of the pipe diameter as it offers the lowest resistance of flow. The height of the channel was given an optimization variable that could be obtained through experiment or numerical simulation but was not determined in the paper. However, it was noted that the

smaller the height of the channel, the closer the magnets would be and consequently increases the driving pressure, yet also increasing the flow resistance, and that these factors must be balanced to maximize the volumetric flow. The electrode parameters are easily determined by the channel parameters and the connecting lead, but the length should be large so to increase the contact area with the liquid metal.

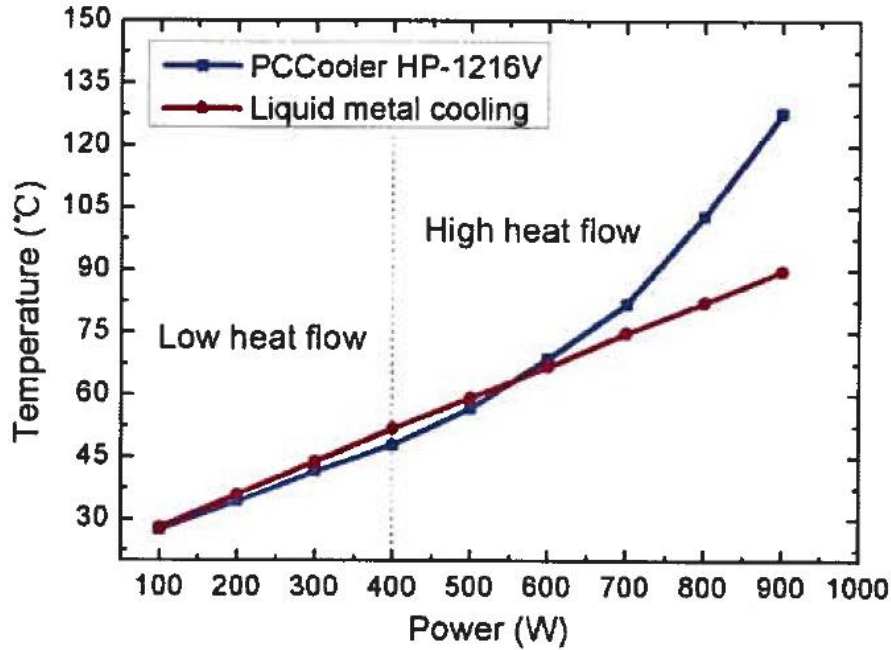


Figure 2.15: Active cooling with LM showing cold pate temperature of LM cooling product and PCCooler- HP-1216V (copper/aluminum Heat pipe CPU Cooler). Under increasing heat flow, LM cooler shows better efficiency for power dissipation over 600watts.

In the study of CPU cooling system with liquid metal, the results show that it could compete with high-performance CPU cooling devices in the current market. However, some of the challenges faced by using LM as a coolant was the corrosion and alloy freeze issues (Deng et al, 2013). Recently, researchers investigated the use of LM as the coolant for the thermal management system for lithium ion battery packs of electric vehicles to keep the temperature of each battery cell in a temperature range of 20-45 °C and to maintain a uniform temperature distribution across the whole battery pack with a 5

°C tolerance. 24 Li-ion battery cells, arranged in a 4 x 6 array with cooling channels between each row, were used to compose the battery pack but the mathematical analysis of the system was simplified into a one-dimensional problem. Each battery cell is a uniform heat source, neglecting the heat dissipation from the top and bottom of the pack and the focusing on the heat flux primarily in the direction across the cooling medium. The temperature of a cell at a specific location further down the cooling channel was said to be dependent solely on the thermo-physical properties and volumetric flow rate of the coolant. The liquid metal, having a much higher thermal conductivity, consequently had much better cooling capabilities than water under the same cooling channel shape and volumetric flow rate. The power usage of the pumps used to drive the different coolants was also included in the mathematical analysis. An electromagnetic pump was used for the liquid metal, and a mechanical pump was used for the water. Given the generally higher efficiency of electromagnetic pumps, it was calculated to achieve the same flow conditions while consuming less than half of the power than the mechanical pump. Therefore, the results of the mathematical analysis was that the LM could dissipate more heat and at a lower power consumption rate. The FEM results show the advantage of LM over water as a coolant for thermal management of Li-ion battery packs. The difference in performance between the two becomes even more apparent at higher discharge rates and higher volumetric flow shown in Fig. 2.16.

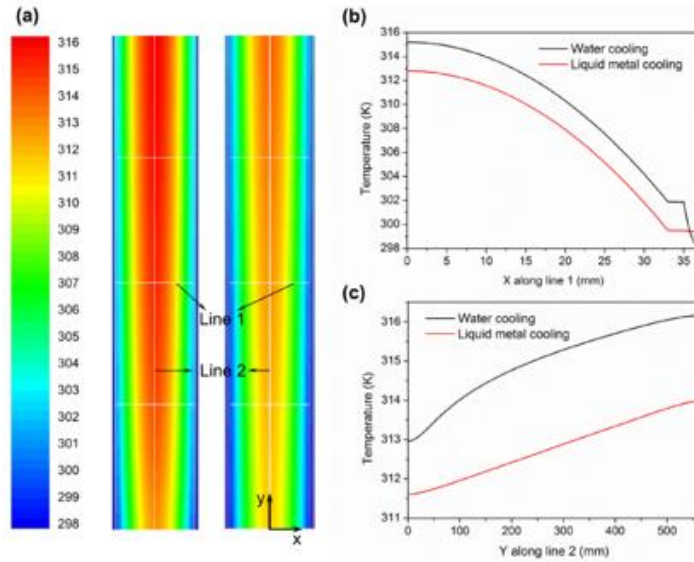


Figure 2.16: Temperature distribution in the computational domain with LM cooling and water-cooling, under discharge rate of 3C and inlet velocity of 0.1 m/s. (a) Contour images of temperature, water-cooling on the left and LM cooling on the left

The benefit of the LM was attributed to its higher convective material properties over water. This allows LM to cool the system to the same module temperature at much lower volumetric flow rates. Another benefit of having a higher surface tension, it becomes more difficult for LM to leak through small holes. The performance of LM coolant vs water are demonstrated in Figs. 2.17 and 2.18.

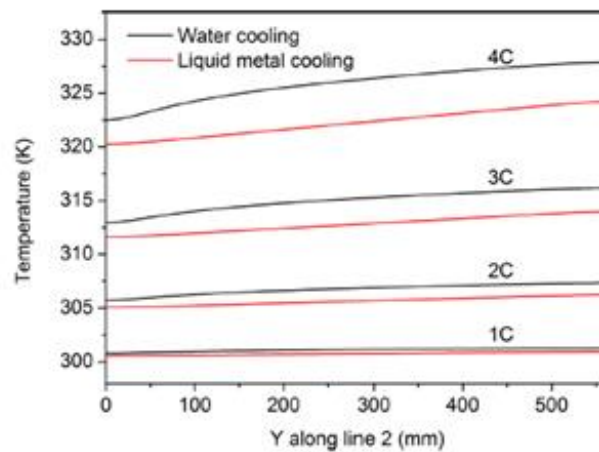


Figure 2.17: Cell center temperature distribution under different discharge rate, with coolant flow velocity of 0.1 m/s

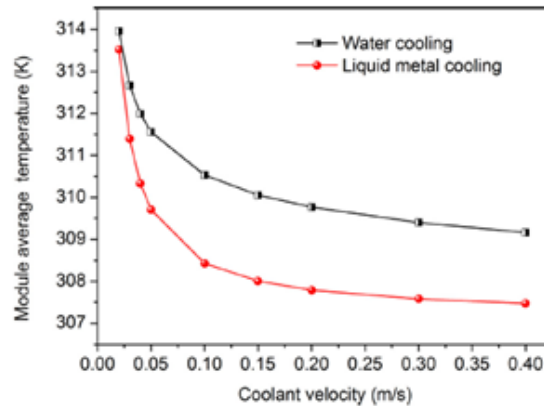


Figure 2.18: Average temperature of the four cells under different coolant velocity, with discharge rate of 3C.

However, when the number of cells in the y direction exceeds 12, the volumetric flow rate of LM needs to increase in order to continue to outperform water as a coolant medium. Another disadvantage was the jacket material that can be used in conjunction with LM as a widely used material is aluminum, but the combination will result in corrosion. An alternative could be expensive and heavy, which would result in a much heavier system since the density of LM is already 6 times higher than water (Xiao-Hu et al, 2016). Scientists also exhibited different approach of using LM for thermal management system. A LM droplet was integrated with a sodium hydroxide (NaOH) coolant and was energized with a square wave signal across it, which creates a surface tension gradient that then drives the flow of the coolant from the lower to higher surface tension area. In this study they make the pump by simply pipetting 40 ul into a reservoir and applying square wave signal across it, additionally, NaOH solution reacts with Galinstan droplet and charge the surface, therefore an electric potential applies across the droplet using the NaOH solution as a conducting fluid. The charge distribution on the surface becomes non-uniform due to the gradient in the potential field, so there is more

charge accumulated on one side of the surface than the other. This induces the Lippman effect, where the surface tension of the fluid is altered near the surface of the Galinstan drop due to the charge density (higher on the right side of the droplet than the left, so there is more tension there). The resulting difference in surface tension causes a pressure drop, that is inversely proportional to the size of the Galinstan drop (Young-Laplace equation). Theoretically, one can do this with any liquid that can react with a metal ball (e.g., Aluminum). Furthermore, the reaction consumes the metal to generate the charge to induce the Lippman effect. As the radius drops, the A_{gap} increases and the pressure drops inversely. The problem of corrosion, practical design, leakage and maintenance were remaining challenges in this study. The temperature change of these cases with respect to the microheater driving voltage can be seen in Fig. 2.19 (Zhu, Tang, Khoshmanesh, & Ghorbani, 2016).

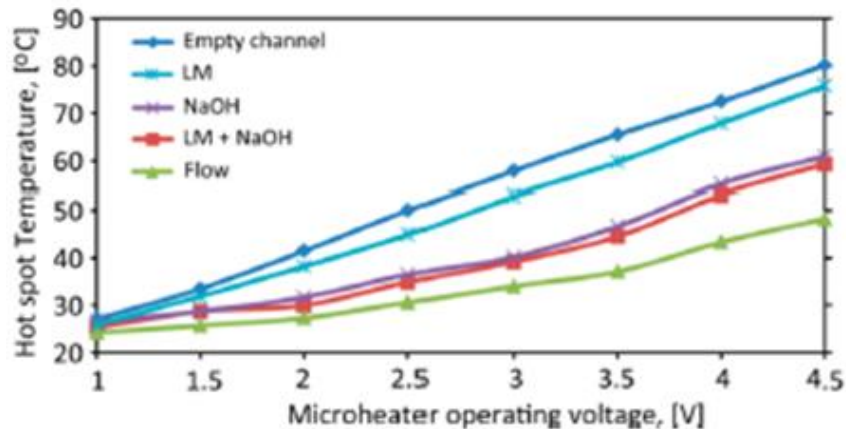


Figure 2.19: Hot spot temperature measured by thermistor when energizing the microheater with different voltages ranging from 1 to 4.5 V.

Regarding novel HX concepts, a shallow bore ground heat exchanger (10 times shorter) consists of phase change material and water numerically modeled to evaluate its performance. In this study, simulation indicated regulating the entering water temperature

for more efficient operation than a conventional vertical heat exchanger under identical condition through the effective use of phase change material. However, the simulation was over predicated once compared to experimental data (Zhang, Liu, Biswas & Warner, 2019).

The efficiency of active cooling systems depends greatly upon microchannels cross-section and liquid media. It is well known that the performance of microchannels is largely dependent on its hydraulic diameter as well as fluid properties. Sharma et al analyzed the performance of trapezoidal and rectangular microchannels and compared for two different coolants, liquid gallium and water. Sharma's analysis is based on following assumptions: Steady state flow, incompressible fluid, laminar flow, constant properties of both fluids and solid and effects of viscous dissipation are negligible. Applied governing equations are continuity, momentum and balance of energy. V-type, A-type and rectangular cross sections are seen in Fig. 2.20 (Sharma et al, 2013)

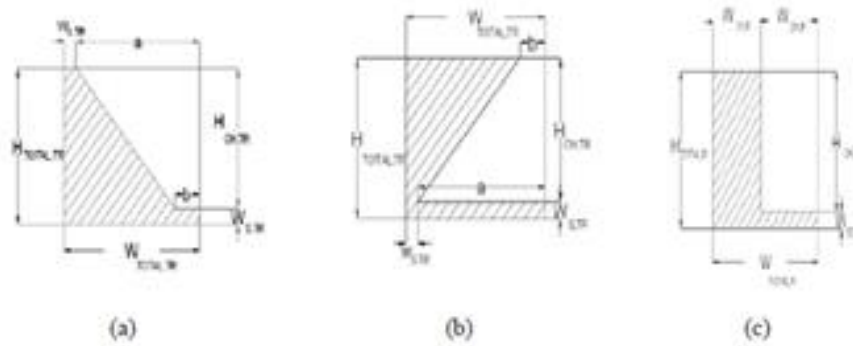


Figure 2.20: Different geometries used in analysis: (a) V-type (b) A-type (c) rectangular. By Sharma et al

For water as coolant the performance of rectangular type is found to be superior in terms of both flow rate and pump power. For liquid gallium as a coolant, microchannels having A-type cross section is found to be performing better followed by V-type then

rectangular type at same flow rate. However on comparison of basis of pump power the rectangular type of geometry is found to be more suitable. Temperature contour of FEM model can be seen in Fig. 2.21.

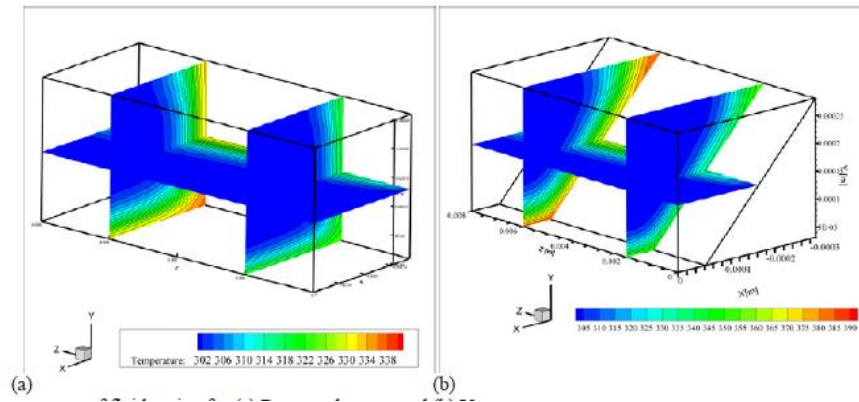


Figure 2.21: Temperature contour for rectangular and V-type cross section of the pipe

NASA GSFC demonstrated a single phase thermal control system consists of electrohydrodynamic (EHD) pump with heterocharge layers by imposition of electrostatic fields, transport tubing, a thermal-hydraulic test section, and a condenser section characterized (1) mass flow rate versus applied voltage and applied current and (2) pressure head developed by the pump as a function of applied voltage and current (3) steady state and operational power requirements. The EHD conduction pump provided immediate recovery from dryout condition by simply increasing the applied voltage. The EHD conduction pump operated at 15kV presented pressure head on the order of 13,000Pa with 2.83W of electric power at -20°C of sink temperature, providing thermal control capacity for 35.8 W/cm^2 of heat flux. This study is also performed to address the feasibility of the EHD two-phase loop for thermal control (Jeong & Didion, 2007; Didion, 2001). Jone's valuable old research was based on a heat pipe of radical design replacing the capillary wick of a conventional heat pipe with an electrode structure,

which provides a net liquid pumping force to ensure the heat pipe operation, which utilizes polarization EHD force effects irrespective of orientation with respect to gravity (Jones, 1974). The highlighted attributes of Jones's concept are built-in EHD heat transfer enhancement in boiling and condensation by a nonuniform electric field, reliable priming and startup, bubble ejection from axial flow structure, low liquid friction factor in comparison to that of a capillary wick, and direct voltage control of the pumping mechanism. Another research by Didion's team in thermal management is to use an electrical field to move a liquid film in the absence as well as in the presence of gravity by rewetting the heater surface during liquid film flow boiling. Terrestrial results show a 62% increase in critical heat flux when the electrohydrodynamic pump is moderately activated and the microgravity results onboard the parabolic flights witnessed promising results of electrohydrodynamic-driven liquid film flow boiling onboard the International Space Station (Didion, 2007).

2.6 Conclusion

Based on previous researches, there is clearly potential to develop reliable LM-based heat exchangers, if it is possible to create a multifunctional interface by encapsulating the LM with a compatible container that prevents corrosion while transporting enough heat for thermal performance. In upcoming chapters, we develop these multifunctional interfaces based on AM techniques, active thermal management system with no moving parts for avionics packaging, its optimality and mission context in space-like environment.

Chapter 3: Interfacial Thermal Resistance of HXs Packaged by Conventional Assembly Methods in Avionics

3.1 Introduction

In this chapter, key subjects are conventional thermal management aspect of avionics packaging, governing laws of interface contact resistance and development of active cooling prototype assembled by conventional manufacturing techniques to be compared with prototypes fabricated by AM in future chapters. The term avionics is a portmanteau of the words aviation and electronics and avionics packaging deals with putting together electronics and associated assemblies in aerospace industry to meet the general environmental verification standards including corrosion, vacuum, thermal, humidity, mechanical shock, low frequency random vibration, radio frequency noise emission and electrostatic discharge, response to rapid decaying of the pressure of spacecraft during launch. Avionics packaging comprises electronic devices ranging from a transistor, measuring four-billionths of a meter and embedded in a single silicone crystal, to large devices up to multiple systems such as science instruments, solar array, attitude control and communications, power control electronics, command and data handling electronics, star trackers etc. Avionics packaging is a conglomeration of different disciplines such as mechanical, electrical, software, metallurgy and aerospace engineering to apply engineering principles to fulfill form, fit and functionality requirements of the design (Pecht, 2017). According to Moore's law, the observation that the number of transistors in a dense integrated circuit doubles about every two years, an efficient thermal system becomes crucial for dissipating the generated heat for future

application. The trend of rapid advancement in electronics in accordance with Moore's law is seen in Fig. 3.1.

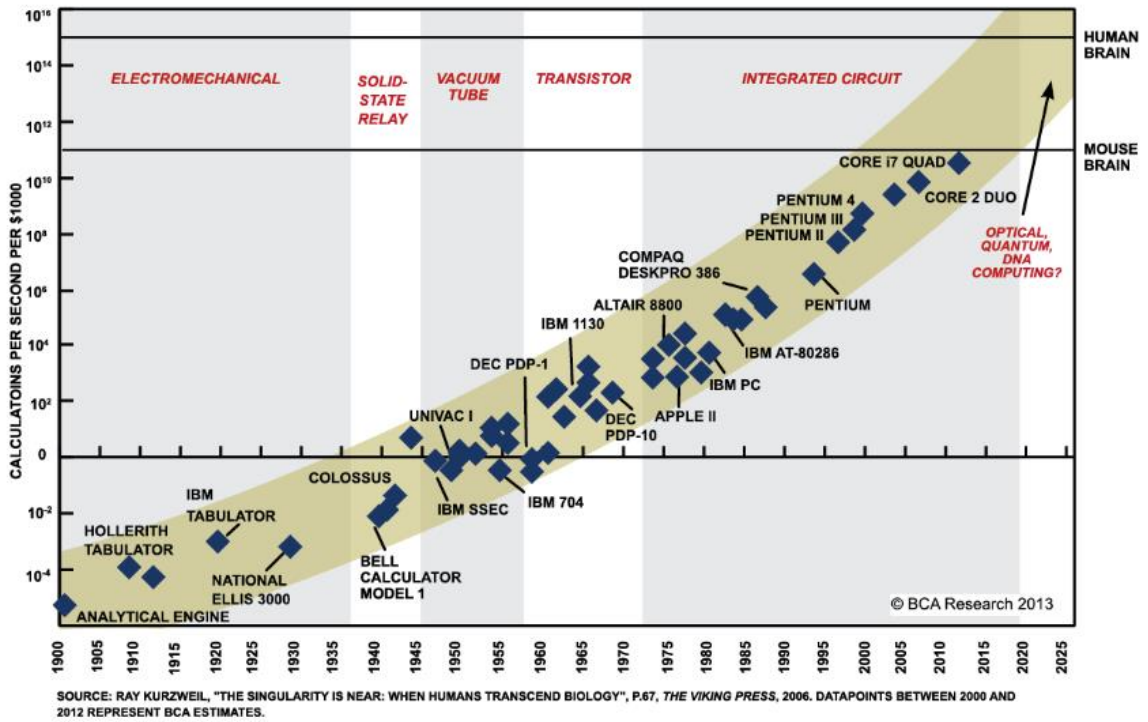


Figure 3.1: A plot of CPU transistor counts against dates of introduction. (courtesy of BCA research 2013)

We will go over challenges between "engineering based on assumptions" and the "need for fundamental characterization and knowledge" of active thermal management system manufactured and assembled by conventional techniques. To satisfy this need we initially focus on creating active cooling prototype with "simple model structures" manufactured by conventional manufacturing methodologies that would permit 1-D thermal characterization of the interface to determine how it should be designed in this chapter and mature the design through evolution by advanced techniques in subsequent chapters. In present chapter, both active and passive thermal management systems are

investigated with emphasis on active cooling utilizing LM and pumping system with moving parts.

3.2 Levels of Avionics Packaging

In general, avionics packaging has five levels and is seen in Fig. 3.2 (Pecht, 2017):

Level zero - "Chip", protecting a bare semiconductor die from contamination and damage.

Level one - Component, such as semiconductor package design and the packaging of other discrete components.

Level two - Etched wiring board (printed circuit board).

Level three – Circuit card assembly (CCA), one or more wiring boards and associated components.

Level four - Module, assemblies include CCAs, heat spreader, interstices card locks and etc. integrated in an overall enclosure.

Level five - System, an array of modules combined and linked together usually via back plane or motherboard.

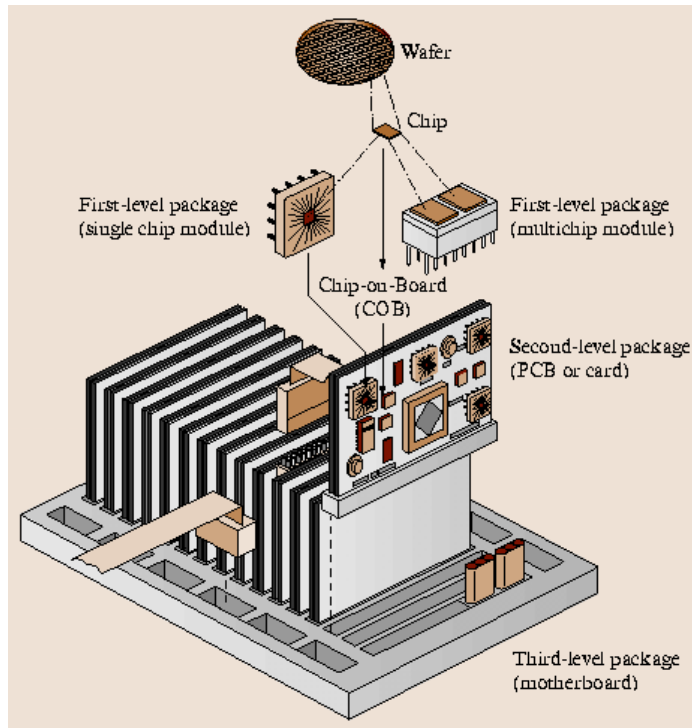


Figure 3.2: Levels of avionics packaging. Courtesy of Michael Pecht, 2017

In typical spacecraft avionics enclosure, heat energy is transferred by direct contact conduction mechanism governed by Fourier's law $Q = -k\nabla T$ where Q is the local heat flux density, $W \cdot m^{-2}$, k is the material's conductivity, $W \cdot m^{-1} \cdot K^{-1}$ and ∇T is the temperature gradient $K \cdot m^{-1}$. Radiation effects (transfer of energy with the help of electromagnetic waves) are negligible considering mounting location of avionics package is not in direct contact with solar system and are electromagnetically shielded from adjacent avionics causing radiation. Finally, convection does not occur in vacuum since convection works by particles colliding and transferring energy. Therefore, the heat is transferred from power dissipating source to the boundary condition that is established by setting the mounting plate temperature of enclosure at the qualification level per requirement. For thermal analysis, the total thermal resistance of electronic packages is generally broken down into (1) component level of junction to case resistance, (2)

package level resistance of case to boundary that the heat flows from the surface of the heat-dissipating component to the boundary through avionics packaging components including thermal vias in PWB, interstices mounted on heat sink, card locks, chassis panels. For the component level, integration of heatsink module at level zero significantly reduces the transistor junction to case resistance for electronics component but interface resistance and conductivity interfaces at higher level of avionics packaging remains a thermal efficiency challenge in cooling paths to the cold plate or boundary.

3.3 Interface Contact Resistance

Conduction mechanism governed by Fourier's law shows that heat energy is transferred by direct contact. For 100% contact in solids the Fourier's law expands as shown in Fig. 3.3 and the following equation:

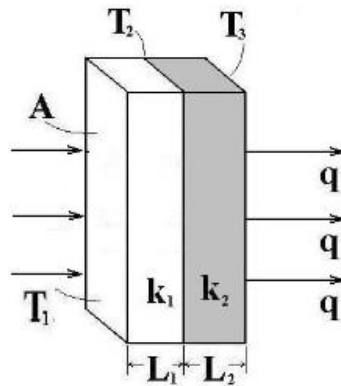


Figure 3.3: 1D Conduction in solid layers in series for assuming 100% contact

$$Q = \frac{\Delta T}{R_{total}}$$

$$R_{total} = R_1 + R_2 = \frac{L_1}{K_1 A} + \frac{L_2}{K_2 A}$$

$$Q = \frac{T_1 - T_3}{\frac{L_1}{K_1 A} + \frac{L_2}{K_2 A}} \quad (2)$$

Where, Q is heat flow in W , K is thermal conductivity $\frac{W}{m \cdot K}$, A is surface area normal to the flow of heat in m^2 , ΔT temperature difference in $^{\circ}K$, L is length parallel to the flow of heat in m . However, thermally conductive piece parts of avionics packaging such as heat sinks, interface panels of enclosures and etc. are fabricated by techniques such as CNC machining, electric discharge machining (EDM), die casting, sheet metal, and so on. One of the drawbacks of having assembly hierarchy manufactured by conventional manufacturing is contact resistance in solid interfaces that are inherently rough and actual contact area is significantly less than the apparent contact area in lieu of careful consideration of dimensions and tolerances and precision of fixture design. Therefore, in real world, two surfaces in contact do not transfer heat perfectly as seen in Fig. 3.4.

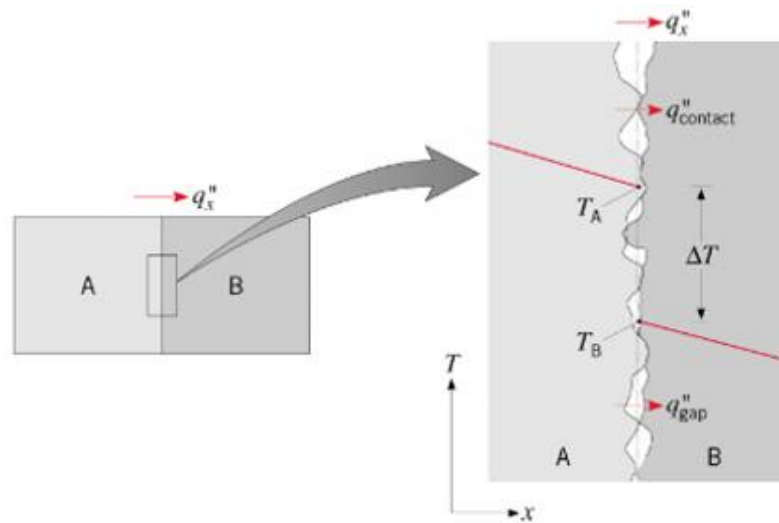


Figure 3.4: Thermal bottleneck creates a "contact" resistance to conducting heat across the interface

Inherent contact resistance at interface depends on contact pressure, surface finish, conductivity of materials, hardness, and elastic modulus. The heat energy is transferred by direct contact conduction mechanism governed by Fourier's law and total contact resistance between two block (Fig. 3.4) is as following:

$$R_{cr} = \left[\frac{1}{\frac{\delta}{(2K_A A_c)} + \frac{\delta}{(2K_B A_c)}} + \frac{1}{\frac{\delta}{K_f(1 - A_c)}} \right]^{-1} \quad (3)$$

Where, R_{cr} is total contact resistance at interface between two blocks with thermal conductivities as K_A and K_B , A_c is assumed direct contact area, δ average gap at interface (thickness of interstitial) and K_f is thermal conductivity of interstitial.

Application of low thermally conductive interstitial material such as foil or grease used in interstices to reduce resistance still not optimal technique for heat transfer application as shown in Fig. 3.5.

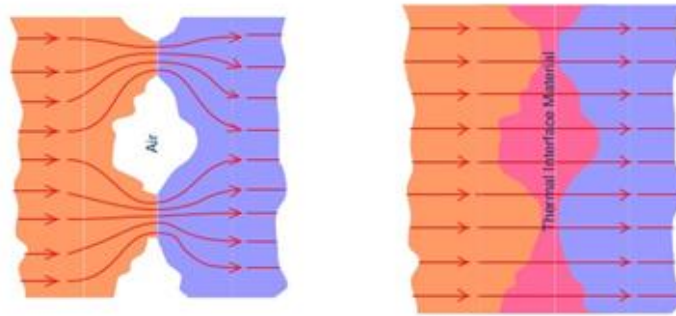


Figure 3.5: Application of thermal interface materials between two solids to fill the air gaps in order to improve the heat conduction

Bonded interfaces have lower thermal conductance (less than %5 of Aluminum 6061) and also have disadvantages such as thermo-mechanical stress imposed on contact surface due to mismatch between coefficients of thermal expansion. Thermal conductivity of various state of matters at room temperature and pressure is seen in Fig. 3.6.

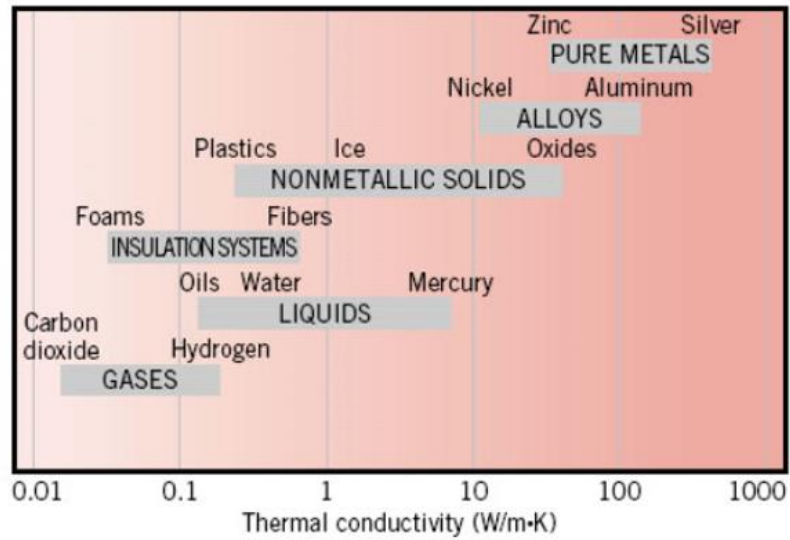


Figure 3.6: Range of thermal conductivity for various states of matter at normal temperature and pressure. (courtesy of GE crops)

However, it was observed that a dramatic change in the enhancement of conductivity takes place with temperature. See Fig. 3.7.

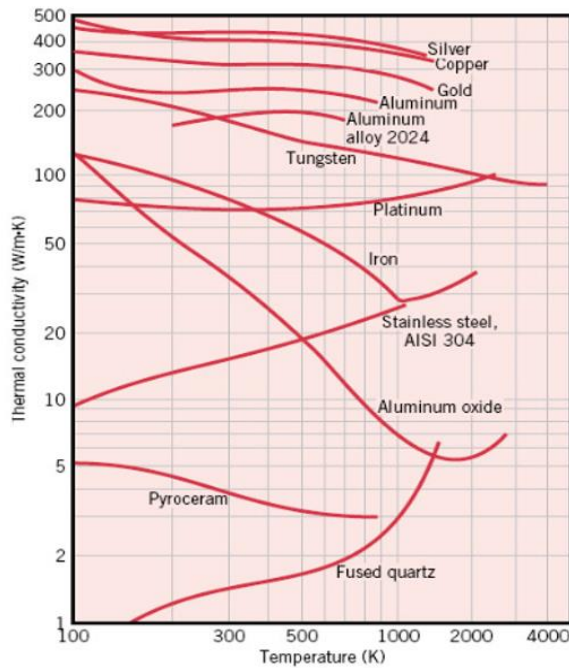


Figure 3.7: Temperature dependence of thermal conductivity for various selected solids. (courtesy of GE corp.)

To further elaborate on the relationship of temperature and thermal conductivity, it is worth mentioning that in metals, heat conductivity is mainly due to the free electrons and thus thermal conductivity increases with temperature, often proportionally to temperature. Additionally, chemical bonds in quartz are also covalent, meaning that electrons are shared between the atoms and thermal conductivity increases by increasing temperature.

As discussed, another factor to take into account is the effect of applied load or torque values on a compression thermal interface. The thermal resistance changes at various standard assembly pressures - when the grease remains in situ shown in Fig. 3.8 (courtesy of Indium Corp.).

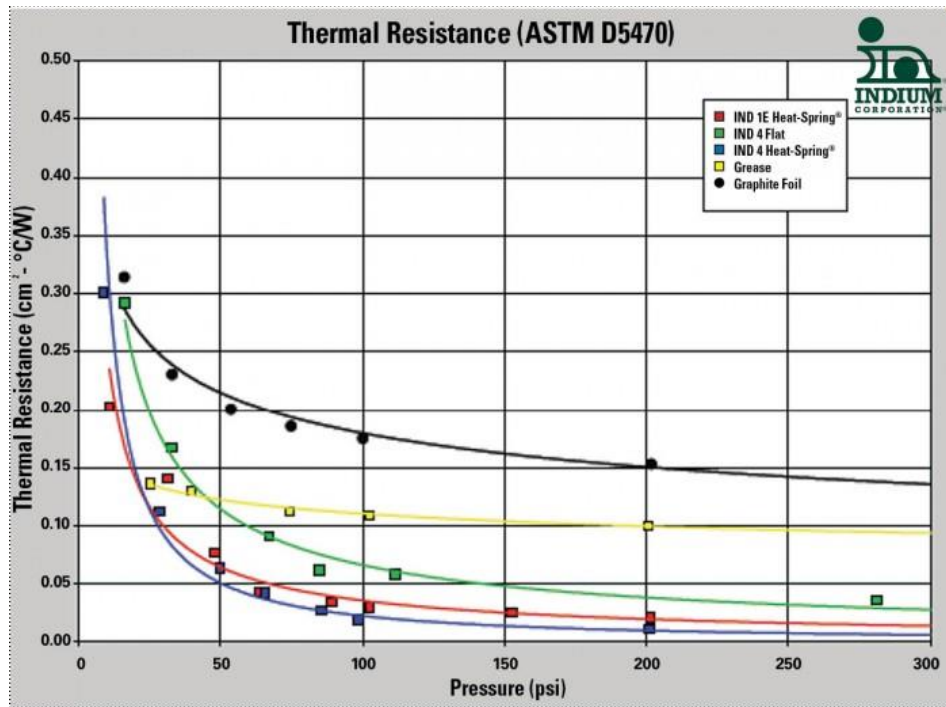


Figure 3.8: Performance of compressible thermal interface materials changes with pressure

The influence of variations of surface finish on the thermal contact conductance between different metallic joints is worth mentioning here. Determinations were done by

experiments or modeling the deformation at the interface for different values of surface finish and contact pressure over the range of interface temperatures considering both elastic and plastic deformation. GE corporation has determined contact conductance vs applied pressure measured by ultrasonic waves for various metallic joints and the values are seen in Figs. 3.9 and 3.10.

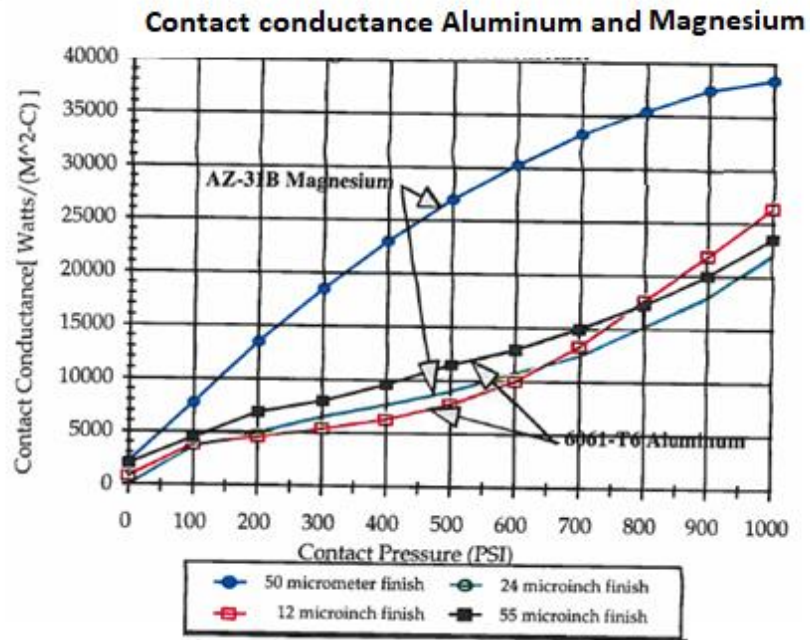


Figure 3.9: Effect of surface finish on contact conductance of Aluminum and Magnesium. (courtesy of GE corps)

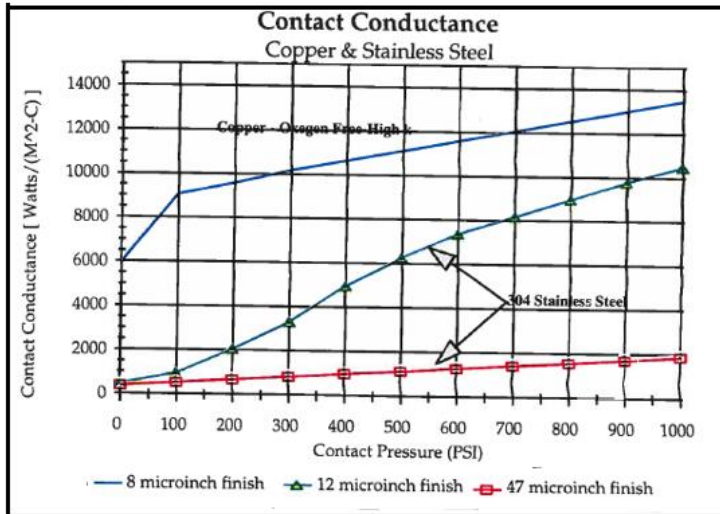


Figure 3.10: Effect of surface finish on contact conductance of 304 Stainless Steel and Copper. (courtesy of GE corps)

3.4 Categorizes of Thermal Management Systems

Thermal management is subcategorized into two categories: (1) passive techniques (2) active techniques, as illustrated in Fig. 3.11.

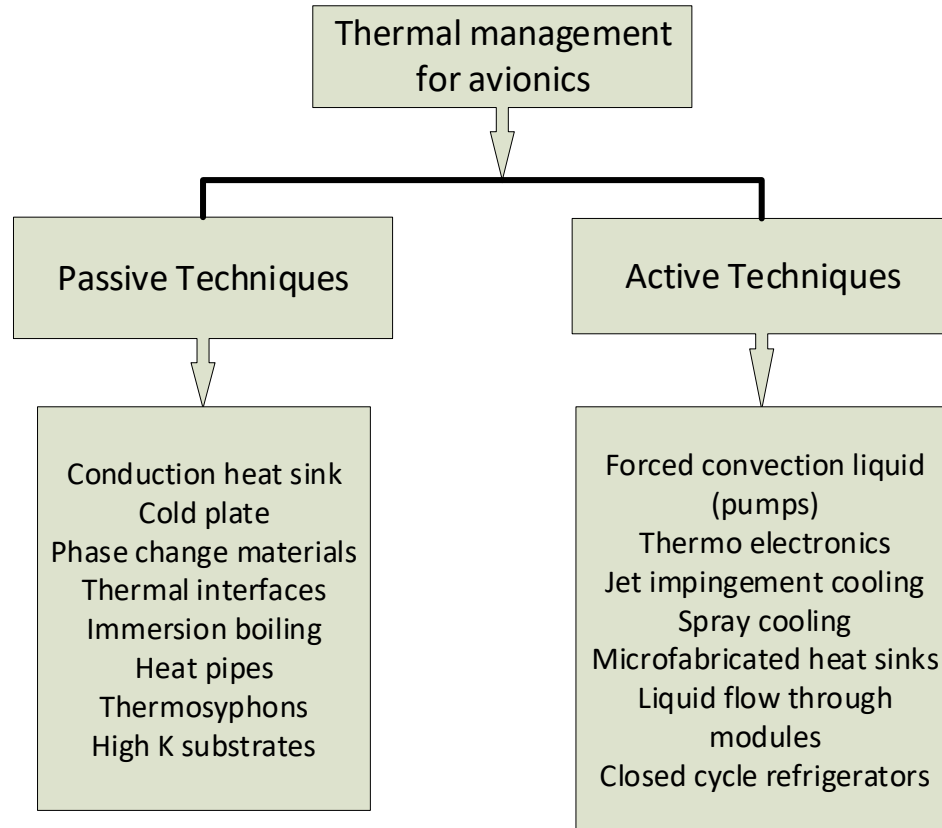


Figure 3.11: Categories of thermal management systems

Avionics cooling includes various styles of heat sinks, thermoelectric coolers, forced air systems, heat pipes, and others. In cases of extreme low environmental temperatures, cryogenics behavior of materials at very low temperatures should be investigated and it might be necessary to heat the electronic components for qualification criteria (www.osha.gov). Passive thermal cooling happens mainly through heat sink that is a metallic part brought into contact with a hot surface of heat dissipating components in avionics packaging to reduce their temperature through increased thermal mass and heat dissipation (primarily by conduction and convection and to a lesser extent by radiation). A heat sink usually consists of a metal structure with flat surfaces (with provision to mount interstitial material) to ensure good thermal contact with the components to be cooled, and an array of fin like protrusions to increase the surface

contact with the air (for none vacuum and air cooled application). For space application, circuit card assembly is laminated to the heat sink using silicone adhesive and chemical film finish for heat sinks (chemical conversion coating primarily used to protect aluminum from corrosion) is required per specifications. Recommended surface finish for CNC machined heat sinks is 16-32 microns. Heat sink transfers heat from an object at relatively high temperature to a second object at a lower temperature with a much greater heat capacity. Efficient function of a heat sink relies on rapid transfer of thermal energy from the first object to the heat sink, and the heat sink to the second object. The high thermal conductivity of the metal and geometrically optimized large surface area of heat sink result in the rapid transfer of heat to cooler. Use of fluids and thermal interface material ensures good transfer of thermal energy to the heat sink. High thermal conductors such as silver, gold, copper, or aluminum alloy are among the most-frequently used materials for heat sink within avionics packaging, however, copper heat sink due to heavy weight and lower modulus of elasticity are not an optimal choice for space application and might fail in low frequency random response vibration test. Furthermore, a clamping mechanism, stiffener, screws, or thermal adhesive hold the assembly and heat transfer is a function of applied pressure. Heat sink performance related to material, geometry and contact surfaces, however, efficiency of interfaces and contact resistance remain an active area for research.

In active cooling systems, liquid-cooled cold plate (sandwiched structure including embedded tubes or channels containing coolant in thick plate) as a heat transfer interface between a heat source and any other boundary improves the cooling performance. The power dissipating part is cooled under the thick plate instead of being

cooled in direct contact with the cooling fluid. The conduction plate improves the heat transfer between the heat source and the cooling fluid by conjugate heat transfer optimal manner (see Fig. 3.12).



Figure 3.12: Exploded view of single phase microchannel liquid cooled cold plate. Thermal Stack includes: branched out heat pipe, interface material, metal plate and clamping mechanism

The efficiency of active cooling systems depends greatly upon micro-channels cross-section and liquid media. It is well known that the performance of micro-channels is largely dependent on its hydraulic diameter as well as fluid properties. However, contact resistance between embedded tubes and thick block drastically effects the efficiency of the cold plate.

Another passive system is cooling with two-phase systems, involves condensation and evaporation through wicks by capillary action are far superior on terms of heat transfer coefficient to single-phase systems. (see Fig. 3.13 for comparison).

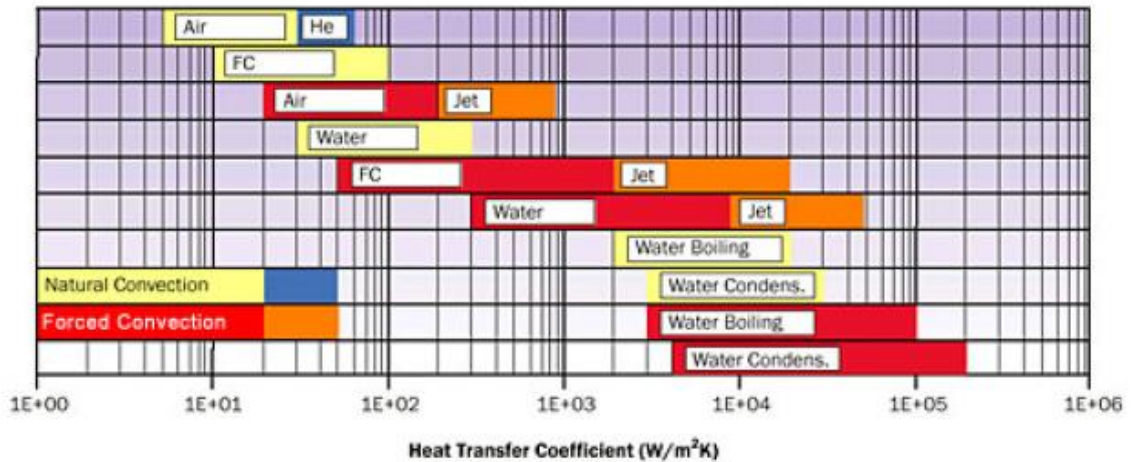


Figure 3.13: Heat transfer coefficients depending on cooling technologies

Evaporative cooling also reduces mass flow rate and reduces temperature gradient. Two phase technologies are widely used include 1). Microchannel flow boiling 2). Spray cooling 3) Jet impingement. In this regard, heat pipe uses condensation and evaporation and of a two-phase coolant to transport heat from the hot to cold interfaces. Usually heat pipe consists of hollow pipe made out of thermally conductive metals such as silver or copper and a wick to return the working fluid from the evaporator to the condenser. The pipe contains both saturated liquid and vapor of a working fluid (such as water, methanol or ammonia). The most common heat pipe for electronics are ammonia heat pipes and wick, with water as the working fluid, methanol is used if the heat pipe needs to operate below the freezing point of water. The advantage of heat pipes is their great efficiency in transferring heat. The thermal conductivity of heat pipes can be as high as 100,000 W/m^{°K}, in contrast to copper, which has a thermal conductivity of around 400 W/m^{°K} (Wojcik et al, 1991). Development of heat pipe is not the subject of this study, however, integration of heat pipes into assemblies to fully dissipate critical components' waste heat and its limitation by contact resistance are.

Active cooling, on the other hand, refers to heat transfer techniques that rely on an external device that requires additional energy i.e. electricity for operation. Through active cooling technologies, the rate of fluid flow increases that consequently increases the rate of removing heat from hot to cold plate. In this chapter, we discuss two types of active cooling solutions: (1) forced liquid by diaphragm pump, and (2) thermoelectric Peltier cooler to simulate boundary condition for proposed prototype. We argue the development of an active cooling prototype with diaphragm pump and assembled by conventional method and in future chapters 4 and 5 we compare its performance with active cooling prototypes packaged by in-situ AM and MHD.

3.5 Development of Metal-Ceramic HX Using Conventional Assembly and Active Cooling with Diaphragm Pump

The assembly of metal-ceramic HX prototype includes the following subassemblies and parts: (1) boundary condition (2) diaphragm pump (3) heat source (4) cold plate including coolant (5) data acquisition unit and thermocouples. See Fig. 3.14

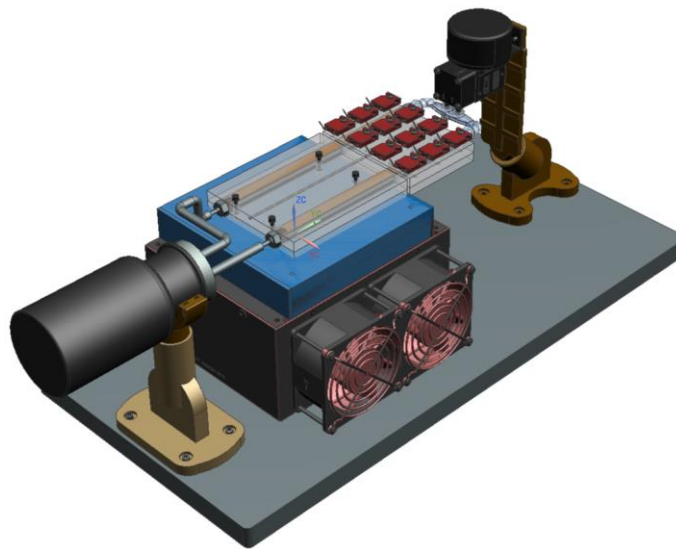


Figure 3.14: CAD model of active cooling prototype including Peltier cooler, diaphragm pump, reservoir, sandwiched structure of conventionally assembled cold plate including embedded copper or silver plates and ceramic tubes

For cold boundary condition of the prototype, Peltier cooler with solid-state heat pumps with no moving parts is used. Heat is transported from top surface where the prototype is screwed to bottom face or vice versa depending on direction of electric current flow. It creates a heat flux between the junction of two different conductors of electricity by applying an electric current. There are no moving parts, so a Peltier plate is maintenance free. It has a relatively low efficiency. However, the solid-state nature of the Peltier plates outweighs their poor efficiency (Gao et al, 2017). The basic physics of a thermoelectric cooler is seen in Fig. 3.15.

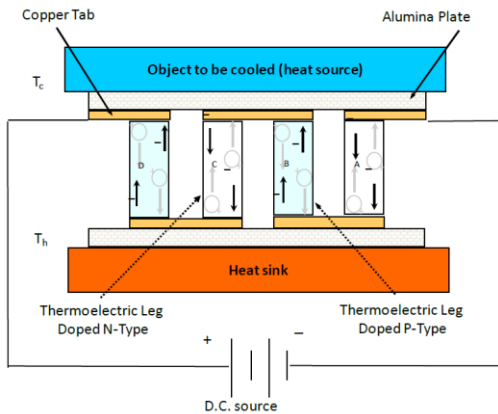


Figure 3.15: Basic physics of thermoelectric Peltier cooler with solid-state construction

Net cooling power of Peltier cooler is related to thermoelectric cooling, Joule heating and heat conduction, and performance graph of TE CP-121 from TE technology used in this study is seen in Fig. 3.16.

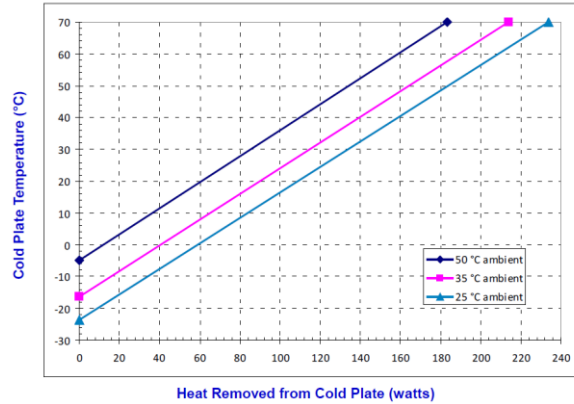


Figure 3.16: Cooling performance graph of CP-121 Peltier cooler from tetch.com

To control the temperature of the Peltier cooler i.e. 10 °C, a cool-only temperature controller from TE technology (P/N: TC-48-20) is used. The controller is connected to the computer via RS232 serial cable for advanced programming as well as data graphing and data logging.

For pumping liquid in proposed prototype, a 12V DC compact brushless direct current diaphragm pump is producing the driving force. It can handle high viscous fluid such as LM and schematic of the diaphragm pump (P/N NF30KPDCB) is shown in Fig. 3.17.

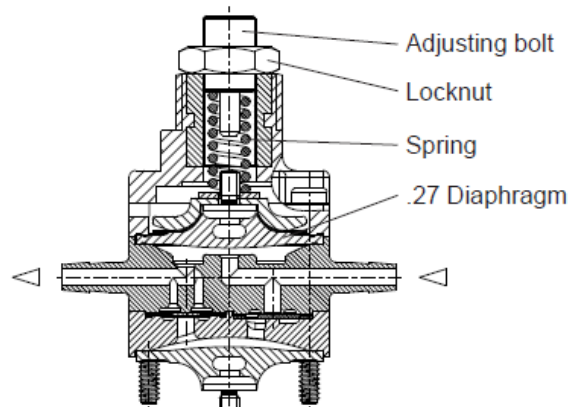


Figure 3.17: Schematic of Diaphragm Pump, flow rate .3 L/min and maximum pressure head 14.5 PSIG

Surface mounted resistors are used as heat source and screwed down to helical coil inserts of metal block and #4-40 screws torqued to 4.7 IN-LB. Figs. 3.18 and 3.19 show the structure, part number and specification of heat source used in this study.

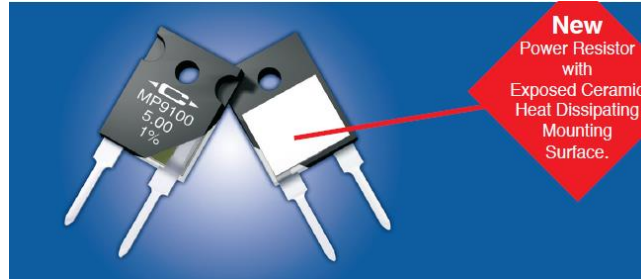


Figure 3.18: CADDOCK, MP9100 Series Power Film Resistors

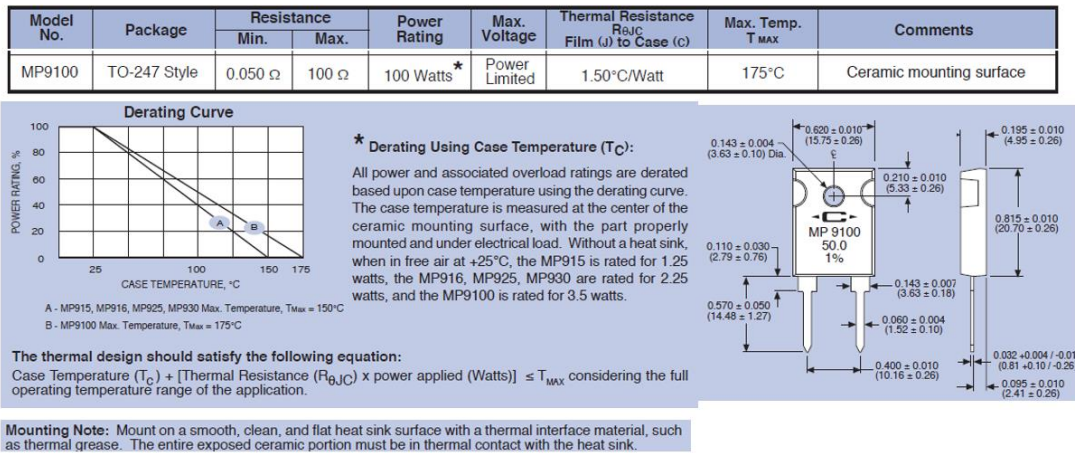


Figure 3.19: Derating curve and specification of mounting resistors (heat source)

The resistors are connected together in parallel fashion to make a thermal grid as seen in following figure to generate required power in watts by applying appropriate voltage and current from DC power supply.

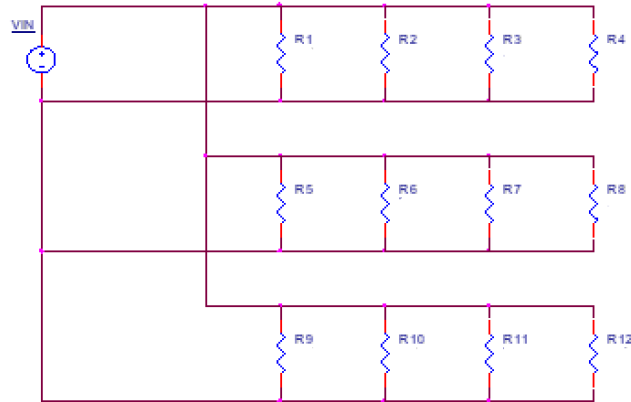


Figure 3.20: Resistors parallel grid providing total electrical resistivity required to generate power to dissipate heat

Cold plate is playing a crucial role in transferring heat and following figure shows the exploded view of cold plate. The cold plate has LM compatible ceramic/polymeric tubes, gauge 20 copper or silver plate (.8mm thick) embedded by conventional assembly method in 3-piece metallic block (sandwiched and bolted structure). The reader is referred to the next chapter, where, under the morphology of embedded tubes, we argued the details and rational to select the shape and material of the tubes. We are going to compare the conventional cold plate presented in this chapter with cold plate fabricated by in-situ SLM introduced in next chapter with emphasis on thermal interface resistance. Therefore, materials and geometries for both cases are identical. Three pieces of metallic block are fabricated by AM SLM out of aluminum alloy (EOS AISI10Mg).

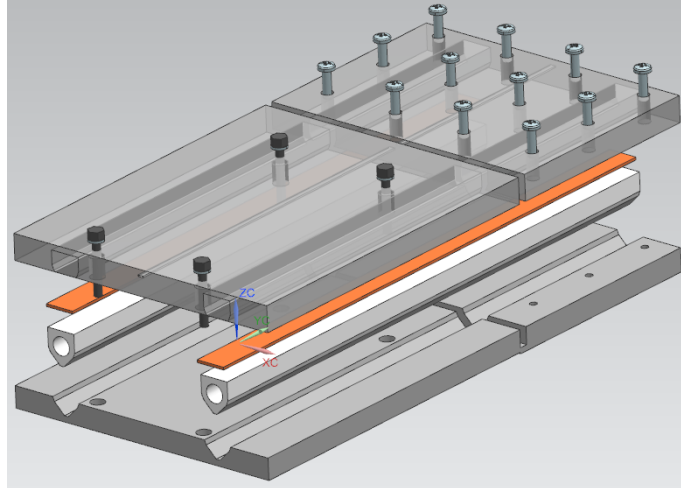


Figure 3.21: Exploded CAD model of cold plate including BN pipes, gauge 20 copper plate (.8mm thick), encapsulated by conventional manufacturing of 3 piece SLM aluminum alloy block (final envelope size is 100x185x18 cubic mm)

Fig. 3.22 shows the fabricated cold plate piece part including Ultem tubes fabricated by FDM technique.

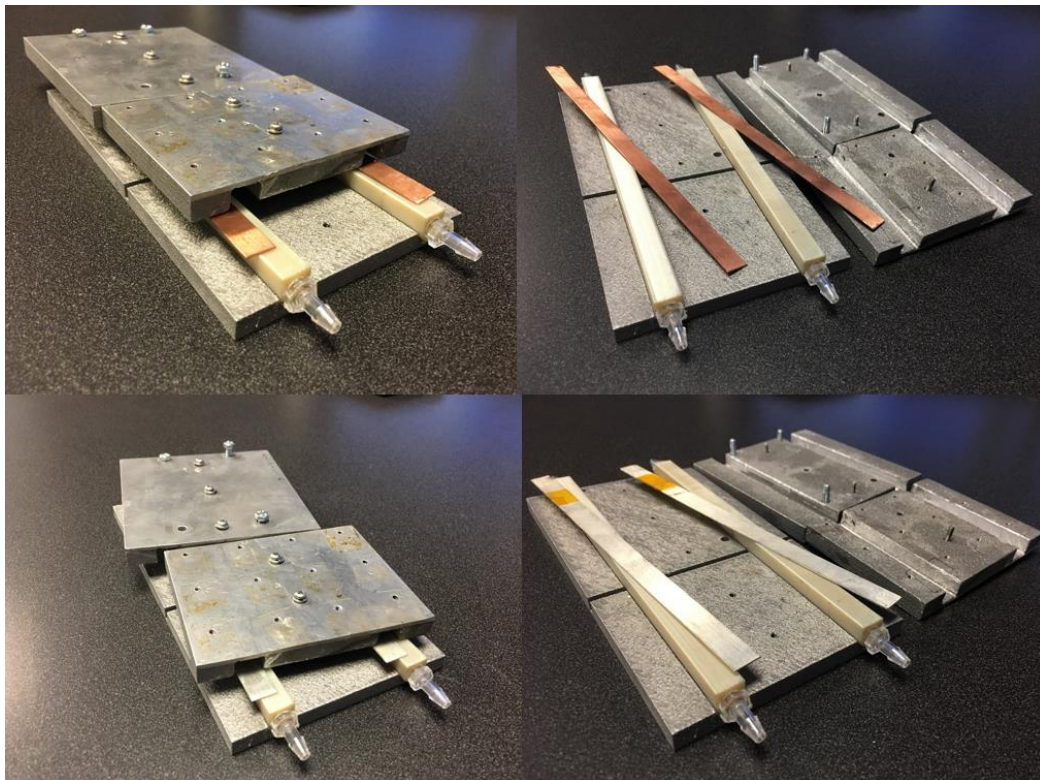


Figure 3.22: Exploded view of conventionally assembled cold plate including FDMed Ultem tube, gauge 20 copper (top row) or silver (bottom row) off-the-shelf plate, fastened with #4-40 screws torqued to 4.7 IN-LB.

Likewise, Fig. 3.23 shows the fabricated cold plate piece parts including ceramic BN tubes. Ceramic tubes are fabricated by CNC machining.

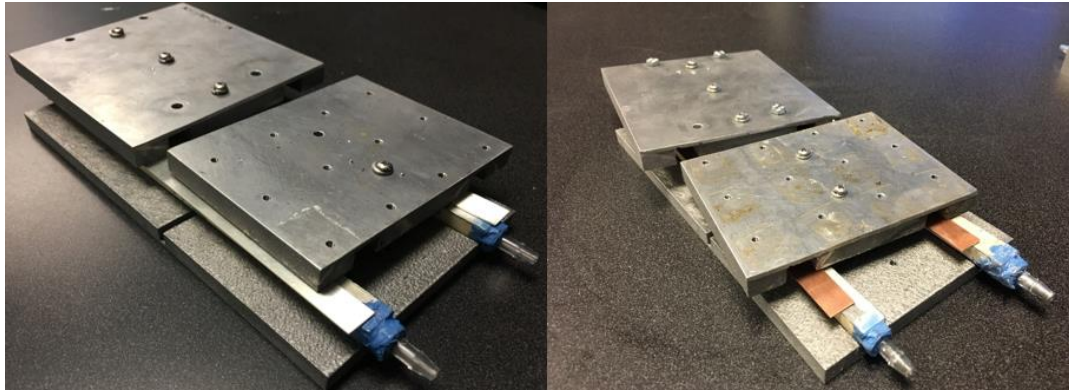


Figure 3.23: Exploded view of conventionally assembled cold plate including ceramic tube, gauge 20 silver (left) or copper (right) off-the-shelf plate and #4-40 stainless steel screws torqued to 4.7 IN-LB to 3- piece SLM aluminum metallic block.

Then, we add flexible tubes to close the flowing loop, so the LM coolant can circulate through channels of the cold plates used in conjunction with a diaphragm pump, thereby comprising a typical pumped liquid cooling loop. Galinstan is selected as coolant for this study which is a low-melting point eutectic gallium alloy (67%Ga, 20.5%In, and 12.5%Sn by volume) and has a broad temperature range of liquid phase and melts at -19°C (-2°F). Its electrical conductivity (3.46×10^6 S/m (room temperature) allowing the liquid to be pumped by more efficient electromagnetic pump and used for specific heat conduction and/or dissipation discussed broadly in chapter 5. However, gallium alloys are corrosive to all metals except tungsten and tantalum and have to be contained in compatible container such as ceramic and polymeric container. Fig. 3.24 shows viscosity of Galinstan dependency to temperature that decreases with increasing temperature.

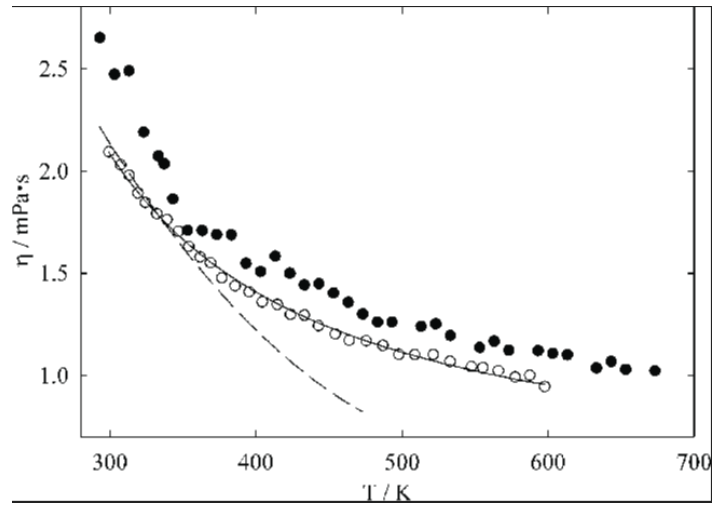


Figure 3.24: Galinstan, viscosity vs temperature curve

A series 2000 variable area flow meter (flowmetrics inc) is included in flow line to measure the LM coolant flow rates, providing accuracies to $\pm 1\%$ of flow rate. Materials of construction are available for the most corrosive process applications and compatible with Galinstan LM.

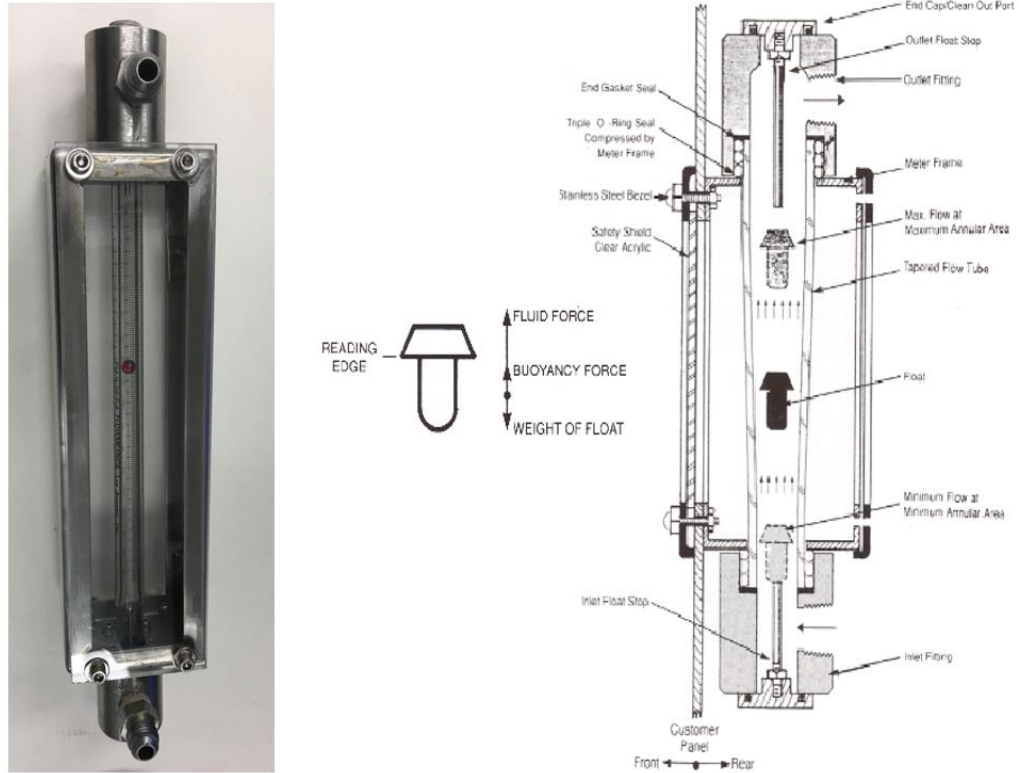


Figure 3.25: LM compatible Series 2000 variable area flow meter (flowmetrics inc) and its schematic view showing subassemblies and piece parts

The variable area flow meter consists of a vertically mounted tapered borosilicate glass tube, a metering float free to move within the tube, as LM flow increases, the sum of the buoyancy force and the fluid force on the float eventually exceeds the weight of the float and the float rises. As the float rises in the tapered tube the annular area between the float head and tube increases until the hydraulic forces acting on the float are in equilibrium with the weight of the float. At this point the float assumes a constant level, changing only with the increase or decrease in flow rate. The unit can be calibrated for operating fluid, the calibration curve for Galinstan is shown in Fig. 3.26.

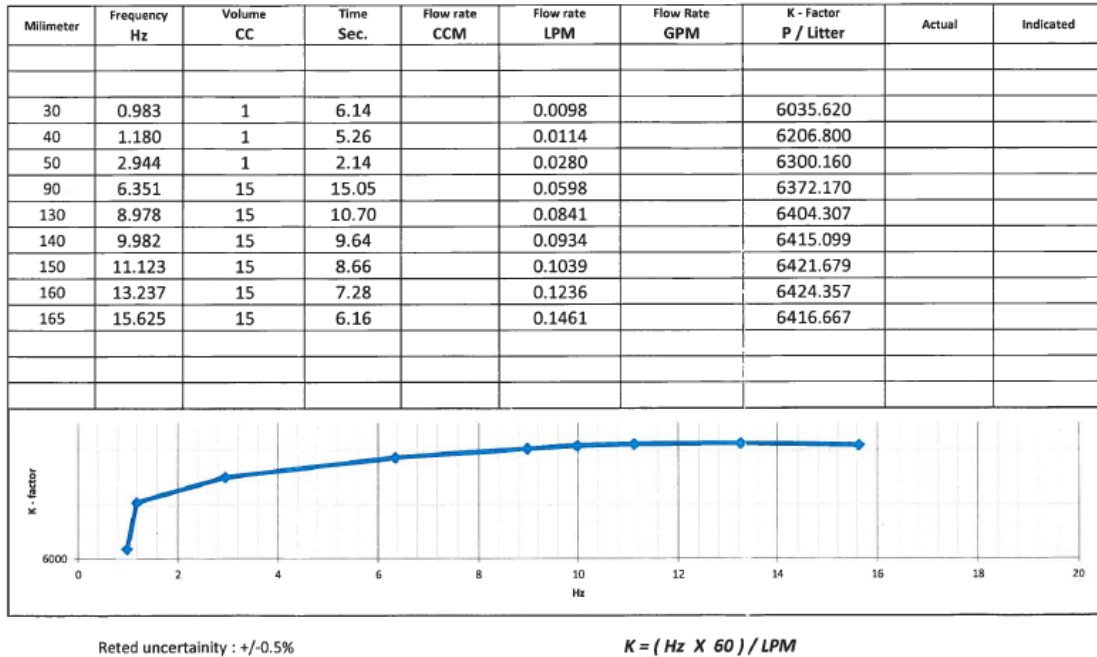


Figure 3.26: Calibration worksheet for Galinstan, Dynamic viscosity= .0024 Pa.s and Density 6.44 g/cm³

During our thermal test, flow meter is removed after measuring of the flow rate because of pressure drop of the flow due to frictional shear forces caused by flow meter and consequently it reduces the efficiency of thermal system. For flowmeters, the manufacturer typically calculates the value of pressure loss for a particular meter and operating fluid.

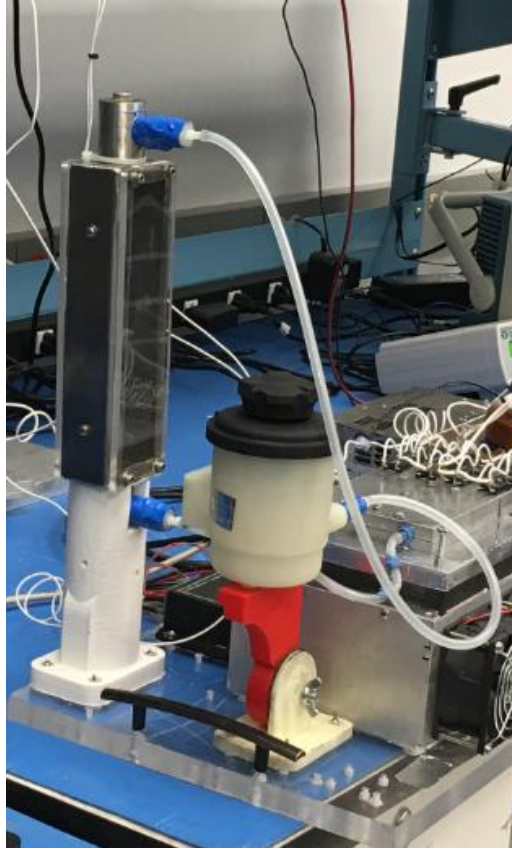


Figure 3.27: Flow meter is connected in series to flow line to measure the flow rate and removed for thermal testing

3.5.1 Computational Fluid Dynamics of Active Thermal Cooling Prototype

Ansys Fluent is used for CFD simulation. Preprocessing efforts include tetrahedron mesh and assigning material properties and conservative 100% contact is assumed at interface of coolant container (ID 6.2mm) and 3-piece SLM aluminum alloy metallic block ($100 \times 185 \times 18 \text{mm}^3$). Preprocessing with adaptive mesh is seen in Fig. 3.28.

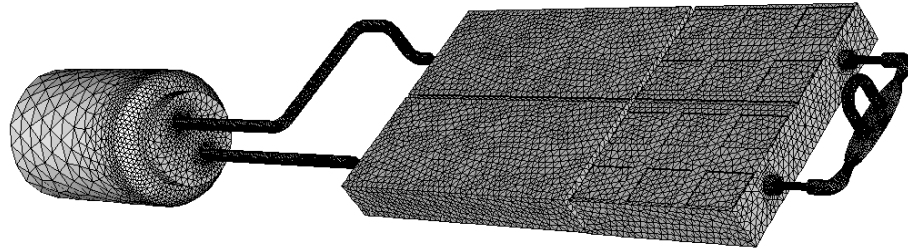


Figure 3.28: Ansys Fluent, preprocessing tetrahedron adaptive mesh of control volume and cold plate of active cooling prototype by diaphragm pumping

Specific boundary condition available in Ansys (fan boundary condition) is used to split the tube as shown in post processing figure to simulate the characteristics curve of the diaphragm pump. Characteristics curve of diaphragm pump is seen in Fig. 3.29.

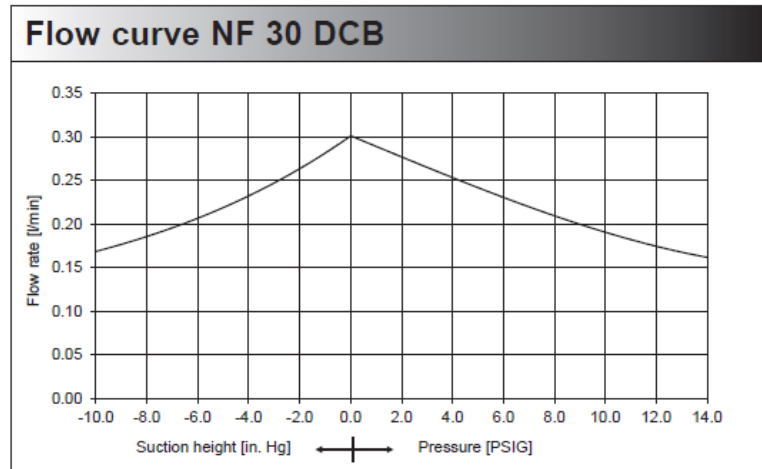


Figure 3.29: Characteristics curve of diaphragm pump, applied in CFD simulation for forced correlation-based convection couplings. (P/N: NF30KPDCB DC compact brushless direct current diaphragm pump extracted from KNF Inc)

To define the boundary condition identified at bottom surface of metallic block touching the Peltier cooler “exterior wall boundary” type is used to specify constant 10°C at interface. The solution is the numerical solution to the active cooling problem that we posed by defining the mesh and boundary conditions. The more accurate the mesh and boundary conditions, the more accurate the "converged" solution. Steady state solution

satisfies the following three conditions: (1) residual root mean square (RMS) inaccuracy values have reduced to an acceptable value ($< .0001$) (2) monitor points for velocities have reached a steady converging solution (3) domain has imbalances of less than 1%.

The converging results are shown in Fig. 3.30.

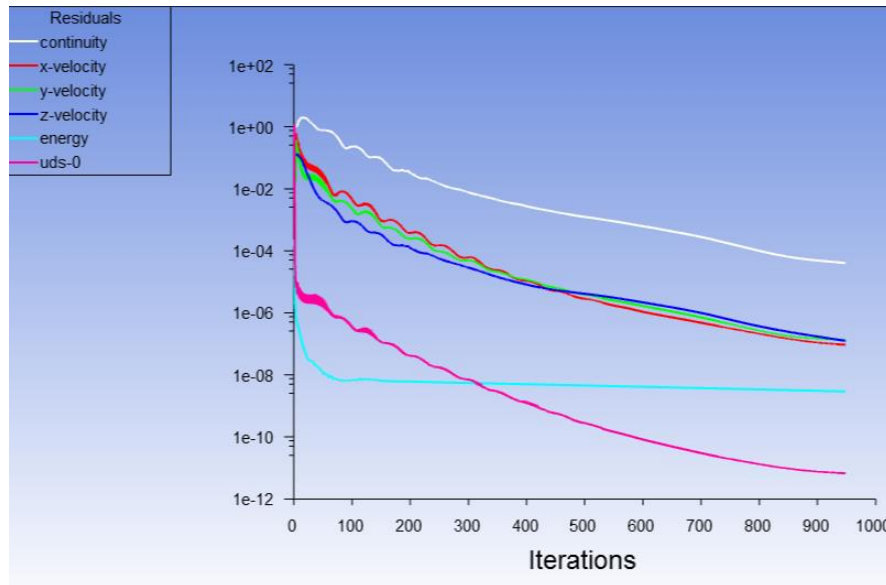


Figure 3.30: Ansys Fluent, steady state converging solution for monitored points for parameters of interest i.e. velocity after several iterations

By solving the energy equation embedded in Ansys FLUENT solver, which results temperature contours of cold plate, the conjugate heat transfer is used to describe heat transfer that involves variations of temperature within solids and LM due to thermal interaction between the solids and LM as seen in Fig. 3.31. In this simulation, we have a fixed heat source ($12 \times 32.5 = 390$ watts) and heat is taken away by the AM cold plate and free convection. The heat transferred by free convection is negligible (less than 10%) and most of heat dissipated to the cold boundary condition via conduction. Fig. 3.31 shows the thermal contour of control volume, cold plate and hybrid tubes.

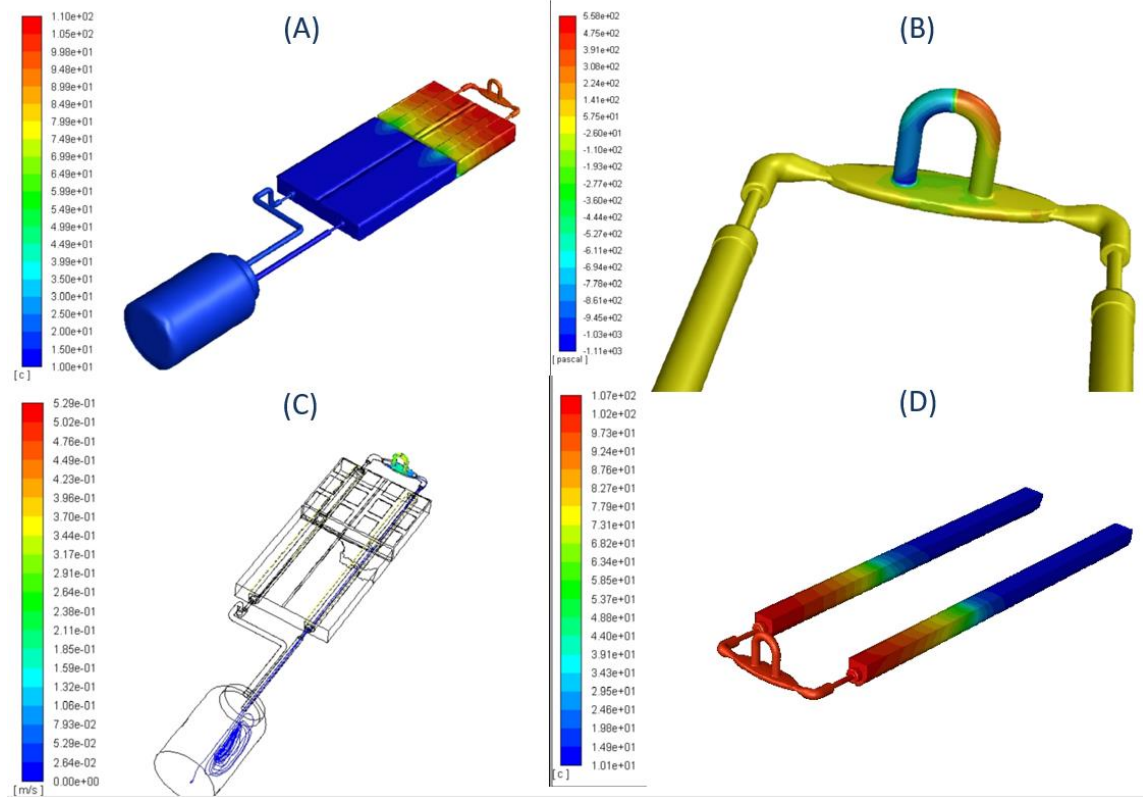


Figure 3.31: Ansys Fluent CFD post processing results of active cooling by diaphragm pump and circulating Galinstan LM coolant through cold plate to reservoir in closed loop. Applied load is 390watts, B.C. is 10°C from Peltier cooler and 25°C from natural convection. (A) Temperature contour (°C) of control volume and AM cold plate encompassing copper plated ceramic tubes, material of cold plate block is SLM Aluminum alloy (AlSi10Mg_200), (B) Static pressure (Pascal) of diaphragm pump applied to fluid, (C) path lines of velocity magnitude of LM (m/s) (D) temperature profile of ceramic tubes and pump coupling (°C).

The following report shows that most of the heat is transferred via conduction of the heat block and active cooling contribution is less than 5%. See Fig. 3.32.

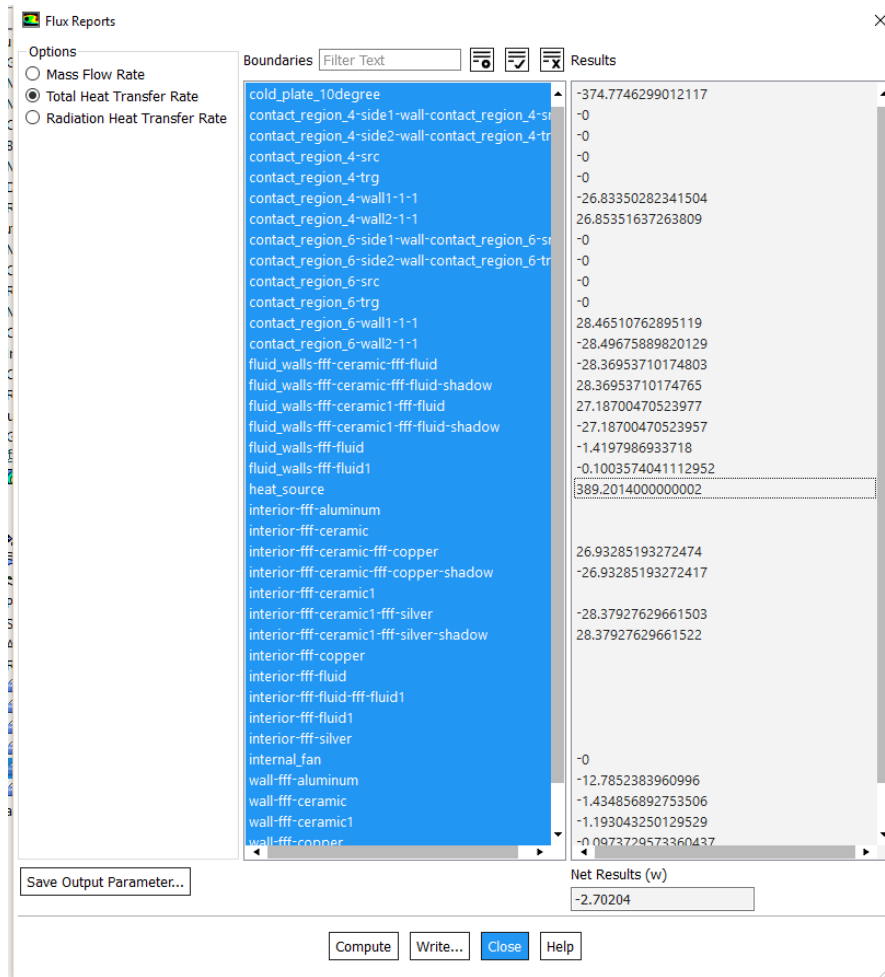


Figure 3.32: Ansys Fluent active cooling by diaphragm pump: post processing report

In this section, we used CFD to virtually test the CAD model of active cooling prototype and get detailed information on its performance. Engineering simulation is insightful, and it is a required step before performing actual costly test to validate the final design. Even though suitable model for CFD simulation includes assumptions and simplifications lacking all thorough parameters, it complements the thermal testing and allows testing multiple iterations and scenarios fast and early in the design process. The CFD results are over predicting but look promising to build the prototype and perform actual thermal test discussed in following section.

3.5.2 Thermal Testing Setup and Data Acquisition Instruments

Thermal testing is the crucial part of qualification and characterization of active cooling prototypes. We use calibrated data acquisition system consists of sensors (thermocouples which produce a temperature-dependent voltage as a result of the thermoelectric effect, and this voltage can be interpreted to measure temperature), actuators and signal conditioning hardware (Omega data acquisition DAQ module (Part Number: USB-TC-AI), a windows 10 quad core computer running laboratory virtual instrument engineering workbench (LabVIEW) DAQ software to process temperature data and controlled room to monitor ambient temperature for natural convection. DAQ module with 4 channels plugged to T-type thermocouple probes and 2 samples/second per input sampling rate is used and linked to LabVIEW environment for generating temperature graphs sensed by thermocouples. The test stopped once the steady state is reached and data recorded. Fig. 3.33 shows the location of thermocouples and main components of thermal cooling prototype using diaphragm pump with moving parts and assembled by conventional manufacturing techniques.

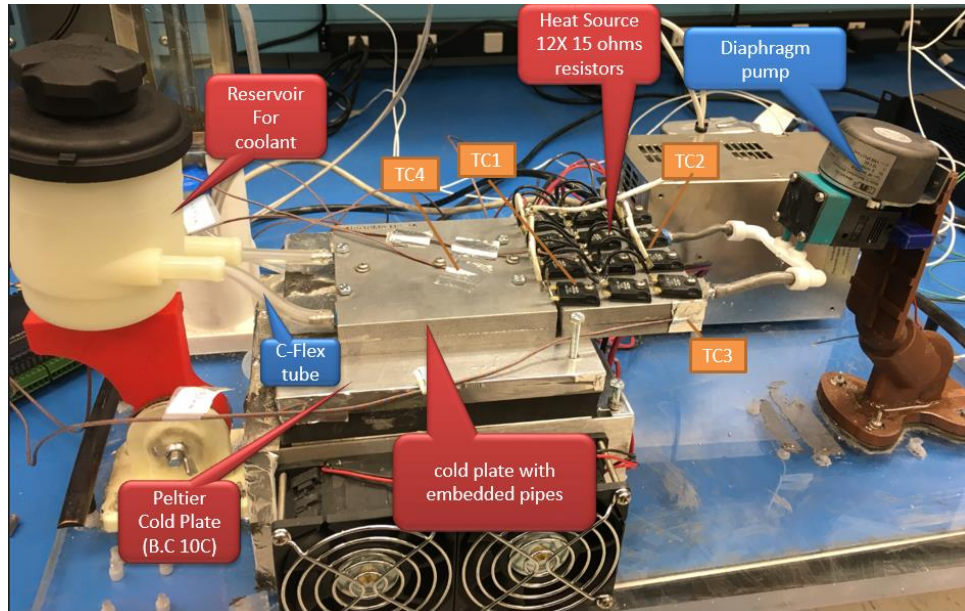


Figure 3.33: Active cooling with moving parts and conventionally packaged cold plate (3-piece cold plate, BN ceramic or FDMed Ultem tubes, and gauge 20 copper or silver plate). TCXs show location of thermocouples.

Thermocouple locations are seen in Fig. 3.33. The thermal test and thermocouple readings are repeated for all fabricated cold plates with conventional manufacturing techniques. At each step, the data needs to be examined to see if it is reasonable, that limits (temperatures, pressures, etc..) of the test equipment are not exceeded and to assure that the next step is reasonable. When repeating a series test, the interval should be adequate to allow the temperature to stabilize. Record the thermocouples reading mounted at critical and identical locations for all specimens after reaching steady state, complete the data sheet and conclude the test. As mentioned earlier, fabricated prototype with conventional assembly technique argued in this chapter will be compared with cold plates fabricated by in-situ AM technique discussed in next chapter. Polycode is used to identify subsets of active cooling prototypes for the purpose of realizing common features for clarification as seen in Fig. 3.34.

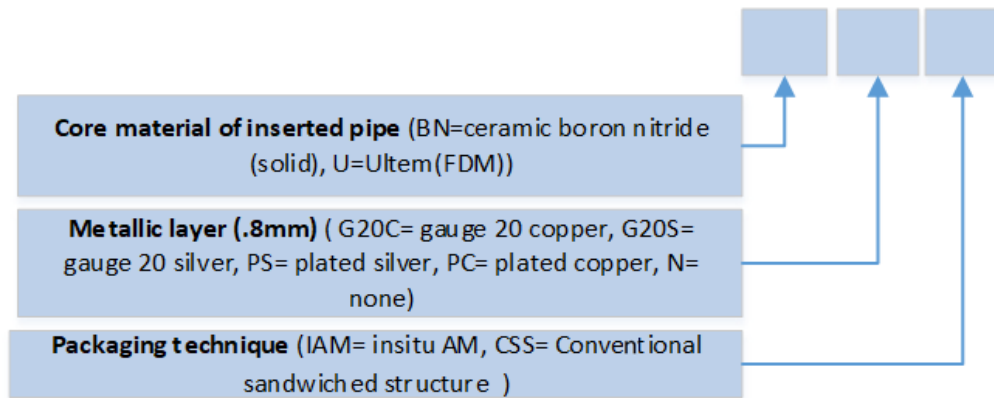


Figure 3.34: Polycode of cold plate types used on Table 3.1 (block material for all cases is AM aluminum alloy AlSi10Mg)

The following table of thermocouples reading from thermal test will be progressed to include data for in-situ AM cold plates and draw conclusion regarding their performance in upcoming chapter, where, under the thermal testing of embedded tubes by in-situ AM technique, we discussed and compared the thermal efficiency of the prototypes.

Table 3.1

Thermocouple Readings of Cold Plate Made of SLM Aluminum Alloy with Different Inserted Tubes and Assembled by Conventional Sandwiched Structure

Run no.	Cold plate type	Thermocouple (TC) readings (°C)			
		TC1 (hot point)	TC2	TC3	TC4
1	BN-G20C-CSS	33.10	27.26	20.35	14.72
2	BN-G20S-CSS	32.46	26.61	22.08	14.65
3	U-G20S-CSS	37.33	29.30	24.06	13.33
4	U-G20C-CSS	38.02	29.93	21.78	14.04

Note. Heat source: 72 watts, Galinstan (coolant), Peltier cooler set to 10°C for B.C., forced convection pumping pressure 2260 Pa, ambient temperature 25°C, steady state reaching time 120 min. BN = ceramic boron nitride, U = Ultem; G20C = gauge 20 copper, G20S= gauge 20 silver, CSS = conventional sandwiched structure.

3.6 Conclusion

Essentially, contact resistance is one of the "disadvantages" of using "stack up assembly" in cooling system including subassemblies packaged together to transfer heat efficiently and continuously for avionics packaging. In this chapter, we reviewed level of avionics packaging with emphasis on challenges associated with thermal conductance at interfaces of levels 4 and 5 governed by Fourier's law. Furthermore, we went over application of viscoelastic interface materials such as thermal grease, pliant thermal gasket, or metallic thin foil, and their thermal performances under applied load, surface finish and contact conductance for metallic interfaces. Moreover, study of passive and active cooling techniques for avionics packaging including performance of their crucial solid components i.e. heat sink, cold plate, two phase heat pipes revealed that contact resistance creates a bottleneck for heat carriers across the interfaces and prevents efficient thermal transport in lieu of thermal efficiency of adjacent elements in both categories. Then we developed the first active cooling prototype "forced convection with conventional diaphragm pumping and LM coolant flowing through embedded tubed in metallic blocks assembled by conventional technique". In upcoming chapters, we will develop enhanced active cooling prototypes packaged by in-situ AM technique and will compare to conventional cooling prototype argued in this chapter to reveal their thermal performances and important attributes to improve reliability of spacecraft avionics packaging.

Chapter 4: Improving Interface Contact Resistance of LM Compatible HXs by In-Situ AM with Embedded Electroplated Ceramic Tubes

4.1 Introduction

In previous chapter, we discussed about the heat transfer in layered structures or stack up assemblies manufactured and packaged by conventional assembly method with the emphasis on interfacial thermal resistance that creates a bottleneck for heat carriers across the interface and how it prevents efficient thermal transport in lieu of efficiency of HX elements. In present chapter, we will demonstrate how additive manufacturing technologies can overcome critical limitations of traditional manufacturing processes to improve heat transfer capability of hybrid heat sink structure and yet reduce secondary operations of assembly that cause additional gaps between seams or on surfaces of inserts. This would allow us to "engineer the interface" through fundamental modeling, in-situ manufacturing and characterization through experimental findings. Therefore, improving efficiency and enhancing reliability of thermal management systems for avionics by reducing contact resistance are the scientific and engineering contributions from this study. Main research themes relevant to the LM compatible HXs packaged by in-situ AM technique with embedded electroplated ceramic tubes are as follows.

4.1.1 Using LMs as A Class of Coolants for Thermal Control of High-Power Avionics

Low viscous metallic alloys that are in liquid form within the operating temperature range of electronics with high molecular thermal conductivity and low Prandtl numbers is a class of coolants, which allow their use in power engineering equipment at high temperatures and low pressure (Zeigarnik et al,1996). Compared to

conventional coolant, first order thermal model of geometrically optimized minichannel heat sinks suggests that Galinstan is a better coolant than water in such configurations, reducing thermal resistance by about 40% (Hodes et al, 2013). Tang et al demonstrated how a LM bead could drive flow of an ionic fluid (salt water) by applying square wave signal across it to create a pressure differential through the Lippman effect (Tang et al, 2014). In active cooling by peristaltic or roller positive displacement pumping system with LM, the fluid contacts only the inside surface of the tubing thereby negating concern for incompatibility and contamination of viscous and shear-sensitive and aggressive LM fluids, however efficiency is limited by liquid viscosity since the flow is pulsed, particularly at low rotational speeds (Ma et al, 2007). The two primary advantages of LMs (superior thermal properties and ability to be pumped by magnetohydrodynamic pump due to its electrical conductivity) permit development of single phase cooling systems. By implementing a closed loop gravity independent high performance pumping, results have shown heat transfer coefficients on the order of $10 \frac{W}{cm^2 K}$ and 8 KPa pumping pressure (Miner et al, 2004). To reduce temperature dependent viscosity of LM, thin wire heater can be implanted into LM or attached to the tube wall to guarantee the flow of coolant bypassing freezing condition (Li et al, 2011). LM Galinstan has been shown to improve thermal conductivity of thermal management structures using Lorentz force MHD pumping for hi-performance CPUs, but rapidly fail due to corrosion (Deng et al, 2013). Despite all of these advances, LMs such as gallium alloys are corrosive to all metals except tungsten and tantalum and have to be encapsulated in compatible thermally conductive ceramic i.e. ceramic or polymeric tubes in HX application (Eichler et al, 2008). However, LM compatible tubes have wear resistance and outgassing issue, and to

overcome the abrasion and erosion weaknesses, we embed ceramic or polymeric tubes in strong thermal structure such as block of metallic cold plate that creates an inefficient thermal transport at interface of tube and metallic block.

4.1.2 Creating Interfaces Between Ceramic and Metal

Limited research exists on basic mechanism of inherent thermal boundary resistance and contact resistance has created a bottleneck for heat transfer due to short path and high temperature differences, preventing efficient thermal transport. Understanding the thermal resistance network, including contacts, is key to determine the optimal design for meeting the thermal management needs. In this regard, He et al used representative volume element (RVE) to predict the thermal conductivity of polymer-matrix composites accounting for the contact resistance and witnessed the lowest contact thermal resistance is achieved for cylindrical fillers due to the highest surface-to-volume ratio (He et al, 2016). Thermal contact conductance is an important factor in avionics, largely because microsystems packaging contain a mechanical combination of two materials and following factors influence contact conductance: contact pressure, surface flatness and roughness, surface cleanliness, interstitial materials and plastic deformation (Zhao et al, 2016). Dongmei et al conducted experimental investigation of the thermal contact resistance between non-conforming rough surfaces of copper and stainless steel revealing effect of thermal conductivity of both solids on thermal resistance, harmonic mean thermal conductivity of dissimilar contact materials and experimental measurement of thermal resistance between thin films. The thermal contact resistance of oxygen free coppers and the thermal conductivity exhibited an exponential relationship under low pressure conditions and a polynomial relationship when the external pressure ranged

from 0.53 to 0.71 MPa. (Dongmei et al, 2020). Additionally, materials typically used to fill interstices (e.g. thermal grease) tend to have poor thermal conductivity. Therefore, the greater thermal conductivity of the individual element that makes them excellent candidates for heat transfer applications, such as hybrid heat spreaders, is negated by the interface resistance, which drastically influenced by manufacturing techniques used to fabricate heat transfer structures.

4.1.3 Manufacturing Metallic HX with Embedded Ceramics by AM

An in-situ AM process enables development of more efficient thermal structures by eliminating secondary operations that cause additional gaps between seams or on surfaces of inserts. In-situ manufacturing technologies have also facilitated researchers to develop geometrically complex heat exchangers so that the fluid tube is laid into channels within the HX structure and using AM to provide a better heat path from the fluid to the structure surface. In this regard, Bruck and Gupta discussed the thermal challenges associated with using thermally conductive filled polymers as a structural material for more effectively managing heat in embedded actuators, realized using in-mold injection molding (Bruck et al, 2009). Through development of experimentally-validated models of the injection molding process and FEA modeling of the temperature fields generated by the actuators, they were able to ensure both thermal and structural functionality to demonstrate feasibility of creating multifunctional structures by embedding actuators in thermally conductive filled polymers using the in-mold assembly process. Coronel et al used robotic insertion of foreign object in FDM structures to fabricate 3D hybrid electronics with embedded circuitry, thermal vias and wire routing (Coronel et al, 2018). Thermal conductivity of the hybrid heat transfer structure is affected by injection molding

process parameters especially with respect to temperature and pressure during the molding process. Bruck et al have also studied the rheology and melt flow for in-mold assembly of pre-molded components in applications such as thermal management (Bruck et al, 2010; Bruck et al, 2012). In-situ placement of foreign part in SLM block with different properties is challenging. Melt pool depth and flow while printing the SLM layer on top of the inserted part require further investigation to understand the characteristics of "processing-structure-property" of fabricated part.

4.1.4 Highlighted Attributes of AM on Thermal Efficiency of HX

AM is capable of producing thermal structures in a wide range of materials, however, every step of these processes has impact on the density, near netshapeness, imperfections and consequently thermal efficiency of the produced parts. For example, thermal performance of the parts fabricated by selective laser melting (SLM) is affected by reflective index of alloy materials, oxide layer and surface roughness of printed layer. McVey et al measured the light reflected from powder with the help of an integrating sphere in order to realize that the distribution of the scattered light and the small absorption in the integrating sphere coating can affect the density and thermal properties of sintered parts (McVey, 2007). Martukanitz et al used a calorimetric scheme to measure the energy absorbed by powders during the SLM process, however they did not account for radiative and convective thermal transport of the melt pool, which effectively increased the absorptivity (Martukanitz et al, 2004). Rubenchik et al used in-situ thermocouples attached to the bottom of a disk covered by thin layer of metallic powder that was uniformly irradiated by a laser light source to gain insight about thermal behavior (Rubenchik et al, 2015). Yadroitsev et al obtained useful insight about the depth

and width of the melt pool using a single-track experiment involving the spreading of a layer of powder on a thin plate, thereby enabling the creation of several tracks at varying laser power and speeds. After cutting the plate and etching/polishing the cross-section, they were able to reveal information about the depth and width of the melt pool (Yadroitsev et al, 2010). While the single tracking technique can ensure sufficient melting locally for a given powder layer thickness, other processing parameters including the overlap between adjacent scan lines and the scanning strategy affect the density and residual stress of the part. In this regard, Ferentz et al simulated the SLM process as the thermo-mechanical response of a nonlinear solid continuum by ignoring flow dynamics in the melt pool and developing the SLM model in the context of a representative volume element (RVE) using balance laws, boundary conditions and material models (Hodge et al, 2014). Likewise, the melt pool that flows under the influence of vaporization recoil and surface temperature gradient drives Marangoni convection and mass transfer due to a gradient of the surface tension (Le et al, 2019). The Plateau-Rayleigh instability in a long, cylindrical melt bead can cause a pinching-off of some sections of the pool from others in AM SLM process (Getling et al, 1998). Khairallah et al have modeled and experimentally validated the sensitivity of laser absorptivity for the Marangoni convection. The melt track is divided into three sections: (1) topological depression, (2) transition region, and (3) tail region, revealing the melt pool bottom and duration of the ramp down of laser power ramp and recoil pressure in the laser for powder bed based fusion of stainless steel for the generated melt pool, material sparking and denudation zone. In the SLM process, material-laser interaction is performed via ray tracking, characterized by the length, direction and separation (hatch spacing) model of melt pool, as well as flow and

convection of the liquid in melt pool (Khairallah et al, 2016). From these researches, we have learned that fabrication of reliable thermal management structure is feasible by adapting and understanding advanced AM processes and the use of enhancements to the printable materials. However, complexity of insertion process and micro level bonding of interfaces have not yet been further identified.

4.1.5 A Strategy to Augment Wettability of Thermal Interfaces

Furthermore, the efficiency of active cooling systems depends greatly upon wettability and surface tension of interfaces, and materials compatibility to assure fusion to provide minimal contact thermal resistance via optimal bonding. In our work, we found that silver or copper electroplating was required to fuse the metal to the ceramic pipe in powder bed based AM process. Other approaches include Keramati et al's work that used AM DMLS technique to fabricate a manifold-microchannel HX as a compacted single part unit to optimize the production process (Keramati et al, 2019). Shen et al studied the improvement of mechanical properties of thick nanocrystalline layer of electroformed copper deposited in neutral aqueous 0.1 M NaCl solution to promote a convenient, controllable and reliable surface (Shen et al, 2019). Research related to the feasibility of near net shape AM products revealed that geometric limitations for inserts, difficulty with powder removal in cavities and micro channels in SLM parts, and cultivated design features for inserted parts fabricated by FDM have all been determined to be challenges in realizing advance thermal management hybrid AM structures (Kumar et al, 2012; Lappo et al, 2003). Zhaohui et al filed a patent for preparing a ceramic package substrate with a copper-plated dam encompassing electrodes and also performing thin film metallization on a surface of a ceramic board. Chemical bonding,

chemical reaction, and the interfacial structure of metal/ceramic interfaces are influenced by temperature, time, pressure and alloying additions. Metal/ceramic interfaces wettability and work of adhesion can be predicted qualitatively from bonding models based on the elements of metal and ceramic. Additionally interfacial energy minimization dominates the atomic structure of metal/ceramic interfaces (Wu, Zhaohui, 2019). Lament et al have used an in-situ AM direct laser writing strategy for creating 3D features to overcome difficulties associated with facilitating the macro-to-micro interfaces required for fluid delivery and effect of microchannel geometry in the sealing performance of a structure (Lamont et al, 2019).

In this chapter, we demonstrate a novel approach to reduce the contact resistance in a newly developed technique for embedding LM compatible structure using AM SLM processes. We then discuss how heat from electronics can be transferred to a LM coolant, circulating through geometrically complex internal channels of the cold plates used in conjunction with a pump, thereby comprising a typical pumped liquid cooling loop. The in-situ AM process enables multi-material structures to be fabricated by melting metal on top of an inserted tube to reduce the contact resistance that occurs with conventional assembly processes. However, there are technical and scientific challenges associated with this in-situ AM processes. The first challenge is related to the feasibility of inserting LM compatible tube into a SLM powder bed, where the embedded part can potentially collide with the powder coater and roller, thereby halting the process. Second, the melt pool depth and flow while printing the first few layers on top of the inserted part requires further investigation to understand the effect on the final fabricated structure. Finally, survival of the delicate features of the embedded part when exposed to thermal stress

associated with localized laser heating is a major challenge. Addressing these challenges are the focus of this study, particularly through: (1) proper selection of AM technology and relevant parameters i.e. laser beam intensity, hatch spacing, laser scan speed, layer thickness, (2) bonding of the major thermal interface, and (3) appropriate design of the geometry and selection of material for embedded part. It is through this in-situ AM process of embedding the tube in the HX structure that the contact resistance is reduced, and in this chapter experimental results showing this reduction is presented.

4.2 Manufacturability of Metal-Ceramic HXs

Adapted SLM, FDM, CNC machining and electroplating are processes used for manufacturing of hybrid HX. We fabricated nine AM cold plate blocks including ceramic and polymeric tubes in two separate iterations. AM cold plates fabricated for first iteration failed, however cold plates of second iteration including copper- and silver-plated ceramic tubes were fabricated successfully based on observations from the first iteration. We elucidate both iterations in this section.

4.2.1 Iteration #1 (Series, Parallel, and Branched Out FDM Polymeric Tube Inserted in SLM Metallic Block of HX)

We have selected four shapes for exterior profile of tube based on overhang constraint for topology optimization of self-supported structures in SLM and FDM processes, as seen in Fig. 4.1.

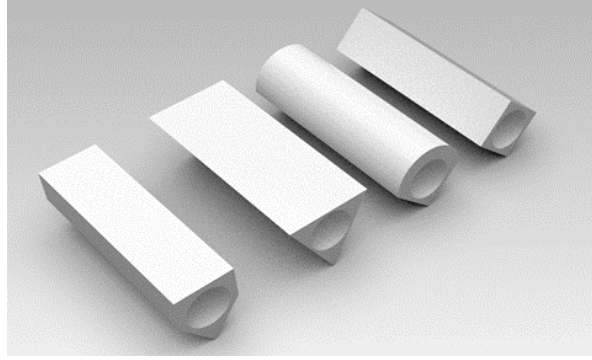


Figure 4.1: Four candidates tubes consideration to eliminate support structure for overhang in AM process and maximizing surface area normal to heat load. Irregular pentagon for exterior profile and circular cross section for interior profile with minimum wall thickness as 1 mm is ideal shape selected for this study (far left).

The morphology of the LM compatible polymeric tube has three features: (a) optimal wall thickness of the tube as 1mm, a compromise between the thinnest wall amenable for manufacturability and the need to minimize thinness for heat transfer. Because of low thermal conductivity of Ultem , the tube should be as thin as possible for optimal heat transfer and still sealed for flow of LM with high surface tension and yet amenable for FDM process. (b) Interior cross-section of the tube that LM flows through as circular. According to Chezy equation with Manning's roughness coefficient in duct flow and approximation of cross sectional area by hydraulic diameter, the interior cross sectional shape of the tube should be circular to minimize flow resistance. (c) Exterior profile of tube interfacing with metallic block in next in-situ insertion step. We embed the fabricated tube inside SLM print bed, inserted tube should have maximum surface area normal to heat source and still amenable for in-situ SLM without collision with roller or blade and yet elimination of support structure for overhang to fabricate the channels inside thermal block. These constraints specify the exterior profile of the cross section of coolant container as irregular pentagon selected from proposed candidates shown in Fig. 4.2.

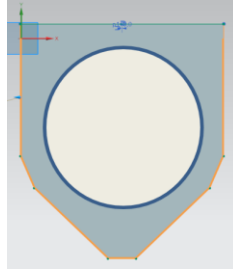


Figure 4.2: Cross section of LM compatible polymeric (Ultem) tube with 1) irregular pentagon for outer profile 2) circular interior profile ID=4 mm and min wall thickness amenable for FDM is 1mm (iteration #1)

For longitudinal profiles of control volume, we have selected closed loop in series, parallel and branched out shapes. Prior to insertion of the tube inside the SLM structure (for details refer to fabrication steps of metal-ceramic HX in iteration #2) and to prevent damage of the polymeric tube encountering hot melting pool generated by laser fusion in SLM process, we electroplated the fabricated tube with .05mm thick copper seen in Fig. 4.3.

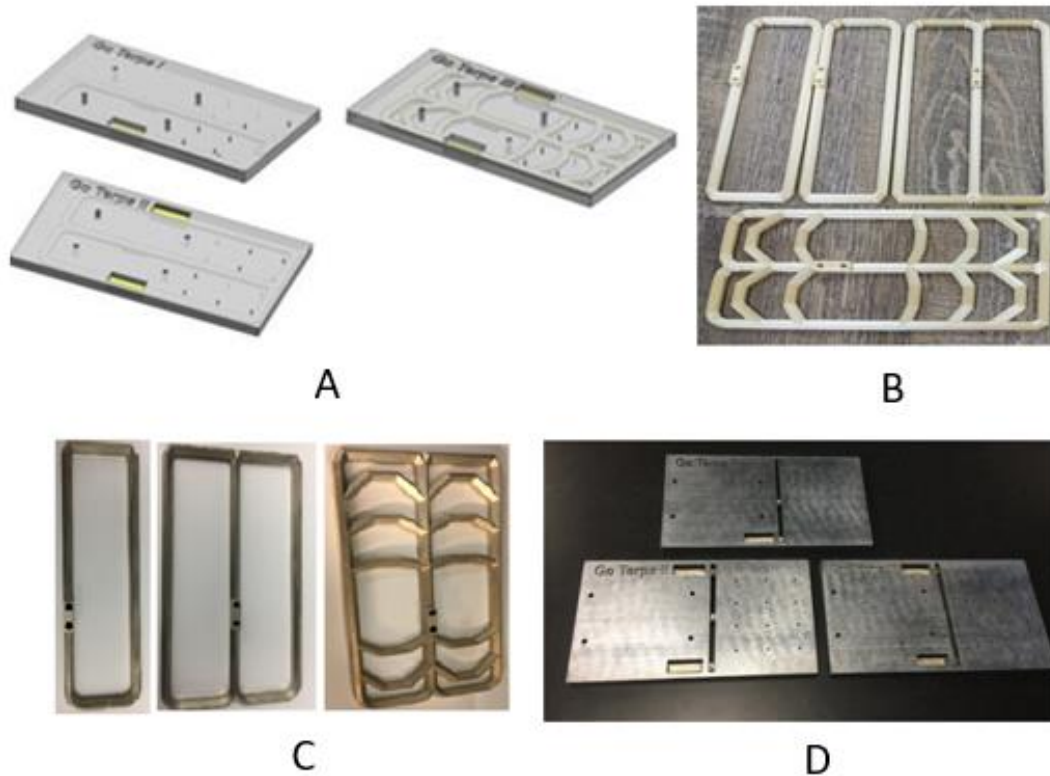


Figure 4.3: A). Isometric view of CAD models (185mmx100mmx18mm), B). Prefabricated channels for insertion in SLM process (ID 4mm), wall thickness 1mm, material: Ultem, C). Post processing of fabricated channels (.05mm thick copper plating and .012 mm nickel plating) D). Fabricated in-situ cold plate by SLM process (EOS290 machine) material aluminum alloy AISI10Mg_200.

Experimental leakage test and x-ray pictures in Fig. 4.4 have shown that the laser radiation of SLM process penetrated through the .05mm copper electroplated layer, melted and damaged Ultem tube causing leakage. Therefore, the efforts to fabricate AM cold plates for first iteration were unsuccessful and thicker plating was used in later iterations.

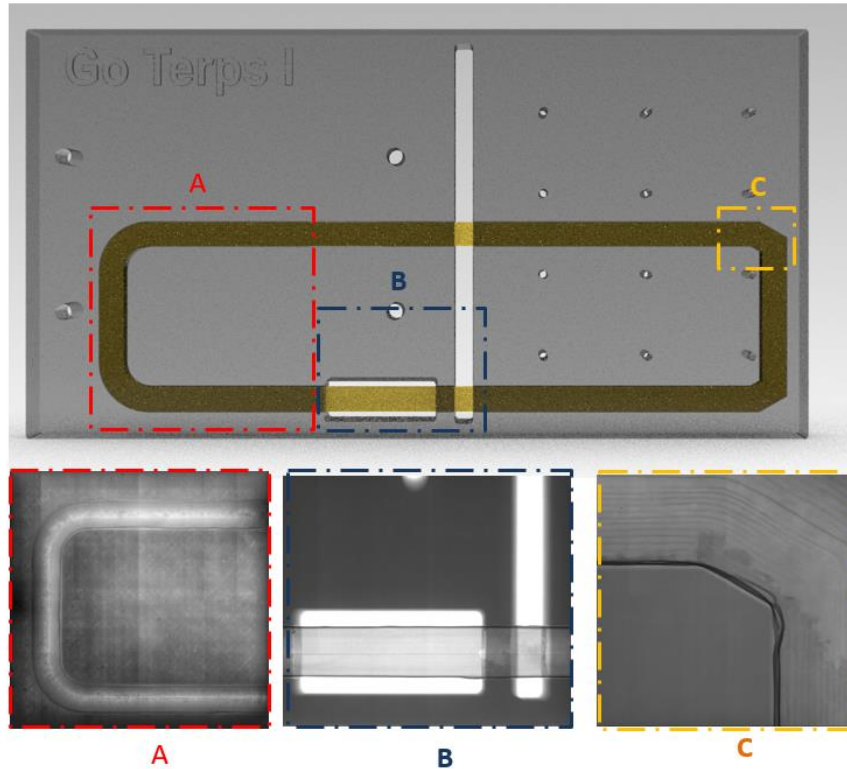


Figure 4.4: X-rays images normal to top surface of insitu DMLS cold plate (model: Go Terps I) at partial locations labeled A, B and C taken by GE Phoenix Nanome/X (140kV, 50UA beam power), showing the damaged copper/nickel plated Ultem pipe inserted in SLM aluminum alloy process. Insitu AM part finished 3D printing but failed and caused leakage due to inadequate thickness of plating of .05mm.

Development of cold plates for first iteration and realizing them through new AM processes that permitted use of what normally would be corrosive LMs has enabled us to demonstrate in-situ AM manufacturing potential. However, laser penetrated through .05mm thick copper electroplating and damaged the Ultem tube. To understand LM flow for cooling and heat transfer properties of LM compatible layered cold plate that includes electroplated films, we performed thermal experiment through iteration #2. In particular, we fabricated simple straight one-dimensional multilayer tubes inserted in AM process to specify the relationship between the thickness of the plating interface and its laser fusion with AM powder to optimize adhesion at interfaces and to reduce interfacial defects that can retard thermal performance. Moreover, BN solid ceramic was used as tube material,

because of high melting point, capable of withstanding SLM laser temperature, compatibility with LM and high thermal conductivity up to 130 W/m·°K. Furthermore, we discussed the tradeoff between flow forces, viscosity affected by the wettability of BN.

4.2.2 Iteration #2 (1D Straight Ceramic/Polymeric Tube Embedded in Metallic AM HX)

4.2.2.1 Fabrication of ceramic or polymeric LM compatible 1D tube

For CNC machining of ceramic BN tube, 2D detailed drawing was prepared and shown in following figure. Similarly, identical STEP file was generated for FDM of Ultem.

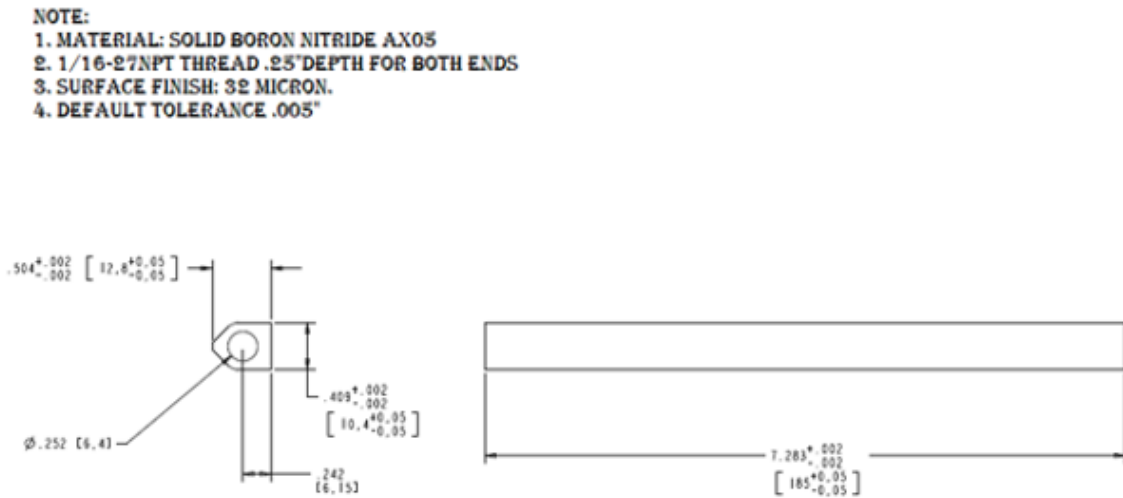


Figure 4.5: Simplified 1-D profile of LM tube with irregular pentagon as outer profile and circular inner profile feasible for CNC machining or FDM process of iteration #2

4.2.2.2 Electrodeposition of outer surface of tube

Electroplating before insertion will facilitate fusion of the silver or copper plated ceramic with the melted metal powder by reducing defects associated with the surface tension of the melt and the wettability of the ceramic. For solid grade AX05 hexagonal

boron nitride ceramic tube, the plated layer is laser fused nicely with SLM aluminum alloy (EOS AISI10Mg_200) powder compared to failed fusion between bare BN ceramic and SLM aluminum alloy powder (see Fig. 4.6). Laser sinter process is characterized by extremely rapid melting and re-solidification and has a certain anisotropy due to layered built method. The melt pool temperature in DMLS process for EOS AISI10Mg is 670°C-750°C, and melting point of electrodeposited copper (1085°C) or silver (961.8°C) are lower than that of BN (2973 °C) creating better amalgamation of metal-metal rather than ceramic-metal during SLM insertion step.

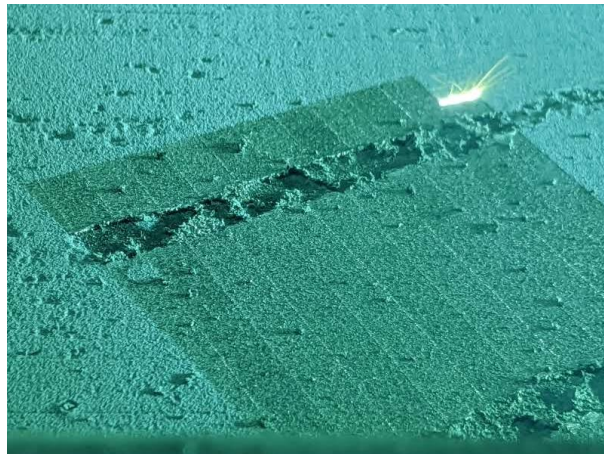


Figure 4.6: In-situ SLM process showing inserted bare solid BN ceramic tube in aluminum alloy block, when scanning the layer on top of the ceramic, the powder was unable to adhere causing the build to fail.

Similarly, for reliability issues and preventing melting of inserted FDM tube in SLM print bed (melting point of Ultem 350°C), FDM tube is copper or silver-plated (see Fig. 4.7).



Figure 4.7: Copper electroplated (.8mm thickness) ceramic BN tubes in electrolytic solution during electrodeposition process, required surface of ceramic is metalized prior to deposition process.

Thick layer of plating (i.e. 2 mm) is prone to voids and porosity due to limitation of plating techniques that would affect thermal conductivity of plated layer. Conversely, thin layer (i.e. .05 mm) of plating fused during SLM laser scanning would cause the build to fail since the metallic powder could not adhere to thin electroplated layer, additionally laser radiation can penetrate through the thin layer and melt low melting base material of tube such as Ultem.

Required thickness of plating is specified by the depth of melt pool, penetration of laser while printing the SLM layer on top of the inserted part and absorbed radiation energy. Actual absorbed energy depends on the coupling of the laser and mixed layers containing particle of inherently light aluminum-silicon powders (with high melt fluidity and relatively low shrinkage) interfacing silver or copper electroplated layer. For instance, a 60 W laser with a pulse width of 20 microseconds focused to a 0.3 mm spot size generates $17 \frac{mJ}{mm^2}$. EOS SLM machine with 300 W laser power and focus down to around 0.1 mm, can fully melt a number of metals including copper and silver. In addition, an Nd-Yag laser with a wavelength of one micron would couple a 30-micron

particle spread on silver or copper plate. Moreover, the melt pool conditions can be determined through transient heat conduction equations as

$$d = \sqrt{4\alpha t} \quad (4)$$

Where α is the thermal diffusivity and t is the pulse thickness of the laser and d is the depth of laser penetration. For example, thermal diffusivity of silver is $16.5 \times 10^{-5} \frac{m^2}{s}$, copper is $11.1 \times 10^{-5} \frac{m^2}{s}$ and aluminum is $9.7 \times 10^{-5} \frac{m^2}{s}$. Therefore, a 20 microseconds pulse width, on average would penetrate 100 microns of silver and aluminum mixture, far more than required for 28 to 48 microns particles to amalgamate with plated surface. Furthermore, the intensity of penetration into the powder bed is governed by Beer–Lambert–Bouguer law that relates the attenuation of light to the properties of the material through which the light is travelling.

$$A = \epsilon l c \quad (5)$$

Where A optical attenuation, ϵ is the molar attenuation coefficient or absorptivity of the attenuating species, l is optical path length, c is the concentration of the attenuating species. The molar attenuation coefficient in Beer–Lambert–Bouguer equation depends on the geometry of the particles and the material. For metals, the decay is very fast, with high molar absorptivity (30,000–100,000), and laser light in SLM process is absorbed at more than the particle diameter. That is why the z-resolution of SLM machines is typically around the diameter of the particles.

For this study, due to the transient heat conduction and intensity of penetration equations, failure caused by inadequate plating thickness realized from first iteration and for comparing thermal performance of in-situ cold plate to cold plate packaged

conventionally, the thickness of plating selected to be equal to thickness of gauge 20 copper or silver solid plates (.813 mm).

To gain insight about fusion of electroplated layer on top surface of ceramic tube and AM powder, x-ray images were taken of areas of interest for in-situ blocks. The x-ray pictures in Fig. 4.8 show that copper electroplated BN pipe has fused nicely with aluminum alloy powder during in-situ AM process and finished ceramic-metal AM cold plate successfully.

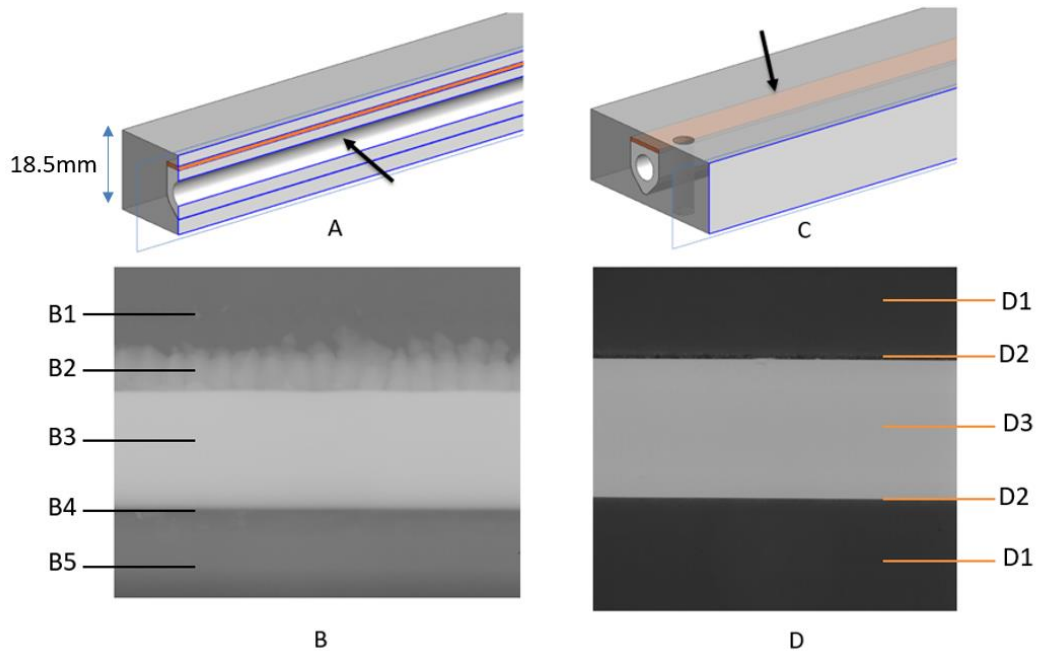


Figure 4.8: X-ray images from GE Phoenix Nanome/X (140kV, 50UA beam power) of ceramic-metal in-situ AM cold plate. Thickness of Cu plating on top side of BN tubes is .8mm and fused to aluminum alloy powder (EOS AlSi10Mg_200) by in-situ AM process. (A) Cutoff end and x-ray direction shown normal to cross section (B) x-ray image from direction shown in “A” including B1: AlSi10Mg top layers, B2: joint fused layers of electroplating and AlSi10Mg powder, B3: Solid BN tube, B4: gap between tube and channel due to .05 mm (.002”) tolerance, B5: AlSi10Mg bottom layers (C) x-ray direction perpendicular to top surface (D) x-ray image from direction shown in “C” including D1: AlSi10Mg section, D2: gap between tube and channel due to insertion tolerance, D3: electroplated BN tube.

For DoE (design of experiment) and understanding the heat transfer properties of plated and unplated LM compatible tubes, we have fabricated 16 samples and there are described in Figs. 4.9 and 4.10.

Quantity of LM compatible tubes (plated vs nonplated)			
Plating	Solid Boron Nitride	Utem 9085	Thickness (dimension T in following figure)
Silver plate	2	2	.504" (thickness of BN+ thickness of Ag plating)
Copper plate	2	2	.504" (thickness of BN+ thickness of Cu plating)
No plating	2	2	.504"
No plating	2	2	.466"

Note: The length for all specimens is 185mm and the width of all specimens is 10.4mm, only height is different [height is either 12.8 mm(.504") or [11.8mm(.466")]

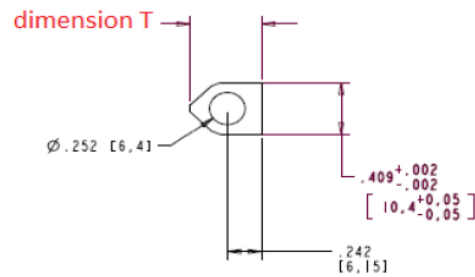


Figure 4.9: LM compatible tubes (plated vs nonplused) prepared for cold plate



Figure 4.10: Set of LM compatible tubes. The core material of the tubes is either CNC machined solid BN ceramic (white), or FDMed Ultem polymeric (black or gold color). Electroplating of silver or copper applied for fusion purposes during in-situ SLM AM process as next embedding step of fabricating cold plate.

4.2.2.3 Cultivation of CAD model of cold plate block for in-situ SLM

Firstly, link CAD model of tubes to SLM block model in NX modeling software, offset cross section of tube per maximum tolerances of SLM process ± 0.002 " [50 microns] and tubes except for top flat surface. Least material condition of top surface will be taking care of by added powder layer in SLM process. Then place and subtract (Boolean operation) the solid model of tubes from cold plate block in NX modeling software. Note that cold plate is designed for 6U CubeSats and heat sources are mounted to right side of the block, separated from left side that is mounted to Peltier cooler.

4.2.3 In-Situ SLM Operation to Insert Tubes

Start SLM process to print the metallic block and interrupt the process once the cavity is printed. To do this step, cut the stereolithography (STL) file of the block from top of the cavity for channels, to generate two separate pieces and set up two separate builds. However, parameters of EOS machine such as psw/eosprint will apply upskin and

downskin exposures at the seam with the standard EOS_DirectPart exposure. To avoid the upskin and downskin exposure at the seam, one can set a start height and final (end) height for the build in setup interface of EOS 290 machine. Change the *Final height* for the first half and the technician won't have to be present to stop the build. Once the first build having cavities for channels is fabricated, open the gate of SLM machine to access inside of the build chamber. Clean unsintered powder inside the channels of the metallic block. Place the tube inside the cavity such that the flat face is toward the laser beam. After insertion, the large plated surface of the tube is flush with the partially printed block and as such it will not collide with roller of powder bed base AM process. Set the *Start height/Final height* for the second half and uncheck the boxes in the DMLS tab of EOS machine, unless a double exposure is needed at the beginning layers of the second half build. One can stop the build at a certain height (.020/.040) mm increment heights for 15-5, 17-4 and maraging Inconel steel and .030 mm for AlSi10mg and Ti64.

Resume the SLM process to finish the 3D. A rift line where the build was paused would not significantly affect the mechanical properties of the part. Fig. 4.11 shows the insertion steps.

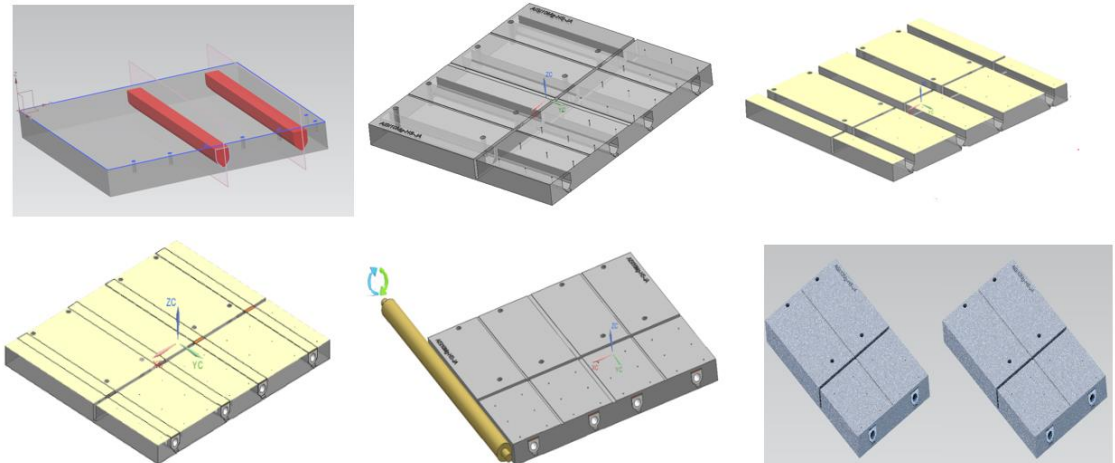


Figure 4.11: Upper row (left to right) 1. Cultivation of CAD model for in-situ AM showing embedded tubes for subtraction 2. Finalized CAD model 3. Partially printed block ready for insetion. Lower row (left to right) 1. Inserted tubes inside channels of SLM block. 2. Finished in-situ AM cold plate (roller of AM SLM process is shown) 3. Removed cold plates from print bed by electrical discharged machining (EDM)

Six in-situ SLM cold plates were fabricated and during the thermal test, their performances to be compared to cold plates assembled by conventional assembly technique discussed in previous chapter. The AM cold plates are seen in Fig. 4.12.

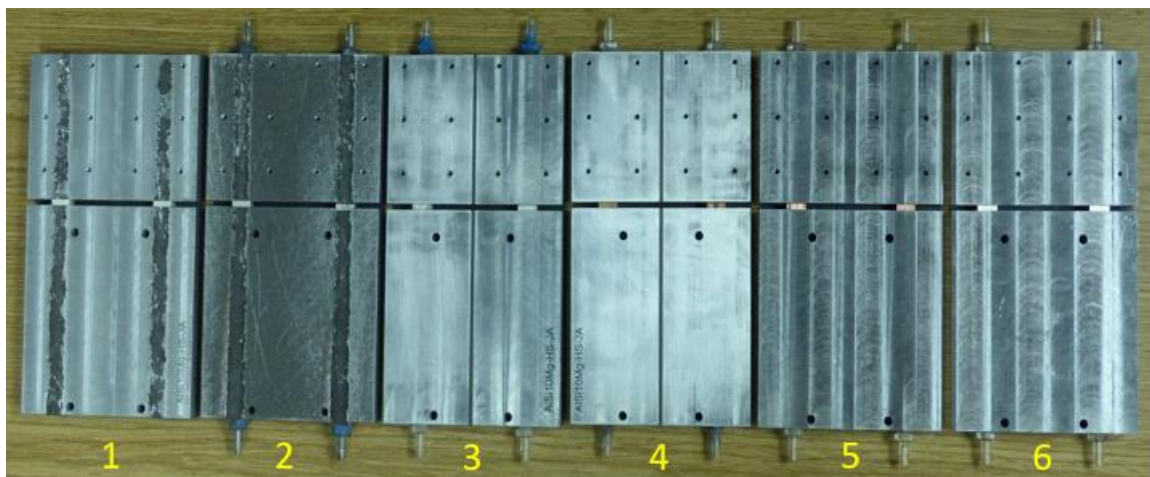


Figure 4.12: (left to right) In-situ SLM (EOS AISI10Mg_200) cold plate including 1).Bare inserted ceramic tubes. The aluminum delaminated from the ceramic and failed to finish 3D 2). Bare BN ceramic tubes are glued and sprinkled aluminum powder on flat surfaces prior to insertion, failed to finish 3D 3). Silver plated Ultem inserted tubes 4). Copper plated Ultem inserted tubes 5). Copper plated solid BN inserted tubes 6). Silver plated solid BN inserted tubes (iterations 3 to 6, successfully finished SLM).

4.3 Assembly Model of In-situ AM Active Cooling Prototype

The assembly of in-situ AM HX prototype is identical with HX prototype packaged by conventional assembly technique and discussed in previous chapter with the exception that in situ AM cold plate is swapped with 3-piece cold plate. The prototype is demonstrated in Fig. 4.13.

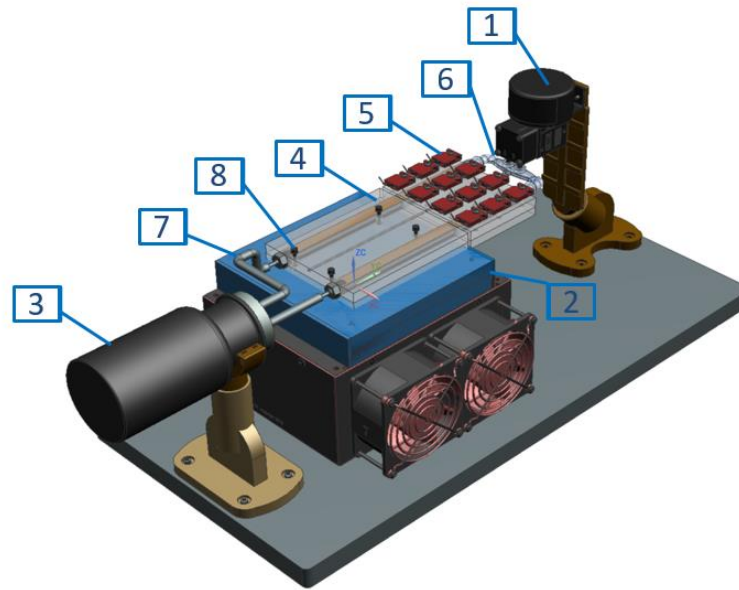


Figure 4.13: CAD model of active cooling prototype including 1) diaphragm pump, 2) Peltier cooler, 3) LM reservoir, 4) in-situ SLM cold plate with embedded copper plated ceramic tubes 5) MP9100 Caddock resistor (12x) 6) Nylon coupling 7) Polypropylene flex tube 8) #4-40 mounting hardware (4x)

4.4 Thermal Test and Experimental Data

We conducted tests to determine the thermal contact resistance of fused interfaces of AM cold plates fabricated by the presented technique and compared the results to cold plates packaged by conventional assembly method (sandwiched and bolted structure). Materials and geometries in both cases were identical. The transparent isometric view of 3D model of in-situ AM cold plate, exploded view of 3D model of conventional cold plate

and fabricated and packaged cold plates by in-situ and conventional techniques are shown in Figs. 4.14 and 4.15.

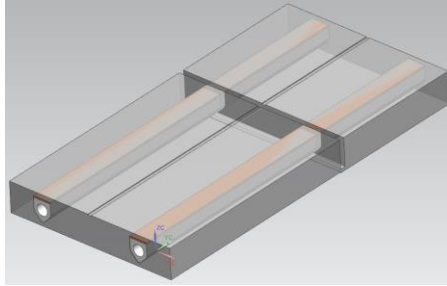


Figure 4.14: CAD model of in-situ SLM cold plate including two copper plated (0.8 mm) solid BN ceramic tubes (100 mm x 185 mm x 18 mm)

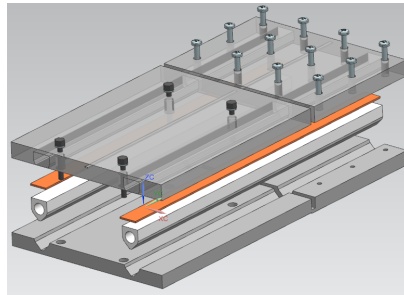


Figure 4.15: Exploded CAD model of cold plate including BN pipes, gauge 20 copper plate (0.8 mm thick), encapsulated by conventional manufacturing of three-piece SLM aluminum alloy block (final envelope size is 100 mm x 185 mm x 18 mm)

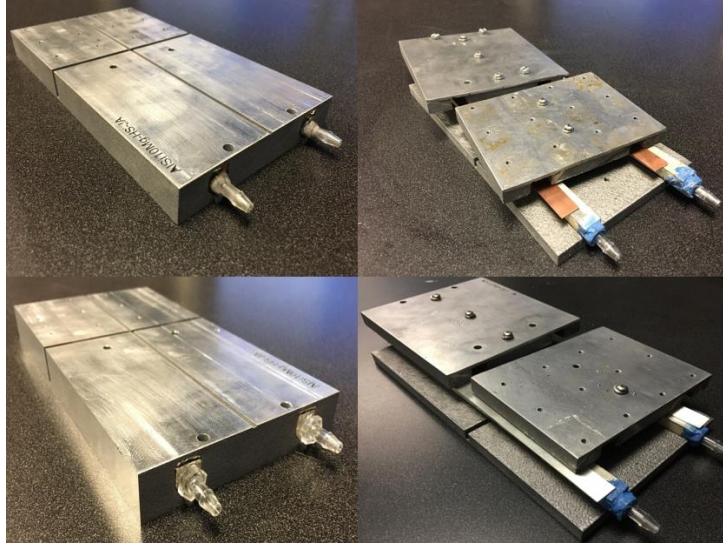


Figure 4.16: In-situ SLM cold plates including copper- or silver-plated BN ceramic pipes creating superior bonding by fusion of silver (or copper) with aluminum alloy AM powder (left) compared to conventionally assembled cold plates (right) including three-piece SLM aluminum alloy block, gauge 20 copper or silver off-the-shelf plate. Assembly fastened with #4-40 SS screws torqued to 4.7 lb-in. Note: surface flatness 0.08 mm and surface roughness 64μ inch at top surface (interface to heat source) and bottom surface (interface to Peltier cooler) for all pieces (right)

Thermocouples wired to data acquisition system and placed at critical locations.

The setup is identical for all prototypes with different cold plates, and thermocouple locations and active cooling of prototype by diaphragm pump are seen in Fig. 4.17.

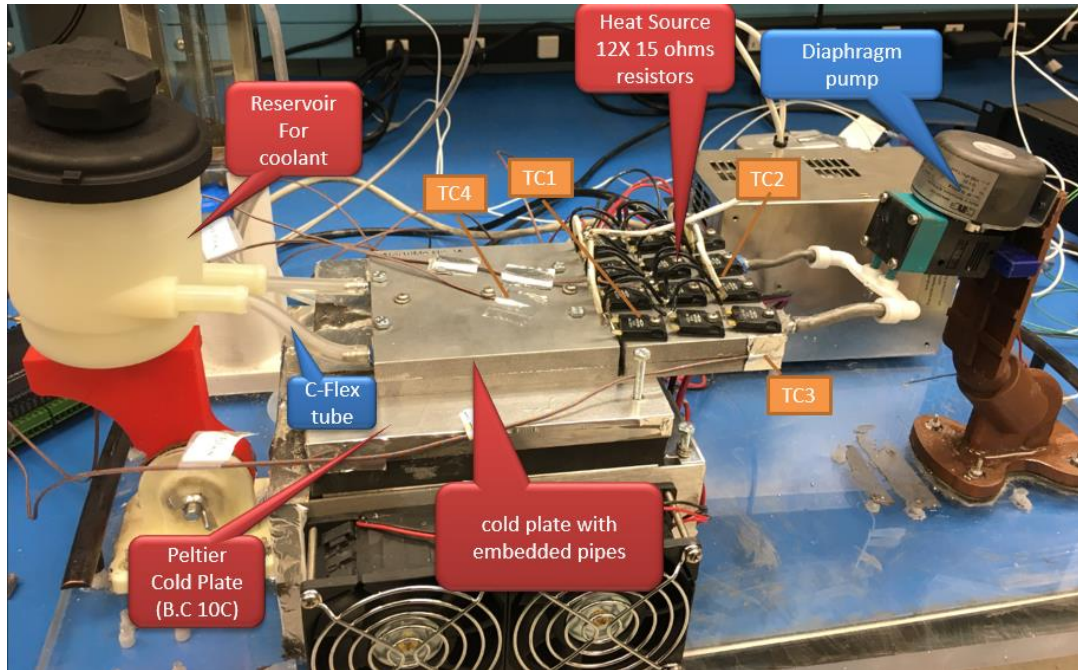


Figure 4.17: Assembly of active cooling prototype and location of thermocouples (TC#). For each test, steady state temperatures of designated points were sensed by TCs and recorded by data acquisition unit.

In Table 4.1, to determine the heat transfer improvement of the in-situ AM cold plates relative to conventionally assembled ones discussed in chapter 3, the ratios of steady state temperature of hottest point (i.e., TC1) for both cases were determined and compared. As seen in Table 4.1, silver-plated ceramic BN inserted in SLM aluminum block has the highest efficiency, transferring heat 1.72 times better than conventionally placed and bolted BN tube with silver plate in a three-piece block. Similarly, in-situ SLM aluminum alloy block with copper-plated BN ceramic inserts showed 1.64 times improvement compared to the three-piece cold plate packaged by conventional technique with identical geometry and material properties.

Table 4.1

Results of Thermal Test and Type T Thermocouple Readings to Evaluate the Thermal Performance of Cold Plate Made of SLM Aluminum Alloy with Different Inserted Tubes and Packaged by In-Situ AM or Conventional Sandwiched Structure

Run no.	Cold plate type	Thermocouple (TC) readings				Max heat transfer improvement of AM cold plate relative to conventional assembled cold plate
		TC1 (°C) (hot point)	TC2 (°C)	TC3 (°C)	TC4 (°C)	
1	BN-G20C-CSS	33.10	27.26	20.35	14.72	1.64
	BN-PC-IAM	20.15	16.83	14.04	10.35	
2	BN-G20S-CSS	32.46	26.61	22.08	14.65	1.72
	BN-PS-IAM	18.90	15.48	13.78	10.33	
3	U-G20S-CSS	37.33	29.30	24.06	13.33	1.40
	U-PS-IAM*	26.74	21.30	16.04	10.39	
4	U-G20C-CSS	38.02	29.93	21.78	14.04	1.33
	U-PC-IAM*	28.58	22.50	17.42	10.44	
5	BN-N-IAM**	22.63	19.27	15.36	11.05	N/A

Note. Heat source: 72 watts, Galinstan (coolant), Peltier cooler set to 10°C for B.C., forced convection pumping pressure 2260 Pa, ambient temperature 25°C, steady state reaching time 120 min. BN = ceramic boron nitride, U = Ultem; G20C = gauge 20 copper, G20S= gauge 20 silver, PS = plated silver, PC = plated copper, N = none; IAM = in-situ AM, CSS = conventional sandwiched structure.

*Leaking due to possible microscopic damage of Ultem inserts noticed during the test but finished SLM.

**Part failed to finish 3D and did not meet the near net shape requirement of the 3D.

Additionally, to show validity and repeatability of the experiment, the steady state test was repeated for different applied DC heat loads as 36, 54, 72 and 110.25 watts through mounted resistors for in-situ AM cold plates (see Fig. 4.18 below). The test showed that all controls worked as expected. Thus we conclude that the experiment worked as intended and that results were due to the effect of the tested variable.

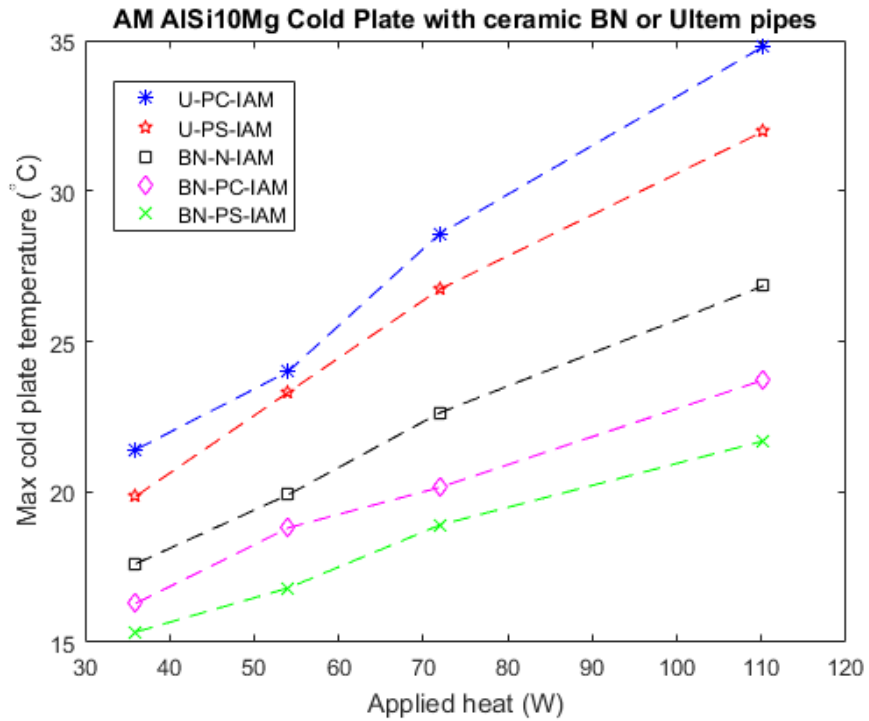


Figure 4.18: Comparison of cold plates fabricated by in-situ SLM technique. Silver-plate ceramic BN inserts had the best efficiency compared to other in-situ AM specimens.

4.5 Conclusion

In conclusion, this study demonstrated how AM technologies have overcome critical limitations of traditional manufacturing and packaging processes to reduce thermal contact resistance at interfaces of layered thermal structures such as metal–ceramic LM compatible cold plate. Chemical compatibility, thermal efficiency and manufacturing feasibility are the hallmarks of fabricated prototypes by the in-situ AM technique.

We used Galinstan LM as coolant in active thermal prototypes. Low-melting-point LM alloys such as Galinstan have great potential to increase thermal efficiency and reduce the mass/size of active cooling systems for spacecraft avionics system due to high molecular thermal conductivity, ability to withstand dramatic thermal expansion

mismatch, extremely low Kapitza resistance, low Prandtl number, and a eutectic that is liquid at most electronics operating temperature. However, the behavior of LM flow is different from polar coolant such as water because of the surface tension, viscosity being affected by the wettability of boundary walls, and corrosiveness. To take advantage of thermophysical properties of LM as a coolant and overcome its inherent incompatibility with metallic structure, machinable ceramic BN was used as tube material to contain LM, because of minimal wettability and chemical compatibility of solid BN with LM and its high thermal conductivity.

Selection of BN tube is a wise choice where corrosion resistance is more important than wear resistance and solid BN is not amenable for application under mechanical loads. Therefore, we needed to encapsulate BN tube in metallic block to overcome its mechanical weaknesses for avionics structures encountering vibration and mechanical stresses. Embedding tubes inside a metallic block creates thermal contact resistance at interfaces that are inherently rough, causing “thermal bottleneck.” This study has enabled us to demonstrate in-situ AM manufacturing potential to improve contact resistance. In particular, we studied the relationship between the transient heat conduction and intensity of laser penetration in the SLM process to the convection of SLM melt pool and heat transfer properties of interface layers including electrodeposited films to optimize fusion at interfaces and to reduce interfacial defects that can retard thermal performance.

By in-situ AM technique, we synergistically complemented the interruption of the SLM process with morphology of the insert to eliminate its collision with the powder-spreading device in the AM process. The geometrically optimized insert (tube) has

thermally enhanced features in accordance to Fourier's law, including maximized surface area normal to heat source, minimized thickness of the tube, and an irregular pentagon profile that facilitates insertion in integrated channels of AM block through this innovative in-situ AM process. Development of a geometrically optimized tube by CNC machining with minimal surface roughness allowed us to minimize the Moody friction factor of viscous LM flow.

We observed the following key features from fabrication and thermal testing of prototypes. Firstly, this study revealed that inserting bare ceramic into SLM process failed to complete 3D because the powder was unable to adhere to the ceramic.

Additionally, silver- or copper-plated Ultem tubes showed deformation and leakage during thermal tests due to thermal stress in the in-situ SLM process but finished 3D. A silver-plated BN tube inserted in SLM aluminum alloy block by in-situ AM technique successfully printed and the cold plate had the highest thermal efficiency. According to data from the thermal experiment and under identical test conditions, the hybrid cold plate fabricated by in-situ AM technique showed up to 1.72 times heat transfer improvement compared to cold plates manufactured by conventional packaging methodology sandwiched by fasteners.

In the next chapter, we replace the pumping system of active cooling conventional prototype with MHD to further improve the reliability of cooling system.

Chapter 5: MHD Thermal Management for Avionics Using LM Alloys in Geometrically Complex Structures Realized through AM

5.1 Introduction

In previous chapter, we demonstrated how additive manufacturing technologies could overcome thermal bottleneck of heat exchanger manufactured by conventional techniques as a result of improving contact resistance at thermal interface and yet resolving inherent chemical incompatibility issue causing corrosion of LM. In present chapter, we replace the diaphragm pump of active cooling prototype by MHD pumping. The presented cooling system using liquid metals and MHD cooling is simple, compact, rugged, silent and more reliable for spacecraft avionics due to no moving parts. The key subjects argued in this chapter are fundamentals of MHD and its application complemented by multi AM technologies such as DMLS, SLM, SLS and FDM also traditional manufacturing such as CNC machining and electroplating that enable us to fabricate reliable MHD thermal management system operable in space-like environment to meet the power requirements for spacecraft avionics (Fig. 5.1).

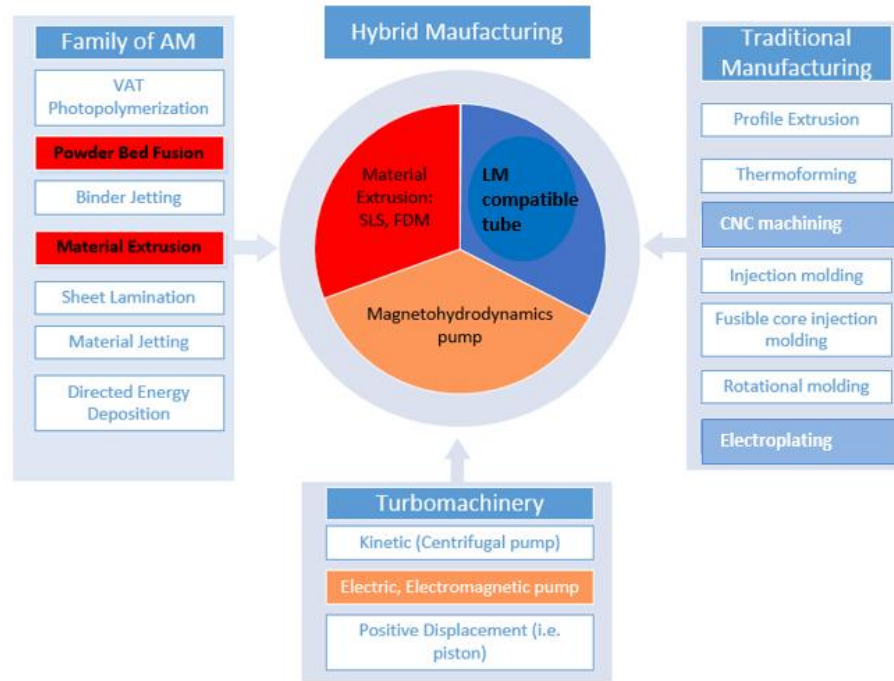


Figure 5.1: Technologies applied to development of MHD thermal management

5.2 Magnetization and Governing Laws in Electromagnetism

In classical electromagnetism, magnetization of magnetic materials is reliably represented by two main values: magnetic field strength H and magnetic flux density B . Other parameters such as permeability (B/H), losses ($H-dB/dt$), polarization J ($J = B - \mu_0 H$), magnetization ($\frac{B}{\mu_0} - H$) and magnetizing curve $B=f(H)$ depends on these two values (Tumanski, 2011).

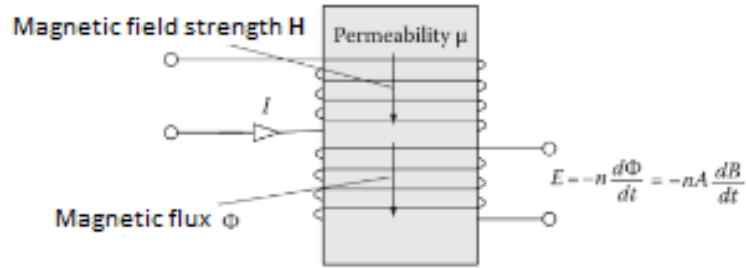


Figure 5.2: Response of magnetic material represented by permeability under influence of the magnetic field strength H , which is generated by the current I flowing in the coil. This field gives rise to the magnetic flux ϕ , and $B = \frac{\phi}{A}$. This flux density is detected as electric voltage induced in the secondary coil with n turns- the value of this voltage depends on the time derivative of B .

Between the exciting magnetic field strength H and the response B , there is a relatively simple relationship in theory, $B = \mu H = \mu_0 \mu_r H$. However, in practice, this relationship is more complex and in most typical magnetic materials, the relation between magnetic field strength and the flux density is highly nonlinear. Therefore, generally it is necessary to use the whole relation $B=f(H)$ known as the magnetization curve (see Fig. 5.3, courtesy of cartech.com).

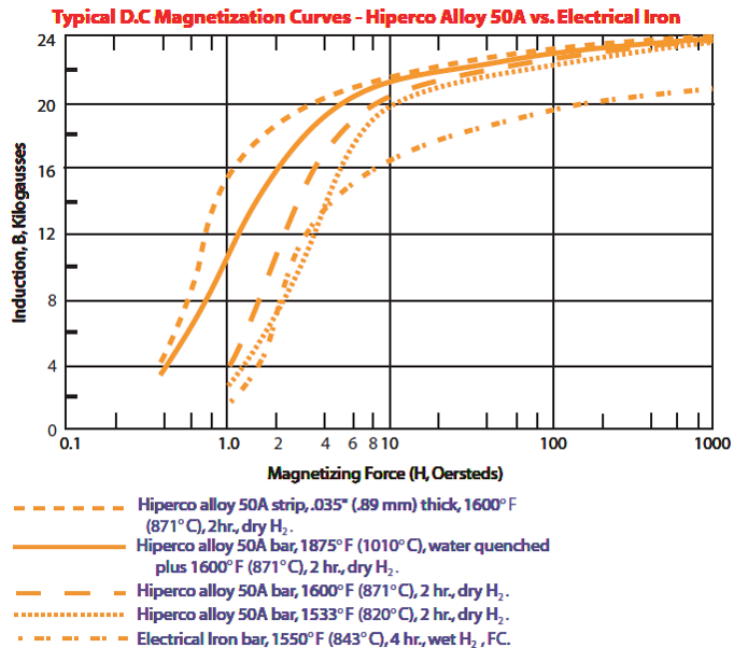


Figure 5.3: B-H curve, Hiperco50A and Iron- Induced Field vs Applied Field

Additionally since distribution of flux density is strongly depends on the shape of the design article, we cannot simply discuss the magnetic properties of the material. Generally, the magnetization is non uniform in the whole body and we can only determine the mean value. Moreover, because of non_uniformity of magnetic field, it is widely accepted in standards that sinusoidal flux density is required in case of AC testing and the result of the test is highly dependent on the frequency of magnetization, in reality, both magnetic field strength and magnetic flux density can be non-sinusoidal. Finally, even we ensure correct core shape and correct magnetizing waveform, the anisotropy of materials cause problems in determination of the direction of magnetization and permeability can be only described in a form of complicated tensor notation. The fundamentals of applied MHD are as following.

5.2.1 Biot-Savart Law

Biot–Savart Law describes the magnetic field generated by a constant electric current, i.e. calculation of magnetic strength from an arbitrary point distanced from a long conductive wire carrying electrical current $H = \frac{I}{2\pi x}$

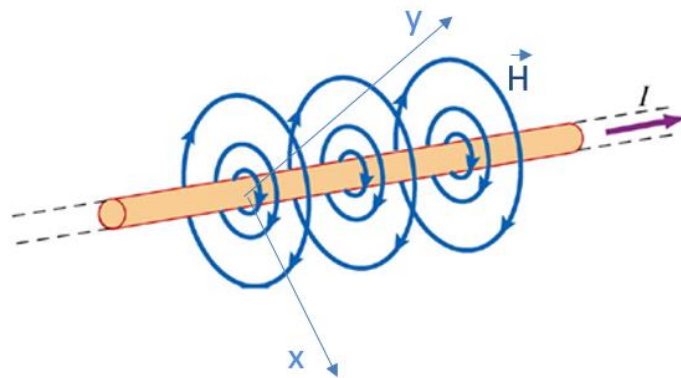


Figure 5.4: Magnetic field lines of a long conductive wire carrying electrical current

Now, let us consider the magnetic field inside a long solenoid as shown below, for long coil (solenoid), at the center of the coil and distance x from center the magnetic field is as following (Tumanski, 2011).

$$H = \frac{nI}{4L} \left[\frac{L+x}{\sqrt{a^2 + (L+x)^2}} + \frac{L-x}{\sqrt{a^2 + (L-x)^2}} \right] \quad (6)$$

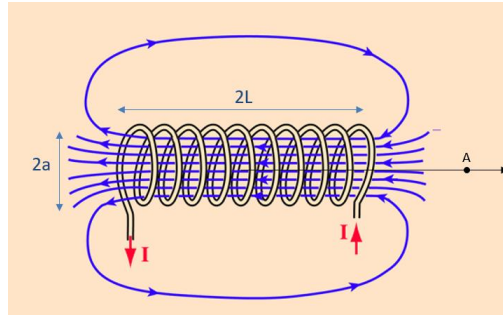


Figure 5.5: Magnetic field inside a long solenoid with n turn and electrical current I

For multilayer solenoid with inner diameter $2r_1$ and outer diameter $2r_2$:

$$H = \frac{nI}{4L(r_2 - r_1)} \left[(L+x) \ln \frac{r_2 + \sqrt{r_2^2 + (L+x)^2}}{r_1 + \sqrt{r_1^2 + (L+x)^2}} + (L-x) \ln \frac{r_2 + \sqrt{r_2^2 + (L-x)^2}}{r_1 + \sqrt{r_1^2 + (L-x)^2}} \right] \quad (7)$$

5.2.2 Ampere's Circuital Law

Ampere's law helps calculation of magnetic field generated around a closed loop conducting a current

$$I \times n = H \times L \quad (8)$$

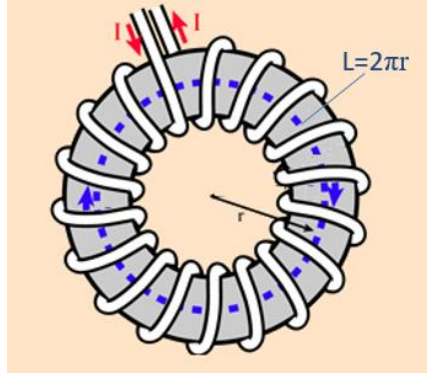


Figure 5.6: The circuital law used to determine the magnetic field strength (H) in a toroidal magnetic circle with n turns and electrical current I

5.2.3 Faraday's Law of Induction

It determines electromotive force (voltage) induced in closed circuit in magnetic field B .

$$V = -\frac{d\phi}{dt} \quad (9)$$

Meaning if a closed conducting loop is moving in the magnetic field, the voltage is induced in this loop (this is how generator works). If a non-movable loop placed in varying magnetic field then we obtain induced voltage (transformer principle). If the conducting material is moving in magnetic field or is placed into time-varying magnetic field, the eddy currents are induced in this material (material thickness is d and resistivity of material is ρ).

$$J_{eddycurrent} = -\frac{d}{2\rho} \frac{dB}{dt} \quad (10)$$

The eddy currents generate magnetic field that tends to oppose the external magnetic field and eddy current dissipates heat is one source of energy loss in magnetic material (AC MHD electromagnet principle).

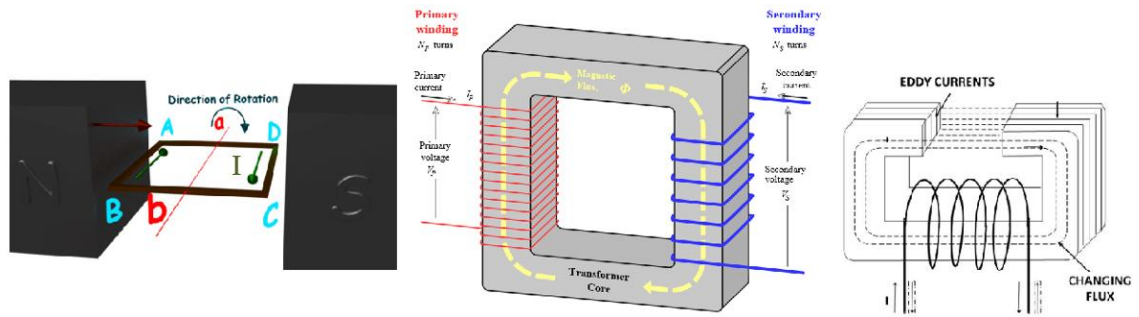


Figure 5.7: Schematic of a DC generator (left), a transformer (middle) and eddy current (right)

In order to determine the magnetic flux density from a voltage induced in n turns of a coil, it is necessary to use integrating circuit. For pure sinusoidal voltage $V = V_m \sin \omega t$, we can determine the flux density as:

$$B(t) = \frac{1}{2\pi f n A} V_m \cos \omega t \quad (11)$$

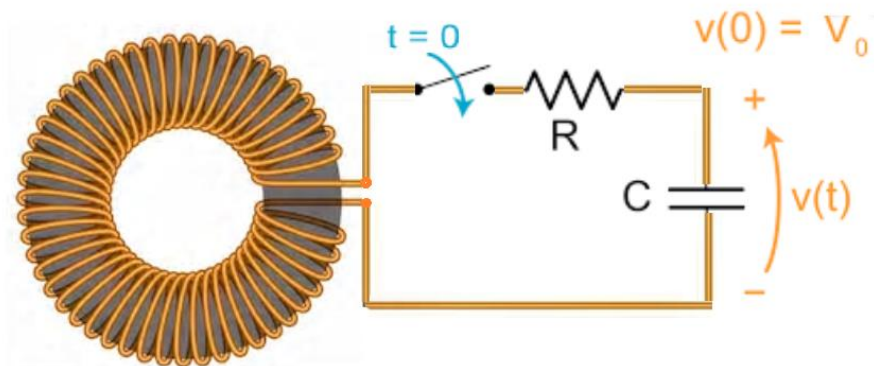


Figure 5.8: The principle of measuring of the flux density B in a magnetic circuit

5.2.4. Lorentz Force

If an electric particle q is moving with velocity v in the Electromagnetic field E and B , then a force F (Lorentz force) acts on this particle, given as

$$F = q(E + v \times B) \quad (12)$$

If we consider only magnetic field B , this force is called as magnetic force or Laplace force used in MHD cooling concept in this study and its formula is as following:

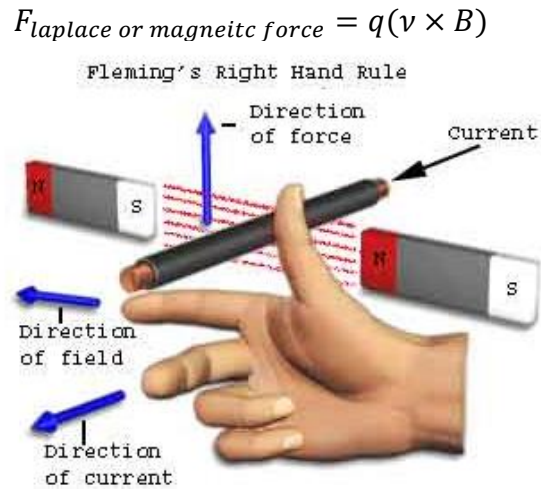


Figure 5.9: Fleming's right hand rule showing direction of Lorentz force

5.3 Development of MHD Cooling Prototype

Any movement of an electrically conducting material in a magnetic field generates electric currents which in turn induce their own magnetic fields and also induce forces on the medium known as Lorentz force (Hannes Alfvén, 1942). The concept of MHD defined in previous sentence that involves fluid circulation fits conceptually with active thermal cooling that circulates a coolant to transfer heat from one heat source to cold boundary. Moreover, space compatible electromagnetic field can travel through vacuum at speed of light. Consequently, MHD active cooling system can be explored to beat the heat at avionics packaging for space application. In this regard, the following steps having put a suitable approach to divide assembly of MHD cooling system into subsystem and components, analyze each subsystem to determine its performance and optimize magnetic-flow-thermal parameters of simple subsystem to be able to synthesize iteratively as a whole and predict thermal characteristics of the subtle cooling system. In

the context of breaking down MHD cooling key components for analysis, it simply has I). A device that moves coolant ‘MHD pump’ and II). A medium that coolant passages transfer the energy from heat source to cold boundary ‘MHD cold plate’.

5.3.1 MHD Pump Design

The MHD moving device (MHD pump) generates magnetic field through magnetization of magnetic material (core) that is reliably represented B-H curve described in previous section. MHD pump consists of a magnetic core assembly and a LM compatible coupling for mounting electrodes and passage of electrically conductive LM.

5.3.1.1 Magnetic core assembly

Magnetic core assembly of MHD cooling prototype in this study consists of copper windings, DC or AC powering systems and ferromagnetic C-shaped core. Most of ferromagnetic materials are polycrystalline and strong magnetic anisotropy of crystal is caused by spin-orbit-lattice interaction. It is important to eliminate anisotropy because it generates losses. Magnetic materials are classified as hard or soft based on coercivity that measure the ability of a magnetic material to resist demagnetization. Hard magnetic materials such as permanent magnets have high coercivity, while soft magnetic materials such as electrical steel have low coercivity. Remanence is the residual magnetization that remains when no magnetic field is applied to a magnetic material that was previously

magnetized to saturation (see Fig. 5.10). Note: for calculating losses in ferromagnetic materials, Poynting's vector is used.

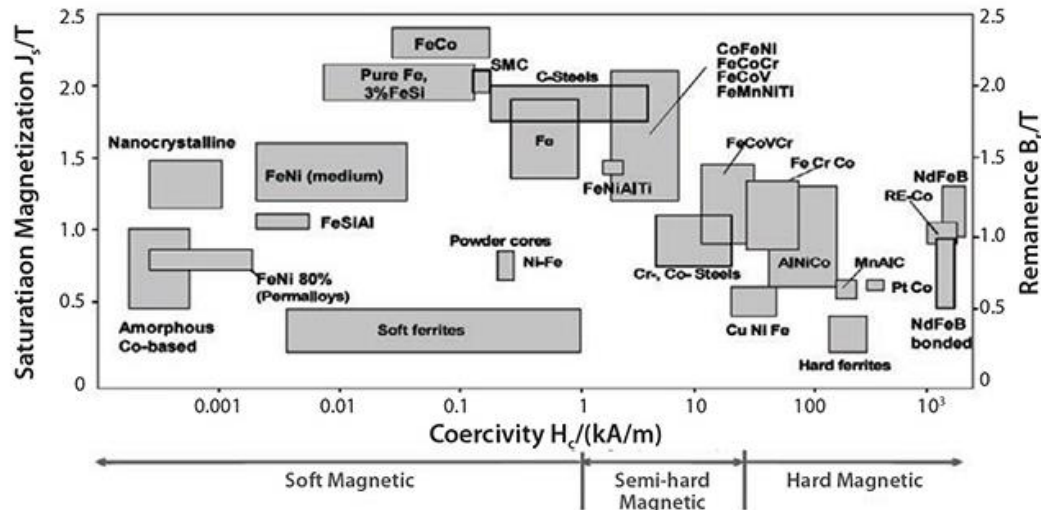


Figure 5.10: Coercivity, saturation magnetization, and remanence of various magnetic materials (courtesy of Weickmann, 2009)

To increase the possible flux density range in electromagnets, often ferromagnetic materials with highest possible saturation polarization are used for the poles, for this study, granulized Hiperco 50A an alloy of 49% Cobalt, and 2% Vanadium, balance Iron is selected for core material that has the highest magnetic saturation of all soft-magnetic alloys.

For the shape consideration of the magnetic core, Gauss's law in magnetism states that the total magnetic flux passing through a closed surface is zero, meaning that magnetic monopoles do not exist, therefore, C-shaped core is selected as optimal form of magnetic core per implementation of Gauss's law. Although according to Lenz's law, the magnetic field in the gap of C-shaped core depends mainly on the ampere-turns, the core geometry plays an important role as the flux concentrator. The magnetic field can be generated by electromagnets or magnets or permanent magnets, in the case of permanent magnet, the magnetic field, usually not exceeding 1.3-1.4T and about 2T in the case of

electromagnets. By correct design it is possible to obtain up to 3T in the air gap of electromagnet (Fiorillo, 2004).

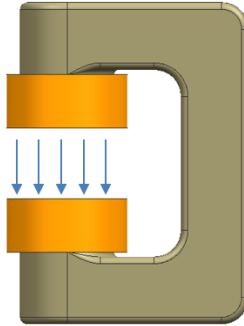


Figure 5.11: Electromagnet as a source of magnetic field with inefficient flat tips

The magnetic field generated by permanent magnet source in the gap of figure above is as following:

$$H = \frac{J_m}{\mu_0} \left[1 - \frac{\frac{l_g}{D}}{\sqrt{1 + \left(\frac{l_g}{D}\right)^2}} \right] \quad (13)$$

Where D is the diameter of the magnet pole and J_m is polarization and l_g is the air gap length.

For $\frac{l_g}{D}$ reaching zero, magnetic field is maximum $H_{max} = \frac{J_m}{\mu_0}$, therefore to make D larger than gap, tapering is used.

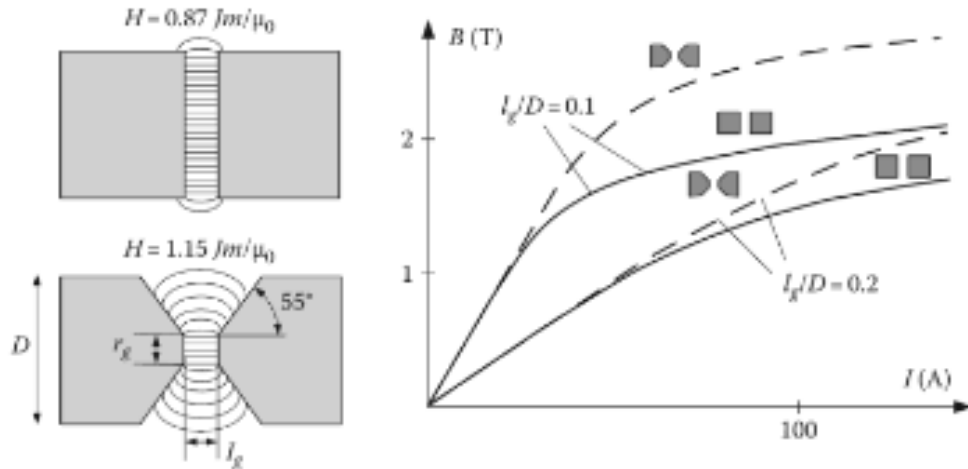


Figure 5.12: Flat and tapered poles of magnet or electromagnet i.e. $D=250\text{mm}$, (courtesy of Fausto Fiorillo, 2004)

In the case of tapered pole, the magnetic field in the gap can be estimated as

$$H = \frac{2J_m}{3\mu_0\sqrt{3}} \ln \frac{r_0}{r_g} \quad (14)$$

Where $r_0=D/2$, Similar effect cannot be obtained when electromagnet is used with moderate current, but if the yoke is in saturation, the tapering will increase the magnetic field even more per following equation.

$$B = \mu_0 H = \mu_0 \frac{nI}{l_g} \quad (13)$$

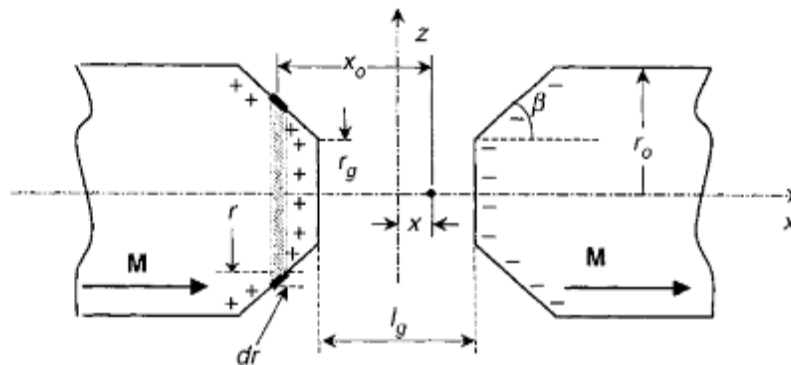


Figure 5.13: Tapered pole of electromagnet. For given radius and gap width, the maximum axial magnetic field is obtained with a taper angle of 54.74° , courtesy of Fausto Fiorillo, 2004”

Therefore, the optimized electromagnet core for our study has the following shape (see Fig. 5.14):

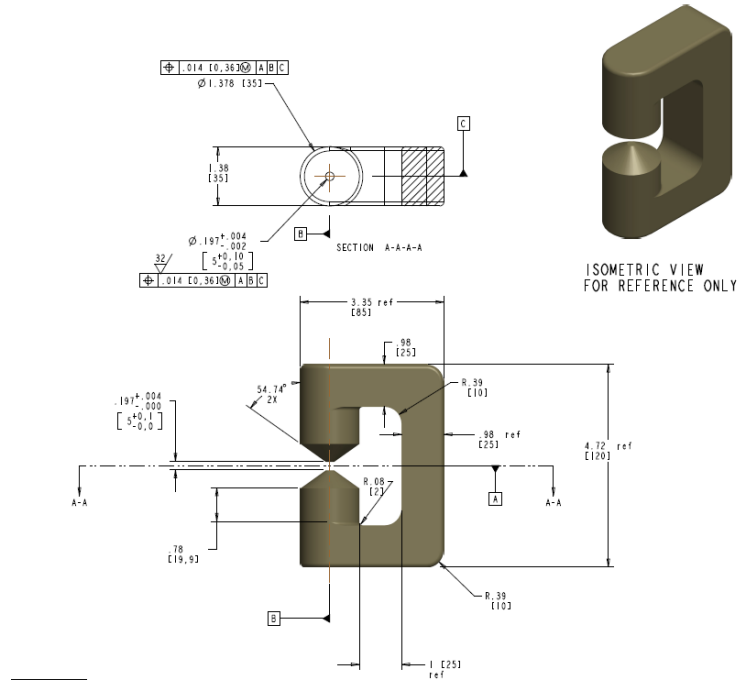


Figure 5.14: Morphology of electromagnet C-shaped core, 2D drawing for CNC machining of hiperco50A core

One of the challenges for implementation of MHD pumps is saturation of electromagnet, which puts a practical limit on the maximum magnetic fields achievable in ferromagnetic-core electromagnets and increase the size of the electromagnetic pump. Selection of hiperco50A is used to improve saturation issue. Additionally, for the location of winding, the closer the winding to the gap the higher the magnetic field applied within the gap. A pair of identical multilayer Helmholtz impregnated coil with 650 turns of gauge 22 magnetic wire, with the appropriate gap and electrical insulator on core structure wound to electromagnetic core. The mean magnetic field between two coils by mean of thickness of winding as r and length as L of the multilayer coil is as following:

$$H = H_1 + H_2 = \frac{nI r^2}{2} \left\{ \left[r^2 + \left(\frac{L}{2} + x \right)^2 \right]^{-\frac{3}{2}} + \left[r^2 + \left(\frac{L}{2} - x \right)^2 \right]^{-\frac{3}{2}} \right\} \quad (14)$$

If $r=L$ the magnetic field uniformity is highest, and for $x=0$ and $r=L$ the magnetic field at the geometric center for n number of turn and I applied current is

$$H_0 = .7155 \frac{nI}{r} \quad (15)$$

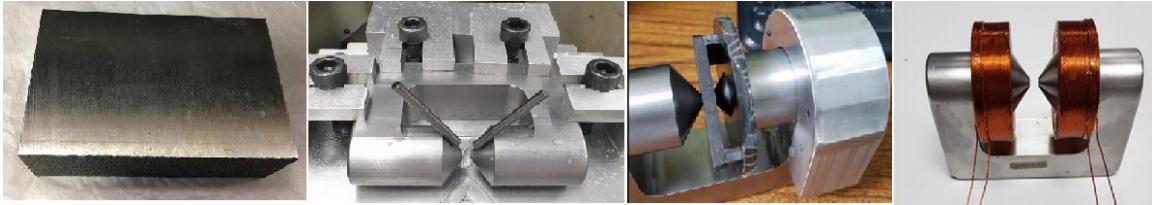


Figure 5.15: From left to right: granulated Hiperco50A block(5"x3.4"x5.2"), fixture for CNC machining, tooling for winding, C shape tapered hiperco50A magnetic core with magnetic wounds (2x650 turns AWG 22)

Both AC and DC are used for powering of electromagnetic pump to determine the tradeoff in performance. Properties of AC magnetic field depends on the frequency of the magnetization and the presence of harmonics in the flux density waveform, for this purpose signal generator with harmonic waveform and signal amplifier are used in this study. Furthermore, we have fabricated two geometrically identical electromagnets with different materials for C-shaped core as Hyperco50A and stainless steel 718. Both include impregnated coil with 650 turns of gauge 22 magnet wires (total 1300 turns), top and bottom windings are attached in parallel manner to generate unidirectional magnetic field per Faraday's left hand rule. The electromagnets are seen in Fig. 5.16.



Figure 5.16: MHD pump electromagnets with two magnetic materials for C-shaped core (hiperco50A vs magnetic stainless steel)

Furthermore, for space flight hardware, to block the electromagnetic influence of magnetic field generated by electromagnet, a Faraday cage is required. The core shall be placed in shielded enclosure and magnetic field does not go through the ferromagnetic layer such as shielding film made from an amorphous cobalt alloy (Mills, 1993). The effectiveness of shielding of closed volume is described by shielding factor S as the relationship between external and internal magnetic fields. For a cube with length a , magnetic permeability μ and wall thickness t the S factor is (Tumanski, 2011).

$$S = 1 + \frac{4\mu t}{5a} \quad (16)$$

Additionally, gaskets at interfaces for hermetically sealing is used. However for space application, during launch, decompression of sealed volume may have resulted in pressure gradient forces and causing structural failure due to rapid change of spacecraft external pressure. Therefore, small orifices or pressure control valve are needed to drop the internal pressure and rigorous analysis of venting area is required to eliminate an over pressure with respect to the spacecraft launching pressure derived by Bernoulli's principle.

5.3.1.2 Elliptic LM container and shape anisotropy

When electrically conductive LM is magnetized, it creates its own magnetic field and poles are induced at its ends. This demagnetizing field H_d opposite of induced magnetization and is shape dependent and can be expressed by demagnetization factor $N_d M$.

$$H_{in} = H - N_d M \quad (17)$$

The demagnetization field is non uniform and difficult to calculate with one exception for ellipsoid, the demagnetization factor is as following:

$$N_d = \left| \left(\frac{1}{k^2} (\ln 2k - 1) \right) \right| \quad (18)$$

Where k is length/diameter ratio, for example for sphere k=1 and therefore $N_d = 1/3$

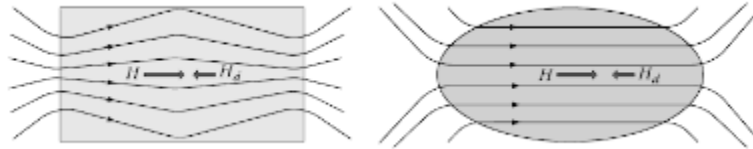


Figure 5.17: Ferromagnetic material under magnetic field creates its own magnetic field (the magnetized sample operates as a magnet due to poles induced at its ends). This demagnetizing field depends on the shape of the specimen; the sample is magnetized nonuniformly in a uniform external field (a) with exception of optimal ellipsoid shape (b)

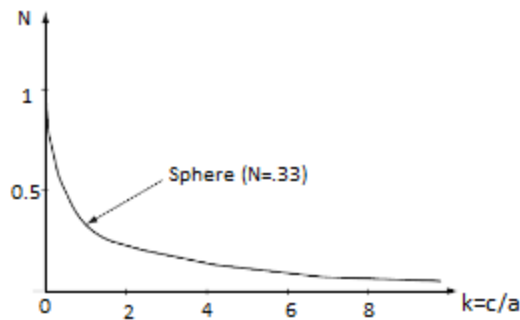


Figure 5.18: Dependence of the demagnetizing factor of ellipsoid on its shape factor c/a (length to diameter ratio)

The demagnetizing field significantly deteriorates the apparent permeability of a ferromagnetic sample.

$$\mu_c = \frac{\mu_r}{1 + N_d(\mu_r - 1)} \quad (19)$$

Also, both the magnetization curve and the hysteresis loop can be significantly affected by shape anisotropy (Tumanski, 2011). Other researchers have studied the approximate effective demagnetizing factor along applied magnetic field for elliptic shape in 3D (Prozorov et al, 2018). Demagnetization factor is shown in Fig. 5.19.

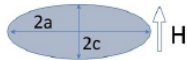
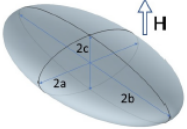
Shape	Geometry	Demagnetizing factor along applied field
Strip, elliptical		$N^{-1} = 1 + \frac{c}{a}$
Ellipsoid (exact)		$N = \frac{1}{2} \frac{b}{a} \frac{c}{a} \int_0^{\infty} \frac{ds}{(s + \frac{c^2}{a^2}) \sqrt{(s+1) (s + \frac{b^2}{a^2}) (s + \frac{c^2}{a^2})}}$

Figure 5.19: Demagnetizing factor along applied field for elliptic shape (courtesy of Prozorov et al)

To optimize the morphology of LM coupling per demagnetization criterion, a slim ellipsoid shape is selected with major diameter in flow direction to minor diameter in magnetic field direction as eight and major diameter in electric field direction to minor diameter in magnetic field direction as two. See Fig. 5.20.

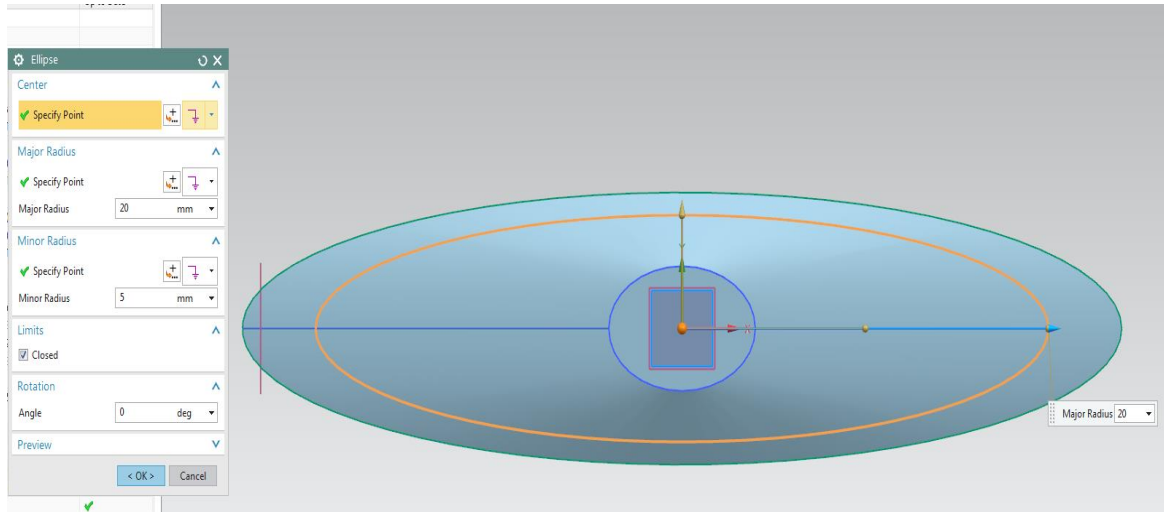


Figure 5.20: major and minor diameters of LM container in x-y plane

The following factors also influenced the design of elliptic shape as 1) minimum amenable wall thickness for fabrication of elliptic container by selective laser sintering (SLS) technique of nylon 6,6 as 1 mm. 2) the closer the magnetic poles the higher the intensity of magnetic flux with consideration to leave enough cross section for the flow to eliminate choking and clogging of flow due to viscous layer. Slim ellipsoid shape has major diameter of 40mm along the flow direction, and minor diameters of 5 and 10 mm along the direction of magnetic field and electric field respectively. The detailed views of LM container containing 90° inlet and outlet for liquid flow and holes for electrode wires are seen in Fig. 5.21.

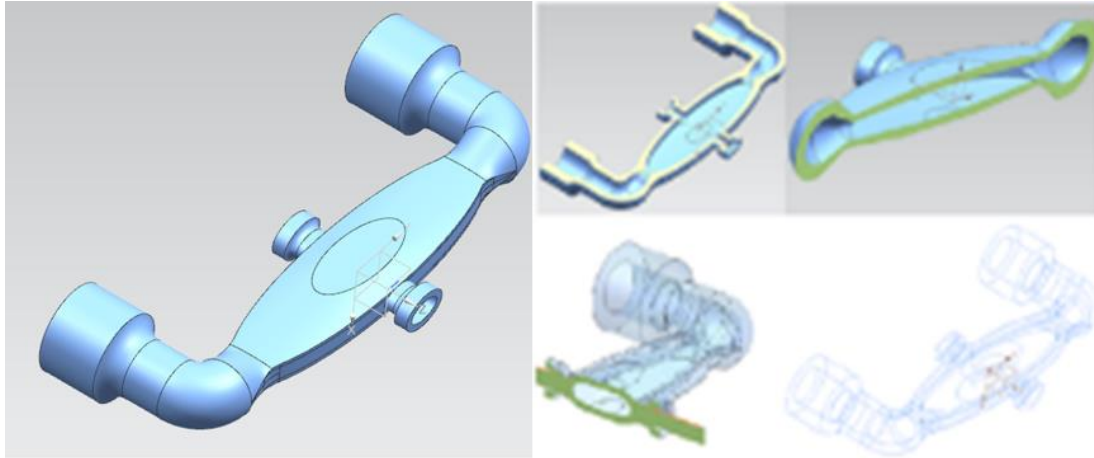


Figure 5.21: Isometric and projection views of ellipsoid LM container in MHD pumping, including inlet and outlet for LM, provision for insertion of copper electrodes generating electric field required for Lorentz force. Ellipsoid dimension is 40mmx10mmx5mm

The lines of applied external magnetic field to LM inside elliptic coupling in xz plane is seen in Fig. 5.22.

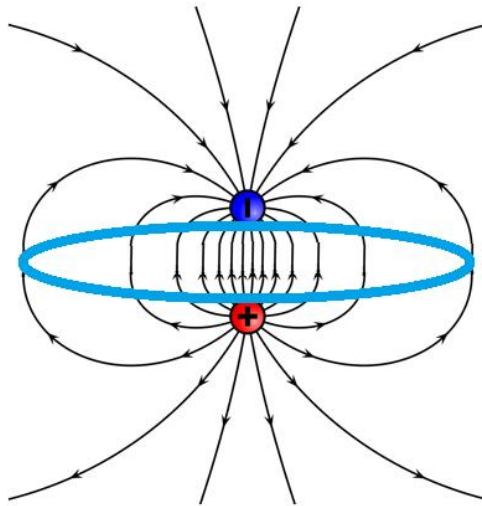


Figure 5.22: Magnetic curves, encompassed in ellipsoid container to reduce eddy current

The induced magnetic field to LM is also influenced by the material of elliptic coupling and according to Hartmann wall effect, insulating walls are suitable for this application. Elliptic coupling with 1mm wall thickness is fabricated by AM SLS process out of high performance Nylon 6,6 material. The electrical current flowing between

electrode is directly proportional to the surface area contacting fluid and inversely proportional with the distance between electrodes, therefore tungsten/copper plate is soldered and inserted as shown below. Size of the inserted plate is (4.5mm x50mmx.8mm) seen in Fig. 5.23.

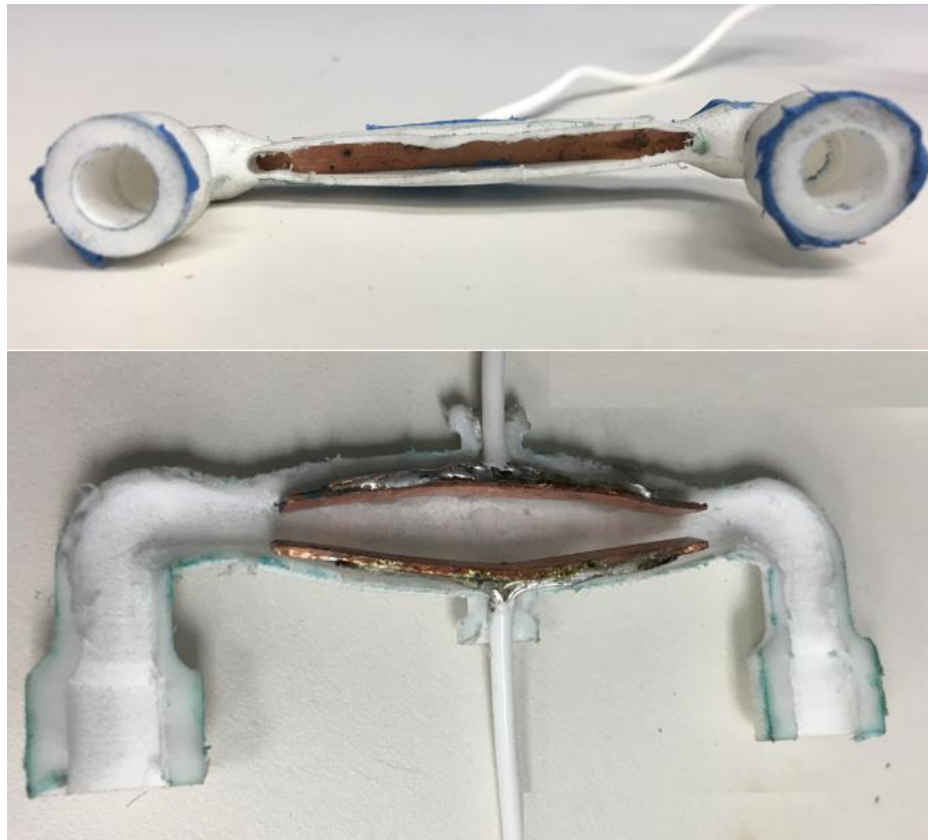


Figure 5.23: Inserted tungsten plated copper electrodes of MHD pump (4.8mmx50mmx.8mm)

A set of wired elliptic coupling with electrodes inside are assembled for both AC and DC MHD pumping. See Fig. 5.24.

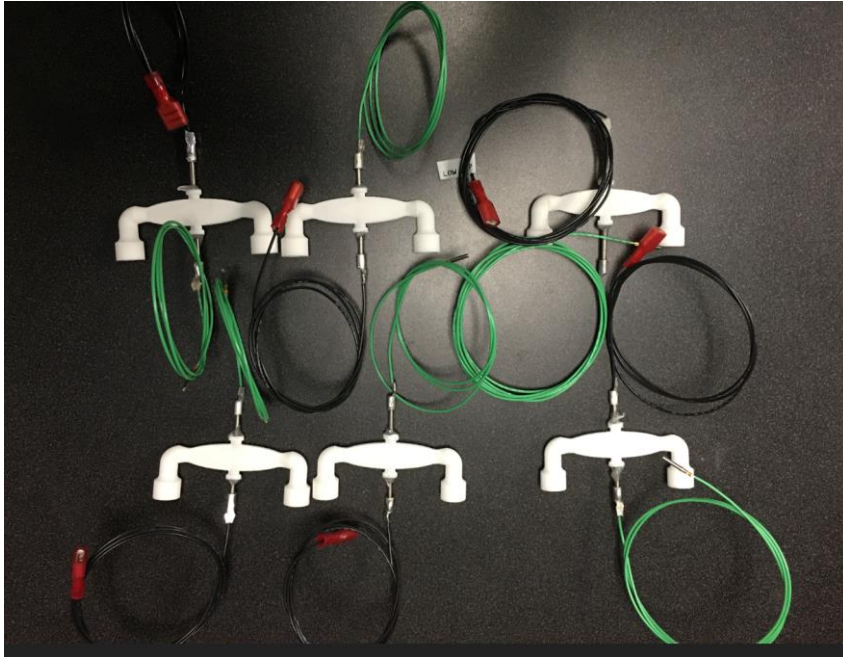


Figure 5.24: AM SLS Nylon 6,6 with wired electrodes elliptic coupling for AC and DC powering

5.3.1.3 Electrical Resistivity between Electrodes

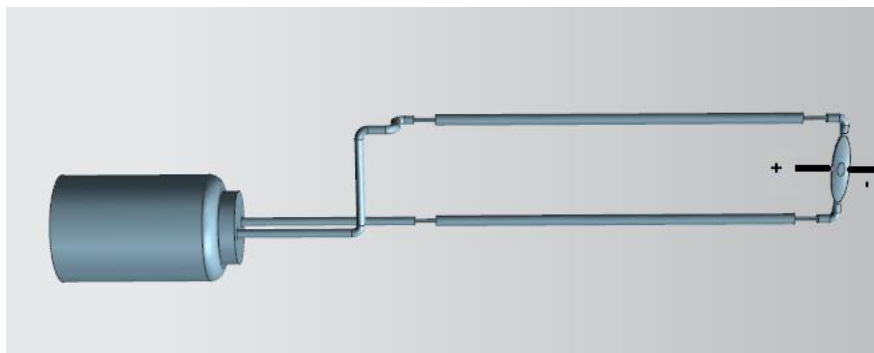


Figure 5.25: Electric current flows through closed loop of control volume of LM, with major will take the path of least resistance that is shortest distance between electrodes and perpendicular to magnetic field

Both electrodes are in touch with LM encapsulated in closed loop of control volume, the question is “how does electricity know which is the shortest and easiest path? Electric current will flow through ALL paths including longest closed loop to reservoir through conductive liquid metal. However, the majority will take the path of least resistance and will send the most energy through the easiest path defined by shortest

distance between electrodes. Therefore, the resistivity between the electrodes is approximated as $R \approx 35 \text{ m}\Omega$ according to following equation:

$$R = \rho \frac{L}{A} \quad (20)$$

where L is the shortest distance between electrodes (.012 m)

A is the cross-sectional area of electrodes ($1.32 \times 10^{-6} \text{ m}^2$)

ρ is the electrical resistivity of LM ($2.9 \times 10^{-7} \Omega\text{m}$)

Moreover, to understand the effect of electrically conductive Hartmann walls on mass flow rate of LM in MHD vs thermal conductivity of cooling system, the LM compatible containers are copper and also silver plated. All these elliptic coupling will be tested and evaluated in experimental testing. Figs. 5.26 and 5.27 shows nylon 6,6 elliptic coupling parts with silver plated, copper plated with gold finish and bare SLS during and after plating.

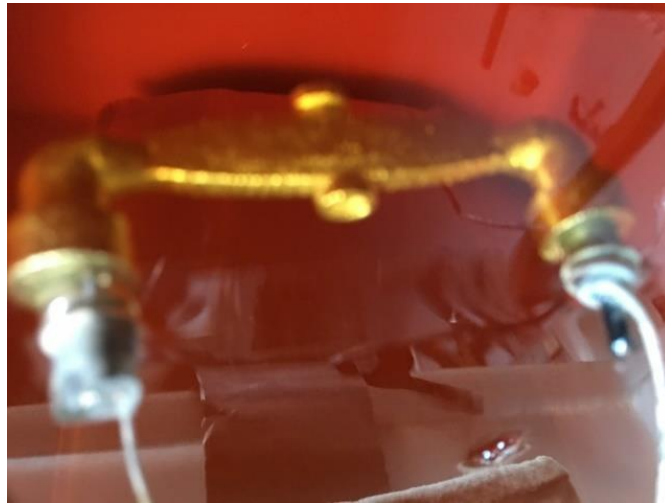


Figure 5.26: Copper electroplated with gold finish on SLS nylon 6,6 inside immersed in electrolyte solution during electrodeposition process.



Figure 5.27: Fabricated elliptic coupling with AM SLS technology: (left to right) 1). Electroless .1" silver plated nylon 6,6 . 2) Electroforming .1" copper with gold finish nylon 6,6 and 3). Bare nylon 6,6. (lengths of coupling are 50,20 and 5mm along flow, electrode and magnetic flux directions respectively)

5.3.2 MHD Cold Plate

Galinstan with electrical conductivity (3.46×10^6 S/m at room temperature)

allowing the liquid to be pumped by Lorentzian force. It is corrosive and have to be contained in ceramic and polymeric tubes, fabricated BN ceramic and Ultem plastic tubes embedded in SLM aluminum alloy blocks manufactured by DMLS AM technique (as discussed in chapter 3) are used as thermal transport cold plate for MHD pumping. Tubes and cold plates are seen in Fig. 5.28.

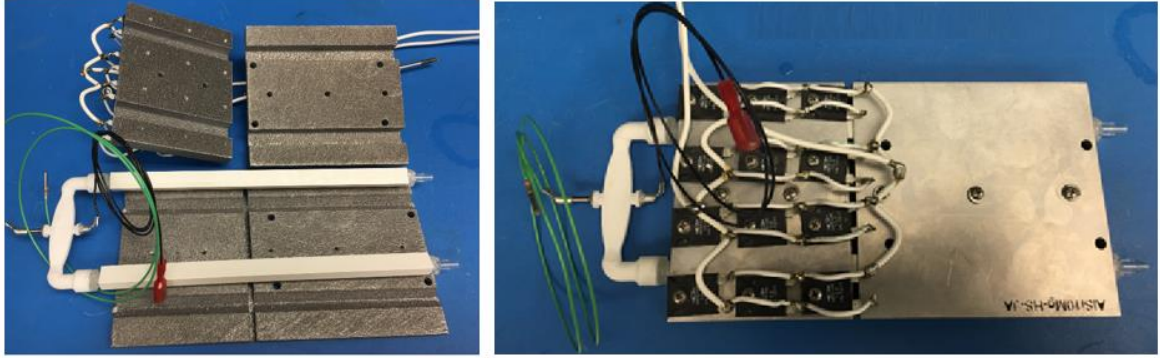


Figure 5.28: Components (left) and assembly (right) of cold plate including: AM Aluminum alloy (AlSi10Mg_200) 3 piece block (total size: 185mmx100mmx18mm), embedded LM compatible thermally efficient solid BN tubes (internal diameter= 6.2mm), also heat source (12x15 Ohms parallel resistors) and elliptic Nylon 6,6 SLS coupling with embedded electrodes ,#4-40 stainless steel fasteners torqued to 4.7 LB-IN.

5.4 CAD Model of MHD Cooling Prototype and Boundary Condition

After discussion about pieces parts and subassembly of active cooling by MHD, now we can develop the top-level assembly and our MHD active cooling prototype. Fig. 5.29 shows the MHD active cooling assembly, it includes surface mount resistors as heat source mounted on hybrid cold plate containing BN heat tubes interconnected to MHD pump via elliptic coupling. Galinstan circulates through closed loop reservoir hook up to heat tubes by MHD pump. AM fabricated heat block is mounted to the Peltier cold plate and hardware torqued to appropriate values. Thermal testing will be performed in thermally controlled operational room providing natural convection set to 25°C constant temperature.

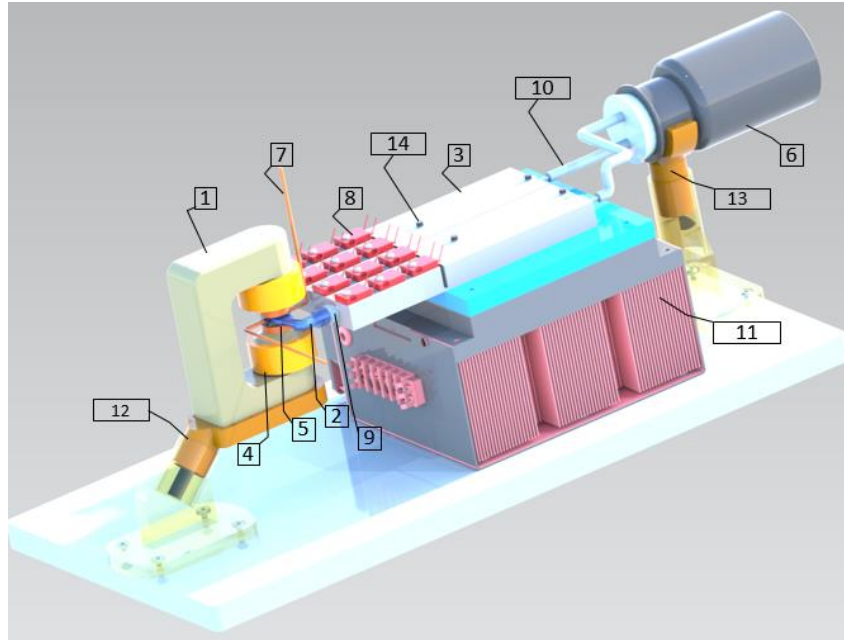


Figure 5.29: MHD cooling system: 1) hiperco50A CNC machined, 2) elliptic coupling SLS Nylon66 3) DMLS hybrid (AlSi10Mg_200) heatsink with embedded BN ceramic heat tube 4) gauge 22 AWG magnetic wire 5) tapered tip of core 6) Glass reservoir containing Galinstan 7) tungsten plated copper electrode 8) MP9100 Caddock resistor 9) Nylon tube fitting 10) Polypropylene tube 11) Peltier cold plate P/N TE CP121 12) MHD pump bracket 13) reservoir holder 14) mounting hardware

5.5 Ansys Maxwell Simulations of MHD Cooling Prototype

Before fabrication of prototype and experimental testing, we perform simulation to provide a risk-free way to test the cooling idea. Simulation offers the quantitative and qualitative insight needed to prove that the concept works and advantage of one design over another, however due to limitation of simulations, engineering testing and experimental data needed for final analyses of data and drawing plausible conclusion. MHD active cooling simulation approximated Maxwell equation combined with Navier-Stokes equations as followings.

We use the James Clerk Maxwell fundamental equations to all analyses of magnetic and electric fields. First, Maxwell equation is similar to Ampere's law (magnetic field (H) generated by the current or by the charge of an electric field(E).)

$$\oint H \cdot dl = I + \frac{\partial}{\partial t} \oint \epsilon_0 E \cdot dS \quad (21)$$

Second Maxwell equation is similar to Faraday's law (induced electric field relationship with changes of magnetic field.) Faraday's law Determines electromotive force (voltage) induced in closed circuit in magnetic field B as following:

$$\oint E \cdot dl = - \frac{\partial}{\partial t} \oint \mu_0 H \cdot dS \quad (22)$$

Third Maxwell equation states that the total magnetic flux passing through a closed surface is zero (magnetic monopoles do not exist).

$$\oint \mu_0 H dS = 0 \quad (23)$$

The fourth Maxwell equation is Gauss's laws for electric and magnetic fields. It states that electric field is produced by electric charge and the flux of electric field passing through closed surface depends on the charge contained in volume.

$$\oint \epsilon_0 E dS = q \quad (24)$$

Where q is electric charge in (C), ϵ_0 permittivity of free space, μ_0 is permeability of free space, H magnetic field strength (A/m), E is electric field strength (V/m) and electric current (A). Note that permittivity is the measure of capacitance that is encountered when forming an electric field in a particular medium (C/V m). Keep in mind, $B = \mu H$, vector magnetic potential is defined as $B = \nabla \times A$ and scalar magnetic potential is defined as $B = -\mu_0 \nabla \psi$ are useful for magnetostatics.

These equations combined with Lorentz force are the fundamentals of classical electromagnetics and are the basis of magnetic field computation. The induction equation

is Maxwell's equation coupled with flow field and electric field. The induction equation can be derived as:

$$\frac{\partial B}{\partial t} + (U \cdot \nabla)B = \frac{1}{\mu\sigma} \nabla^2 B + (B \cdot \nabla)U \quad (25)$$

Where, B is magnetic field, μ is magnetic permeability, σ is electrical conductivity of fluid and U is velocity field of fluid. Ansys MHD module solves induction equation once mean value of external magnetic field in XYZ directions and perpendicular electrical current density as boundary condition are applied to the meshed control volume to calculate the Lorentz force and velocity of LM as explained in following section.

MHD active cooling simulation categorized into three sections: I) for DC excitation Maxwell magnetostatic and for sinusoidal AC current Ansys Maxwell eddy current FEA solver is used that is an electro-magnetic tool suitable to analyze low-frequency phenomena, II) for CFD simulation, add-on MHD module in Ansys Fluent that refers to interface between an applied electromagnetic flux and flowing of an electrically conductive fluid is used, III) for thermal analysis, energy equation is turned on in Ansys Fluent (or Ansys Icepak in case of CCAs) to generate temperature gradient of cold plate under applied thermal load. Preprocessing effort in Ansys Maxwell starts with linking geometry from Siemens NX CAD package, defining region, adaptive tetrahedron meshing refinement to maximize accuracy of magnetic flux density. Defined rectangular closed region is shown in Fig. 5.30.

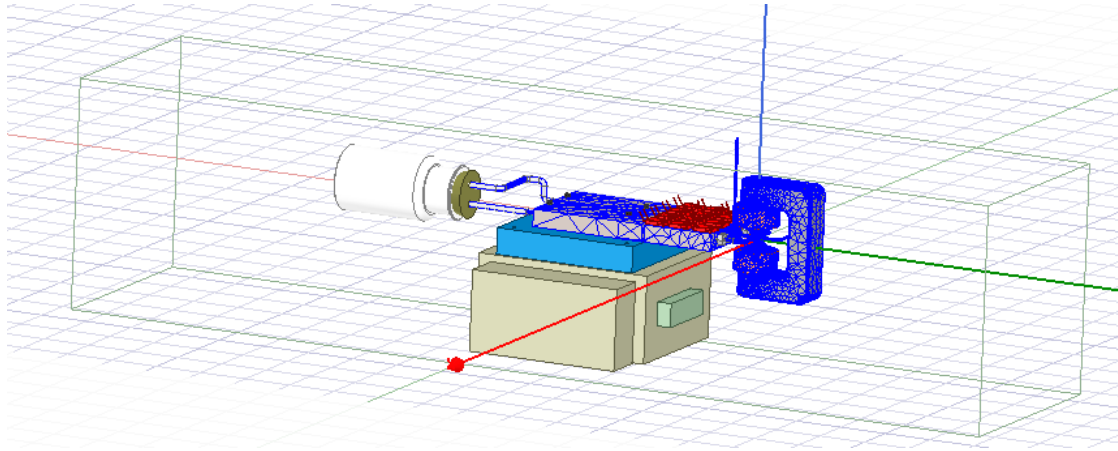


Figure 5.30: Ansys Maxwell preprocessing, defining rectangular open region that best fits the MHD cooling prototype

Material properties includes assigning B-H curve characterizing relationship between the induced magnetic flux density (B) and the magnetizing force (H) in C-shaped core. Table 5.1 shows the material properties of MHD cooling.

Table 5.1

Material Properties of MHD Cooling

Material name	Chemical formula/composition	Melting temperature (°C)	Density(kg/m ³)	Specific heat capacity J/(kg°C)	Thermal conductivity W/(m°C)	Dynamic viscosity Pa·s	Magnetic permeability, (susceptibility)	Electrical conductivity S/m
Galinstan (liquid metal, coolant)	68% Ga, 22% In, and 10% Sn	-19	6440	296	16.5	0.0024	diamagnetic(-4)	3.46×10 ⁶
Hiperco50A (C-shaped core)	49% Cobalt, and 2%Vanadium, balance Iron	1427	8110	420	29	n/a	15000	2.5×10 ⁶
Silver (electroless plating)	Si	961.8	10490	240	429	n/a	diamagnetic (-2.6)	63×10 ⁶
Copper (electroless plating)	Cu	1085	8940	386	385	n/a	diamagnetic (-1)	59.8×10 ⁶
Boron Nitride (heat pipe)	BN Solid Grade AX05	2973	1850	350	78(130)	n/a	nonmagnetic	n/a
DMLS Aluminum (heat sink block)	AlSi10Mg_200C	672	2670	900	173	n/a	paramagnetic(2.2)	35×10 ⁶
SLS Nylon (elliptic coupling)	Polyamide 22	220	930	1600	0.25	n/a	nonmagnetic	n/a

The relationship between magnetic field (B) and magnetizing force (H) is seen in Fig. 5.31.

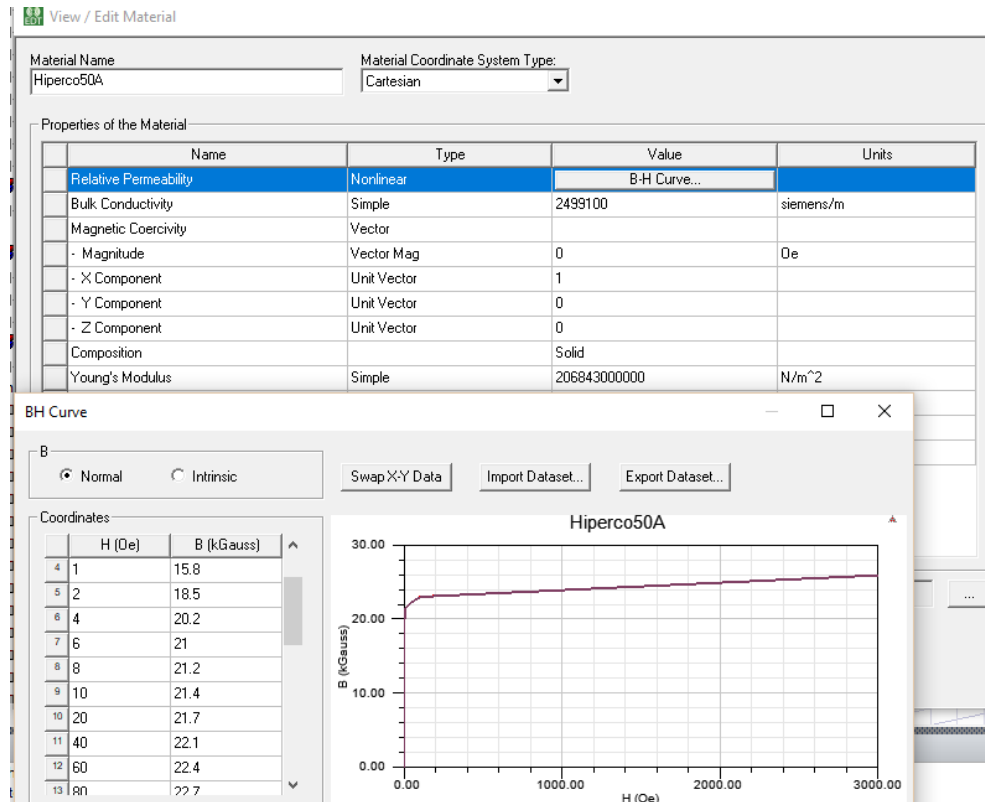


Figure 5.31: ANSYS Maxwell preprocessing, assigning B-H curve for C-shaped hiperco50A

Preprocessing in Ansys Maxwell concludes by applied electric loads (ampere-turns) to copper windings in two position to generate a series magnetic fields. Note that electrical current applied to electrodes will be applied as boundary condition in Ansys MHD fluent.

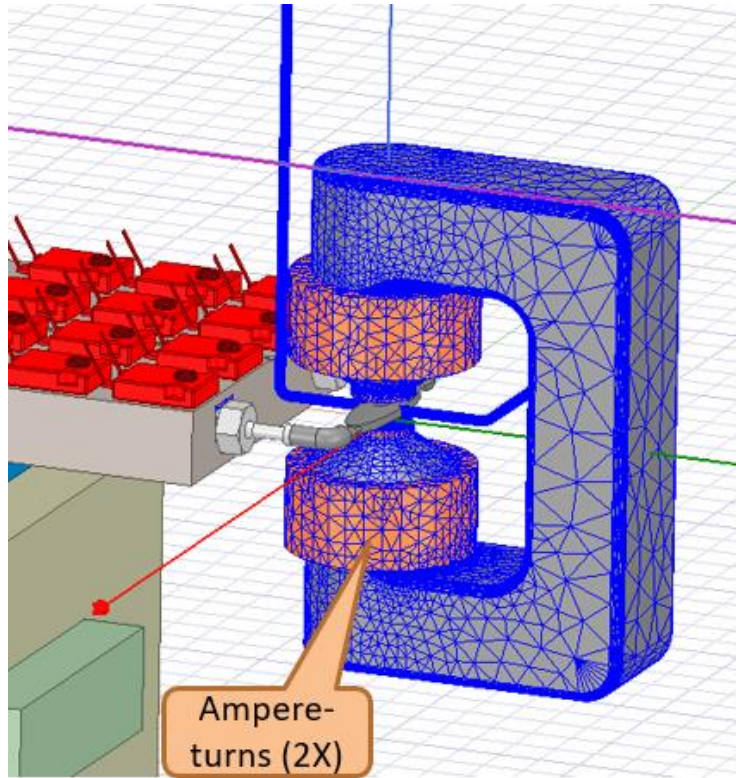


Figure 5.32: Preprocessing in Ansys Maxwell, showing adaptive tetrahedron meshing refinement applied to elements of the MHD pump to maximize accuracy of magnetic flux density, excitations (6 Amp-650turns) to two copper winding with AWG 22 magnetic wire.

Maxwell solves the electromagnetic field problem by solving Maxwell's equations in a finite region with applied loads and applicable boundary conditions. Post processing results in Ansys Maxwell shown in Figs. 5.33 and 5.34.

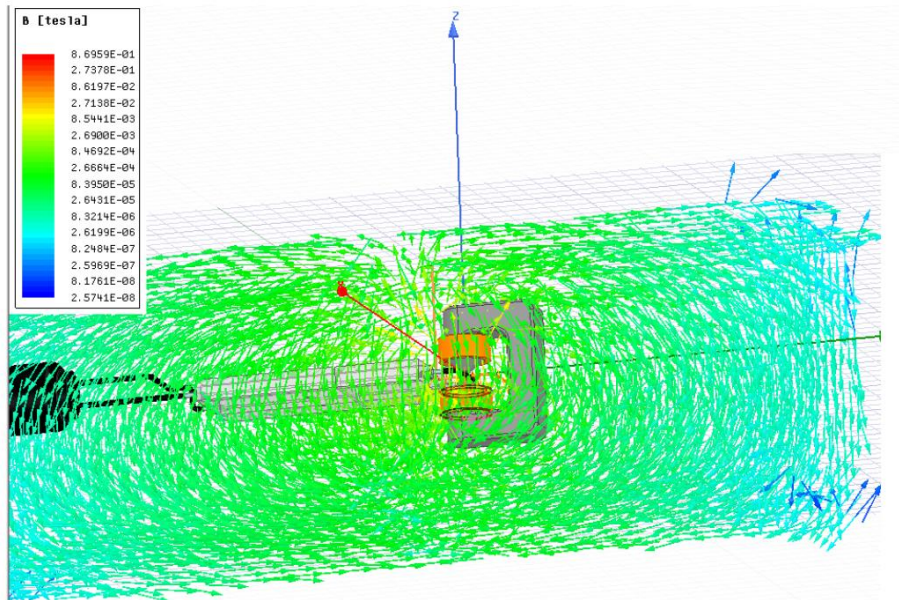


Figure 5.33: Ansys Maxwell, magnetic field contour of finite region, witnessing needs for EMI shielding

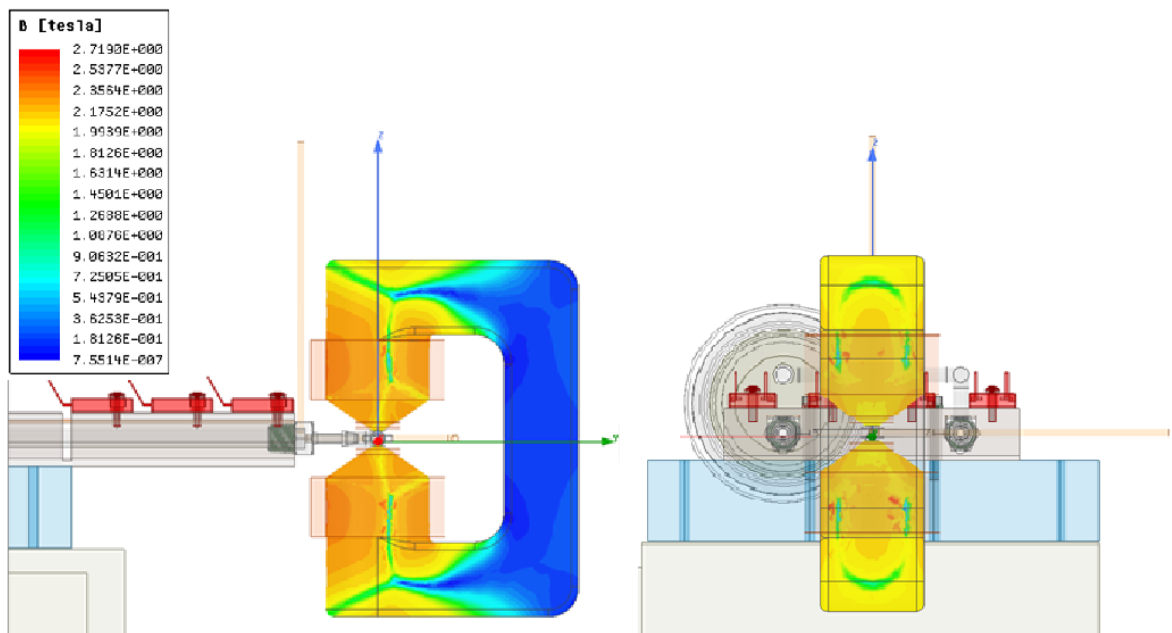


Figure 5.34: Post processing in Ansys Maxwell, showing projection views distribution of magnetic flux density by applying (650 turns 6 amp) to windings.

Post-processing results of extremal magnetic field generated by powered electromagnet will be applied to elliptic section of control volume perpendicularly in Ansys MHD Fluent package through the magnetic induction option as seen in Fig. 5.35.

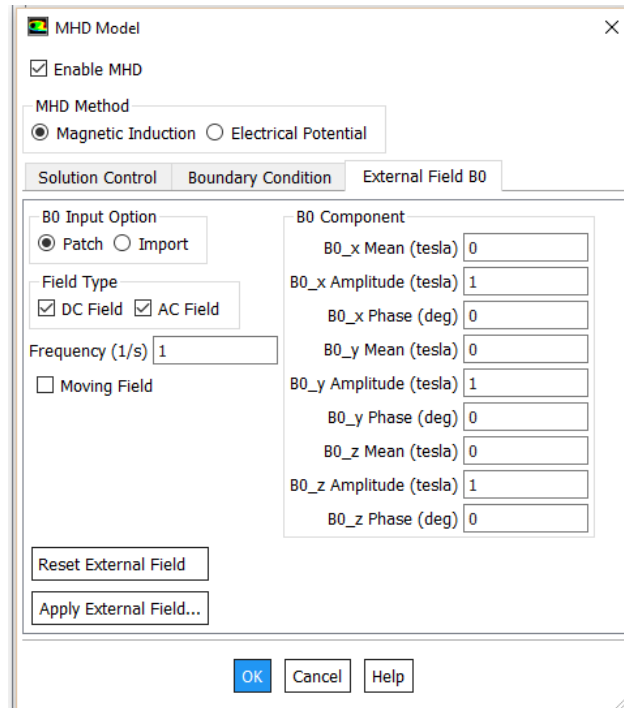


Figure 5.35: ANSYS Fluent MHD module, for enabling application of Lorentz force to fluid by induced magnetic field to LM

The MHD module is included in the CFD package of Ansys Fluent, and it can be activated with the Text User Interface (TUI) command: *define/models/addon-module 1*. For preprocessing, the adaptive tetrahedron meshing of MHD cooling prototype and assigned boundary conditions is seen in Fig. 5.36.

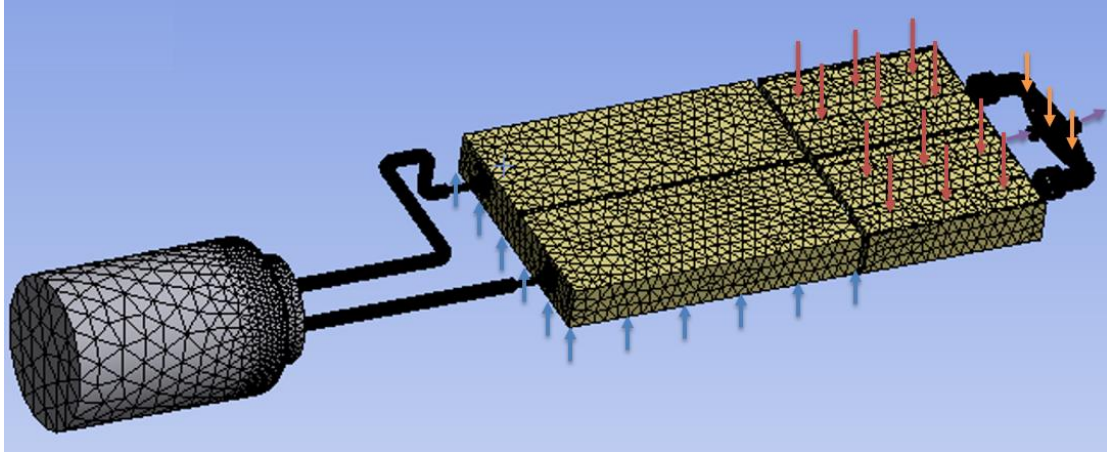


Figure 5.36: ANSYS FLUENT Preprocessing with adaptive tetrahedron meshing, boundary condition (10°C boundary condition) in blue arrows for the Peltier cooler, heat source in red arrows, induced magnetic field in orange arrows and electrical current to electrodes in purple arrows.

Mesh convergence affects the accuracy of post processing results, following figure ensures that the results of steady state incompressible CFD analysis are not affected by changing the size of the mesh.

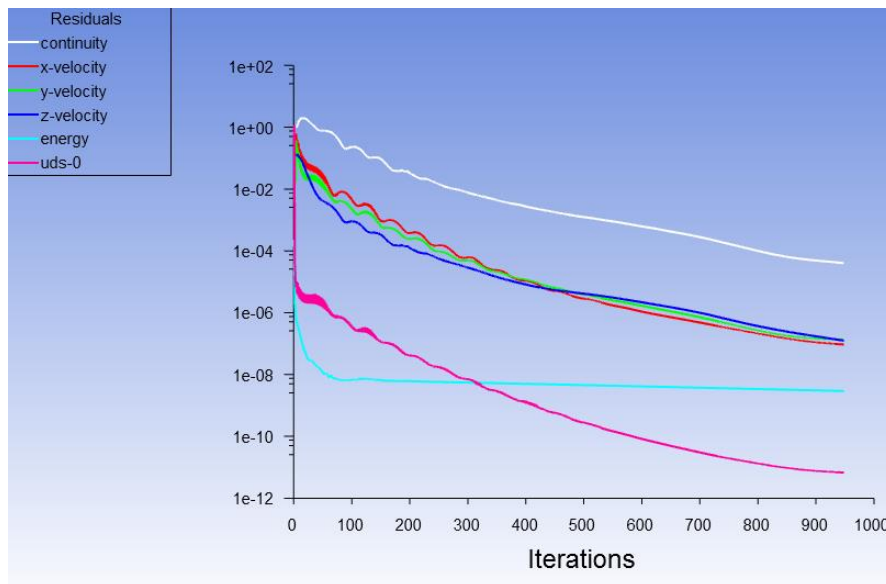


Figure 5.37: Ansys Fluent MHD, converge solution of critical parameters

Post processing results of CFD analysis are as shown in Figs. 5.38–5.41.

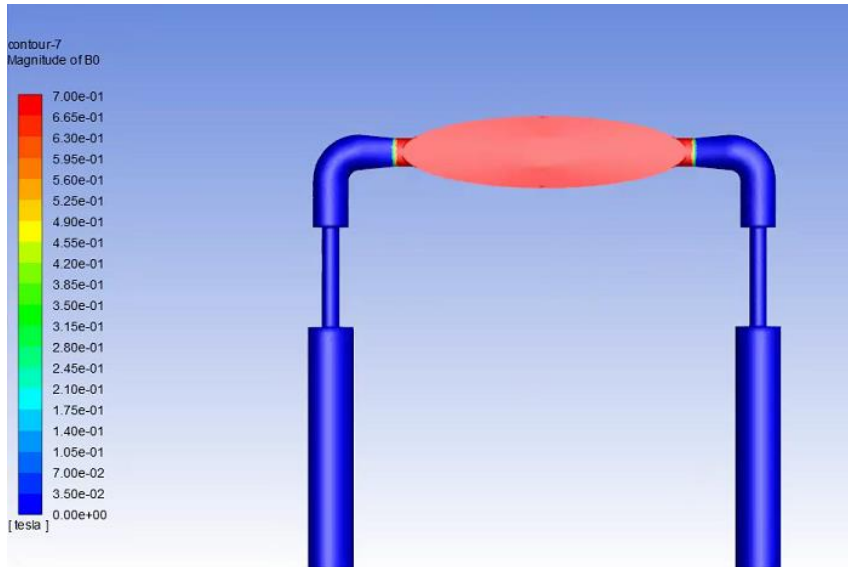


Figure 5.38: Ansys Fluent MHD, boundary condition : induced magnetic field applied to LM, generated from external magnetic field from C-shaped core in tesla

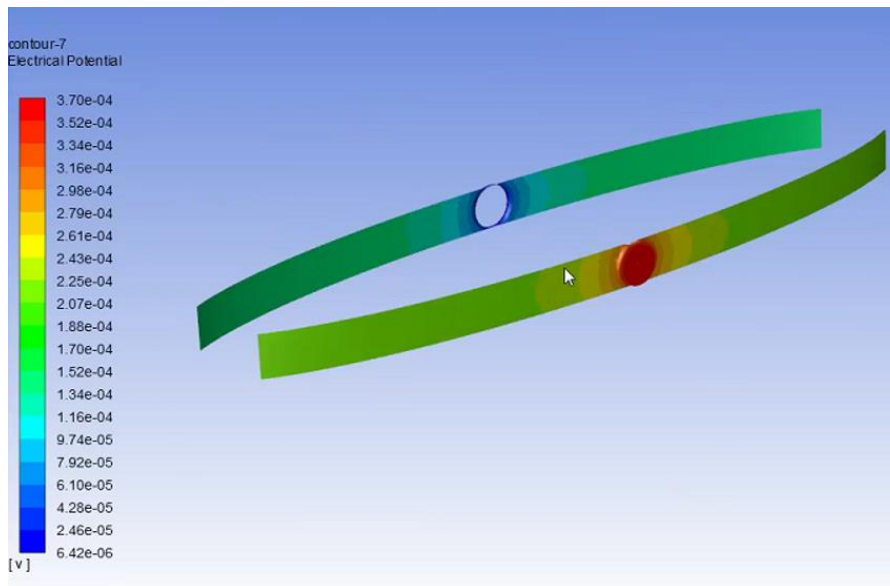


Figure 5.39: Ansys Fluent MHD, boundary condition : applied electrical field to electrodes in volts

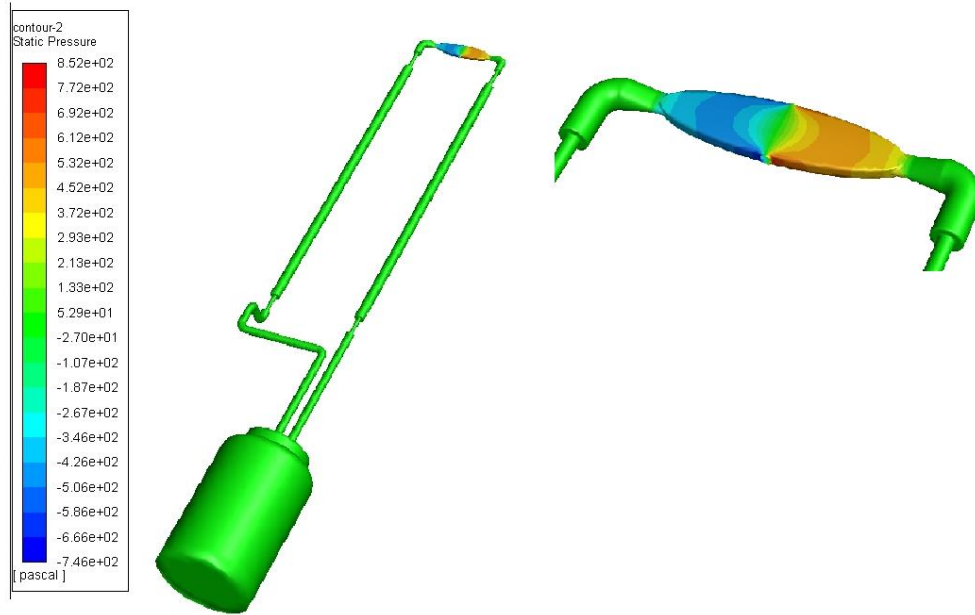


Figure 5.40: MHD Fluent, post processing, pressure profile of control volume due to Lorentz force (left), scaled view of elliptic portion of control volume (right) in pascal

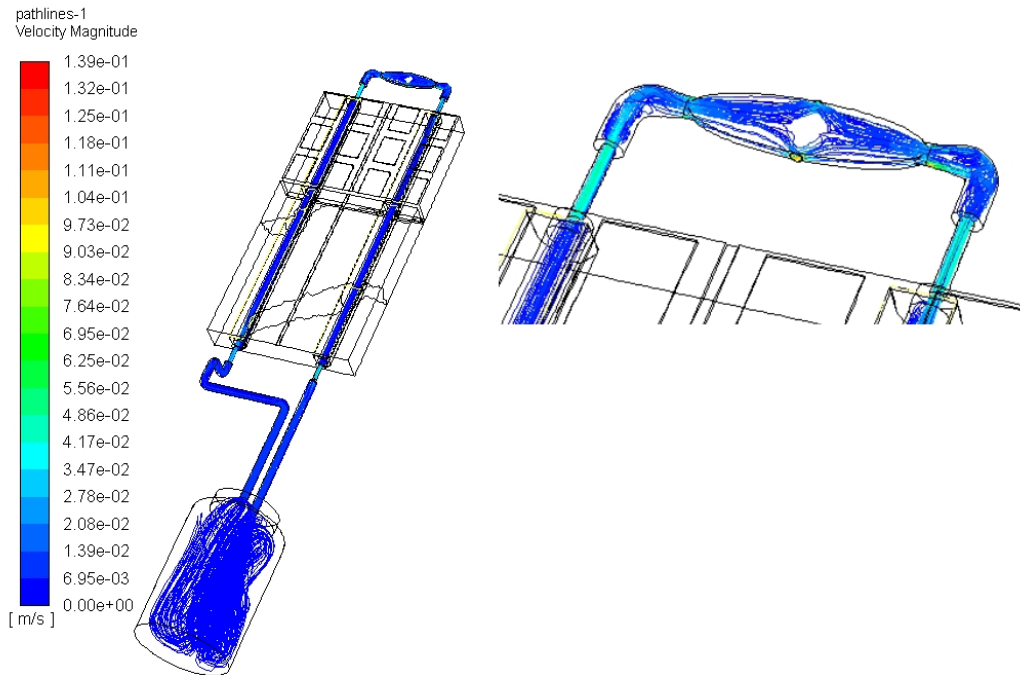


Figure 5.41: MHD Fluent, post processing, velocity profile of control volume due to Lorentz force (left), scaled view of elliptic portion of control volume (right) in meter per second

In solving the energy equation to gain insight about the temperature profile, the conjugate heat transfer is used to describe heat transfer that involves variations of temperature within solids and liquid metal, due to thermal interaction between the solids and LM as seen in Fig. 5.42.

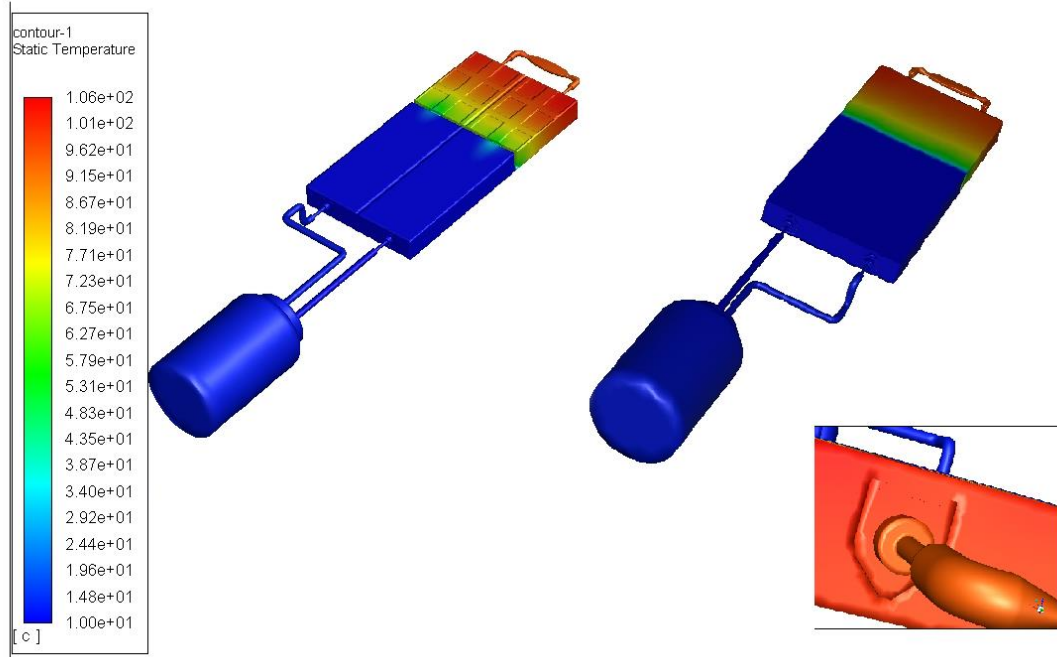


Figure 5.42: MHD Fluent, post processing, Temperature profile of heat sink block in active cooling system derived by MHD pump running Galinstan (top and bottom views), scaled view showing interfaces of tube inside the block (conjugate convective heat transfer) in °C

Due to limitation of the MHD module in Ansys Fluent, the magnetic flux density excitation could not be linked directly from Ansys Maxwell. Therefore, conservatively we assumed a portion of external magnetic field generated from electromagnet is induced to LM (.7T) and we applied it uniformly to the elliptic portion of control volume in Ansys MHD as shown in postprocessing figure. Although the model was overpredicting due to assuming full contact at interfaces, postprocessing results showed the concept is pertinent

and promising. Additionally, simulation flux report in Ansys revealed that 374.7 watts out of 390 watts is transferred via conduction of cold plate.

5.6 MHD Active Cooling Thermal Experiment

In previous step, multiphysics analyses of MHD cooling system was performed in Ansys workbench to predict the behavior of the system based on solving equations for conservation of mass, momentum, energy and electromagnetism and gain insight about the magnetic/electric fields applied to the cooling system. After gaining assurance from the simulation, we fabricated the prototype to test how the MHD cooling processes work under a specified condition. This repeatable and controlled experiment provides insight into cause and effect by demonstrating the outcome when subsequent design variables are manipulated. In this regard, we tested the effect of electrodeposition on elliptic SLS nylon 6,6 coupling (electrically conductive wall) on flow rate and consequently thermal behavior of the cooling system. The behavior observed from incompressible MHD flow is dramatically different from polar liquids because of the surface tension, Hartmann flow and M-shaped velocity profile since streamlines near conductive walls are pulled back and conducting walls result in significantly higher pressure losses of non-homogenous MHD flow. Silver or copper plating can improve heat transfer due to their high thermal conductivities; however, there is a tradeoff between effects of electroplating (conductive wall) on MHD pressure drop and heat transfer improvement due to added electroplated film and we studied this relationship.

Furthermore, we studied the effect of core material of electromagnet (soft-magnetic Hiperco50A alloy vs. stainless steel 718) on magnetic flux. Ferromagnetic materials are mostly polycrystalline and magnetic anisotropy of crystal generates

magnetic losses and coercivity. It is important to eliminate anisotropy. Hiperco50A with high saturation polarization is used as optimal material for electromagnetic core.

Selection of ceramic tube for MHD cold plate that permitted use of what normally would be corrosive LMs has enabled us to overcome compatibility issue of LM. However, among other ceramics, machinable BN was used as tube material, because of high thermal conductivity up to $130 \text{ W/m}\cdot\text{°K}$, minimal wettability with LM and suitable for MHD application due to its electrically insulating properties. We tested the tradeoff between Lorentzian forces, viscosity affected by the wettability of BN. Additionally, Ultem tube is selected as an alternative to compare the relative performance of the proposed cooling approach with ceramic. Lastly, to determine the tradeoff in performance of MHD pump vs diaphragm pumping for thermal management, a characteristic curve is required for diaphragm pump since the pumping speed of the diaphragm pump varies; however, the MHD pump generates a uniform constant pumping due to Lorentzian force, a major advantage for reliability consideration.

5.6.1 Experimental Setup and Instrumentations

To conduct a controlled thermal experiment, we set up the MHD cooling prototype in a temperature controlled room, as shown in following figure. During the test and at each step, the data were examined to determine limits of the test equipment were not exceeded. Moreover, first set of specified data (constants) were fixed by design: geometric dimensions, size of magnetic wire (AWG 22 copper mag wire), size/material of electrode, type of LM (Galinstan), number of turns of magnetic wire. Additionally, second set of specified data were controlled during the test: power load as heat source (Caddock resistor P/N MP9100), boundary conditions (i.e., temperature of Peltier cooler

and environment temperature), applied current to electrode, applied current to electromagnets, and type of diaphragm pump for active cooling test with moving parts. Independent variables were (a) material of tubes, (b) material of electromagnet core, (c) type of plating of elliptic LM container, and (d) type of applied current (AC or DC). The dependent variables (effects) we measured were (a) temperature of hybrid cold plate, (b) flow rate and pressure of coolant, and (c) magnetic flux of the gap of electromagnet (external magnetic field generated in the gap of core). Following figure shows the MHD prototype and instruments used for testing.

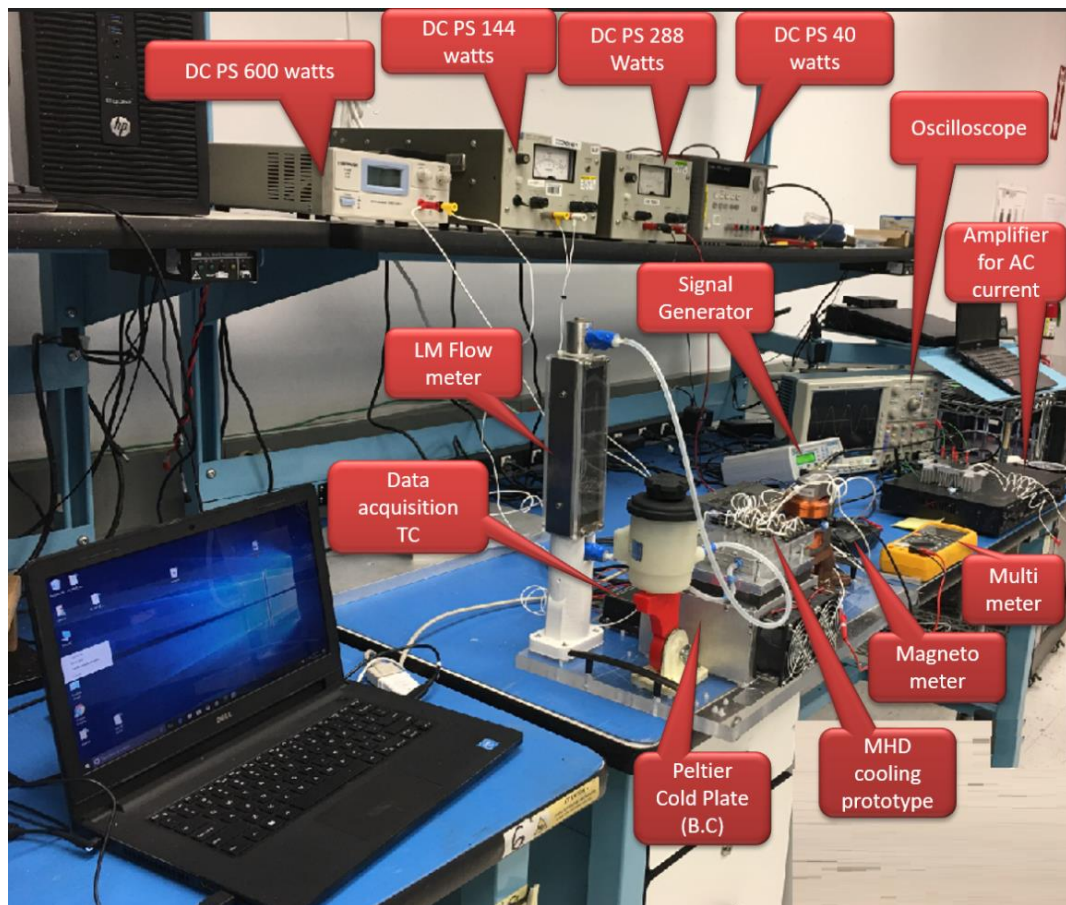


Figure 5.43: MHD active cooling test components, showing components of AC and DC power setup, Peltier cooler (B.C.) set to 10°C, and ambient temperature of 25°C

LM compatible variable area flow meter is included in flow line to measure the LM coolant flow rate. Flow measurement devices removed from the closed loop during thermal test due to head loss and affecting the mass flow rate of LM coolant.

5.6.2 Conducting Experiment and Analyzing Data

Thermal testing was initiated with no LM coolant flow and no pumping system, by inputting 10 watts and waiting for temperatures to stabilize with $>1\text{C}/10$ minute change. Then, we increased thermal load to 80 watts and waited for temperature to stabilize. We repeated this step until either maximum temperature, power, or some other obvious limit on the experiment was reached such as the 165°C maximum temperature at the base of the power resistors. Then, we repeated the passive test with filling LM coolant and still no pumping system and recorded the data reaching derating temperature after several iterations. We turned on the MHD pump with coolant circulating in the system, measured the flow rate and recorded thermocouple readings after the temperature stabilized (see Fig. 5.44). We repeated the active cooling test for all scenarios tabulated in Table 5.2. After each step, we prepared a preliminary plan as to the next power steps. During the test, we modified these power steps as reasonable and recorded the thermocouples reading mounted at critical and identical locations for all scenarios.

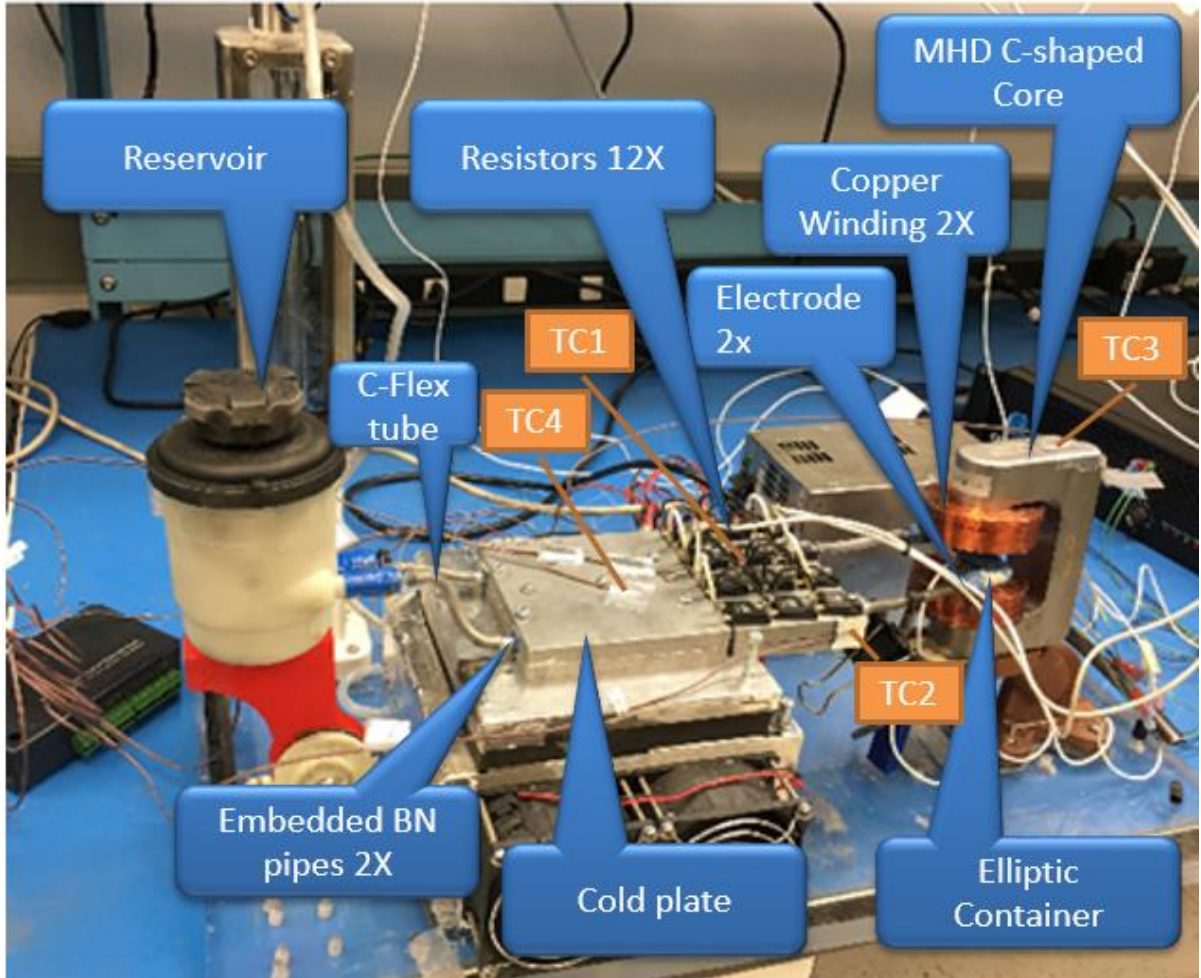


Figure 5.44: Prototype I: Active cooling with no moving parts (MHD pumping) and location of thermocouples (TC#) identical with diaphragm pumping

We replaced the MHD with a diaphragm pump and ran the test again (Fig. 5.45), recorded the thermocouples reading after temperature stabilized, and concluded the test. The alternate pumping technique with moving parts tested in this study was a diaphragm pump, a reciprocating-type positive displacement with up to 97% efficiency that can handle highly viscous liquids such as Galinstan and results of the tests are presented in Table 5.2.

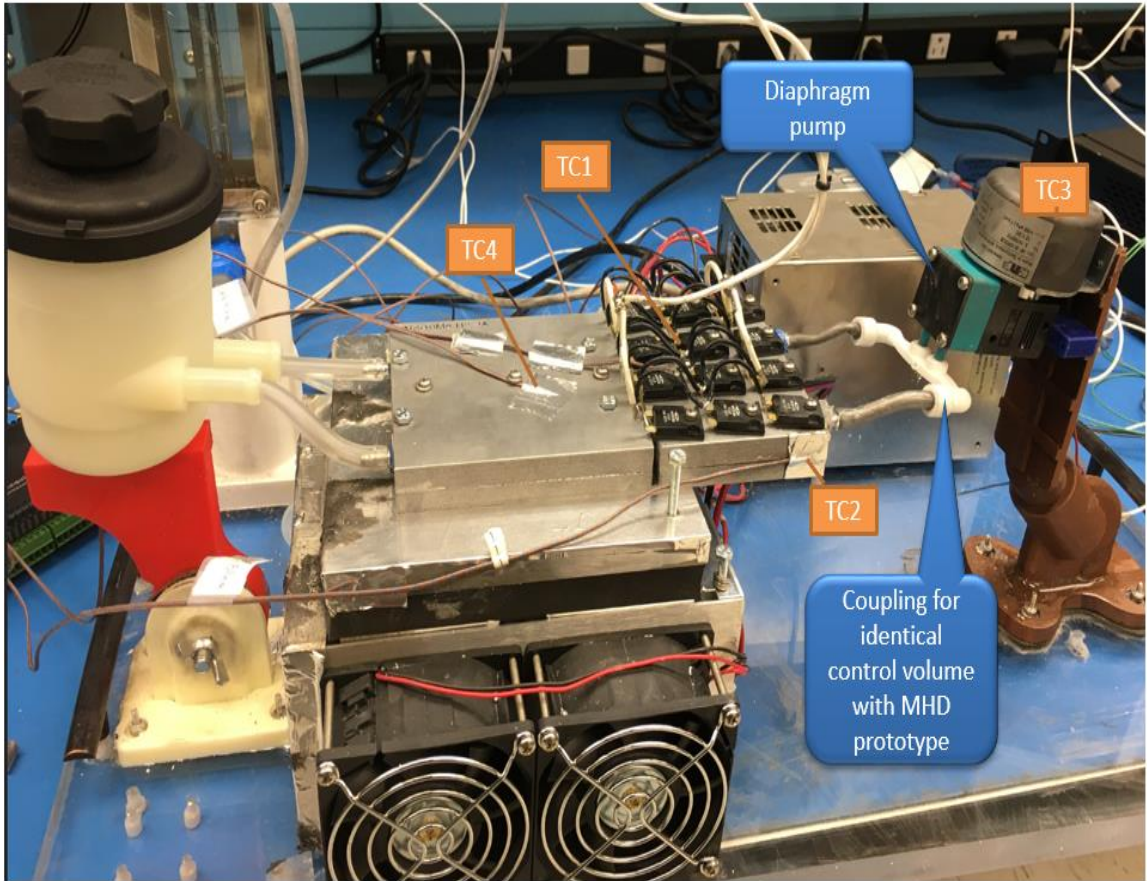


Figure 5.45: Prototype II: Active cooling with moving parts (diaphragm pump), identical setup with MHD cooling including similar cold plate geometry and material, control volume, applied load ,boundary condition and location of thermocouples (TC#)

Table 5.2

Thermal Test of the Prototypes, Showing Results of Passive (Conduction), Active Cooling With No Moving Parts (MHD), and With Moving Parts (Diaphragm Pump)

Run no.	Test article ^a			Thermocouple readings (°C)					External magnetic field (Gauss)	Gauge pressure (Pa)	Flow rate (mm ³ /s)	Power consumption of pump (W)	Temperature difference of heat source(TC1) relative to test article 1 (°C)	Heat transfer improvement of test articles relative to passive test article 1
	Tube material	Pump System	Coolant	Material of elliptic container	TC1 center of heat source	TC2	TC3	TC4						
1	Boron Nitride	None	None	SLS Nylon 6,6	164.3	123.2	NA	65.3	NA	NA	NA	NA	Ref.	Ref.
2	Boron Nitride	None	Galinstan	SLS Nylon 6,6	159.5	120.7	NA	64.1	NA	NA	NA	NA	4.8	1.030
3	Boron Nitride	Diaphragm, DC(1A,12V)	Galinstan	SLS Nylon 6,6	146.0	115.0	37.7	60.1	NA	2260	2681	12	18.3	1.125
4	Boron Nitride	MHD using 718 Stainless Steel core-DC to electrode(3.5A,7.8 V), DC to coils(7A,21.4V)	Galinstan	SLS Nylon 6,6	159.5	120.7	49.0	64.1	240	0	0	177	4.8	1.030
5	Boron Nitride	MHD using 718 Stainless Steel core-AC to electrode(3.5A,7.8 V), AC to coils(7A,21.4V)	Galinstan	SLS Nylon 6,6	159.5	120.7	42.0	64.1	168	0	0	177	4.8	1.030
6	Boron Nitride	MHD using 718 Stainless Steel core-rectified AC to electrode(3.5A,7.8 V), rectified AC to coils(7A,21.4V)	Galinstan	SLS Nylon 6,6	159.5	120.7	45.0	64.1	148	0	0	177	4.8	1.030

Run no.	Test article ^a			Thermocouple readings (°C)					External magnetic field (Gauss)	Gauge pressure (Pa)	Flow rate (mm ³ /s)	Power consumption of pump (W)	Temperature difference of heat source(TC1) relative to test article 1 (°C)	Heat transfer improvement of test articles relative to passive test article 1
	Tube material	Pump System	Coolant	Material of elliptic container	TC1 center of heat source	TC2	TC3	TC4						
7	Boron Nitride	MHD using Hiperco50A core-DC to electrode(3.5A,7.8 V), DC to coils(7A,21.4V)	Galinstan	SLS Nylon 6,6	155.9	118.0	78.0	62.7	8000	229	650.9	177	8.4	1.054
8	Boron Nitride	MHD using Hiperco50A core-DC to electrode(3.5A,7.8 V), DC to coils(7A,21.4V)	Galinstan	Silver plated SLS Nylon	158.5	119.9	78.0	63.7	8000	75	212.6	177	5.8	1.037
9	Boron Nitride	MHD using Hiperco50A core-DC to electrode(3.5A,7.8 V), DC to coils(7A,21.4V)	Galinstan	Copper plated SLS Nylon	159.5	120.7	78.0	64.1	8000	0	0	177	4.8	1.030
10	Ultem	MHD using Hiperco50A core-DC to electrode(3.5A,7.8 V), DC to coils(7A,21.4V)	Galinstan	SLS Nylon 6,6	159.3	120.5	78.0	64.0	8000	207	590	177	5.0	1.031

Note: Ambient temperature is 25°C, Peltier cold plate 10°C (BC), control volume of all cases is identical. Heat source(power = 320 W). The pump turned on before reaching derating temperature of resistors (165°C). ^aBlock material of cold plate: SLM Aluminum Alloy (AISI10MG_200).

From the data in Table 5.2, several conclusions could be drawn. Following testing using the MHD pump, the calculated dimensionless MHD incompressible flow parameters from the experimental data for the most efficient MHD prototype achieved by nylon elliptic coupling without electroplating and BN tubes in aluminum cold plate were determined. MHD dimensionless parameters are based on subsequent formulas:

Hartmann number

$$Ha = \left(\frac{\text{Electromagnetic forces}}{\text{Viscous forces}} \right)^{\frac{1}{2}} = B_0 L \sqrt{\frac{\sigma}{\nu \rho}} \quad (26)$$

Reynolds number

$$Re = \frac{\text{Inertia forces}}{\text{Viscous forces}} = \frac{U_0 L}{\nu} \quad (27)$$

Magnetic Reynolds number

$$Re_m = \frac{\text{Convection of } B}{\text{Diffusion of } B} = \frac{\text{Induced field}}{\text{Applied field}} = \frac{U_0 L}{\nu_m} = \mu_0 \sigma U_0 L \quad (28)$$

Stuart number or Interaction parameter

$$N = St = \frac{\text{Electromagnetic forces}}{\text{Inertia forces}} = \frac{Ha^2}{Re} = \frac{\sigma L B_0^2}{\rho U_0} \quad (29)$$

Where L is the length of control volume, σ is electrical conductivity of LM (Galinstan), ν is dynamic viscosity of LM, ρ is density of LM, U_0 is velocity of LM, μ_0 is its magnetic permeability and B_0 is applied external magnetic field from C-shaped core.

The Hartmann number was 556.5, Reynolds number was 0.06, which resulted in a ratio of Hartmann to Reynolds was 9,902; therefore, the core flow was laminar. The Stuart number was about 23,445. Therefore, it appears that viscous forces dominated over the inertial forces and electromagnetic forces. The calculated magnetic Reynolds number

was 0.04, indicating the induced magnetic field to LM was small compared to the applied field of 8000 Gauss from the C-shaped Hiperco50A core.

According to (Muller & Buhler, 2001), pressure of a flow in a rectangular duct under MHD can be evaluated by following equation for Ha greater 1.

$$P = Ha \left(1 - \alpha * \frac{1}{d} * Ha^{-\frac{1}{2}} - Ha^{-1} \right)^{-1} \quad (30)$$

Where d is the size of sidewall and coefficient alpha depends on conductivity of the wall and for insulated wall (nylon) is .825. The experiment revealed that elliptic coupling without plating has improved the flow pressure drop by a factor of 4.3 (229 Pa/52.19 Pa) compared to analytical pressure drop calculated for a 5mm x 5mm square coupling placed between poles instead of elliptic coupling.

The heat transfer improvement of MHD prototype relative to passive one was 1.054 and diaphragm pump improves heat transfer 1.125 relative to passive prototype. This indicated that the diaphragm pump was more efficient than MHD pump. However, MHD has many important advantages over the diaphragm pump, including compatibility with space-like environments, high reliability, simplicity, ruggedness in operation, silence due to no moving parts, and easier fabrication. Heat generated from the magnetic cores can contribute to thermal management however the effect of heat on avionics is minimal due to its distance from electronics.

The testing also was able to demonstrate the conductive Hartmann wall effect on MHD when an additively manufactured LM-compatible coupling is electroplated. Regarding the effect of the plating on the flow rate in MHD pumping, an unplated elliptic SLS nylon 6,6 container had the highest efficiency to induce the external magnetic field to LM since electrically insulating walls result in significantly higher MHD flow rate.

Electroplated copper on nylon blocked the external magnetic field, and the magnetic pump was not able to circulate the LM coolant. This effect was less obvious with silver-plated nylon. Electroless silver plating reduced the flow rate about 3 times compared to the unplated nylon. About 1/3 of the external magnetic field passed through the silver wall relative to the bare nylon coupling. Silver is ideal for heat transfer applications, but it blocks the magnetic field in MHD pumping due to its high electrical conductivity. Therefore, silver is not an optimal choice for the MHD cooling system. The relationship among the magnetic field strength (H), response of the magnetic core (B), and the magnetic field induced to the LM is complex and highly nonlinear. Further investigation is required to realize the relationship.

Even though the core was geometrically optimized, the soft-magnetic material drastically influenced the magnetic flux density in AC, DC, and rectified AC excitation due to coercivity and core losses. Table 5.3 shows the comparison of the test results and measured magnetic field at the tip of the tapered core. DC produced the highest magnetic flux density, and the effect of saturation was negligible in low-frequency 60Hz. Therefore, we concluded that the application of AC powering was irrelevant to overcome the magnetic saturation in this study.

Table 5.3

Measured Magnetic Field (Gauss) at the Tip of Geometrically Optimized C-Shaped Core Under Direct and Alternate Current Excitation for Two Different Materials: Soft-Magnet Hiperco50A and Stainless Steel 718

Core material, Applied Current (A)	Applied DC	Applied AC 60Hz sine wave	Rectified AC 60Hz sine wave
Hiperco50A			
7A	8000	5520	7120
5A	6000	4140	5340
4A	4700	3243	4180
1.3A	1800	1250	1600
Stainless steel 718			
7A	240	175	220
1.3A	52	38	47

Prototype systems were used to determine saturation thresholds of electrodes and electromagnets under direct current (DC) and eddy alternating current (AC). Electrical field intensity is inversely proportional to the distance between the plates and directly proportional to surface area of the electrodes in contact with LM. For tungsten-plated copper maximum allowable applied current and voltage before reaching the saturation were observed at 3.5 amp and 7.8 volts during the experiment. Regarding magnetic saturation, the maximum allowable current to the magnetic wire of Hiperco50A electromagnets was 7 amp and 21.4 volts before reaching the saturation point at 8000 Gauss (before exceeding the ampacity of magnetic wire).

5.7 Conclusion

In this chapter, we studied the development of a reliable, rugged, and silent thermal transport system for avionics, allowing significantly higher power dissipation and realizing it using an AM techniques to embed ceramic thermal management structures

capable of handling corrosive LMs as a coolant being driven by MHD. The three AM techniques used, DMLS, SLM, SLS, and FDM, enable the cost-effective fabrication of the aluminum alloy cold plate, nylon 6,6 elliptic coupling, and Ultem tubes, respectively. Subtractive manufacturing was used to fabricate BN solid ceramic tubes and the electromagnetic core to complement the innovative AM techniques used to fabricate a prototype MHD active cooling system with no moving parts, which is ideal for operating in space-like environments.

There were several key findings in this investigation. Since LMs are corrosive to most metals, there was the need to encapsulate the LM in thermally conductive ceramic tubing. A solid BN ceramic tube was chosen due to its high thermal conductivity and its low outgassing property necessary for space application. Since ceramics are very brittle and break easily under thermomechanical loading, an approach was developed for embedding the BN tube in a metallic block using SLM in order to enhance the mechanical integrity of the ceramic component.

The geometry-dependent demagnetizing field was found to be opposite of the applied magnetic field, which weakens the magnetic flux. Therefore, an ellipsoid shape offered optimal magnetic flux. Fabrication of a ceramic ellipsoid is not cost-effective by AM or conventional machining. Thus, we fabricated a geometrically optimal elliptic container by the AM SLM process out of LM compatible nylon 6,6 instead of BN ceramic. The tradeoff between the metallic wall effect on the induced magnetic field and thermal conductivity of the metallic wall in the MHD cooling system is not well understood. To gain more insight about the conductive wall effect of elliptic coupling, we metallized the outer surface of the LM-compatible plastic elliptic coupling with copper

and silver plating to characterize the effect of plating on the flow rate and subsequent cooling performance.

While a diaphragm pump is efficient and can be used to pump LMs, it tends not to pump very accurately at minimum flow rates, is noisy due to moving parts, suffers wear and tear from friction and movement of components, and has sealing and leaking issues at the inlet and outlet of the pump. Conversely, the MHD operating principle is straightforward and involves moving an electrically conductive fluid by the Lorentz force, resulting from the cross-product of an electric current with a perpendicular magnetic field. The highly reliable attributes of a MHD pump have tended to outperform its low efficiency due to simplicity, space compatibility, silent operation, rapid changes in driving force, lack of influence by pitch, roll, and yaw of spacecraft, scalability, easier fabrication, and minimal maintenance due to operation with no moving parts. Thus, MHD cooling is highly suitable for long duration space missions.

Chapter 6: Optimality of MHD Active Cooling System

6.1 Introduction

In previous chapter, multiphysics analyses of MHD cooling system was performed in Ansys workbench to predict the behavior of the system based on solving equations for conservation of mass, momentum, energy and electromagnetism. Engineering simulation is a valuable tool that complements physical testing by reducing the total effort and cost required for experimentation and data acquisition. However, we are dealing with some quite computationally expensive and time-consuming analyses and experiments. Even though the cooling experiment to reach steady state takes less than 2 hours, however in simulation, single approximation of partial differential equation with finite volume method with Ansys MHD Fluent solver can take quite a long time since each time step could be as small as $1e-4$ second to ensure convergence of each step. That would need $6e+6$ time steps and each step needs several iterations i.e. 20 iterations to converge so that it is not doable with decent engineering workstation and super computer with multiple cores is needed for the analysis. Recent advancements in the field of optimization have led to surrogate models for computationally expensive models as an alternative to gain insights that might approximate the solution and converge to optimal solution with approximation-assisted multiple objective (AAMO) approach. Therefore, it is likely that surrogate modeling will indeed be an appropriate way forward for MHD cooling study of avionics packaging after verification and validation. In this chapter, the focus is MHD cooling design via surrogate modeling and optimality coding in MATLAB and the roadmap to build surrogate mod screening design of experiments (DOE) with meta-modeling is seen in Fig. 6.1.

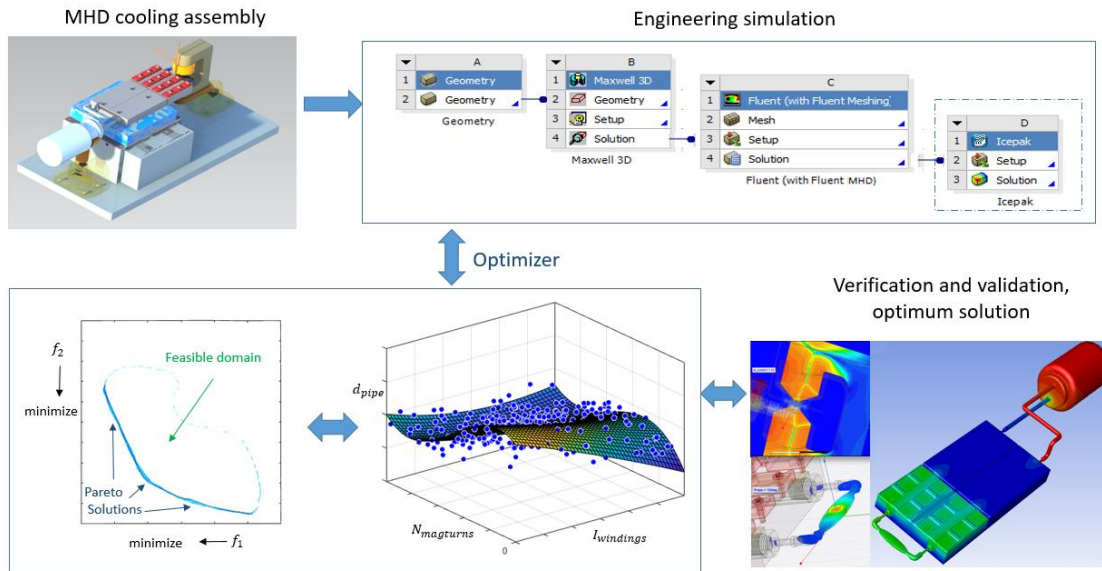


Figure 6.1: Roadmap of AAMO: screening design of experiments (DOE) meta-modeling, verification exploring and exploiting

6.2 Standard Design of MHD Active Cooling Optimization Model

The design of MHD cooling system is a complex process. Assumptions must be made to develop suitable models that can be subjected to mathematical analysis by the available simulation methods and the model must be verified by experiments. This iterative design, analysis and experiment processes implied several trial designs one after another until a satisfactory design is achieved. The time-consuming and painstaking challenge to design any efficient and cost-effective engineering problem without compromising the integrity of the system leads us to optimum design method. To formulate the MHD cooling problem as a multi objective optimization problem, the cost functions are defined that measures the merits of different designs. Then we find an n -vector $x = \{x_1, x_2, \dots, x_n\}$ of design variables to minimize the cost functions or objective functions subject to equality and inequality constraints. The simple bounds of design variables are also included in the inequality constraints (Forrester, 2008). Final design

optimization model of MHD cooling problem is shown as follows and in this chapter we argued in details the formulation of optimality problem to get to final model.

Cost functions

$$\begin{cases} \min f_1 = Temp_{\max} (D_{pipe}, I_{winding}, N_{magturns}) \\ \min f_2 = Gauge_{pressure}(D_{pipe}, I_{winding}, N_{magturns}) \end{cases} \quad (31)$$

Subject to:

- 1). Ohmic loss constraint:

$$.0121 \times I_{winding}^2 \times N_{magturns} + .0001 \leq .22P_d \quad (32)$$

Losses less than 22% of power dissipation of electronics.

- 2). Pressure drop (Bernoulli's principle) constraint and alpha is specified in

MATLAB:

$$\Delta P_{total} \leq \alpha [Pa] \quad (33)$$

- 3). Derating temperature constraint

$$Temp_{\max} \leq 80^\circ C \quad (34)$$

- 4). Geometric constraint of heat sink

$$D_{pipe} \leq .01875 \text{ m} \quad (35)$$

- 5). Weight constraint

$$f(D_{pipe}, N_{magturns}) \leq 2 \text{ kg} \quad (36)$$

And limits of design variables are as followings:

$$D_{pipe} \in [4.7\text{mm}, 10\text{mm}] \quad (37)$$

$$I_{winding} \in [.1\text{Amp}, 7.4\text{Amp}] \quad (38)$$

$$N_{magturns} \in [200, 1200] \quad (39)$$

Details of these equations are elaborated in following section.

6.2.1 Formulation of Optimality Problem

Definition of Design variables: $(D_{pipe}, I_{winding}, N_{magturns})$

A design variable is a numerical input that is allowed to change during the design optimization; the design variables we specify below affect pressure of MHD system and consequently the temperature of cold plate.

D_{pipe} = internal diameter of LM container

$I_{winding}$ = current in Amp applied to the solenoid

$N_{magneticturns}$ = number of mag wire turns for MHD pump (AWG 22 copper wire)

Specified data: Applied power load (heat source), boundary conditions, material properties, geometric dimensions, and manufacturing limitations discussed in previous chapters are intact and applied to optimization problem as well.

Cost functions:

a). In active cooling system, it is desired to minimize temperature of the heat sink block at its highest point (vicinity of power dissipating component interfacing heatsink) $\min f_1 = Temp_{max} (D_{pipe}, I_{winding}, N_{magturns})$

b). similarly our other goal is to reduce gauge pressure of MHD pump

$$\min f_2 = Gauge_Pressue (D_{pipe}, I_{winding}, N_{magturns})$$

Specifying upper and lower bounds of design variables: $D_{pipe}, I_{winding}, N_{magturns}$

1). Continuity equation

In incompressible flow (ρ is constant), the mass continuity equation simplifies to a volume continuity equation, which means that the divergence of velocity field is zero everywhere.

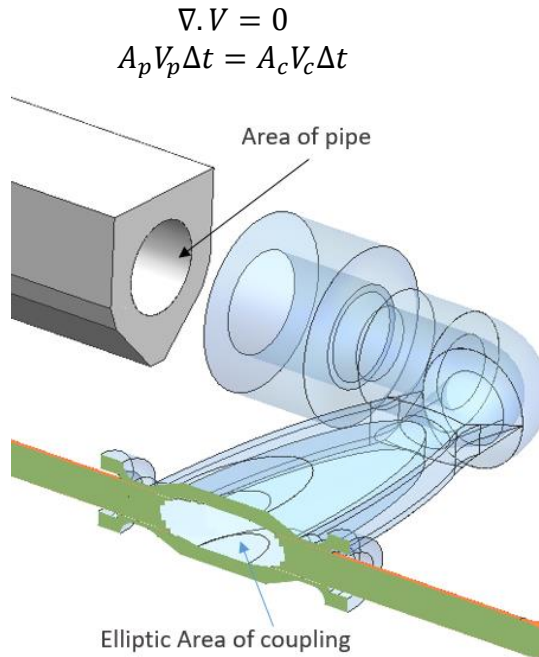


Figure 6.2: Inlet of magnetic flow (area of coupling) vs area of pipe are shown

The hydraulic diameter, D_H , is used to handle the flow in non-circular tubes and channels.

$$D_H = \frac{4A_c}{P_{we}}$$

A_c is the cross-sectional area of the flow.

$$A_c = \pi ab = \pi(3 \times 10) = 94.25$$

P_{we} is the wetted perimeter of the cross-section. (%15 not wetted)

$$P_{we} = .15 \times P_c = .85 \times 43.86 = 37.3$$

$$D_H = \frac{4 \times 94.25}{37.3} \approx 10 \text{ mm}$$

Therefore to optimize the flow (area goes down velocity goes up) the continuity constraint specifies the upper bound of the pipe diameter.

$$D_{pipe} \leq 10 \text{ mm} \quad \text{Upper bound}$$

2). Electromagnetic skin depth (for AC current)

Skin depth is a measure of how current density concentrated at the surface of a conductor carrying an alternating current. Skin depth in meters is defined as follows:

$$\delta = \sqrt{\frac{2}{\omega\mu_r\mu_0\sigma}}$$

Where ω is angular frequency ($2\pi f$), the conductor's conductivity is σ [S/m] and $\mu_0 = 4\pi \times 10^{-7} \frac{H}{m}$ and μ_r are permeability of free space and relative permeability.

In our case (i.e. frequency is 60 Hz, $\mu_r = 60$ and $\sigma = 1.5 \times 10^6$ S/m

$$\delta = .0047 [meter] = 4.7 \text{ mm}$$

To optimize the magnetic flow, the induced current creates an electric field which opposes the change in current intensity should be minimized. This opposing electric field is called “counter-electromotive force” (back EMF), therefore the diameter of the conductive coolant should be greater than skin depth which defines the lower bound of the pipe diameter.

$$D_{pipe} \geq 4.7 \text{ mm Lower bound}$$

3). Limitation of power supplies and electronics equipment i.e. amplifier, signal generator, rectifier and also electrical saturation of electrodes applied to LM, specified the upper and lower bound of current as followings:

$$.1 \text{ Amp} \leq I_{winding} \leq 7.4 \text{ Amp}$$

4). Geometric constraint of C-shaped core defines the maximum number of turns in electromagnetic core. Morphology of electromagnet core is studied in previous chapter and it defines the outer diameter of the winding that shall not exceed 25.4 mm as shown in Fig. 6.3:

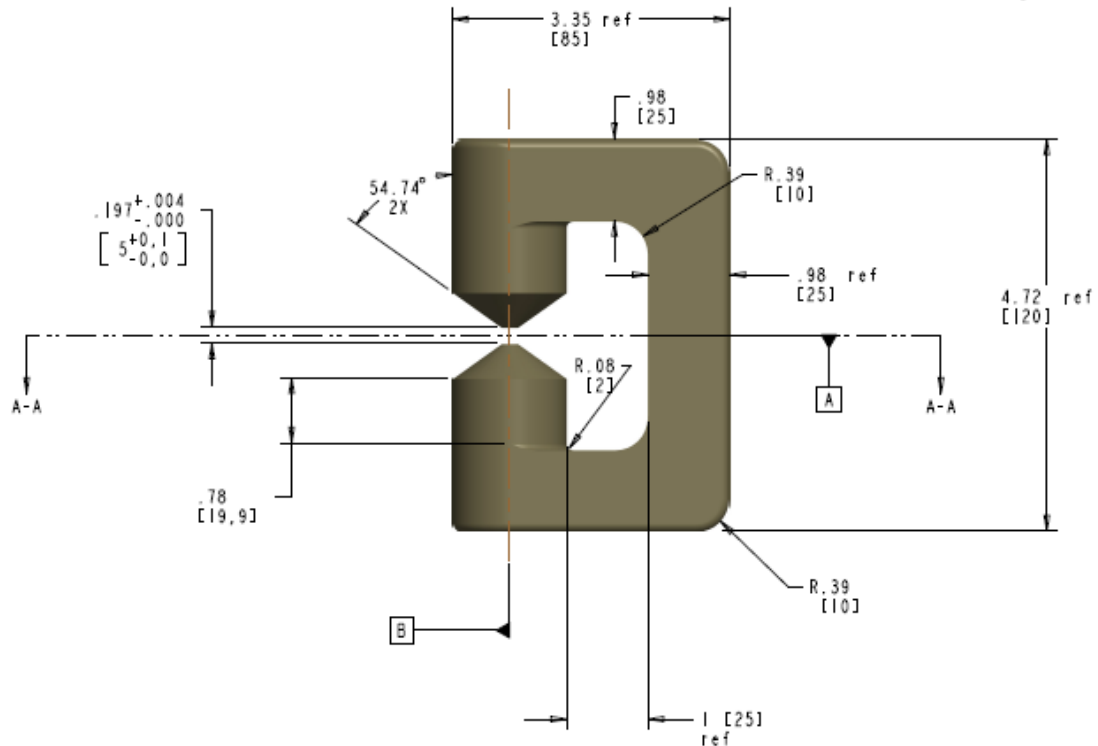


Figure 6.3: Geometric Details of magnetic core

A gauge 22 AWG magnetic wire is selected to handle maximum current applied to coils. See Table 6.1.

Table 6.1

Characteristics of Gauge 22 Magnetic Copper Wire, Computed Based on 100% IACS Conductivity of 58.0 MS/m and at 68 °F

AWG	Diameter		Turns of wire, without insulation		Area		Resistance/length	
	(in)	(mm)	(per in)	(per cm)	(kcmil)	(mm ²)	(mΩ/m)	(mΩ/ft)
22	0.0253	0.644	39.5	15.5	0.642	0.326	52.96	16.14

Therefore, maximum number of turns for each horizontal layer is $25.4/0.644 \approx 40$ [turns/layer] and maximum number of turns in vertical direction is $19.9/0.644 \approx 30$ [turns along axis], average radius of the winding ($r_{average}$) $\approx (35+25.4)/2=60.4/2= 30.2$ [mm] and maximum allowable length of winding wire = average circumference of the winding

multiply by total number of turns = $2\pi rN = 60.4 \times 1200\pi = 227$ [meter] therefore maximum allowable number of turns “N” is as following:

$$\text{number of mag wire turns} \leq 1200$$

The lower bound of the number of turns for magnetic wire is determined from the specification of electronic equipment (i.e. for AC current the amplifier used to excite the core).

Lowest copper wire resistance that amplifier can handle (Amplifier model: Pyle-PDA7BU) is 4 Ohms (2 ohms for each winding). Therefore, the average length of the copper wire can be calculated from the following formula

$$R = \rho \frac{L}{A}$$

The resistivity of pure copper is $1.7 \times 10^{-8} \Omega m$

$$L_{\min} = \frac{R \cdot A}{\rho} = \frac{2 \times 326 \times 10^{-6}}{1.7 \times 10^{-8}} = 38 \text{ m}$$

Minimum number of winding is approximated as following:

$$\text{min \# of mag wire turns} = \frac{L_{\min}}{2\pi r} = \frac{38}{60.4 \times 10^{-3} \times \pi} \approx 200$$

Therefore:

$$200 \leq N_{\text{magturns}} \leq 1200$$

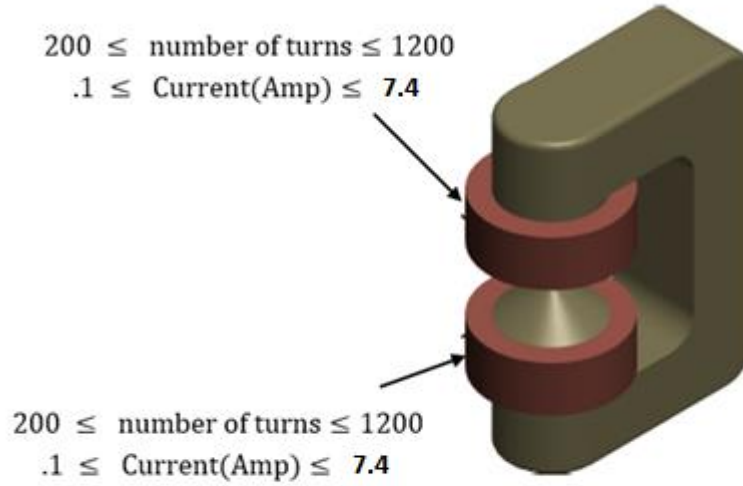


Figure 6.4: Electromagnet core including two coils, showing limits of design variables

6.2.2 Constraints

1. Power loss constraint

The solenoid of MHD pump is modeled as a resistor and an inductor in series with a phase shift in the circuit due to AC current. The effect of inductor loss is trivial for low frequency application and the ohmic loss ($I_{rms}^2 \cdot R_{DC}$) specifies the first constraint for optimization problem as following.

$$\begin{aligned}
 \text{Ohmic loss of solenoid} &= I_{rms}^2 \cdot R_{DC} = I_{winding}^2 \cdot \rho_{ref} \frac{l_w}{A_w} \cdot \langle 1 + \sigma \Delta T \rangle \\
 \text{Ohmic loss of solenoid} &= \rho_{ref} \frac{\langle 1 + \sigma \Delta T \rangle}{A_w} \cdot I_{winding}^2 \cdot l_w \\
 &= \rho_{ref} \frac{\langle 1 + \sigma \Delta T \rangle}{A_w} \cdot I_{winding}^2 \cdot 2\pi r_{average} \cdot N_{mag_turns}
 \end{aligned}$$

Where

$$\begin{aligned}
 A_w &= .326 \text{ mm}^2, \sigma = 0.003862, \rho_{copper@25^\circ\text{C}} = \rho_{ref} = 1.68 \times 10^{-8} \Omega\text{m} \\
 R_{DC} &= R_{ref} \langle 1 + \sigma \Delta T \rangle
 \end{aligned}$$

$$\text{Ohmic loss of electrode} = I_{\text{electrode}}^2 \cdot R_{\text{DC_electrode}} = I_{\text{electrode}}^2 \cdot \frac{1}{A_e} [\rho_{\text{ref}} l_e \langle 1 + \sigma_e \Delta T \rangle +$$

$$\rho_{\text{galinstan}} l_{\text{galinstan}} \langle 1 + \sigma_{\text{galinstan}} \Delta T \rangle] = .1 \text{ mW}$$

$$A_e = A_{\text{galinstan}} = \frac{\pi}{4} d_e^2 = 4.3 \text{ mm}^2$$

$$l_e = 25.4 \text{ [mm]}, I_{\text{electrode}} = .17 \text{ Amp}$$

$$\text{Total Ohmic loss} = \rho_{\text{ref}} \frac{\langle 1 + \sigma \Delta T \rangle}{A_w} \cdot I_{\text{winding}}^2 \cdot l_w + .0001$$

$$= \rho_{\text{ref}} \frac{\langle 1 + \sigma \Delta T \rangle}{A_w} \cdot I_{\text{winding}}^2 \cdot 2\pi r_{\text{average}} \cdot N_{\text{magturns}} + .0001$$

$$\text{Total Ohmic loss} = \rho_{\text{ref}} \frac{\langle 1 + \sigma \Delta T \rangle}{A_w} \cdot I_{\text{winding}}^2 \cdot l_w + .0001$$

$$= \rho_{\text{ref}} \frac{\langle 1 + \sigma \Delta T \rangle}{A_w} \cdot I_{\text{winding}}^2 \cdot 2\pi r_{\text{average}} \cdot N_{\text{magturns}} + .0001$$

Assume total ohmic loss to be less than 22% of power dissipation of heat source:

$$\text{Total Ohmic loss} \leq .22 \times P_{\text{dissipation_of_component}} \leq 73 \text{ watts}$$

Therefore, the ohmic loss constraint will be as following:

$$\rho_{\text{ref}} \frac{\langle 1 + \sigma \Delta T \rangle}{A_w} \cdot I_{\text{winding}}^2 \cdot 2\pi r_{\text{average}} \cdot N_{\text{magturns}} + .0001 \leq 73 \text{ watts}$$

Constraint #1: Ohmic loss constraint

$$.0121 \times I_{\text{winding}}^2 \times N_{\text{magturns}} + .0001 \leq 73 \text{ watts}$$

Note: inductor loss is trivial and it related to winding loss due to AC current and core loss – Hysteresis loss ($\text{hysteresis loss} \propto f \cdot B_m^\alpha$) & Eddy current loss ($\text{Eddy current loss} \propto f^2 \cdot B_m^2$). Modified Steinmetz equation (MSE) estimates hysteresis and eddy current losses due to AC flux in the core as following but its trivial effect is negligible.

$$\text{MSE: } (P_v = K_1 \cdot f^\alpha_{\text{eq}} \cdot \Delta B^\beta \cdot f)$$

2. Pressure loss constraint

The total pressure loss includes the followings:

2-1. Loss in fluid pressure between two points along a straight line, level and uniform duct, in which the flow is incompressible and fully developed, can be calculated by the Darcy-Weisbach formula:

$$\text{Laminar flow: } \Delta P_{\text{pipe}} = \frac{\rho U^2}{2} \frac{fL}{D_h}$$

ρ density of liquid metal

ν kinematic viscosity

f friction factor = $F\left(\text{cross section}, \frac{UD}{\nu}, \frac{\varepsilon}{D}\right)$, and for laminar flow $f = \frac{k}{Re}$, $k = 1.20 + \frac{38}{Re}$

L length of the container.

U Velocity of LM.

2-2. Pressure loss due to localized bends and fitting losses is as follows:

$$\Delta P_{\text{bend}} = \frac{\rho U^2}{2} \sum_{n=1}^n K_n$$

K hydraulic pressure loss is shown in Table 6.2 (Robert D. Blevins, 2008).

Table 6.2

Hydraulic Pressure Loss in Fittings

Fitting	K
Well rounded inlet	0.05
90 ⁰ elbow, threaded	
Regular	1.4
Long radius	0.75
90 ⁰ elbow, flanged	
Regular	0.31
Long radius	0.22
45 ⁰ elbow, threaded, regular	0.35
45 ⁰ elbow, flanged, regular	0.17
Return bend, threaded, regular	1.5
Return bend, flanged	
Regular	0.3
Long radius	0.2
T-joint, threaded	
Through flow	0.9
Branch flow	1.9
T-joint, flanged	
Through flow	0.14
Branch flow	0.69
Sudden expansion	
d ₁ /d ₂ = 0.5	0.75
d ₁ /d ₂ = 0.7	0.51
d ₁ /d ₂ = 0.9	0.19
Sudden contraction	
d ₂ /d ₁ = 0.5	0.3
d ₂ /d ₁ = 0.7	0.2
d ₂ /d ₁ = 0.9	0.1

Therefore, total pressure loss is calculated as:

$$\Delta P_{total} = \Delta P_{pipe} + \Delta P_{bend} = \frac{\rho U^2}{2} \frac{fL}{D_{pipe}} + \frac{\rho U^2}{2} \sum_{n=1}^n K_n$$

Constraint #2: Bernoulli's principle (pressure drop)

Bernoulli's principle states that an increase in fluid velocity occurs simultaneously with a decrease in static pressure or a decrease in potential energy of fluid. If we assume velocity of the LM should be greater or equal 5 mm/s then the maximum pressure drop shall not exceed .2681Pa (alpha value in following formula).

$$\Delta P_{total} = \frac{\rho U^2 f L}{2 D_h}$$

$$\Delta P_{total} \leq \alpha [Pa]$$

3. Maximum Temperature constraint

Heat source used in this experiment is surface mount resistor, model number MP9000 series Kool-Pak from Caddock Electronics Inc and its derating temperature curve is as shown in Fig. 6.5.

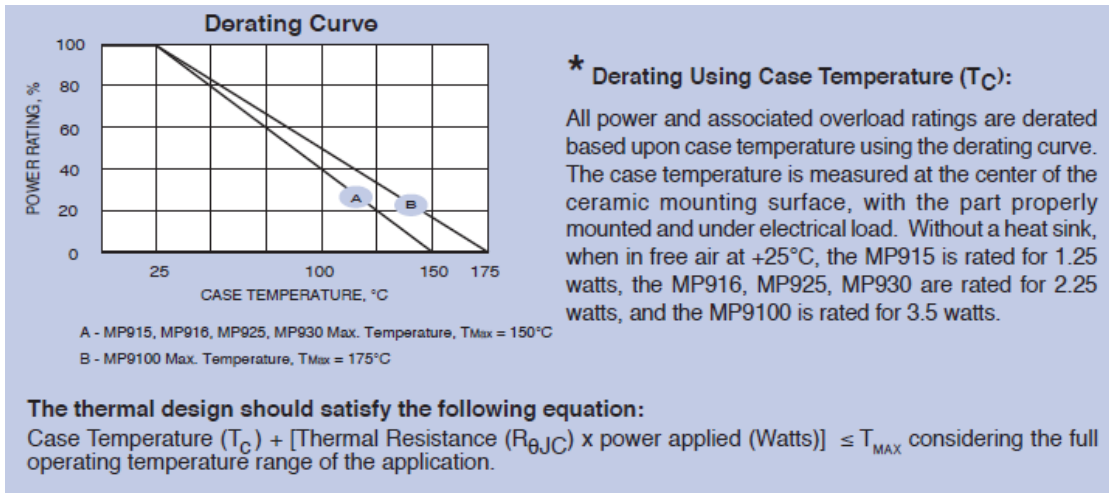


Figure 6.5: Derating temperature for curve resistor MP9000 Series Kool-Pak from Caddock electronics Inc.

According to EEE-INST-002 max temperature derating shall be 75% of the maximum rated case temperature specified by the manufacturer or 80 °C, whichever is lower. Consequently, this criterion defines the next optimization constraint (Derating temperature of electronics) as following:

$$Temp_{max} \leq 80^\circ\text{C}$$

Additionally temperature difference between boundary and hot surface mount shall be less than 75°C .

$$Temp_{max} - T_{BC} \leq 75^\circ\text{C} , s. t. T_{BC} = 10^\circ\text{C}$$

Therefore the constraint to satisfy both limitation shall be:

$$Temp_{max} \leq 80^{\circ}C$$

Note: Thermal chamber shall be capable of operating during a temperature change rate of 3 °C/Min for a rate of change constraint (if applicable).

4. Geometric constraint

The cold plate including LM compatible pipes is seen in Fig. 6.6.

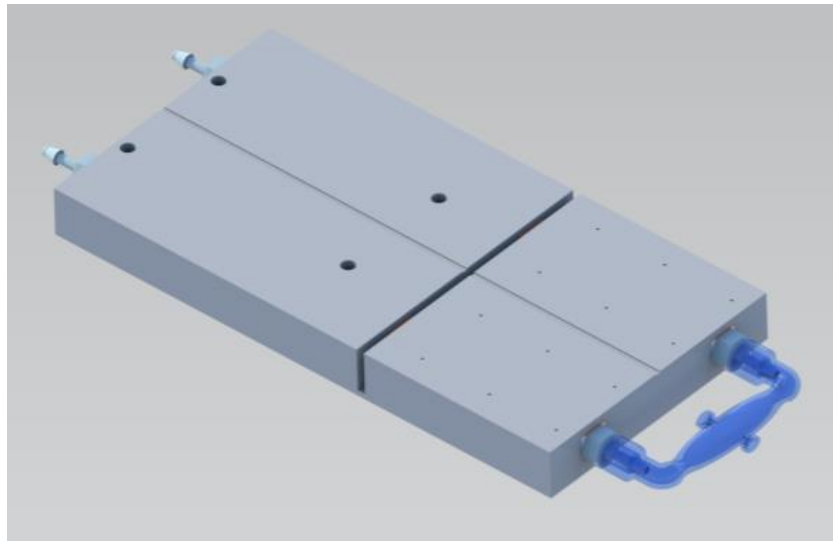


Figure 6.6: Isometric view of geometrically optimized cold plate with embedded ceramic pipes, the gap between pipes is influenced by length of elliptic coupling defined by magnetization criterion for elliptic shape.

Geometric constraint of cold plate is a geometry setting, which has a given set of geometric elements and a relationship of geometric constraints between the elements, which could be non-parametric (thickness of the pipe, offset between channels to insert pipe) or parametric (diameter of ceramic pipe). The goal is to find the positions of geometric elements in 2D cross-sectional that satisfy the given constraint. The cold plate devised for mounting CubeSat that is made up of multiples of 10 cm × 10 cm × 10 cm cubic units, therefore maximum allowable width of 100 mm shall be satisfied.

$$2 \times D_{pipe} + 4 \times t_{pipe} + 2 \times dx_{edge} + offset \leq 100 \text{ mm}$$

Where

t_{pipe} , thickness of the ceramic pipe due to manufacturing limitation is 2 [mm].

dx_{edge} , distance of the cutout for BN pipe to the edge of block is assumed $2.25 \times D_{pipe}$

and *offset* is the middle gap between the cutout for insertion of ceramic pipes.

The offset is calculated based on the demagnetization criterion in the core and major radius of elliptic coupling and can be expressed by demagnetization factor N. The demagnetizing field $H_d = N.M$ deteriorate the apparent permeability of the specimen and it should be minimized for an optimal design. Prozorov et al have studied the approximate effective demagnetizing factor along applied magnetic field and it is extracted from Fig. 6.7 (courtesy of Prozorov et al).

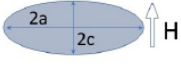
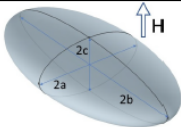
Shape	Geometry	Demagnetizing factor along applied field
Strip, elliptical		$N^{-1} = 1 + \frac{c}{a}$
Ellipsoid (exact)		$N = \frac{1}{2} \frac{b}{a} \frac{c}{a} \int_0^{\infty} \frac{ds}{(s + \frac{c^2}{a^2}) \sqrt{(s+1) (s + \frac{b^2}{a^2}) (s + \frac{c^2}{a^2})}}$

Figure 6.7: Demagnetizing factor along applied field for elliptic shape

Value of minor diameter of the ellipsoid is equal to the gap between the troncoconical pole tips. See Fig. 6.8.

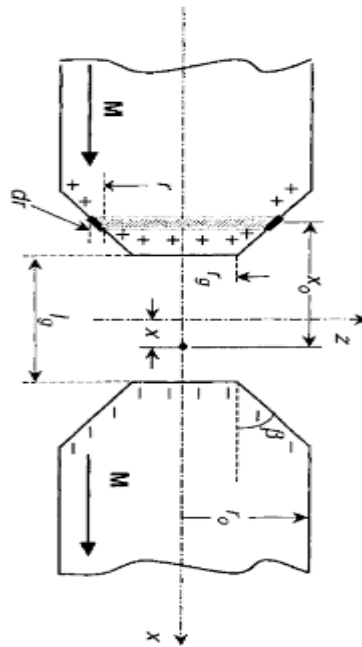


Figure 6.8: Field generation in the gap of permanent magnet polar pieces with troncoconical pole tips. For given radius r of the flat pole faces, the maximum axial field is obtained with a taper angle $\beta = 54.74^\circ$. Since the free charges at the opposing gap surfaces have opposite signs, their fields add within the gap and subtract within the material. The flux lines are back-closed by a soft magnetic yoke. (courtesy of Fausto Fiorillo).

The magnetic poles need to be as close as possible to maximize magnetic field between the poles, however SLS manufacturing limitation to fabricate the elliptic nylon coupling that goes between the tips of electromagnet to carry LM, and also enough cross sectional area for passage of LM open up the gap to be 5 mm. On the other hand demagnetizing factor depends on the ration of major diameter (length) to minor diameter as seen in Fig. 6.9.

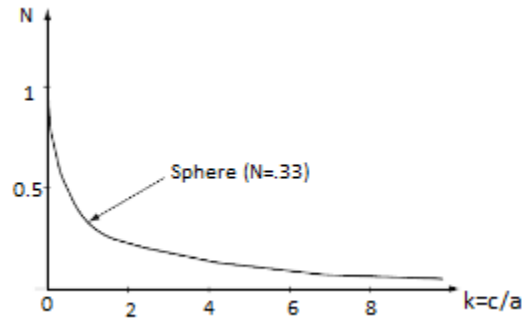


Figure 6.9: Dependence of the demagnetizing factor of ellipsoid on its shape factor c/a (length to diameter ratio)

The larger the ratio of major diameter to minor diameter of ellipsoid (b/c), the smaller the demagnetizing factor N , therefore the greater the external magnetic field applied to LM. Dimension of optimal elliptic coupling is seen in Fig. 6.10.

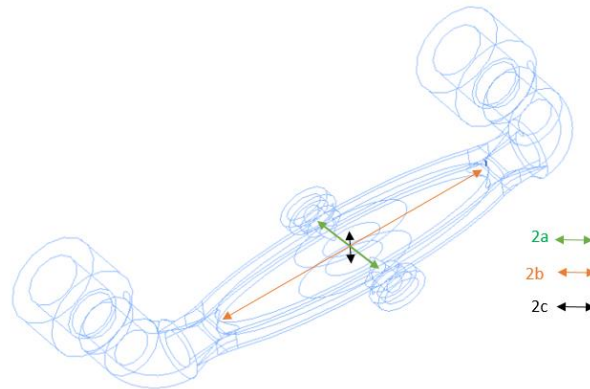


Figure 6.10: Optimal shape for magnetic MHD pump coupling, to reduce demagnetization effect, $a=5\text{mm}$, $b=20\text{mm}$, $c=lg=2.5\text{mm}$, magnetic field is in line with 'c' dimension, perpendicular to 'b' and 'a'

Therefore, the offset between the grooves in cold plate is a function of "b" major diameter of the elliptic coupling and it is fixed to 49.5 mm.

$$2 \times D_{pipe} + 4 \times t_{pipe} + 2 \times dx_{edge} + offset \leq .1 \text{ m}$$

$$2 \times D_{pipe} + 4 \times .002 + 2 \times .0025 + .0495 \leq .1 \text{ m}$$

5. Weight constraint

The weight of the C-shaped magnetic core made out of hiperco50A is fixed, but the weight of the solenoids and cold plate vary. The former is related to the diameter of magnetic wire and the latter to the diameter of ceramic pipe and we assumed the total mass to be less than 2 kilograms.

$$\text{mass of heat sink} + \text{mass of solenoids} \leq 2 \text{ kg}$$

$$\begin{aligned} \text{mass of solenoid} &= 2\pi r_{\text{average}} \times N_{\text{magturns}} \times A_w \times \rho_{\text{cu}} \\ &= 2 \times \pi \times .0302 \times .326 \times 10^{-6} \times 8960 \times N_{\text{magturns}} \\ \text{mass of solenoid [kg]} &= 5.54 \times 10^{-4} N_{\text{magturns}} \end{aligned}$$

Now mass of cold plate is as following:

$$\text{mass of cold plate} = \text{mass of metallic block} - \text{mass of LM containers}$$

mass of metallic block

$$\begin{aligned} &= \rho_{\text{Al}} * (\text{height_block} * \text{Width_block} - 2 * (A_{\text{rectangle}} + A_{\text{triangle}})) \\ &* L_{\text{pipe}} \end{aligned}$$

mass of metallic block

$$\begin{aligned} &= \rho_{\text{Al}} * ([2 \times D_{\text{pipe}} + t_{\text{plating}} + 2 \times \text{dist}_{\text{wall}}] \times [2 \times D_{\text{pipe}} + 4 \times t_{\text{pipe}} \\ &+ 2 \times dx_{\text{edge}} + \text{offset}] - 2 \times (A_{\text{rectangle}} + A_{\text{triangle}})) * L_{\text{pipe}} \end{aligned}$$

mass of metallic block

$$\begin{aligned} &= \rho_{\text{Al}} \times L_{\text{pipe}} \\ &\times \{ [2 \times D_{\text{pipe}} + t_{\text{plating}} + 2 \times dy_{\text{edge}}] \\ &\times [2 \times D_{\text{pipe}} + 4 \times t_{\text{pipe}} + 2 \times dx_{\text{edge}} + \text{offset}] \\ &- 2 \times \{ [(2 \times t_{\text{pipe}} + D_{\text{pipe}}) \times (D_{\text{pipe}} + .001)] + [A_{\text{triangle}}] \} \} \end{aligned}$$

$t_{\text{pipe}} = .002$ [m] manufacturing limitation for minimum wall thickness of ceramic

$t_{\text{plating}} = .001$ [m] identical to thickness of gage 20 copper and silver sheet

$dy_{\text{edge}} = .0025$ [m] assumed minimum wall to the edge

$$dx_{edge} = 2.25 \times D_{pipe} \text{ assumed distance to prevent crack propagation}$$

$$edge_{triangle} = D_{pipe} + .001 \text{ meter}$$

$$base_{triangle} = 2 \times t_{pipe} + D_{pipe} \text{ meter}$$

$$s = (2 \times edge_{triangle} + base_{triangle})/2$$

$$A_{triangle} = \sqrt{s(s-a)(s-b)(s-c)} \text{ Heron's formula for area of triangle}$$

$$A_{triangle} = \sqrt{\frac{1}{2} \times [2 \times (D_{pipe} + .001) + (2 \times t_{pipe} + D_{pipe})] \times \frac{1}{2} \times [2 \times t_{pipe} + D_{pipe}] \times \frac{1}{2} \times [2 \times t_{pipe} + D_{pipe}] \times [D_{pipe} + .001]}$$

$$A_{triangle} = \sqrt{\frac{1}{8} \times [2 \times (D_{pipe} + .001) + (2 \times t_{pipe} + D_{pipe})] \times [2 \times t_{pipe} + D_{pipe}] \times [2 \times t_{pipe} + D_{pipe}] \times [D_{pipe} + .001]}$$

$$A_{triangle} = \frac{(2 \times t_{pipe} + D_{pipe})}{2} \sqrt{\frac{1}{2} \times (D_{pipe} + .001) \times [2 \times (D_{pipe} + .001) + (2 \times t_{pipe} + D_{pipe})]}$$

After insertion of $A_{triangle}$ to the mass of metallic block, then

mass of metallic block

$$= \rho_{Al} \times L_{pipe}$$

$$\times \left\{ [2 \times D_{pipe} + t_{plating} + 2 \times dy_{edge}] \times [2 \times D_{pipe} + 4 \times t_{pipe} + 2 \times dx_{edge} + offset] - 2 \times [(2 \times t_{pipe} + D_{pipe}) \times (D_{pipe} + .001)] + \left[\frac{(2 \times t_{pipe} + D_{pipe})}{2} \sqrt{\frac{1}{2} \times (D_{pipe} + .001) \times [2 \times (D_{pipe} + .001) + (2 \times t_{pipe} + D_{pipe})]} \right] \right\}$$

Total mass of metallic block and solenoids should be less than 2 kilograms; therefore the

weight constraint is defined as following

$$\text{mass of heat sink} + \text{mass of solenoids} \leq 2 \text{ kg}$$

$$\left\{ \rho_{Al} \times L_{pipe} \right. \\
\times \left\{ [2 \times D_{pipe} + t_{plating} + 2 \times dy_{edge}] \times [2 \times D_{pipe} + 4 \times t_{pipe} + 2 \times dx_{edge} + offset] \right. \\
- 2 \\
\times \left. \left. \left[(2 \times t_{pipe} + D_{pipe}) \times (D_{pipe} + .001) \right] \right. \right. \\
+ \left. \left. \left[\frac{(2 \times t_{pipe} + D_{pipe})}{2} \sqrt{\frac{1}{2} \times (D_{pipe} + .001) \times [2 \times (D_{pipe} + .001) + (2 \times t_{pipe} + D_{pipe})]} \right] \right\} \\
+ 5.54 \times 10^{-4} N_{magturns} \left. \right\} \leq 2 \text{ kg}$$

The above equation specified the fifth constraint for optimization problem.

Constraint #5: mass constraint

$$\text{Mass constraint: } f(D_{pipe}, N_{magturns}) \leq 2 \text{ kg}$$

In conclusion, we defined two objective functions, 5 constraints, 3 design variables and specified data for active cooling system with MHD pumping and we can use surrogate modeling to approximate the optimal solution in next session.

6.3 Surrogate Modeling and Approximation-Assisted Multiple Objective (AAMO) of MHD Cooling System

Surrogate models have been shown to be effective approaches in developing fast models that represent the characteristics of computationally expensive and complex systems. The basic idea in the surrogate model approach is to avoid the temptation to invest one's computational budget in answering the question at hand, and instead, invest in developing fast mathematical approximation to the long running simulation codes

(Forrester et al, 2008). Two key requirements here: (1) a significant increase in speed of use (2) useful accuracy.

Numerous methods exist to generate optimized surrogate models, each with their relative merits. Examples include: rational functions, Kriging models, Artificial Neural Networks (ANN), spline, and Support Vector Machines (SVM) (Forrester 2009; Duvigneau, 2015; Azarm et al, 2012; Miam, 2011; Wu & Azarm , 2001). We applied Forrester’s surrogate model to our optimization problem, and Fig. 6.11 shows the roadmap of constrained multi-objective optimization of the MHD cooling system using approximation assisted approach.

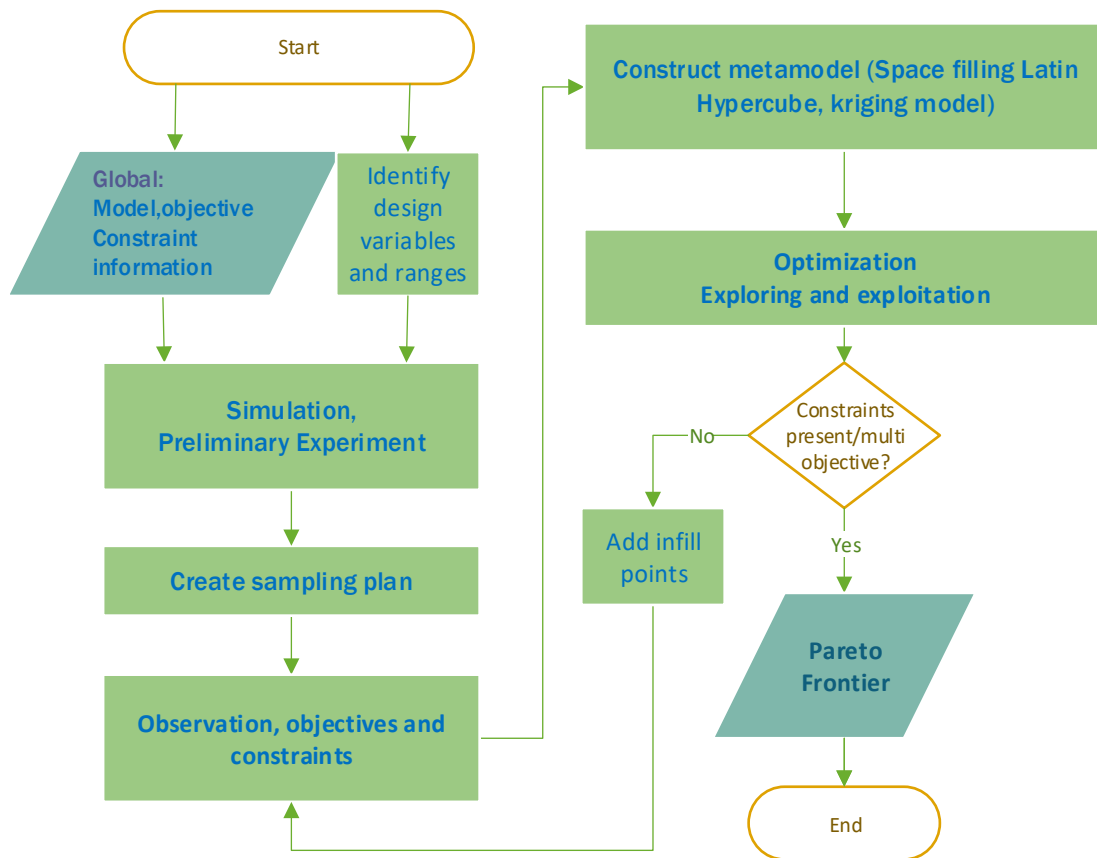


Figure 6.11: Constrained multi-objective optimization of the MHD cooling system using Approximation Assisted Approach

6.3.1 Simulation, Preliminary Experiment

After collecting data to specify the MHD system, then we identify inputs or design variables (x_1, x_2, \dots, x_k) and their ranges that have significant impact on outputs or cost functions. In our case the design variables are diameter of ceramic tube, number of turns of magnetic wire and electric current applied to coils and the outputs are gauge pressure and maximum temperature of cold plate, next step is to recruit n (often small number) of these k -vectors, as it is constrained by the cost associated with obtaining each observations. These steps requires the judgment of observer and they are crucial tasks. As a result, initially for surrogate modeling, a number of possible candidate designs are generated and analyzed, using Ansys simulation workbench, after running several simulations in Ansys Fluent MHD, the pressure objective curve can be fitted using a set of design variables information and minimizing of least square approach.

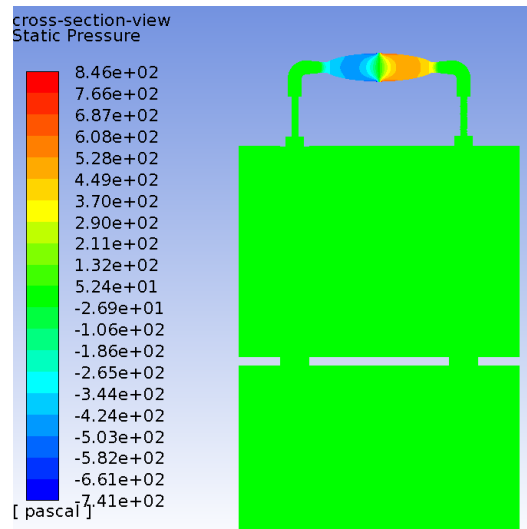


Figure 6.12: Extracted data from Ansys Fluent for first objective of optimization (generated gauge pressure) for $d=6.2\text{mm}$, $I=1.7\text{A}$ and 650 turns for mag wire

Output of MATLAB program for least square approximation of guage pressure is as following:

$$Guage_pressure_{(d_{pipe}, I_{winding}, N_{magwire_turns})} = \frac{8576}{d_{pipe}^2} + .05 \times N_{magwire_turns} \times I_{winding}^2$$

Similarly, to fit second-order Taylor polynomial of other objective (maximum temperature of the metallic heat sink), we use polyfitn MATLAB function to fit extracted points from several Ansys simulation for a set of design variables.

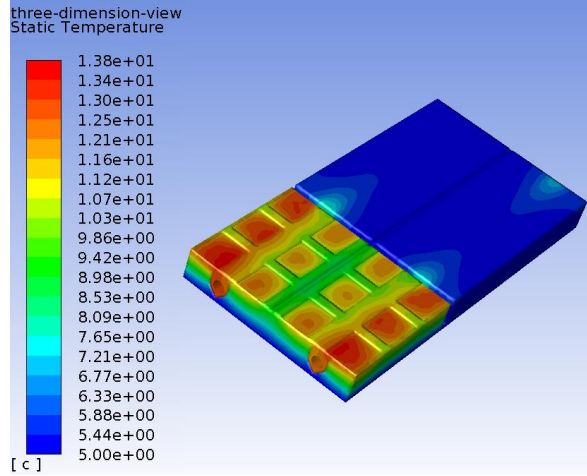


Figure 6.13: Extracted data from Ansys Fluent for Second objective of optimization (maximum temperature of heat sink) for $d=6.2\text{mm}$, $I=1.7\text{A}$ and 650 turns for mag wire

The output of MATLAB program (polyfitn) to generate second-order Taylor series to fit temperature of cold plate as a function of design variables is as following:

$$\begin{aligned} Temperature_{(d_{pipe}, I_{winding}, N_{magwire_turns})} = & 271 + 969465 * D_pipe^2 + \\ & 791 * D_pipe * I_winding + 20 * D_pipe * N_magturns - 27905 * D_pipe - 0.638 * I_winding^2 \\ & + 0.019 * I_winding * N_magturns - 15.09 * I_winding + 7.3916e-05 * N_magturns^2 - \\ & 0.27 * N_magturns; \end{aligned}$$

Note that result of simulations are almost always subject to errors due to the limitations of simulation software. These departures from the ‘true’ result come from three main resources: human error, systematic error and random error which are crucial for the Gaussian process based approximation technique, a deterministic computer code

as realizations of a stochastic process providing output upon which the approximation will be built and discussed in next step (Binois et al, 2016).

6.3.2 Sampling Plan

In optimization, continuous cost functions or performance metric of any system or process defined by a set of design variables i.e. diameter of ceramic tube, electric current applied to coils and number of turns of electromagnet. Beyond continuity, the only insight we can gain into cost function is through discrete samples or observations from simulation and preliminary experiment that we did in previous curve fitting step for MHD cooling system. These are time consuming and therefore must be used carefully. The task is to use these samples from ANSYS simulation complemented by preliminary experimental data to construct approximation cost functions which can be used to make a cheap performance prediction for any design variable from design space in MHD cooling system. Therefore, the goal is to construct a simple “metamodel” of the MHD cooling system that emulates the costly simulations. Sampling plan is very important to generate a well-posed surrogate model at predicting unseen data. In this technique, a systematic technique is used to select the objective function sampling locations for building sampling plans that will enable the surrogate model to be built to generalize well.

A constant level of accuracy throughout the design space requires a uniform spread of points (i.e. rectangular grid of points). A sampling plan possessing this feature is said to be *space-filling* but this is a full factorial sampling technique causes the curse of dimensionality, so it has major flaws. To generate a sampling plan that is stratified on all dimensions “*Latin hypercube sampling*” which is a statistical method for generating a randomizing sample of parameter values from a multidimensional distribution,

normalizing the plan and some measure of uniformity to qualify the points is used (Tang, 1993). One of the most measures to evaluate the uniformity (space-fillingness) of a sampling plan is the maximin metric introduced by Johnson et al. (1990). Morris and Mitchell (1995) defined the scalar-valued criterion function used to rank competing sampling plan in optimization algorithm for pairwise comparisons.

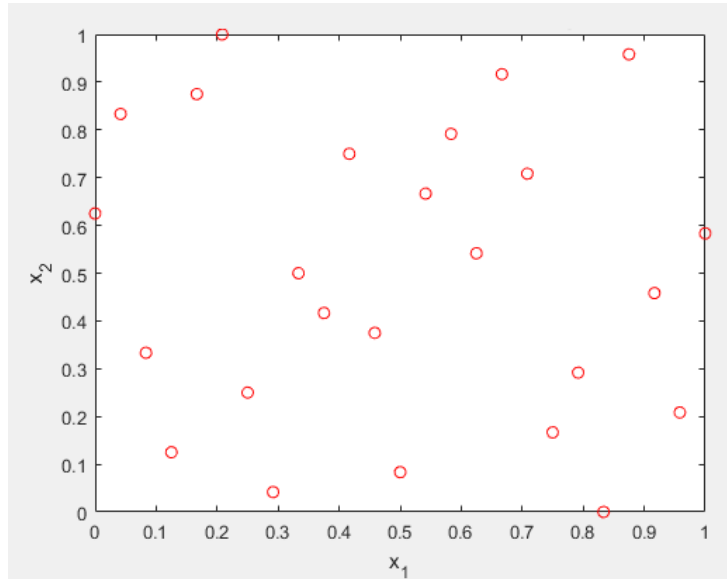


Figure 6.14: Space filling Latin Hypercube Morris-Mitchell optimum sampling plan of MHD cooling, A randomly generated Latin hypercube design (LHD) is structured for MHD cooling model

6.3.3 Infill criteria and optimizing

Following previous step, a suitable form of surrogate model must be selected and fitted to the available data. Since the initial design selections made to produce the first set of data will almost predictably miss certain features of the landscape, the construction of a useful surrogate often requires further, judiciously selected calls to the analysis codes. These additional calls are termed *infill points* and the process of applying them is known as *updating* iteratively. The selection of such points is often made using an optimization-based search over the surrogate and is the hallmark of the knowledgeable designer.

Having established a criterion that we can use to assess the quality of a Latin hypercube sampling plan, we now need a systematic means of optimizing this metric across the space of Latin hypercubes. This is not a trivial task and the challenge is to make sure that the search process always stays within the space of hypercubes, in addition to evolutionary operation (EVOP) algorithm, Morris and Mitchell (1995) use a simulated annealing (SA) algorithm to optimize the space of Latin hypercubes.

6.3.4 Exploring and Exploiting

The optimization methods fall into two categories: local optimizers and global search, also there is another two-way split within this class of search algorithms. Firstly, gradient based optimizers i.e. Newton method and direct search method (global explorer) i.e. genetic algorithm (Jones , 2001). In prediction based exploitation, for multimodel functions where the initial model does not approximate the whole function well, an infill strategy that can search away from the current minimum and explore other regions is required. On the other hand, for error based exploration, calculated error from the gaussian process based model can be used to position infill points. In balanced exploitation and exploration, with the observed data, model parameters, correlation matrix, its Cholesky factorization statistical lower bound can be calculated and this method of storing and passing surrogate model information to infill functions is used. Additionally, for conditional likelihood approaches, goal seeking assess objective function value at a given point such as optimum (if exists), we know the value of objective function and seeking for x for that value. For our study, however, which has more complex objectives and constraint functions the $E[I(x^*)]$ criterion can offer significant improvements over exploitation based infill criteria. $E[I(x^*)]$ is expected

improvement between the observed value (\hat{y}) and value from original data (y) given the mean and variance (Forrester, 2009).

6.3.5 Convergence Criteria

Choosing a suitable convergence criterion to determine when to stop the surrogate infill process is rather subjective. Exploitation (interpolation and finding the smallest value), exploration (global quality of surrogate model), and saturation of infill is objective and balanced of two.

6.3.6 Combining the Concepts for Optimum Latin Hypercube Sampling Process

Having the random hypercube generator as a starting point for the optimization process, the ‘space-fillingness’ metric that we need to optimize, the optimization engine that performs this tasks and the comparison function that selects the best of the optima found for the various candidate’s, all together generate the optimum points. A set of approximation assisted optimization MATLAB programs written by Forrester et al used to optimize MHD cooling program and pareto frontier curve for MHD system seen in Fig. 6.15.

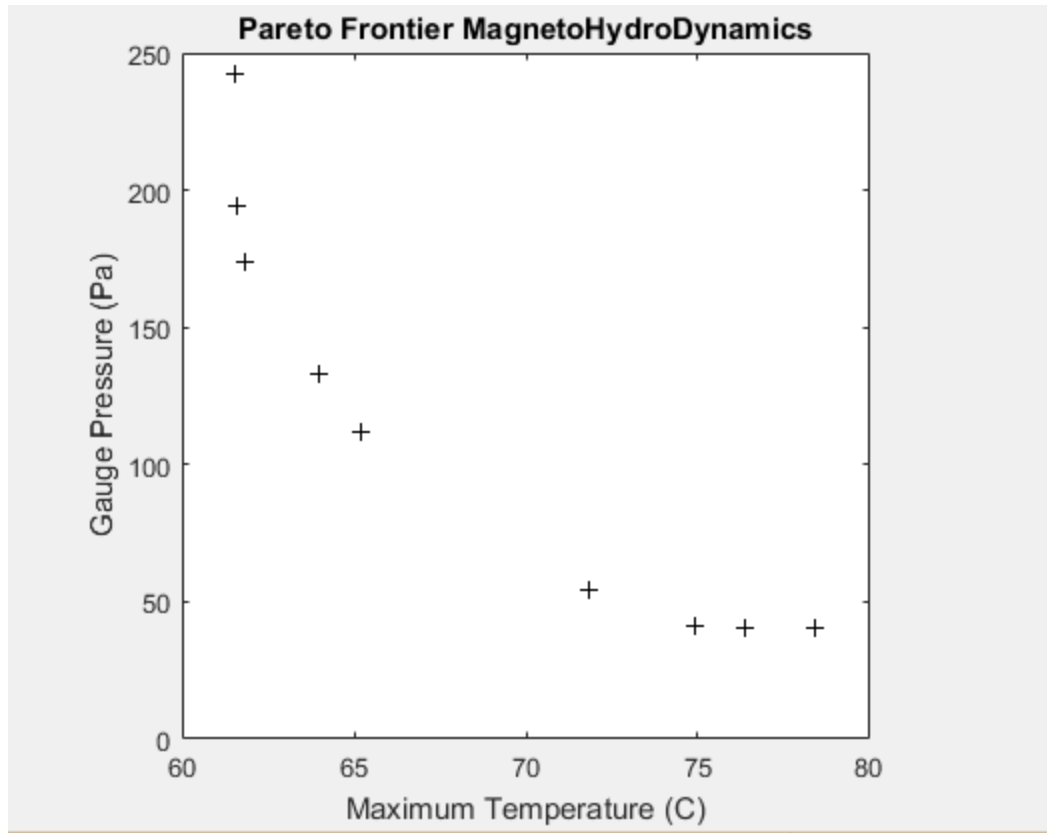


Figure 6.15: Pareto Frontier of MHD cooling extracted from approximation assisted optimization multi objective approach

Fourth-generation Bezier curve fitting technique is used to smooth the curve of generated Pareto frontier from optimum points shown in Fig. 6.16.

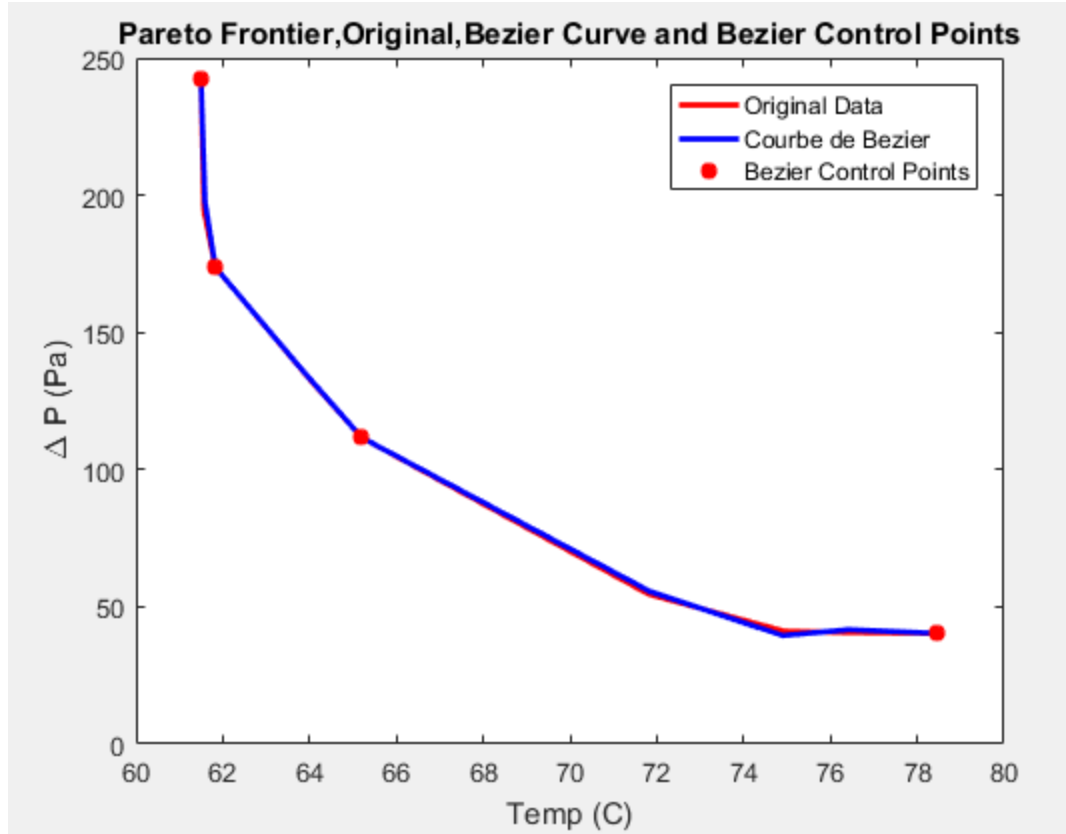


Figure 6.16: Pareto frontier of MHD from Pareto points by 4th generation Bezier smoothing technique

One of the optimal set generated from MATLAB for design variables (output of MATLAB approximation assisted optimization program for MHD cooling) are as following:

D_pipe= 9 mm, I_winding = 3.39 Amp and N_turns (number of winding turns) =201

6.4 Optimal Model Verification and Validation

To test the approximation assisted optimization surrogate model, we simply take a set of test data and a set of predictions at the locations of the test data and calculate root mean squared error and error naturally should be as small as possible as the number of test samples increases. For this purpose, we use Kriging or Gaussian process regression, a

method of interpolation for which the interpolated values are modeled by a Gaussian process governed by prior covariance built in MATLAB program.

To verify the optimality values of objective functions, the optimized values of design variables (pipe diameter, number of turns of magnetic wires and electric current applied to coils) extracted from MATLAB program is used to modify the CAD model and run the simulation in Ansys workbench. Post processing results are seen in Figs. 6.17 and 6.18.

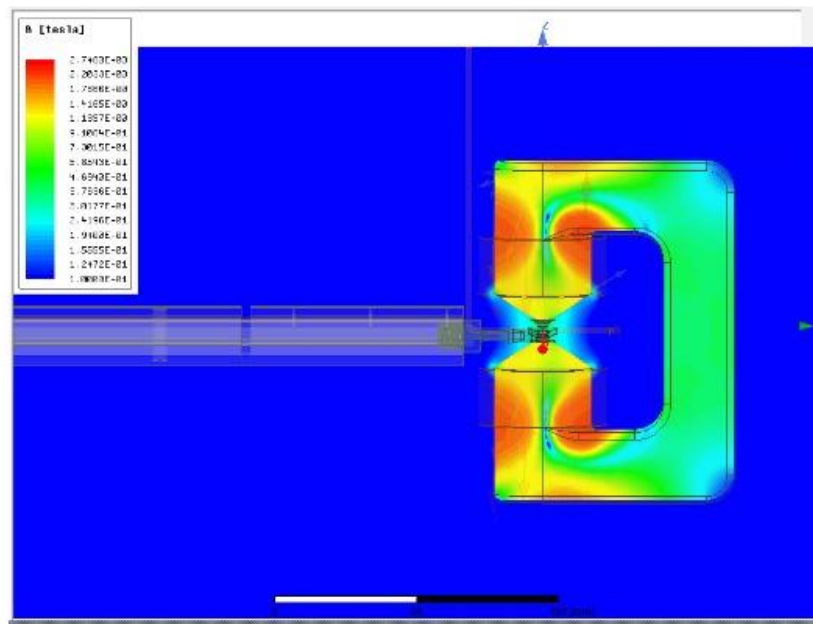


Figure 6.17: Ansys Maxwell simulation for verification per optimal surrogate model (magnetic field) for 201 turns of magnetic wires and 3.39 Amp applied current.

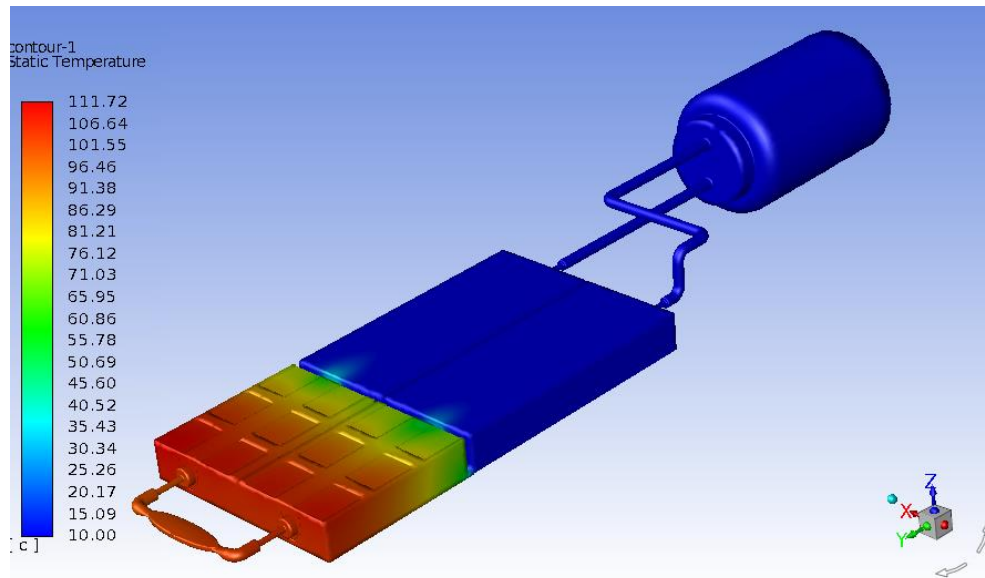


Figure 6.18: Ansys Fluent MHD module simulation for verification per optimal surrogate model (temperature profile) for 201 turns of magnetic wires and 3.39 Amp applied current and 9 mm for internal diameter of ceramic pipe

With larger diameter of the ceramic tube, the flow speed declined and the temperature became slightly higher than the original model as shown below (The highest temperature is around 112 °C). The velocity magnitude, pressure contour and electrical potential of optimal design are shown in Figs. 6.19–6.21.

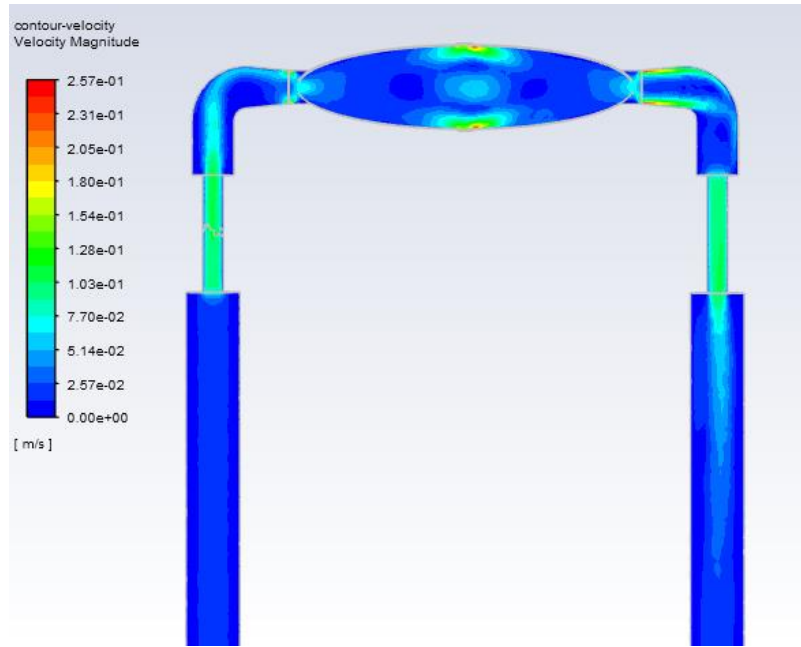


Figure 6.19: Ansys Fluent MHD simulation for verification per optimal surrogate model (velocity profile) for 201 turns of magnetic wires and 3.39 Amp applied current and 9 mm for internal diameter of ceramic pipe

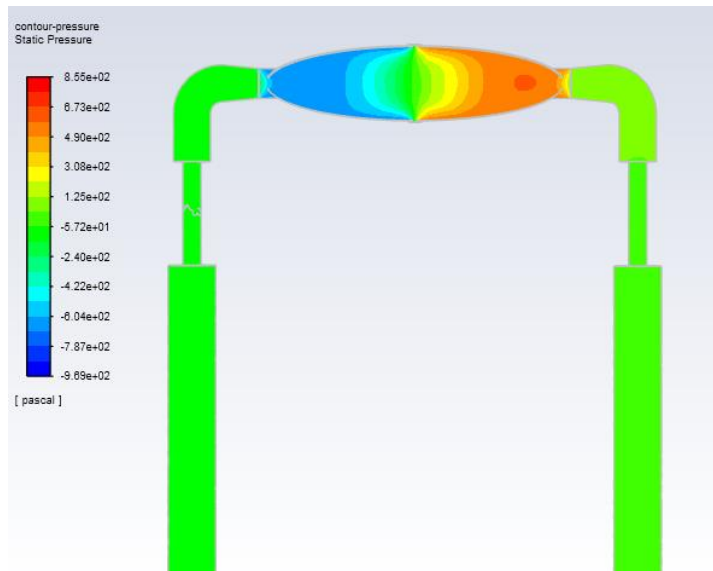


Figure 6.20: Ansys Fluent MHD simulation for verification per optimal surrogate model (pressure profile) for 201 turns of magnetic wires and 3.39 Amp applied current and 9 mm for internal diameter of ceramic pipe

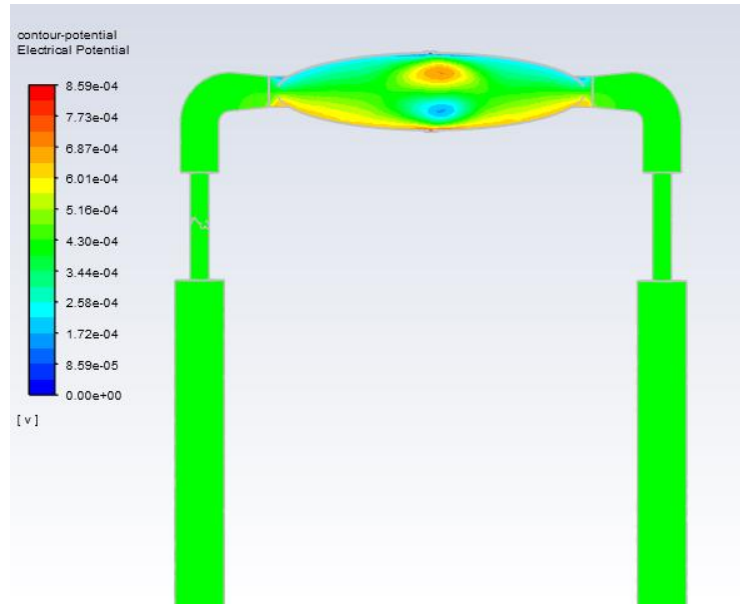


Figure 6.21: Ansys Fluent MHD simulation for verification per optimal surrogate model (electrical potential) for 201 turns of magnetic wires and 3.39 Amp applied current and 9 mm for internal diameter of ceramic pipe

After a thousand iterations, the model was fully converged, as shown in Fig. 6.22.

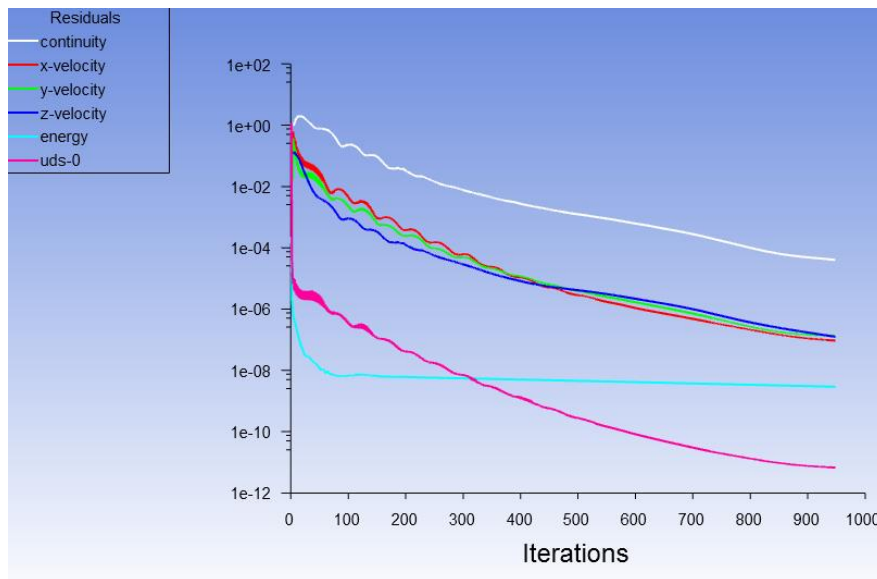


Figure 6.22: Ansys Fluent MHD converged results from inputting optimized variables 201 turns of magnetic wires and 3.39 Amp applied current and 9 mm for internal diameter of ceramic pipe

6.5 Conclusion

The methodology of surrogate model is to learn about mapping of input variables in the form of vector and scalar output values without knowing about the physics that converts vector x into a scalar output y . This technique is used to minimize objective function(s) over the space of all Latin hypercube of a certain size n (number of samples) and dimensionality k (number of design variables). The surrogate model (meta model) technique is applied to MHD cooling case and optimal points for selected design variables generated and verified using Kriging or Gaussian process regression methodologies and objective functions are verified per optimal values in Ansys Fluent MHD (sensitivity analysis). For future work and validity of optimal values through testing, thermal conductivity experiment documented in pervious chapter can be repeated for optimal design variables extracted from approximation assisted optimization program and objectives can be compared to Pareto frontier values through proper procedures for a specific heat test experiment on our active cooling prototypes.

Chapter 7: Mission Context and Assessing Impact of MHD Cooling Technology at Spacecraft System Level

7.1 Introduction

In previous chapter, we asserted the optimality of the MHD cooling prototype through development of surrogate model representation of the system. Optimization involves finding the best solution from a set of feasible solutions (Arora, 2004), and requires using simulation applications i.e. computational fluid dynamics, electromagnetism to evaluate designs and certainly the mathematical effort of solving the optimality problem is the primary challenge. Selecting a system solely based on optimization criteria can be inappropriate, however, in situations when there is insufficient information to formulate an optimal problem or there is no consensus on the objective functions. Therefore, implementing a rigorous decision-making process that requires gathering valued information about the alternatives and uses mathematical model for evaluating them to select the best alternative leads to the perspective of decision-making. The essence of decision making to select from many possible choices has three perspectives: (1) the problem solving perspective (2) the decision-making process perspective, and (3) the decision making system perspective (Herrmann, 2015). In problem solving context, scientific theories are universal statements that applied to suitable model of the problem to rationalize and to master it. That is the methodology implemented in previous chapters, where, we developed avionics cooling prototypes using AM and complemented by MHD from problem solving perspective or subsystems development of smaller scope (e.g., 1D characterization of LM flow and etc.) without sufficient evidence of incorporating into a mission context.

In present chapter, we argue the impact of active cooling techniques developed in this dissertation at a system level and prove to be a benefit through the essence of decision-making criteria. Decision-making involves generating and evaluating alternatives and selecting the most preferred choice that satisfies given requirements (Ravindran et al., 2006). The paradox of choices might create a confusion if a disciplined approach not used to select the appropriate alternative. In this regard, multiple criteria decision making (MCDM) is a technique to show how the “problem of choice” can be addressed by different strategies and to rank many choices that can perform needed functions while satisfying certain requirements. In following section we apply MCDM to thermal cooling systems developed in this dissertation.

7.2 Thermal Management Alternatives Developed in This Dissertation

Through previous chapters, we have developed four thermal management alternatives for avionics cooling using LM as followings:

- 1). Development of metal-ceramic MHD active cooling using geometric complex structures realized through AM (Chapter 5).
- 2). Development of metal-ceramic active cooling using in-situ AM and ceramic tubes with electroplated films and diaphragm pump (Chapter 4).
- 3). Development of metal-ceramic active cooling packaged by conventional assembly technique and diaphragm pump (Chapter 3).
- 4). Development of metal-ceramic passive cooling packaged by conventional assembly technique (Chapter 3).

For validity of evaluation analysis, all alternatives have identical geometry, boundary condition, applied loads and material properties, therefore they can be

practically compared and in present section we go over pros and cons of each thermal management system.

1). Development of metal-ceramic MHD active cooling using geometric complex structures realized through AM

Implementation and characteristics of MHD cooling prototype has been discussed previously and it is seen in Fig. 7.1.

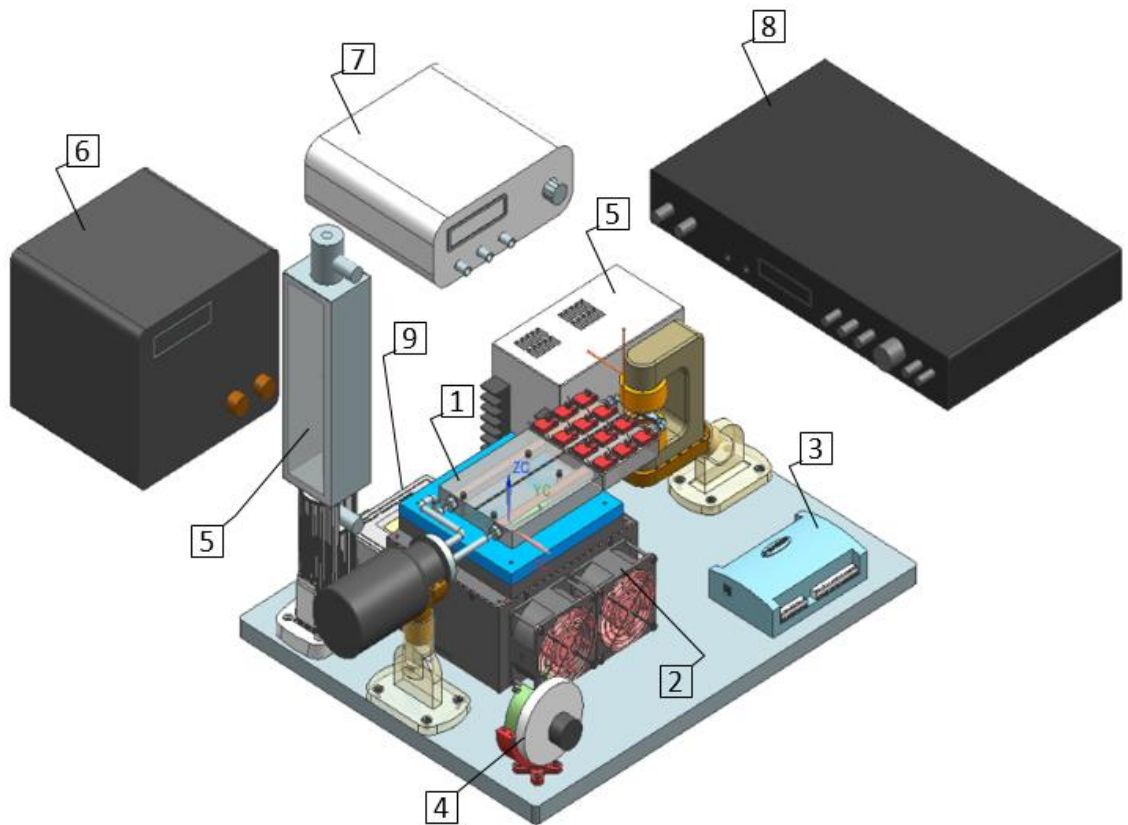


Figure 7.1: Prototype #1: MHD active cooling system including 1) MHD HX including conventionally assembled aluminum alloy block, gauge 20 silver off-the-shelf plate and ceramic pipe 2) Peltier cooler 3) Data acquisition unit 4) Potentiometer 5) flowmeter 6) High voltage power supply 7) AC Signal generator 8) Amplifier 9) Temperature controller

Highlighted attributes of MHD pump used for driving LM coolant are summarized as:

Advantages of MHD pump: (Al-Hababbeh et al , 2016)

- I) It can stand very high temperature, the coolest thing about LM is that, as circumstances get extreme, so does its behaviors.
- II) Simple and compact, mostly the electromagnetic MHD assembly contains electrically conductive liquid, magnetic core of high permeability material, copper winding, electrodes, potentiometer, power supply, amplifier and signal generator.
- III) Silence due to no-moving-parts, therefore it is more reliable since there is no wear and tear caused by friction and movement of components.
- IV). Short transient time since the circuit does not have energy storing elements i.e. inductor and capacitor and reaches to steady state in short period of time.
- V). Minimal maintenance including functional checks, servicing, repairing or replacing of necessary devices, highly suitable for long mission space applications.
- VI). High power density, applicable for cooling of energy transformers and power supplies including batteries, fuel cells, motors etc.
- VII). Scalability and easier fabrication at micro and macro scale.

Disadvantages of MHD pump:

- I). MHD pump is not efficient.
- II). Even though we optimized the electromagnetic core by implementing of tapered tips, due to saturation issues we still need a bulky magnet.
- III). EMI interference and shielding prevents wider use
- IV). Application of governing equations in electromagnetics and fluid mechanics are not a trivial task and cannot be solved analytically and exactly.

V). M-shaped distribution of the fluid velocity profile, back flow at the end of magnetic field and non-homogenous flow under certain operating conditions are major drawbacks.

2). Development of metal-ceramic active cooling using in-situ AM and ceramic tubes with electroplated films and diaphragm pump

The prototype is seen in Fig. 7.2 and the pumping unit in a diaphragm pump with unreliable moving parts consists of diaphragm, suction valve, pumping chamber and delivery valve discussed in chapter 3.

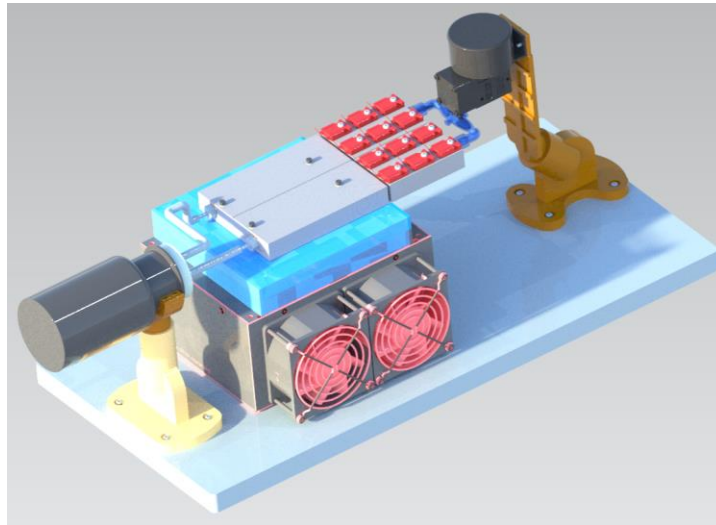


Figure 7.2: Prototype #2: Active cooling prototype including LM compatible diaphragm pump and in-situ hybrid AM cold plate with embedded silver plated ceramic pipes

Highlighted attributes of active cooling pumped by in-situ AM cold plate and diaphragm pump are as follows:

Advantages:

I) Using AM techniques, such as selective laser melting, with prefabricated ceramic tubes, interfacial gaps related to surface roughness and machining tolerances can be reduced through the melting of metal powders around the tubes, resulting in a reduced contact resistance at the metal-ceramic interface.

- II) Diaphragm pumps can handle liquids with high viscosities such as LM. This type of pump can be constructed out of LM compatible materials that can handle pumping high corrosive LMs.
- III) No close fittings or sliding parts are at risk, therefore the pump can operate even when dry without massive damage.
- IV) Highly efficient pump and stable efficiency, there are no rotors, gears, vanes, or pistons, which wear over time and lead to a gradual decline in performance expected of some pumps.
- V) Capable of operating in space application since pitch, roll and yaw movement would not affect the performance of the pump.

Disadvantages:

- I) Reliability issue due to moving parts, these types of pumps tend not to pump very accurately at their bottom end.
- II) Noisy due to moving-parts, wear and tear caused by friction and movement of components.
- III) Sealing issues at inlet and outlet of the pump, the leak can occur between the pump and coolant line and causing corrosion of metallic heat sink.

3). Development of metal-ceramic active cooling packaged by conventional assembly technique and diaphragm pump

For this prototype, cold plate consists of 3-piece metallic block and ceramic pipes fastened together and heat is transferred from the hot component through several thermal interfaces to reach boundary temperature (Peltier cooler), therefore it is not efficient. We have developed the prototype in chapter 3 and its isometric view can be seen in Fig. 7.3.

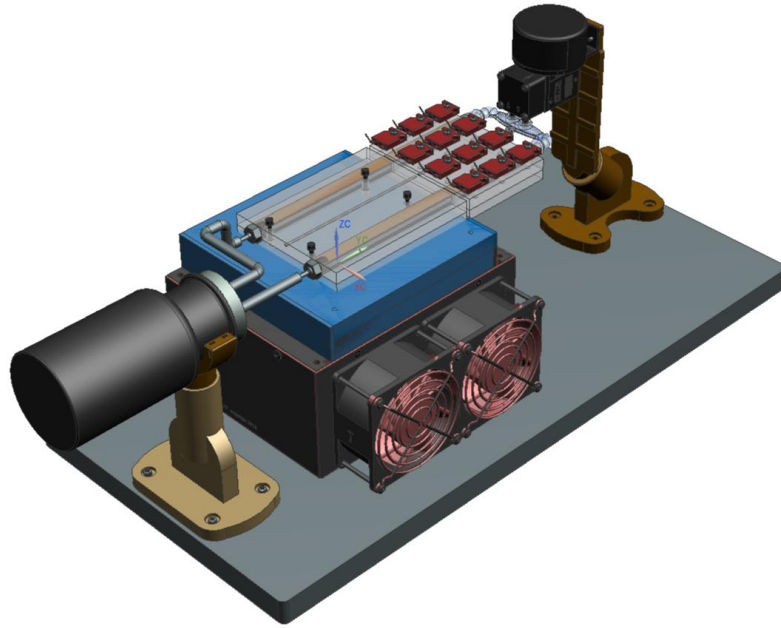


Figure 7.3: Prototype #3: Active cooling by diaphragm pump and conventionally assembled cold plate including 3-piece SLM aluminum alloy block, gauge 20 silver off-the-shelf plate.

4). Development of metal-ceramic passive cooling packaged by conventional assembly technique

Basically, this is prototype #3 with no pumping. Dominant in avionics packaging for low thermal density application due to its simplicity. Heat is transferred through interfaces occurs primarily through conduction, it is cost effective with less complexity but limited in scope. Bulky heat sink will be needed for high power thermal transport.

Passive cooling prototype #4 is seen in Fig. 7.4.

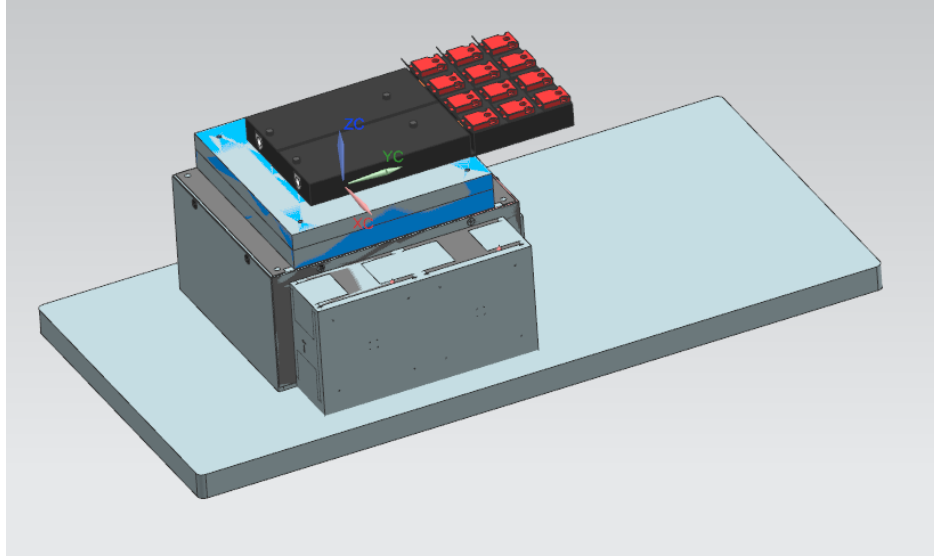


Figure 7.4: Prototype #4: Passive cooling heat source mounted to conventionally assembled cold plate including 3-piece SLM aluminum alloy block, gauge 20 silver off-the-shelf plate, ceramic pipes with LM inside.

7.3 Multiple Criteria Decision Analysis

The alternatives of thermal management for avionics have been discussed in previous section. In this section multicriteria decision making approach is applied to the set of choices to identify the more efficient and more effective cooling systems studied in this dissertation. The analytic hierarchy process (AHP) is a structured technique for organizing and analyzing complex decisions and we applied AHP to thermal management alternatives with selected attributes.

Selecting the best alternative when different objectives conflict is a recurring challenge. It depends on the attributes and the weighs of attributes from decision makers' point of view. In our thermal management system, the attributes of the systems could be simplicity, reliability, CoP of a thermal system (ratio of useful cooling provided to power required), cost of operation, volume of the system etc.

We compare four alternatives of thermal management systems on three different attributes (these numbers are solely based on decision maker's judgment and they are arbitrary numbers):

- Attribute 1 can be cost of operation or maximum temperature of the system (°C) or etc.
- Attribute 2 can be simplicity attribute or required power (watts) to run the system or etc.
- Attribute 3 can be volume or weight (grams) of the system or etc.

The performance of these thermal management systems are given in Table 7.1.

For example, lower value of attribute 1, less value of attribute 2 and lightweight or smaller volume (attribute 3) are ideal scenario.

Table 7.1

The Performances of Four Thermal Management Alternatives Based on Three Attributes (Values Are Arbitrary and Solely Based on Decision Maker's Judgment)

Cooling technology	Attribute 1	Attribute 2	Attribute 3
Prototype #1	55	10	600
Prototype #2	65	1	1200
Prototype #3	75	2	300
Prototype #4	55	10	700

7.3.1 Step 1 of AHP Approach

The following tables show the pairwise comparison matrices for these three attributes. The tables are populated based on the engineering judgment and worthiness of each attributes, for example, the worth of attribute 1 when it is 55 is 2 times the worth of attribute 1 when it is 75.

Table 7.2

Pairwise Comparison of Cooling Technologies Attribute #1

Attribute #1	55	65	75
55	1	1.5	2
65	0.67	1	1.5
75	0.5	0.67	1

MATLAB script for attribute #1 is shown below to calculate the eigen vectors, values, one minus norm_eigenvector (shows relative weights among the compared elements), scale_norm_eigenvector (largest is 1):

```
Attribute1=[1 1.5 2; .67 1 1.5;.5 .67 1];
eig(temp)
[eig_vector , eig_value]=eig(temp)
v=[.7643 .5299 .3674]
v_normed = v / norm(v, 1)
scaled_v=v_normed/.46
landa= 3.0015; %eigenvalue
n= 3; %size of the matrix
CI=(landa-n)/(n-1)
RI_3=.52 % random index
CR=CI/RI_3
```

Then the output of MATLAB program is as followings for eigen related analysis.

Table 7.3

MATLAB Program Output for Eigen Related Analysis Attribute #1

eigen_vector	one minus norm_eigenvector	scale_norm_eigenvector_so_largest_is_one
0.76	0.46	1.00
0.53	0.32	0.69
0.37	0.22	0.48

Eigenvalue=3.0015, consistency ratio is less than .1 so pairwise comparison is sufficiently consistent.

Table 7.4

Pairwise Comparison of Cooling Technologies Attribute #2

Attribute #2	1	2	10
1	1	1.2	9
2	0.83	1	8
10	0.11	0.125	1

MATLAB script for attribute #2 to calculate the eigen vectors, values, one minus norm_eigenvector (shows relative weights among the compared elements), scale_norm_eigenvector (largest is 1):

```
Attribute2=[1 1.2 9;5/6 1 8;1/9 1/8 1];
eig(power)
[eig_vector , eig_value]=eig(power)
v=[.7588 .6461 .0825]
v_normed = v / norm(v, 1)
scaled_v=v_normed/.5102
landa= 3.0005; %eigenvalue
n= 3; %size of the matrix
CI=(landa-n)/(n-1)
RI_3=.52
CR=CI/RI_3
```

Then the output of MATLAB program is as followings for eigen related analysis.

Table 7.5

MATLAB Program Output for Eigen Related Analysis Attribute #2

eigen_vector	one minus norm_eigenvector	scale_norm_eigenvector_so_largest_is_one
0.76	0.51	1.00
0.65	0.43	0.85
0.08	0.06	0.11

Eigen value=3.0005 and consistency ratio is less than .1 so pairwise comparison is sufficiently consistent.

Table 7.6

Pairwise Comparison of Cooling Technologies Attribute #3

Attribute #3	300	600	700	1200
300	1	3	5	9
600	0.33	1	2	9
700	0.2	0.5	1	7
1200	0.1	0.1	0.14	1

MATLAB script for attribute #3 to calculate the eigen vectors, values, one minus norm_eigenvector (shows relative weights among the compared elements),

scale_norm_eigenvector (largest is 1):

```
Attribute 3=[1 3 5 9;.333 1 2 9;.2 .5 1 7;1/9 1/9 1/7 1];
eig(weight)
[eig_vector , eig_value]=eig(weight)
v=[.8874 .3924 .2358 .0548]
one_minus_v_normed = v / norm(v, 1)
scaled_v=one_minus_v_normed/one_minus_v_normed(1)
landa= 4.2109; %eigenvalue
n= 4; %size of the matrix
CI=(landa-n)/(n-1)
RI_4=.89
CR=CI/RI_4
```

Then the output of MATLAB program is as followings for eigen related analysis.

Table 7.7

MATLAB Program Output for Eigen Related Analysis Attribute #3

eigen_vector	one minus norm_eigenvector	scale_norm_eigenvector_so_largest_is_one
0.89	0.57	1.00
0.39	0.25	0.44
0.24	0.15	0.27
0.05	0.03	0.06

Eigen value =4.2109 and consistency ratio is less than .1 so pairwise comparison is sufficiently consistent.

7.3.2 Step 2 of AHP Approach

To compare the attributes, three hypothetical alternatives are compared: H1, H2, H3, i.e. H1 has superior performance on attribute #1(its score is equal to 1) but it is worthless on the other two attributes (scores are zero).

Table 7.8

Hypothetical Alternatives

Hypothetical alternative	score on attribute 1	score on attribute 2	score on attribute 3
H1	1	0	0
H2	0	1	0
H3	0	0	1

Table 7.9 shows pairwise comparison including the decision maker’s assessments of the relative worth of three hypothetical alternatives.

Table 7.9

Pairwise Comparison of the Hypothetical Alternatives

Hypothetical alternative	H1 (attribute1)	H2(attribute2)	H3(attribute3)
H1(attribute1)	1	3	5
H2(attribute2)	0.33	1	2
H3(attribute3)	0.2	0.5	1

MATLAB script for hypothetical attribute to calculate the eigen vectors, values, one minus norm_eigenvector (shows relative weights among the compared elements), scale_norm_eigenvector (largest is 1):

```

hypothetical=[1 3 5; 1/3 1 2;1/5 1/2 1]
eig(hypothetical)
[eig_vector , eig_value]=eig(hypothetical)
v=[0.9281 0.3288 0.1747]
one_minus_v_normed = v / norm(v, 1) % using the 1-norm and n = norm(X,1)
returns the 1-norm of X.
%scale so the largest value is equal to one
scaled_v=one_minus_v_normed/max(one_minus_v_normed)
landa= 3.0037; %eigenvalue
n= 3; %size of the matrix
CI=(landa-n)/(n-1)
RI_3=.52 % for 3x3 matrix is calculated by Saaty by randomly pairwise
%comparison
CR=CI/RI_3

```

Then the output of MATLAB program is as shown in Table 7.10 for eigen related analysis. Eigen value is 3.0037 and CR is less than .1 (consistent).

Table 7.10

MATLAB Program Output Step 2

eigen_vector	one minus norm_eigenvector	scale_norm_eigenvector_so_largest_is_one
0.93	0.64	1.00
0.33	0.23	0.35
0.17	0.12	0.18

7.3.3 Step 3 of AHP Approach

The decision maker uses the weights from Table 7.9 (.64, .23 and .12) to combine the scores and determine the following total scores shown in Table 7.10.

Table 7.11

AHP Total Scores for Attributes

Attribute	scale norm eigen vector
Attribute #1	
55	1.00
65	0.69
75	0.48
Attribute #2	
1	1.00
2	0.85
10	0.11
Attribute #3	
300	1.00
600	0.44
700	0.27
1200	0.06

The scores for 4 alternatives are as followings:

The scores from MHD prototype 1 is as follows:

$$\begin{aligned}
 &.64*(\text{scale_norm_eigen_vector_attribute_one } 55) \\
 &+.23*(\text{scale_norm_eigen_vector_attributetwo } 10) \\
 &+.12*(\text{scale_norm_eigen_vector_attributethree } 600)= \\
 &.64*1+.23*.11+.12*.44=.71
 \end{aligned}$$

The scores from prototype 2 is as follows:

$$\begin{aligned}
 &.64*(\text{scale_norm_eigen_vector_attribteone } 65) \\
 &+.23*(\text{scale_norm_eigen_vector_attributetwo } 1) \\
 &+.12*(\text{scale_norm_eigen_vector_attributethree } 1200)=.68
 \end{aligned}$$

The scores from prototype 3 is as follows:

$$\begin{aligned}
 &.64*(\text{scale_norm_eigen_vector_attributeone}75) \\
 &+.23*(\text{scale_norm_eigen_vector_attributetwo}2) \\
 &+.12*(\text{scale_norm_eigen_vector_attributethree}300) = .62
 \end{aligned}$$

The scores from prototype 4 is as follows:

$$\begin{aligned}
 &.64*(\text{scale_norm_eigen_vector_attributeone}55) \\
 &+.23*(\text{scale_norm_eigen_vector_attributetwo}10) \\
 &+.12*(\text{scale_norm_eigen_vector_attributethree}700) = .69
 \end{aligned}$$

Based on the specific criteria and selected attributes, the score for active cooling prototype 1 is the highest and that alternative should be selected.

7.4 Brief Overview of System Level Approach of MHD Cooling Technology for Spacecraft Avionics and Big Picture

In a complicated context, the MHD cooling technology for spacecraft avionics engulfed in cause-and-effect relationships that are knowable but not obvious, expert diagnosis is needed, and there are known unknowns (Snowden and Boone, 2007). Up to this point, this dissertation rigorously involved in avionics cooling technology from problem solving perspective or subsystems development of smaller scope (e.g., components, instruments, materials), in present section, we briefly assess its impact at a system level and prove to be a benefit. Additionally, scaled MHD cooling can be incorporated across different systems and shown how that in-space MHD cooling would improve reliability of the system as a whole. MHD cooling is compared for system-level impacts of different technologies and how it produces system-level metrics that would allow the benefit of MHD cooling technology to shine through and implemented at system level. To synthesize the system level impacts of compared technologies, decision making from system perspective that are “control systems” and “transformation systems”

is modeled for MHD cooling. A control system continually monitors the state of another system (i.e. temperature sensors) and makes decision that determines the instructions (actuators) that should be sent to the other system so that it meets its goals (i.e. operate below derating temperature). A transformation system is a decision making system that receives information from external sources (i.e. monitored temperature) and then makes decisions that generate new information that another system will use. Both types of systems involve decision making, which creates information from other information (Hermann, 2015).

7.4.1 Why the Big Picture Matters

When you are deep in design and engineering, it is easy to lose track of the “big picture and decisive goals”. The Systems-Level approach keeps you on track and it is important throughout the process. Additionally, once in research and development, teams whose members only possess soloed experience tend to focus solely on their area of expertise. This exposes the research to costly oversights, especially as it is in higher level of technology readiness development stage. For example, the thermal engineers may care little for what the manufacturing engineers are doing or how they do it. These are a few classic weak points in research team that prevent the most effective and efficient solutions as whole (Rametsteiner, 2006; Mehr et al ,2006). Therefore, system level approach is a tool to prove the worthiness of the research with a strong return on investment (ROI) model and weighed against possible impacts to market acceptance for managements in big corporations.

7.4.2 Reuse of Electromagnetic Energy for MHD Thermal Cooling

At system level, an emergent process across disciplines is energy recovery or recycling through realization the potential of combining wasted energies and reuse them. Energy recycling can significantly increase efficiency and witnessing the benefit at system level. The future work for this study could be done in the form of reusing and combining available electromagnetic energy produced by avionics and recovery of the wasted electromagnetic radiation for cooling purposes. In this regard, spacecraft consists of assemblies and subassemblies that are linked and connected together to perform certain tasks. These avionics generate electromagnetic energy, we can harvest energy not only from natural sun radiation, but also from all the artificial radiofrequency subassemblies that are increasing in number as a consequence of information and communications technology (ICT) revolution. For example, exploded view of subsystems of NASA LCROSS robotic spacecraft operated by Northrop Grumman Corporation is seen in Fig. 7.5 extracted from wikipedia.org

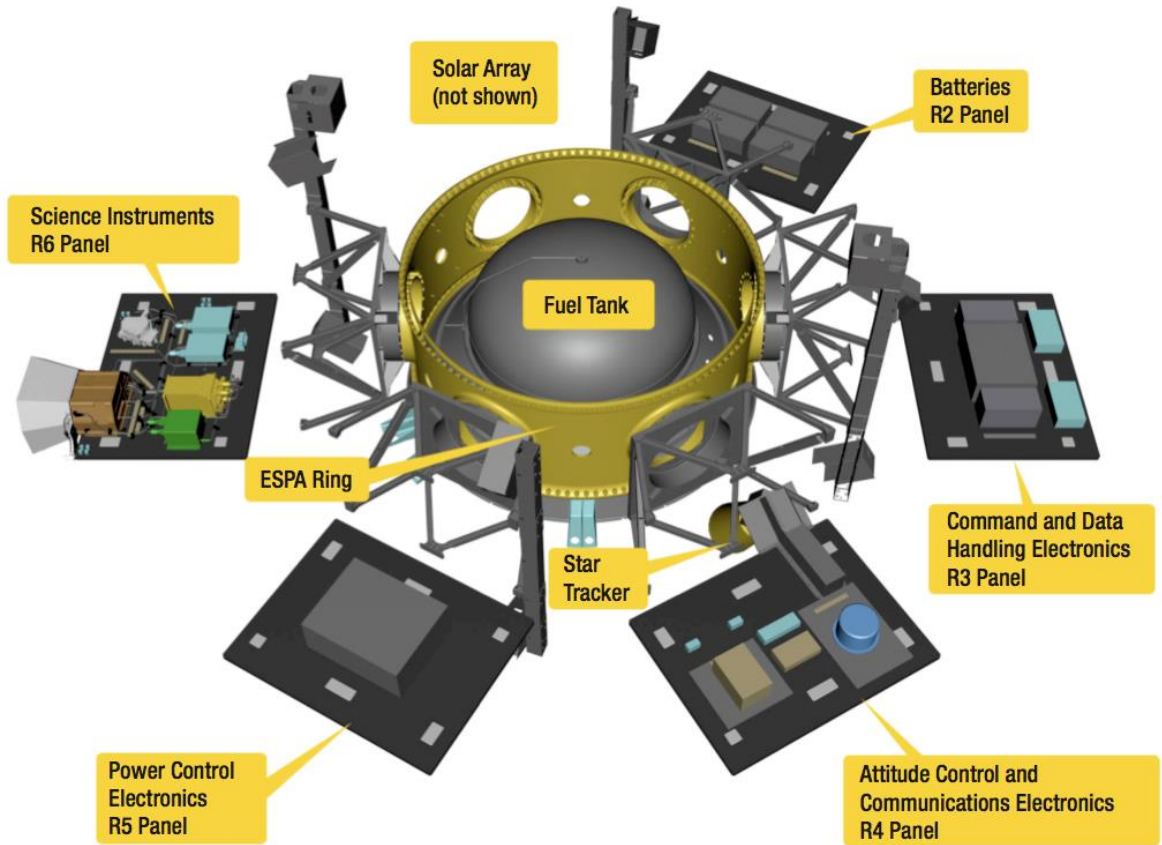


Figure 7.5: Exploded view of NASA LCROSS Robotic Spacecraft including subsystems generating undesired electromagnetic energy

In recycling of electromagnetic wave in the form of electric and magnetic fields for cooling, we are interested in describing how the energy of these waves from different sources is transmitted, channeled and collected to be harvested and used to push electrically charged coolant in active cooling system. In order to reuse wasted electromagnetic energy associated to an electromagnetic wave, we have to characterize its wavelength, propagation speed and magnetic flux density. Several reports and papers have been published in the past years presenting harvesters of electromagnetic radiation in the infrared and visible spectrum. The bottleneck of the technology remains in the rectification process (Futchun et al, 2013). Noise suppression has become an important issue, particularly with regard to electromagnetic interference (EMI) and electromagnetic

compatibility (EMC). Ferrite noise suppressor are used to mitigate crosstalk and noise. The other methods to mitigate crosstalk are increasing space, grounding, limiting the length of lines and reduction in rise or fall time of the signal.

In addition to mitigation of undesired electromagnetic radiation, there are devices for channeling for longitudinal magnetizing and transversal magnetizing (SST testing from Berkley, 1983) and simple and quite effective method of improving of uniformity of magnetic field in a 2-3 mm thick copper plate inserted between magnetizing winding (Dannatt plate). Typically, harvesters would provide 5 percent efficiency in recovering electromagnetic energy, however, a research team at American university of Sharjah was able to minimize its harvester's energy consumption and to raise efficiency to more than 80 percent. In this study, the goal is recycling and reusing of electromagnetic radiation for cooling of electronics. Moreover, the sun's magnetic field has two poles, like a bar magnet and can be considered as an available energy source in space. A solar wind composed of charged particles carries the magnetic field away from the sun's surface and through the solar system, sun's radiation flux density has a magnitude of .3Tesla and enough for pushing electrically charged coolant in magnetic cooling system.

7.4.3 Summary and Root Cause

The root definition of the purposeful activity of MHD cooling technology to be modeled at system level is: "Utilize undesired, leaked and generated magnetic field in the spacecraft electronics systems such as open cores, inductors, solar and also added magnetic pumps by collecting, channeling, and guiding uniform and resultant magnetic fields in order to contribute to achieving active cooling system for avionics and improve the efficiency of the system."

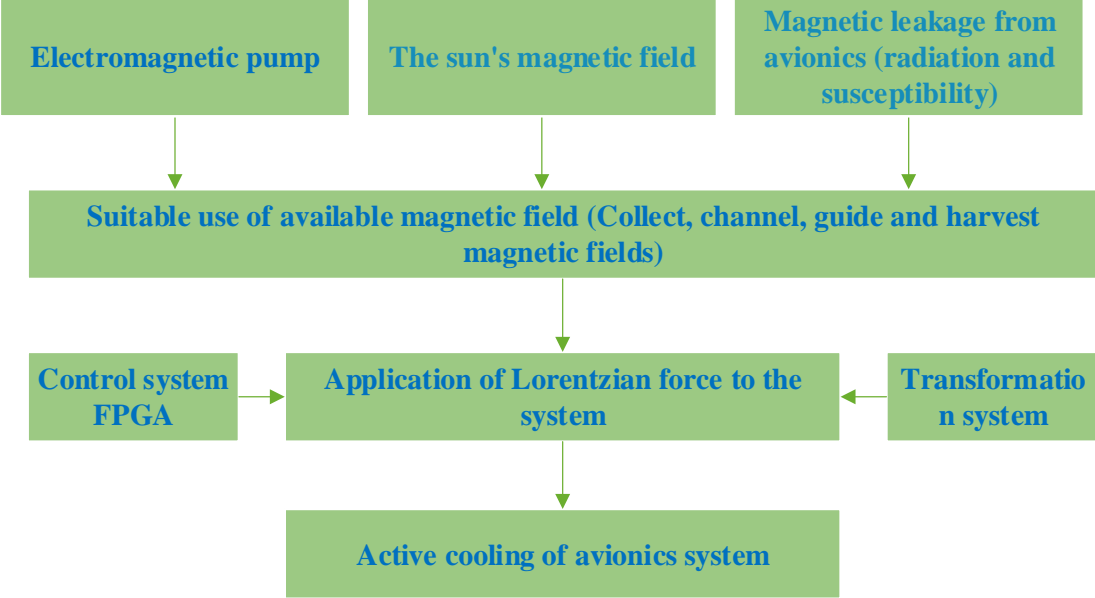


Figure 7.6: Root definition for MHD cooling technology at spacecraft system level

Utilizing magnetic field is what the cooling system does, channeling, guiding, applying Lorentzian force to phase change material through additively manufactured structures are how the system does it, and recycling electromagnetic radiation and susceptibility and using radiant flux density for actively cooling avionics is why the system does it.

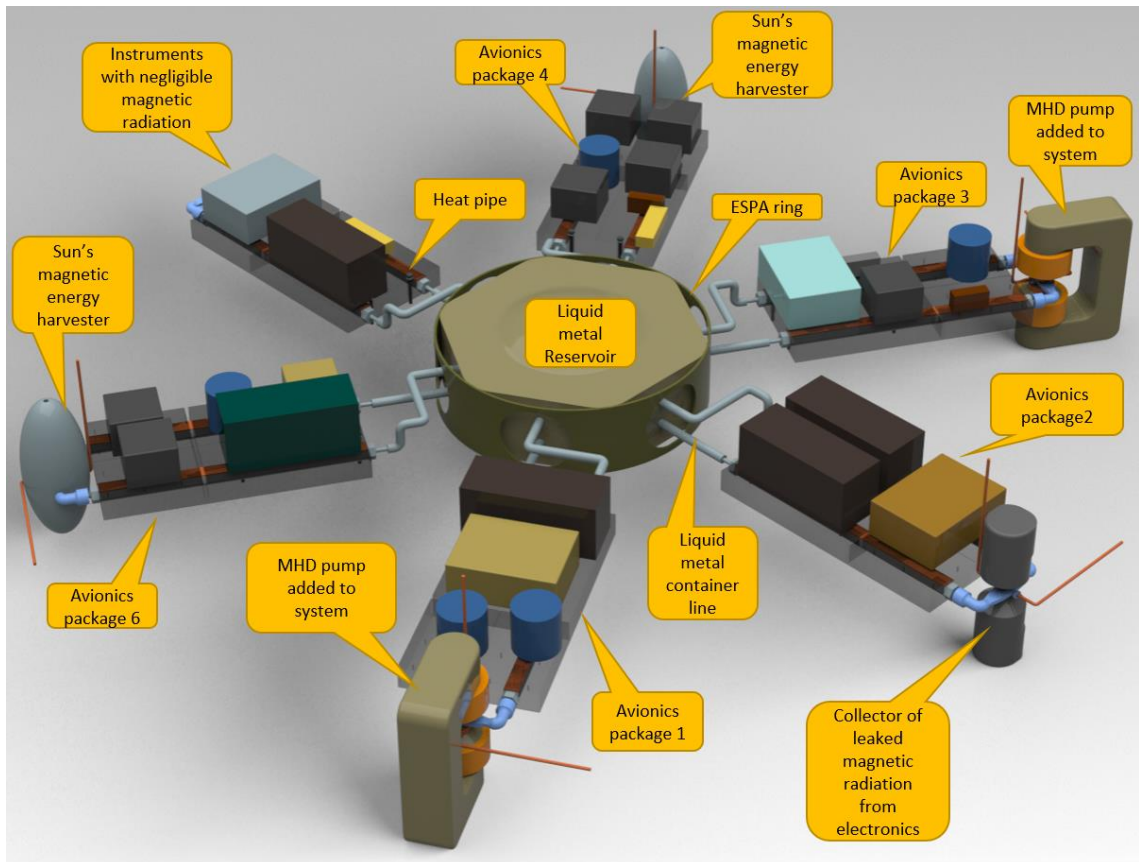


Figure 7.7: Conceptualized exploded view of spacecraft avionics including MHD cooling, magnetic field is generated from leaked undesired magnetic fields from electronics, sun's magnetic energy and magnetic pump.

7.5 Conclusion

In summary, we briefly argued the system level impact of MHD cooling for spacecraft avionics through scientific observations and consequently selecting suitable thermal management to satisfy the specified requirements subject to attributes and goals. AHP is one of MCDM methods to derive ratio scales from paired comparisons. The input can be obtained from actual measurement such as temperature, weight etc., or from subjective opinion such as satisfaction feelings and preference. AHP allows some small inconsistency in judgment because human is not always consistent. The ratio scales are derived from the principal Eigen vectors and the consistency index is derived from the

principal Eigen value. AHP structures complexity through the use of a hierarchy, it measures judgment using a ration scale, and it synthesizes these judgments using a hierarchy (Hermann, 2015).

For future work, by demonstrating a novel concept and enabling advancement of aeronautics-related technologies the forthcoming cooling techniques at system level can be developed and optimized by MHD pumping prototypes argued in this dissertation. The goal is to recycle sun's magnetic energy, reuse of undesired magnetic radiation from components and implementation of electromagnet to push LM coolant which is capable of storing and releasing large amounts of heat from spacecraft systems.

Chapter 8: Dissertation Summary

8.1 Introduction

For this study, multiple AM technologies were synergistically complemented with cross platform tools such as MHD to solve the corrosion problem in the use of low melting eutectic alloy with high molecular thermal and electrical conductivities in geometrically complex patterns of active cooling system for spacecraft avionics. This dissertation covered five major areas:

1. Using LM for improving heat transfer in avionics packaging.
2. Creating efficient thermal interfaces between ceramic tubes and metallic block.
3. In-situ AM technology to embed LM compatible ceramic tubular insert.
4. Driving LM coolant through geometrically complex control volume using MHD.
5. Optimality and assessing impact of MHD cooling technology at the spacecraft system level.

To accomplish these tasks the prototypes of active cooling systems were conceptualized, modeled, analyzed, optimized, synthesized, manufactured, assembled, tested and finally compared to alternatives to determine the tradeoff in performance. Primarily, the main advantage of LM as a coolant is its low viscosity with metallic properties as it is in liquid form within the operating temperature range of most electronics. However LMs such as Galinstan or EGaIn are corrosive to metals with the exception of except tungsten and tantalum, and so have to be contained in compatible containers such as ceramic or polymeric tubes. LM compatible tube such as thermally conductive solid BN which is a diffusion bonded ceramic is fragile and has outgassing issue. Similarly, polymeric containers such as FDMed Ultem tubes are prone to fail under

vibration and low frequency random response loads. To resolve their structural issues, LM containers (tubes) are encapsulated in the channels of metallic block.

This introduces the second major area of this dissertation focusing on the creation of efficient thermal interfaces between ceramics/polymers within metals. Interfacial thermal resistance creates a bottleneck for heat carriers across the interface and prevents efficient thermal transport in lieu of the efficiency of coolant and housing. The efficiency of the cold plate depends on the material properties of the tube, tube geometry and contact area, surface roughness, hardness and flatness and more importantly, which manufacturing or packaging technique is used to embed them in the metallic block. Using in-situ AM techniques, such as the powder bed based with prefabricated electroplated ceramic tubular insert that eliminates secondary operations and fabricates the hybrid cold plate through the melting of metal powders around the tubes, results in a reduced contact resistance at the metal-ceramic interface. To improve wettability at the interface, CNC machined ceramic tubes are electroplated. Printing metal on top of a copper/silver plated ceramic tube can develop a superior thermal bond and enhance thermal conductivity at interfaces of the multilayer cold plate. This novel in-situ AM SLM technique to fabricate ceramic/metal HX is the third topic of this dissertation. Furthermore, the ability of the LM to be pumped by MHD due to its electrical conductivity permits the development of single-phase active cooling system. MHD or conventional pumping systems can pump LM. However, the reliability of the MHD active cooling systems is due to no moving parts and this attribute is the important parameter for “closed” long mission space applications. We covered “driving LM coolant through geometrically complex control volume using MHD” as the fourth topic of this dissertation. Finally, approximation

assisted optimization and development of a system level model including its mission context and assessing impact at the spacecraft system level of the proposed heat exchanger are modeled for the realization of the thermal characteristics as a whole.

8.1.1 Using LMs for Improving Heat Transfer

The first major area of this dissertation focused on criteria for choosing LMs for improving heat transfer and tailoring its material properties to application. LMs are low-melting point eutectic alloys which are liquid at the operating temperature of most electronics. The advantages of LM as heat transfer material are as followings:

- High thermal conductivity,
- Ability to withstand dramatic thermal expansion mismatch
- Ultra low bondline thicknesses
- Extremely low Kapitza resistance
- Non toxic, low viscosity and low Prandtl numbers

LMs that are electrically conductive allow the liquid to be pumped using an electromagnetic pump with no moving parts. Gallium (Ga) alloys such as Galinstan (EGaIn as alternate) were found suitable for this application:

I. Galinstan (67%Ga, 20.5%In, and 12.5%Sn by volume), which has a broad temperature range of liquid phase melts at $-19\text{ }^{\circ}\text{C}$ ($-2\text{ }^{\circ}\text{F}$) and has electrical conductivity: $3.46 \times 10^6\text{ S/m}$ (room temperature) surface tension: $s = 0.718\text{ N/m}$ (room temperature) and 2.1 times lighter than Mercury.

II. (EGaIn) Gallium-Indium eutectic (75.5% Ga, 24.5% In by weight), melts at $15\text{ }^{\circ}\text{C}$ ($59\text{ }^{\circ}\text{F}$) and has electrical resistivity of $\sim 29.4 \times 10^{-6}\text{ W-cm}$.

However, Ga alloys are corrosive to all metals except tungsten and tantalum and have to be contained in compatible synthetic ceramic or polymeric containers.

8.1.2 Creating Efficient Thermal Interfaces Between Ceramic Tube and Metallic Block

For this study, solid BN with high thermal conductivity $78 (130) \text{ W/m} \cdot \text{K}$ and Ultem with thermal conductivity $.22 \text{ W/m} \cdot \text{K}$ were used as LM compatible materials to circulate LM inside them due to their compatibility with LM and thermal properties. The other suggested backup materials were Polyetherether, PEEK, Polyether ketones PEK, PAI (commonly named Torlon) and Shapal (Aluminum Nitride/Boron Nitride composite), a conductive ceramic hard for CNC machining with tight tolerances). However, these materials have the abrasion and erosion weaknesses, therefore; they were embedded in metallic structure that creates an inefficient thermal transport at the interface of tube and metallic block. Prior insertion of the LM compatible tube inside metallic block, it was confirmed that the tubes have specific morphology in order to satisfy the following objectives:

- Maximize cooling potential and laminar boundary layer consideration i.e. minimized surface roughness according the Chezy equation with Manning's roughness coefficient.
- Increase thermal contact surface area according to Fourier law of conduction
- Reduce surface roughness, flow resistance and hydraulic pressure loss per the Moody chart.
- Temperature gradient uniformity through geometric symmetry.

- Manufacturing feasibility for insertion in the SLM metallic block without colliding with the SLM machine apparatus.

8.1.3 In-Situ AM Technology to Embed LM Compatible Ceramic Tubular Insert

The in-situ AM SLM process is used for the embedding of ceramic tubes in the metallic block and that process has the following attributes:

- Reduction of interfacial gaps related to surface roughness and machining tolerances through the melting of metal powders around the tubes, resulting in a reduced contact resistance at the metal-ceramic interface.
- Geometric optimization of the prefabricated ceramic tubes to prevent collision with the roller or blade of the powder bed based AM machine.
- Ceramic tubes are electroplated prior to embedding, which enhances the fusion of the ceramic with the melted metal powder by reducing defects associated with the surface tension of the melt and the wettability of the ceramic.

“A major advance” of in-situ DMLS process is having a hybrid structure by printing metal on top of an electroplated insert that produces a superior thermal bond, overcoming the “disadvantages” of using a conventional “insertion process” that causes additional gaps between seams and interfaces.

8.1.4 Driving LM Coolant Through Geometrically Complex Control Volume Using MHD

We have studied the MHD flow of LM in geometrically complex and optimized control volume driven by MHD pump. The nature of flow is dramatically different from polar liquids because of the surface tension, Hartmann flow and the so-called M-shaped

velocity profile. The highlighted features associated with implementation of MHD pumping in this experiment are as follows:

- Geometrically and materially optimal design of elliptic coupling to overcome the shape dependent demagnetization issue realized by AM process.
- Electromagnet optimality including geometry, material and its powering to determine electrical and magnetic saturation thresholds of electrodes and electromagnets under DC and AC eddy currents.
- Combination of heat transfer, fluid mechanics and electromagnetic simulation to approximate Maxwell and Navier-Stokes equations by Ansys workbench to determine external magnetic field, velocity profile and pressure contour, and the solution of energy equation to extract temperature gradient of the cooling system.
- MHD dimensionless parameters including Hartmann number, Reynolds number, Magnetic Reynolds number and Stuart number or Interaction parameter revealed that core flow was laminar and the viscous forces dominated the inertial forces and electromagnetic forces.
- The effect of conductive Hartmann wall (electroplated elliptic coupling) on flow rate and pressure drop were determined.
- Conducted a controlled thermal experiment, extracted the MHD cooling data and analyzed the data to gain insight about the performance of the active cooling system.

8.1.5 Optimality and Assessing Impact of MHD Cooling Technology at Spacecraft System Level

To formulate the MHD thermal management as a multi objective optimization problem, the cost functions or objective functions were defined to measure the merits of different designs. The design variables to minimize the cost functions subject to equality and inequality constraints have been specified. The simple bounds of design variables are also included in the inequality constraints and main features of optimization section, which are as followings:

- Surrogate modeling and approximation-assisted multiple objective optimization of MHD cooling.
- Space filling Latin Hypercube Morris-Mitchell optimum sampling plan.
- Suitable convergence criterion to determine when to stop the surrogate infill.
- Verification and validation by Kriging or Gaussian process regression method by comparison of root mean squared errors.
- Pareto Frontier of MHD cooling extracted from approximation assisted optimization multi objective approach.
- 4th generation Bezier smoothing technique of Pareto Frontier and generated optimal values for design variables.
- Update the simulation prototype in Ansys workbench per optimal design variable and rerun the simulations for validation of objectives.

Finally, the MHD cooling concept is investigated from a decision-making perspective and systemic approach. Choosing a thermal cooling system or any system solely based on optimization criteria can be unsuitable particularly in situations when there is inadequate data to formulate an optimal problem or when there is no consensus

on the objective functions, therefore its mission context and assessing impact at the spacecraft system level is worth mentioning for this study and it covers the following topics:

- Alternatives of thermal management for avionics argued in this dissertation and their advantages and disadvantages.
- Multiple criteria decision analysis and analytic hierarchy process applied to thermal management alternatives with selected attributes.
- Brief overview of system level approach of MHD cooling with conceptualized model of spacecraft avionics system and suggested techniques for recycling of electromagnetic energy used for MHD cooling.

8.2 Scientific and Technical Contributions and Intellectual Merit

The following resulted from this dissertation:

1. Developing a thermal system with great power dissipation based on Maxwell's laws coupled with flow field and an electric field that permits higher thermal densities for power electronics and structures, and realizing them through new AM processes and system design that permits use of what normally would be corrosive liquid metals. This required the following: (a) proper selection of compatible materials for the LM container per coercivity as a measure of the ability of a magnetic material to resist demagnetization, (b) geometric optimality realized by AM to enhance the induced magnetic field to drive LM flow, and (c) enhancement of magnetic flux density generated from magnetizing force of soft electromagnetic core (J. Armen and H. A. Bruck, *Development of Magnetohydrodynamic Cooling for Spacecraft Avionics Using Geometric*

Complex Structures Realized Through Additive Manufacturing, submitted to AIAA Journal of Thermophysics and Heat transfer, 2020).

2. Improving thermal conductance of interfaces in layered heat exchanger governed by Fourier's equation, and influenced by rough surfaces as a function of contact pressure. This improvement is achieved by adapting in-situ AM technologies to embed electroplated ceramic tubes, inside of metals without parting surface, resulting in more intimate contact between the metal and ceramic. In addition, wettability, and amalgamation of interface layers during laser fusion process governed by Beer–Lambert–Bouguer and transient heat conduction laws in SLM AM process were investigated (J. Armen and H. A. Bruck, *Improving Contact Resistance in Metal-Ceramic Heat Exchangers using Additive Manufacturing and Ceramic Tubes with Electroplated Films*, submitted to International Journal of Advanced Manufacturing Technology, 2020).
3. Understanding of the MHD flow and heat transfer properties of the system and developing the multi-physics FEA and CFD analyses for accurately predicting the behavior of the system based on approximation of Maxwell and Navier-Stokes partial differential equations. In particular, the following were determined: (1) the electric and magnetic induced fields needed to generate MHD flow on the LM inside the container, (2) the optimal values for the design variables in MHD system in relation to the heat transfer performance (optimal diameter of LM container and its cross-sectional shape, applied electrical voltage or amperage, number of turns in windings, etc.), and (3) the performance of MHD pumping in comparison to a conventional diaphragm pump. The prototypes enabled us to

characterize the physics of this new thermal management concept, and generated data for the models (J. Armen and H. A. Bruck, *Development of Magnetohydrodynamic Cooling for Spacecraft Avionics Using Geometric Complex Structures Realized Through Additive Manufacturing*, submitted to AIAA Journal of Thermophysics and Heat transfer, 2020).

8.3 Conclusions

The future of emerging additive manufacturing relies on advanced techniques to fabricate multiphase materials, parts comprised of ceramics, metals and composite materials in combination as disruptive and valuable innovations to existing methodologies of fabricating hardware. In this study, the efficient HX concept was constructed from multi materials by novel AM techniques containing features that allowed scaling to accommodate a wide range of applications. In summary, this study demonstrated (1) how AM technologies can overcome critical limitations of traditional manufacturing processes to reduce thermal contact resistance at interfaces of multimaterial-multilayer cold plates and improve performance of thermal system by novel insertion technique and (2) how MHD can be used to develop a reliable, very rugged in operation, silence due to a no-moving-parts thermal transport system for avionics packaging and realize them through multi AM techniques that permitted use of what normally would be corrosive LMs.

A summary of the main themes of this dissertation are as followings:

- Tailoring advanced engineering materials to thermal cooling applications including nontoxic LMs with eutectic compositions, machinable composite

synthetic ceramic made up of BN, printable materials for AM processes, soft magnetic composites to reduce saturation of electromagnetic field.

- Development of four different LM compatible cooling prototypes including 1) passive thermal management assembled by conventional manufacturing techniques 2) active cooling packaged by conventional manufacturing techniques and diaphragm pump 3) active cooling packaged by in-situ AM techniques and diaphragm pump 4) active cooling by MHD. The prototypes have enabled us to characterize the physics of these new thermal management concepts, and generate data and comparison of models we have developed.
- Implementation of ceramic tubes to overcome the inherent chemical incompatibility between LM coolant and the metallic block that causes corrosion and yet improve the thermal efficiency.
- Application of electroplating on ceramic tubes prior to insertion to enhance fusion of the ceramic with the melted metal powder by reducing defects associated with the surface tension of the melt and the wettability of the ceramic. Silver-plated ceramic BN inserted in SLM aluminum alloy block which has the highest thermal efficiency at contact interface and the lowest contact resistance and successfully finished 3D printing.
- Geometric optimization of the prefabricated ceramic tubes to prevent collision with the roller or blade of the powder bed based AM machine and yet enhance the thermal transport. Irregular pentagon for (exterior cross section) and circular (interior cross section) with minimum wall thickness feasible for CNC machining

of ceramic tube is the optimal morphology amenable for in-situ AM process to fabricate the hybrid cold plate.

- Subassemblies of the MHD pump includes electromagnet assembly, elliptic coupling with embedded electrodes assembly and cold plate assembly. The experiment revealed that elliptic coupling without plating has improved the flow pressure drop by a factor of 4.3x compared to analytical pressure drop calculated for a square duct with 6mm side wall.
- Determination of dimensionless incompressible MHD metrics to characterize the MHD flow regime including Hartmann number, Reynolds number, magnetic Reynolds number and Stuart number. The ratio of the Hartmann number to the Reynolds number revealed that the electromagnetic flow is laminar. The Stuart number has shown that viscous forces dominate the inertial and electromagnetic forces. The magnetic Reynolds number indicated that the induced magnetic field to LM is small compared to external magnetic field generated in C-shaped core.
- The tradeoff between the metallic wall effects on the induced magnetic field and the thermal conductivity of metallic wall in MHD cooling system. To realize the Hartmann conductive wall effect, we electroplated the nylon elliptic coupling to characterize the effect of metallic wall on electromagnetic flow rate and consequently the cooling performance. The copper plated wall under influence of the external electromagnetic field creates temporary magnetic fields within itself that is opposite to the direction of the external magnetic field. Therefore, the magnetic field has not been induced to the LM to generate Lorentz force in LM (no flow). This blocking effect was less obvious for the silver plated case as about

1/3 of external magnetic field relative to bare nylon coupling passed through the silver plated wall and induced to LM (silver-plated coupling was 1/3 as efficient as the Nylon). Elliptic nylon coupling without plating has shown the best performance in terms of inducing the magnetic field to LM.

- MHD active cooling simulation in Ansys workbench included:
 - Preprocessing: Adaptive tetrahedron meshing refinement, defining region, material properties, assigning B-H curve characterizing soft magnet hiperco50A core, full contact is assumed at thermal interfaces.
 - Solver: (1) Maxwell magnetostatic and Maxwell eddy current FEA solver, (2) MHD module in Ansys Fluent for CFD simulation by magnetic induction method, (3) for thermal analysis, the conjugate heat transfer in Fluent is used to describe heat transfer that involves variations of temperature within solids and LM, due to their thermal interactions.
 - Post processing: Distribution of magnetic flux density in Hiperco50A core per number of turns and applied current to two coils, LM pressure gradient and velocity of LM in MHD flow, temperature contour of cold plate.

Simulation revealed that application of incompressible and steady state electromagnetic flow for cooling of avionics was promising but over predicting due to restriction and implementation of the FEA and CFD models. Additionally, to block the electromagnetic influence of magnetic field generated by electromagnet on electronics, a Faraday cage would be required for effective EMI shielding.

- The MHD cooling prototype was shown to reach volumetric flow rates of up to 650 mm³/sec and generated flow pressure due to Lorentz forces of up to 230 Pa, resulting in heat transfer improvement relative to passive prototype of 1.054. High reliability attributes of the MHD pump have tended to outperform its low efficiency such as simplicity, space compatibility, silence, short transient time, uninfluenced by pitch, roll and yaw of spacecraft, scalability, easier fabrication and minimal maintenance due to operation with no-moving-parts cause MHD cooling highly suitable for long mission space applications.
- Approximation assisted multi objective optimization for MHD cooling to minimize pump pressure and minimize temperature of cold plate subject to inequality constraints were optimized the following design variables of the system: diameter of ceramic tube, applied current to coils and number of winding turns.
- Selecting a cooling system exclusively based on performance benchmark can be misleading, therefore we considered an analytic hierarchy process as an engineering decision making tool for alternatives developed with arbitrary attributes such as minimal maintenance due to operation with no-moving-parts, simple and quiet, easy for manufacturing and etc. Finally, we demonstrated a conceptualized model of MHD cooling at spacecraft system level as an imminent thermal management system.

The root definition of MHD cooling technology as used in this study is as the following: “Utilize, collect and guide magnetic flux density to push efficient coolant to contribute for achieving active cooling system realized by AM hybrid processes for

avionics in space-like environment.” MHD cooling prototype is broken down into subassemblies and components to analyze each subsystem in order to determine its performance and optimize magnetic-flow-thermal parameters of subsystem to synthesize iteratively as a whole to gain insight about its characteristics, performance and highlighted attributes.

8.4 Future Work

Investigation of interfacial thermal resistance of metal-ceramic in-situ HX may conduct a further study to couple with the powder bed fusion process that involves around 130 parameters, such as laser power, speed and beam size that control the length, width, and depth of the melt pool which can be factored in for further understanding contact resistance at interfaces. It is desirable to maintain constant or controlled melt pool geometry, however because the thermal boundary conditions change as a function of the part geometry, the parameters required to achieve desired melt pool characteristics will also be a function of geometry. The experiment can be repeated for different cross section of the tubes and gain insight about the thermal performance of the HX system. Additionally, to increase the thermal efficiency and the dimensional stability of the thin of the wall polymeric container in order to prevent deformation and sealing issues, non-metallic fillers such as carbon micro/nano fiber can be used. Moreover, the insertion technique applied in this study by today's “best available AM technologies” only allowed to fuse one side of the inserted part. Hybrid machining which combines additive and subtractive processes in a single machine might be used to fuse the whole outer surface of the inserted tubes with matrix structure. Furthermore, for feeding LM into structures, low-melting point eutectic alloys are not amenable to conventional AM processes, so new

hybrid manufacturing processes have to be developed using techniques like gravity feed to insert them into the structure and to determine key parameters of materials such as feed rates, wettability, and material swelling.

In-situ AM insertion technique is not limited to the placement of LM compatible tubes inside metallic block, this technique can be used to insert any component or subassembly of avionics to improve the interfacial contact resistance such as populated printed circuit board embedded in heat sink by illumination of inefficient interstitial materials to further improve the efficiency of heat transport path.

For Ansys MHD Fluent simulation effort, instead of magnetic flux distribution applied to moving coolant, only an average magnetic field is allowed to be applied because of the limitation of the software. For future work, Ansys workbench can be modified such that excitation magnetic flux density can be linked to MHD fluent as a direct input and translation for more accurate analysis. Additionally, in preprocessing of Ansys, instead of using full contact at thermal interfaces, the contact resistance findings from this study can be used to link interfaces in applicable scenarios.

Excitingly, researchers have demonstrated techniques to manufacture ceramics with high electrical conductivity (Vazrik Keshishian et al, 2018). LM compatible electrically conductive ceramics can be used as electrodes of MHD pumping instead of the tungsten-plated copper used in this study to further improve reliability. Additionally, in the case of experimental induction MHD, to improve flowability of LM under Lorentzian force, powder with high electrical properties can be proportionally mixed and pretreated in HCL (Hydrochloric acid) to produce suspended Brownian particles in fluid developing more efficient HX operating by MHD pumping. However, the challenges

remain how to overcome the corrosion delinquency of electrically conductive particles inside LM in a multiscale study.

As a final suggestion for future work, the framework has been laid for an emergent process capable of recycling electromagnetic waves in the natural solar spectrum, as well as recovering unwanted electromagnetic radiation from electromagnetic components in avionics packages can be modeled in the form of combined electromagnetic, heat transfer and waste recovery for thermal management and active cooling purposes. In other words, the research in this dissertation can be used to describe how the magnetic energy of these waves from different sources is transmitted, channeled and collected to be harvested and used to push an electrically charged LM coolant in an active cooling system for spacecraft avionics.

Bibliography

- Abe, F., K. Osakada, M. Shiomi, K. Uematsu, M. Matsumoto, 2001, "The Manufacturing of Hard Tools from Metallic Powders by Selective Laser Melting," *Journal of Materials Processing Technology*, Vol. 111, Nos. 1–3, pp. 210–213.
- Al-Hababbeh, Al-Saqqa , Review of magnetohydrodynamic pump application, Elsevier, *Alexandria Engineering journal* (2016) 55, 1347-1358
- Alfvén, H, "Existence of electromagnetic-hydrodynamic waves," *Nature*.150 (3805): 405–406, 1942.
- Ananthanarayanan, A., Gupta, S. K., and Bruck, H. A. (July 22, 2010). "Modeling and Characterization to Minimize Effects of Melt Flow Fronts on Premolded Component Deformation During In-Mold Assembly of Mesoscale Revolute Joints." *ASME. J. Manuf. Sci. Eng.* August 2010; 132(4): 041006.
- Anderson, Ferencz, Hodge "Laser powder bed fusion additive manufacturing of metals, physics, computational, and materials challenges," December 2015 AIP.
- Arlt, T., Priede, J., & Bühler, L. (2017). The effect of finite-conductivity Hartmann walls on the linear stability of Hunt's flow. *Journal of Fluid Mechanics*, 822, 880-891. doi:10.1017/jfm.2017.322
- Arnold, JM, Cramer, CL, Elliott, AM, Nandwana, P, Babu SS, "Microstructure evolution during near-net-shape fabrication of NixAl_y-TiC cermets through binder jet additive manufacturing and pressureless melt infiltration", *International Journal of Refractory Metals and Hard Materials*, Volume 84, November 2019, 104985.
- Arora, JS, *Introduction to Optimum Design*, Elsevier Academic Press, Amsterdam 2004
- ASM Handbook, Alloy Phase Diagrams, Volume 3, ISBN-13: 978-0871703811 ASM International; 10 edition (December 1, 1992)
- Ayeleso, A. O., & Kahn, M. T. (2018). Experimental characterization of a magnetohydrodynamic power generator under DC ARC plasma. *Acta Polytechnica*, 58(1), 1-8.
- Bahrami, M., Yovanovich, M., and Culham, R. "Thermal contact resistance at low contact pressure: Effect of elastic deformation," *International Journal of Heat and Mass Transfer*, vol. 48, no.16, pp. 3284–3293, 2005.
- Baker, R, and Tessier, M, *Electromagnetic Pump Technology*, Elsevier 1997
- Balandin, A.A.; Ghosh, S.; Bao, W.; Calizo, I.; Teweldebrhan, D.; Miao, F.; Lau, C.N. Superior thermal conductivity of single-layer graphene. *Nano Lett.* 2008, 8, 902–907.

Barnett, E. M., Lofton, J. J., Yu, M., Bruck, H. A., & Smela, E. (2017). Targeted feature recognition using mechanical spatial filtering with a low-cost compliant strain sensor. *Scientific reports*, 7(1), 1-14.

Bejgerowski, W., Gupta, S. K., & Bruck, H. A. (2009). A systematic approach for designing multifunctional thermally conducting polymer structures with embedded actuators. *Journal of Mechanical Design*, 131(11).

Bilger, C., Bruck, H. A., & Dasgupta, A. (2017). Electroplated connections between carbon fiber and nickel. *Journal of Electronic Packaging*, 139(1).

Binois, M., & Picheny, V. (2016). Gpareto: Gaussian processes for pareto front estimation and optimization. To appear: *Journal of Statistical Software*.

Blevins, RD “Applied fluid dynamics handbook”, Publisher: Van Nostrand Reinhold Co., ISBN 9780442212964, (2008)

Bogorad, A. L., Deeter, M. P., August, K. A., Doorley, G., Likar, J. J., & Herschitz, R. (2008). Shielding effectiveness and closeout methods for composite spacecraft structural panels. *IEEE transactions on electromagnetic compatibility*, 50(3), 547-555.

Brettel et al, How virtualization, decentralization and network building change the manufacturing landscape: An Industry 4.0 Perspective , World academy of science, international journal of mechanical, aerospace, industrial engineering Vol: 8, No:1, 2014

Bruck et al, Modeling and Validation of Prototype Thermally Enhanced Polymer Heat Exchanger, *Proceedings of the ASME International Mechanical Engineering Congress and Exposition*, 1-13 (2011).

Bruck et al, A Systematic Approach to Designing Multi-functional Thermally Conducting Polymer Structures with embedded Actuators, *Journal of Mechanical Design*, 131, 10.1115/1.4000239 (2009).

Bühler, L., Mistrangelo, C., & Brinkmann, H. J. (2020). Experimental investigation of LM MHD flow entering a flow channel insert. *Fusion Engineering and Design*, 154, 111484.

Burattini, P., Zikanov, O., and Knaepen, B., 2010, “Decay of Magnetohydrodynamic Turbulence at Low Magnetic Reynolds Number,” *J. Fluid Mech.*, 657, pp. 502–538

Busachi , Alessandro, Erkoyuncu, J, Colegrove, P, Martina, F, Watts, C, Drake, R, “A review of Additive Manufacturing technology and Cost Estimation techniques for the defense sector”, *CIRP Journal of Manufacturing Science and Technology*, Volume 19, November 2017, Pages 117-128

Calignano, F, “Design optimization of supports for overhanging structures in aluminum and titanium alloys by selective laser melting With gratitude”, *Materials & Design*, Volume 64, Pages 203-213 (December 2014).

Carle, F., Bai, K., Casara, J., Vanderlick, K., & Brown, E. (2017). Development of magnetic liquid metal suspensions for magnetohydrodynamics. *Physical Review Fluids*, 2(1), 013301.

Caue Goncalves Mancanares, Eduardo de Senzi Zancul, Paulo Augusto Cauchick Miguel, "Sustainable manufacturing strategies: a literature review on additive manufacturing approach", *Journal of Product Management & Development*, vol.13, n1, p.47-56, (2015).

Choi, S.; Kim, J. Thermal conductivity of epoxy composites with a binary-particle system of aluminum oxide and aluminum nitride fillers. *Compos. B Eng.* 2013, 51, 140–147.

Christensen, RM, "Mechanics of Composite Materials", Dover Publications NY 2013, ISBN-13: 978-0486442396

Conn, J, Comparison of Inert and Open Atmosphere laser Metal Deposition Systems. GE, IMTS conference, Sep. 2016 Optomec Inc.

Coronel et al, hybrid manufacturing with FDM technology for enabling power electronics component fabrication, *Solid Freeform fabrication 2018, 29th annual international symposium- an additive manufacturing conference*

Costescu, Ruxandra M.; Wall, Marcel A.; Cahill, David G. (2003-02-27). "Thermal conductance of epitaxial interfaces". *Physical Review B. American Physical Society (APS)*. 67 (5): 054302

Craeghs, T., Clijsters, S., Kruth, J.-P., Bechmann, F., and Ebert, M.-C., Detection of process failures in Layerwise Laser Melting with optical process monitoring, *Physics Procedia*, Volume 39, 2012, Pages 753-759

Cross, N. (2001) "Design/Science/Research: Developing a Discipline," in the 5th Asian Design Conference: International Symposium on Design Science, Seoul, Korea: Su Jeong Dang Printing Company

Dannatt C., (1933), Energy loss testing of magnetic materials utilizing a single strip spectrum, *Journal of Sci Instrument*, 8,276-285

Dariavach, N., & Engelhardt, M. (2019). U.S. Patent No. 10,356,950. Washington, DC: U.S. Patent and Trademark Office.

Das, P, Chandran, R, Samant, R, Anand, S, "Optimum Part Build Orientation in Additive Manufacturing for Minimizing Part Errors and Support Structures", *Procedia Manufacturing*, Volume 1, 2015, Pages 343-354.

Davis, J. R., "Metals Handbook 2nd Edition" ISBN-13: 978-0871706546, ASM International Handbook Committee CRC Press; 2nd edition (December 1, 1998)

Dean, R. N., Harris, D. K., Palkar, A. Y., & Wonacott, G. D. (2012). Liquid metal-filled micro heat pipes for thermal management of solid-state devices. *IEEE Transactions on Industrial Electronics*, 59(12), 4888-4894.

Deepankar Pal et al , An Integrated Approach to Additive manufacturing Simulations Using Physics Based, Coupled Multiscale Process Modeling, *Journal of manufacturing and science* December 2014 (3dsim software)

Deng et al, Optimization and Evaluation of a High-performance Liquid Metal CPU Cooling Product, *IEEE Transactions on Components, Packaging, and Manufacturing Technology*, 3, 1171-1177 (2013)

Denlinger, ER, Heigel, JC, Michaleris, P, Palmer, TA, “Effect of inter-layer dwell time on distortion and residual stress on additive manufacturing of titanium and nickel alloys,” *Journal of Materials Processing Technology*, Volume 215, January 2015, Pages 123-131

Denlinger, ER, Michaleris, P, “Mitigation of distortion in large additive manufacturing parts” *SAGE*, Vol 231, Issue 6, <https://doi.org/10.1177/0954405415578580> , (2017)

Didion, J. R. (2001, February). A prototype electrohydrodynamic driven thermal control system (EHD-TCS). In *AIP Conference Proceedings* (Vol. 552, No. 1, pp. 310-315). American Institute of Physics.

Dixit, P., Chen, X., Miao, J., Divakaran, S., & Preisser, R. (2007). Study of surface treatment processes for improvement in the wettability of silicon-based materials used in high aspect ratio through-via copper electroplating. *Applied surface science*, 253(21), 8637-8646.

Dongmei Bi, Mei Jiang, Huanxin Chen, Shanjian Liu, Yaya Liu, “ Effects of Thermal Conductivity on the Thermal Contact Resistance Between Non-conforming Rough Surfaces: An Experimental and Modeling Study”, *Applied Thermal Engineering*, 2020, 115037

Du, W, Bai, Q, Zhang, B, “A novel method for additive/subtractive hybrid manufacturing of metallic parts”, *Procedia Manufacturing* Volume 5, 2016, Pages 1018-1030 (2016)

Duvigneau, R., *Optimization using surrogate models*, 2015.

Early, M, Lee, S, and Pellilo, M, *Thermal Performance of Interface Material in Microelectronics Packaging Applications*, *Proceedings of the 1995 International Electronics Packaging Conference*, pp. 534-544.(1995).

Egelkraut, S., Heinle, C., Eckardt, B., Kramer, P., Brocka, Z., Marz, M., Ryssel, H., and Ehrenstein, G. W., 2008, “ Highly Filled Polymers for Power Passives Packaging,” *Proceedings of the Second Electronics System Integration Technology Conference*, London, UK, pp. 403-410.

- Eichler et al, Boron nitride (BN) and BN Composites for High-Temperature Applications, *Journal of the European Ceramic Society*, Volume 28, Issue 5, Pages 1105-1109 (2008)
- Fang et al, Centered L2-discrepancy of random sampling and Latin hypercube design, and construction of uniform designs. *Math. Comp.* 71, 275-296 (2002)
- Fang et al. *Design and Modeling for Computer Experiments*. CRC Press, New York (2006)
- Farhang Mehr, A., and Tumer, I. Y. (January 29, 2006). "Risk-Based Decision-Making for Managing Resources During the Design of Complex Space Exploration Systems." *ASME. J. Mech. Des.* July 2006; 128(4): 1014–1022
- Fiorillo, F, *Measurement and Characterization of Magnetic materials*, Elsevier 2004 Italy, ISBN 0122572513
- Flinn, R, Trojan, P, "Engineering Materials and Their Applications", ISBN-13: 978-0471125082, Wiley, fourth edition (January 1, 1990)
- Flowmetrics, <http://flowmetrics.com/wp-content/uploads/2016/02/vaf211.pdf>
- Forrester, Alexander, and Andy J Keane. 2009. "Recent Advances in Surrogate-Based Optimization." *Progress in Aerospace Sciences* 45 (1). Elsevier: 50–79.
- Forrester, Alexander, Andras Sobester, and Andy Keane. 2008. *Engineering Design via Surrogate Modelling: A Practical Guide*. Pondicherry, India: John Wiley & Sons.
- Fritz N, Koo HC, Wilson Z et al (2012) Electroless deposition of copper on organic and inorganic substrates using a Sn/Ag catalyst. *J Electrochem Soc* 159(6):D386–D392
- Gao, Y. W., Lv, H., Wang, X. D., & Yan, W. M. (2017). Enhanced Peltier cooling of two-stage thermoelectric cooler via pulse currents. *International Journal of Heat and Mass Transfer*, 114, 656-663.
- Geim, A.K. Graphene: status and prospects. *Science* 2009, 324, 1530–1534.
- Getling, A.V. (1998). *Rayleigh-Bénard convection: structures and dynamics* (Reprint. ed.). Singapore: World Scientific.
- Glass DE, Camarda CJ, Merrigan MA, Sena JT. Fabrication and testing of Mo–Re heat pipes embedded in carbon/carbon. *J Spacecraft Rockets*. 1999; 36(1):79–86.
- Gouge, M.F., Heigel, J.C., Michaleris, P. et al. Modeling forced convection in the thermal simulation of laser cladding processes. *Int J Adv Manuf Technol* 79, 307–320 (2015).

Gregor, S; Jones, D, The Anatomy of a Design Theory, Journal of the Association for Information Systems. May 2007, Vol. 8 Issue 5, preceding p313-335. 24p. 1 Diagram, 5 Charts.

Griffith ML, Keicher DM, Atwood CL, Romero JA, Smugeresky JE, Harwell LD, Greene DL (1996) Free form fabrication of metallic components using laser engineered net shaping (lens). In: P. Solid Freeform Fab. Symp.s, volume 9, pages 125–131. The University of Texas at Austin.

Griffiths et al, A model of the interfacial heat-transfer coefficient for the aluminum gravity die-casting process, *Metallurgical and Materials Transactions*, 35, 721–733 (2004).

Guido Adam, Detmar Zimmer, “On design for additive manufacturing: evaluating geometrical limitations”, *Rapid Prototyping Journal* ISSN: 1355-2546, (2015)

Haeri, S., Wang, Y., Ghita, O., Sun, J., Discrete element simulation and experimental study of powder spreading process in additive manufacturing, *Powder Technol.*, 306 (2017), pp. 45-54

Hall, Timothy, Subramoniam, Arumugham Vaishnavi, Bruck, Hugh A., and Gupta, Satyandra K, Development of a Fiber Orientation Measurement Methodology for Injection Molded Thermally-Enhanced Polymers, *Proceedings of the ASME 2012 International Manufacturing Science and Engineering Conference*, South Bend, IN, 1-11 (2012).

Haleem, Abid, & Mohd Javaid, “Additive Manufacturing Applications in Industry 4.0: A Review”, *Journal of Industrial Integration and Management*, Vol. 04, No. 04, 1930001 (2019)

Han, Z.; Fina, A. Thermal conductivity of carbon nanotubes and their polymer nanocomposites: A review. *Prog. Polym. Sci.* 2011, 36, 914–944.

Hao Peng, David B.,” Automated Design of Functional Support Structures for Direct Metal Laser Sintering” , Air Force Research Laboratory FA8650-12-2-7230, IMTS conference Chicago, (2016)

Hassen, A.A., J. Lindahl, X. Chen, B. Post, L. Love, and V. Kunc, 2016a, “Additive Manufacturing of Composite Tooling Using High Temperature Thermoplastic Materials,” SAMPE Conference, Long Beach, CA.

Haynes, WM, *CRC Handbook of Chemistry and Physics*, ISBN-13: 978-1498754286, CRC Press; 97 edition (June 24, 2016)

He et al, Modeling Kapitza Resistance of Two-Phase Composite Material, *Composite Structures*, Volume 152, Pages 939-946, (2016).

Heidegger, Martin. ed. Krell, D. F. (1977). The Question Concerning Technology. *Basic Writings*. New York: Harper & Row, Publishers. 294.

Heigel, J. C., and Michaleris, P. "The Impact of Argon Shielding Flow Rate on Laser Engineered Net Shaping (LENS) of Ti-6Al-4V." Proceedings of the ASME 2015 International Manufacturing Science and Engineering Conference. Volume 1: Processing. Charlotte, North Carolina, USA. June 8–12, 2015. V001T02A060. ASME. <https://doi.org/10.1115/MSEC2015-9244>

Heigel, J.C., Michaleris, P., Palmer, T.A. "In situ monitoring and characterization of distortion during laser cladding of Inconel 625", *Journal of Materials Processing Technology*, Volume 220, Pages 135-145, (June 2015)

Heigel, J.C., Michaleris, P., Reutzler, E.W. "Thermo-mechanical model development and validation of directed energy deposition additive manufacturing of Ti-6Al-4V", *Additive Manufacturing*, Volume 5, Pages 9-19, (January 2015)

Heinicke, C., 2013, "Spatially Resolved Measurements in a Liquid Metal Flow With Lorentz Force Velocimetry," *Exp. Fluids*, 54, p. 1560

Hermann, J., *Engineering decision making and risk management*, John Wiley & Sons, ISBN: 978-1-118-91933-0 (2015)

Ho, J. E. (2007). Characteristic study of MHD pump with channel in rectangular ducts. *Journal of Marine Science and Technology*, 15(4), 315-321.

Hodes, M., Zhang, R., Lam, L. S., Wilcoxon, R., & Lower, N. (2013). On the potential of Galinstan-based minichannel and minigap cooling. *IEEE Transactions on Components, Packaging and Manufacturing Technology*, 4(1), 46-56.

Hodge, E., Ferencz, R. M., and Solberg, J. M. Implementation of a Thermomechanical Model for the Simulation of Selective Laser Melting, *Computational Mechanics* Volume 54, Issue 1, pp 33–51 (2014).

Holcomb, S, Brothers, M, Diebold, A, Thatcher, W, Mast, D, Tabor, C, and Heikenfeld, J, "Oxide-Free Actuation of Gallium Liquid Metal Alloys Enabled by Novel Acidified Siloxane Oils" *Langmuir* 2016 32 (48), 12656-12663

Howe, J. M. (1993). Bonding, structure, and properties of metal/ceramic interfaces: Part 1 Chemical bonding, chemical reaction, and interfacial structure. *International materials reviews*, 38(5), 233-256.

Hu, J.; Huang, Y.; Yao, Y.; Pan, G.; Sun, J.; Zeng, X.; Sun, R.; Xu, J.B.; Song, B.; Wong, C.P. A Polymer Composite with Improved Thermal Conductivity by Constructing Hierarchically Ordered Three-Dimensional Interconnected Network of BN. *ACS Appl. Mater. Interfaces* 2017, 13544–13553.

Huang, J., Wang, C., Zhang, X., Jia, W., Ma, R., Yang, Z., & Dong, T. (2019). Facile preparation and thermal properties of Field's alloy nanofluid for heat transfer. *Colloids and Surfaces A: Physicochemical and Engineering Aspects*, 581, 123805.

- Huang, Y., Leu, M. C., Mazumder, J., and Donmez, A. (February 1, 2015). "Additive Manufacturing: Current State, Future Potential, Gaps and Needs, and Recommendations." ASME. J. Manuf. Sci. Eng. February 2015; 137(1): 014001. <https://doi.org/10.1115/1.4028725>
- Ikegami, T., Stocker, M. P., Monaco, K., Fourkas, J. T., & Maruo, S. (2012). Fabrication of three-dimensional metalized movable microstructures by the combination of two-photon microfabrication and electroless plating. *Japanese Journal of Applied Physics*, 51(6S), 06FL17.
- Iman et al, A distribution-free approach to inducing rank correlation among input variables. *Comm. Statist. Part B-Simulation Comput.* 11, 311-334 (1982)
- Incropera, F.P., DeWitt, D.P, Bergman, T.L., & Lavine, A.S., *Fundamentals of Heat and Mass Transfer*, 6th Ed., Hoboken, NJ, John Wiley & Sons, (2007).
- Irshad, W., & Peroulis, D. (2009, December). A silicon-based Galinstan magnetohydrodynamic pump. In *Proc. 9th Int. Workshop Micro Nanotechnol. Power Generat. Energy Convers. Appl* (pp. 127-129).
- Irwin, J., and Michaleris, P. (June 23, 2016). "A Line Heat Input Model for Additive Manufacturing." ASME. J. Manuf. Sci. Eng. November 2016; 138(11): 111004. <https://doi.org/10.1115/1.4033662>
- Jacobsen, J. B., and Hopkins, D. C., "Optimally selecting packaging technologies and circuit partitions based on cost and performance," APEC 2000. Fifteenth Annual IEEE Applied Power Electronics Conference and Exposition (Cat. No.00CH37058), 2000, pp. 31-38 vol.1.
- Jacoby, Liquid metals take shape, *Chemical & Engineering News*, 94, 16-19 (2016).
- Jeon, Y. R., Abbas, Y., Sokolov, A. S., Kim, S., Ku, B., & Choi, C. (2019). Study of in situ silver migration in amorphous boron nitride CBRAM device. *ACS applied materials & interfaces*, 11(26), 23329-23336.
- Jeong, S. I., & Didion, J. (2007). Thermal control utilizing an electrohydrodynamic conduction pump in a two-phase loop with high heat flux source.
- Jin et al. An efficient algorithm for constructing optimal design of computer experiments. *Journal of Statistics Planning Inference* 134, 268-287 (2005)
- Johnson, M. E. Moore, L. M. and Ylvisaker, D. (1990) Minimax and maximin distance designs. *Journal of Statistical planning and interface*, 26, 131-148
- Jones, Donald R, Matthias Schonlau, and William J Welch. 1998. "Efficient Global Optimization of Expensive Black-Box Functions." *Journal of Global Optimization* 13 (4): 455-92.

Jones, T. B. , 1974, “An Electrohydrodynamic Heat Pipe,” Mech. Eng. (Am. Soc. Mech. Eng.) 0025-6501, 96, pp. 27–32.

Jones et al, Taxonomy of global optimization methods based on response surfaces, 2001

Juillet, C, Oudriss, A, Balmain, J, Feaugas, X, Pedraza, F, “Characterization and oxidation resistance of additive manufactured and forged IN718 Ni-based superalloys”, Journal of Corrosion Science, Volume 142, September 2018, Pages 266-276.

Kai, L., Jun, L., & Weiqiang, L. (2017). Thermal protection performance of magnetohydrodynamic heat shield system based on multipolar magnetic field. Acta Astronautica, 136, 248-258.

Keramati et al, Additive Manufacturing of Compact Manifold-Microchannel Heat Exchangers Utilizing Direct Metal Laser Sintering, 2019 18th IEEE Intersociety Conference on Thermal and Thermomechanical Phenomena in Electronic Systems (ITherm), INSPEC Accession 18899301, (2019).

Khairallah, SA, Anderson, AT, Rubenchik, A, & King, WE, “Laser powder-bed fusion additive manufacturing: Physics of complex melt flow and formation mechanisms of pores, spatter, and denudation zones”- Acta Materialia, 108, 36-45, 2016

Khuu, V, Osterman, M, Bar-Cohen, A, Pecht, M, “Thermal Performance Measurements of Thermal Interface Materials Using the Laser Flash Method”, ASME IPACK2007-33554, pp. 405-414, (2007).

Kidalov, S.V.; Shakhov, F.M. Thermal Conductivity of Diamond Composites. Materials 2009, 2, 2467–2495.

Krishnan, “Towards a Thermal Moor’s Law”, Bell Laboratories, 2007

Kruft, J., Shabana, Y., and Bruck, H.A., “Effect of TiO₂ Nanopowder on the Sintering Behavior of Nickel-Alumina Composites for Functionally Graded Materials”, Journal of the American Ceramic Society, 91, 2870-2877 (2008)

Kumar et al, Optimization of Support Material and Build Time in Fused Deposition Modeling (FDM), Applied Mechanics and Materials, 110-116, 2245-2251 (2012).

Kunquan, Ma; Jing, Liu (October 2007). Liquid metal thermal management of computer chips. Frontiers of Energy and Power Engineering in China (Review Article). 1. Higher Education Press, co-published with Springer-Verlag GmbH. pp. 384–402. ISSN 1673-7504. doi:10.1007/s11708-007-0057-3.

Lamont et al, Geometric Determinants of In-Situ Direct Laser Writing, Nature Publishing Group, volume 9, issue 1, page 394 (2019).

Lappo et al, Discrete Multiple material selective laser sintering experimental study, *Proceedings of the Solid Freeform Fabrication Symposium*.109-119 (2003).

- Lasance C. J. M. and Simons R. E., "Advances in High-performance cooling," *Electronics Cooling*, Vol. 11, pp. 22-39, 2005
- Le et al, Effects of Sulfur Concentration and Marangoni Convection on Melt-pool Formation in Transition Mode of Selective Laser Melting Process, *Materials & Design*, Volume 179, 107866 (2019).
- Lemoff, A. V., & Lee, A. P. (2000). An AC magnetohydrodynamic micropump. *Sensors and Actuators B: Chemical*, 63(3), 178-185.
- Leon, A, Shirizly, A, and Aghion, E, "Corrosion Behavior of AlSi10Mg Alloy Produced by Additive Manufacturing (AM) vs. Its Counterpart Gravity Cast Alloy, *Journals of Metals*, Volume 6, Issue 7, 10.3390/met6070148 (2016).
- Lghali, A. (2012). Surrogate based optimization using kriging based approximation. VU BA paper.
- Li, A, Zhang, C, & Zhang, Y-F. (2017). Thermal Conductivity of Graphene-Polymer Composites: Mechanisms, Properties, and Applications. *Polymers*. 9. 10.3390/polym9090437.
- Li, B.; Li, R.; Xie, Y. Properties and effect of preparation method of thermally conductive polypropylene/aluminum oxide composite. *J. Mater. Sci.* 2017, 52, 2524–2533.
- Li, Mian. 2011. "An Improved Kriging-Assisted Multi-Objective Genetic Algorithm." *Journal of Mechanical Design* 133 (7). American Society of Mechanical Engineers: 071008.
- Li, M., Li, G., and Azarm, S. (February 4, 2008). "A Kriging Metamodel Assisted Multi-Objective Genetic Algorithm for Design Optimization." *ASME. J. Mech. Des.*; 130(3): 031401. (2008)
- Li P., & Liu, J. (2011). Self-driven electronic cooling based on thermosyphon effect of room temperature liquid metal. *Journal of Electronic Packaging*, 133(4).
- Li T, Lv Y G, Liu J, et al. A powerful way of cooling computer chip using liquid metal with low melting point as the cooling fluid. *Forsch Ingenieurwes*, 2005, 70: 243–251
- Lin, Y. C., Duh, J. G., & Chiou, B. S. (2006). Wettability of electroplated Ni-P in under bump metallurgy with Sn-Ag-Cu solder. *Journal of electronic materials*, 35(1), 7-14.
- Liu J, Zhou Y X, Lv Y G, et al. Liquid metal based miniaturized chip-cooling device driven by electromagnetic pump. *ASME Electronic and Photonic Packaging, Electronic and Photonic Packaging, Integration and Packaging of Micro/Nano/Electronic Systems*, 2005, 5: 501–510

- Ma, K. Q. , Liu, J., Xiang, S. H. , Xie, K. W. , and Zhou Y. X. , 2009, “Study of Thawing Behavior of Liquid Metal Used as Computer Chip Coolant,” *Int. J. Therm. Sci*, 48, pp. 964–974
- Ma, K., & Liu, J. (2007). Liquid metal cooling in thermal management of computer chips. *Frontiers of Energy and Power Engineering in China*, 1(4), 384-402.
- Manfredi D, Calignano F., Krishnan M , Canali R, Ambrosio E, Biamino S, Ugues D, Pavese M, Fino P. “Additive Manufacturing of Al Alloys and Aluminium Matrix Composites (AMCs)”. *Light Metal Alloy. Appl. InTech* 2014.
- Martukanitz, R. P., Melnychuk, R. M., Stefanski, M. S., & Copley, S. M. Dynamic Absorption of a Powder Layer. In *ICALEO 2004 - 23rd International Congress on Applications of Laser and Electro-Optics, Congress Proceedings (2004)*
- McVey, R. W., Melnychuk, R. M., Todd, J. A., and Martukanitz, R. P., Absorption of laser irradiation in a porous powder layer, *Journal of Laser Applications* 19, 214 (2007)
- Mikhailovskii, A.B., Optimization of computational MHD normal-mode analysis for tokamaks, *Plasma Physics Report*, Vol 35, issue 7, 916-930 (1997)
- Mills J P, “Electromagnetic interference reduction in electronic systems,” First edition Prentice Hall, B003R3RI1Q, 1993.
- Miner, A.; Ghoshal, U. (2004-07-19). "Cooling of high-power-density microdevices using liquid metal coolants". *Applied Physics Letters*. 85 (3): 506–508.
- Moisala, A.; Li, Q.; Kinloch, I.A.; Windle, A.H. Thermal and electrical conductivity of single- and multi-walled carbon nanotube-epoxy composites. *Compos. Sci. Technol.* 2006, 66, 1285–1288.
- Morley, NB, *Magnetohydrodynamic effects in liquid flows*, UCLA, 2006
- Morris, M. D. and Mitchell, T. J. (1995) Exploratory designs for computational experiments. *Journal of Statistical planning and interface*, 43, 381-402
- Muller and Buhler, *Magnetofluidynamics in Channels and Containers*, Springer 2001, ISBN 3-540-41253-0
- Naruskevicius L, Tamasiunaite LT, Zielieni A et al (2012) A Co-based surface activator for electroless copper deposition. *Surf Coat Technol* 206(11–12):2967–2971
- Olabisi, O, Adewale, K ,*Handbook of Thermoplastics (Plastics Engineering)*, CRC Press; 2 edition (December 22, 2015) ISBN-13: 978-1466577220
- Pal, D, Patil, N., Zeng, K., and Stucker, B., "An Integrated Approach to Additive Manufacturing Simulations Using Physics Based, Coupled Multiscale Process Modeling." *ASME. J. Manuf. Sci. Eng.* December 2014; 136(6): 061022.

Park et al, Dynamic thermal model of li-ion battery for predictive behavior in hybrid and fuel cell vehicles, SAE technical paper; 2003.

Patel, V. K., Seyed-Yagoobi, J., Robinson, F., & Didion, J. R. (2016). Effect of Gravity on Electrohydrodynamic Conduction Driven Liquid Film Flow Boiling. *Journal of Thermophysics and Heat Transfer*, (null), 429-437.

Paul, R., Anand, S., and Gerner, F. (March 26, 2014). "Effect of Thermal Deformation on Part Errors in Metal Powder Based Additive Manufacturing Processes." ASME. *J. Manuf. Sci. Eng.* June 2014; 136(3): 031009.

Pautsch G. How is high heat flux cooling technology being driven by supercomputers. Proceedings of the 9th IEEE Intersociety Conference on Thermal and Thermomechanical Phenomena in Electronic Systems, 2004, 2: 702–703

Pecht, M et al, *Electronic Packaging Materials and Their Properties*, CRC Press, 2017

Pecht, M, Radojicic, R, Rao, G “Guidebook for Managing Silicon Chip Reliability (Electronic Packaging Series, Book 5)”, ISBN-13: 978-0849396243, CRC Press; first edition (1998).

Pines, M.L. and Bruck, H.A. “Pressureless Sintering of Particle-reinforced Metal-Ceramic Composites for Functionally Graded Materials: Part II. Sintering Model”, *Acta Materialia*, 54, 1457-1465 (2006).

Pines, M.L. and Bruck, H.A. “Pressureless Sintering of Particle-reinforced Metal-Ceramic Composites for Functionally Graded Materials: Part I. Porosity Reduction Models”, *Acta Materialia*, 54, 1467-1474 (2006).

Prokhorenko S V. Structure and viscosity of gallium, indium, and tin in the vicinity of the crystallization temperature. *Materials Science*, 2005, 41: 271–274

Prozorov and Kogan, Effective Demagnetizing Factors of Diamagnetic Samples of Various Shapes, *Phys. Rev. Applied* 10, 014030 – Published 27 July 2018

Raigrodski, A. J., Malcamp, C., & Rogers, W. A. (1998). Electroforming technique. *Journal of dental technology: the peer-reviewed publication of the National Association of Dental Laboratories*, 15(6), 13-16.

Ramesh, P.; Yu, A.; Sun, X.; Bekyarova, E.; Itkis, M.E.; Haddon, R.C. Enhanced Thermal Conductivity in a Hybrid Graphite Nanoplatelet—Carbon Nanotube Filler for Epoxy Composites. *Adv. Mater.* 2010, 20, 4740–4744.

Rametsteiner, E., & Weiss, G. (2006). Assessing policies from a systems perspective—Experiences with applied innovation systems analysis and implications for policy evaluation. *Forest Policy and Economics*, 8(5), 564-576.

- Ravindran, A., Reklaitis, G. V., & Ragsdell, K. M. (2006). *Engineering optimization: methods and applications*. John Wiley & Sons.
- Revie, W, Uhlig's Corrosion Handbook, ISBN-13: 978-0470080320, Wiley; 3 edition (April 12, 2011)
- Richerson, DW, Lee, WE , “Modern Ceramic Engineering: Properties, Processing, and Use in Design”, (May 10, 2018) CRC Press; 4 edition, ISBN-13: 978-1498716918
- Robinson, F., Cevallos, J. G., Bar-Cohen, A., & Bruck, H. (2011, January). Modeling and validation of a prototype thermally-enhanced polymer heat exchanger. In *ASME 2011 International Mechanical Engineering Congress and Exposition* (pp. 597-606).
- Rodriguez et al, AM Validation & Production Insertion Effort, Northrop Grumman, ES Symposium, (2015).
- Rossinsky, Müllerplathe, “Anisotropy of the thermal conductivity in a crystalline polymer: Reverse nonequilibrium molecular dynamics simulation of the delta phase of syndiotactic polystyrene.” *J. Chem. Phys.* 2009, 130, 134905.
- Rubenchik, A, Wu, S., Mitchell, S., Golosker, I., LeBlanc, M., and Peterson, N., “Direct measurements of temperature-dependent laser absorptivity of metal powders” *Applied Optics* 54(24), 7230 (2015).
- Rubin, I I, *Handbook of plastic materials and technology*, John Wiley & Sons Inc., New York, 1990. ISBN 0-47 1-096342.
- Rubio, E. J. (2016). Intrinsic and metal-doped gallium oxide based high-temperature oxygen sensors for combustion processes.
- Saleh, K. H. (2012). Online approximation assisted multiobjective optimization with heat exchanger design applications (Doctoral dissertation).
- Savolainen, J, Collan, M, “How Additive Manufacturing Technology Changes Business Models? – Review of Literature”, *Journal of Additive Manufacturing*, Volume 32, 101070, (March 2020)
- Y.M. Shabana, M.L. Pines, H.A. Bruck, B. Xu, and J.P. Laskis, "Evolution of Elastic Mechanical Properties During Pressureless Sintering of Powder-Processed Metals and Ceramics", *Journal of Materials Science*, 42, 7708-7715 (2007).
- Sharma et al, Comparative Study of Rectangular and Trapezoidal Microchannels Using Water and Liquid Metal, *Science Direct*, 51 (2013) 791 -796
- Shen et al, Surface Self-nanocrystallization in Copper Electroforming, *Journal of Materials Engineering and Performance*, Volume 28, Issue 1, pp 211–220, (2019).

Snowden David J and Mary E. Boone, “ A leader’s framework for decision making”
Harvard business review, Volume 85, Issue 11, pages69-76, 2007

So, K. P., Lee, I. H., Duong, D. L., Kim, T. H., Lim, S. C., An, K. H., & Lee, Y. H.
(2011). Improving the wettability of aluminum on carbon nanotubes. *Acta Materialia*,
59(9), 3313-3320.

Soghomonian, Z, Soft Magnetic Composites, US patent 2005/0162034A1.

Sproul, R. C. (2000). *The consequences of ideas: Understanding the concepts that shaped
our world.* Crossway.

Standard, A. S. T. M. (2012). F2792. 2012. standard terminology for additive
manufacturing technologies. ASTM F2792-10e1.

Sugano, Y., & Takahashi, S. (2006). Material design of functionally graded plates with
function of electromagnetic noise suppression (quantitative evaluation on suppression
effect of electromagnetic noise). *Nippon Kikai Gakkai Ronbunshu, A Hen/Transactions
of the Japan Society of Mechanical Engineers, Part A*, 72(10), 1585-1592.

Sukhotskiy, V., Karampelas, I. H., Garg, G., Verma, A., Tong, M., Vader, S., ... &
Furlani, E. P. (2017). Magnetohydrodynamic drop-on-demand liquid metal 3D printing.
Proceedings of the Solid Freeform Fabrication.

Tang, B. (1993) Orthogonal array-based Latin hypercubes, *Journal of the American
Statistical Association*, 88(424), 1392-1397.

Tang et al, Liquid metal actuator for inducing chaotic advection, *Advanced Functional
Materials*, 24, 5851-5858 (2014).

Tang et al, Liquid metal enabled pump, *Proceedings of the National Academy of
Sciences*, 111, 3304-3309 (2014).

Temeche, E, Yi, E, Keshishian, V, Kieffer, J, Laine, RM, “Liquid-feed flame spray
pyrolysis derived nanopowders (NPs) as a route to electrically conducting calcium
aluminate ($12\text{CaO}\cdot 7\text{Al}_2\text{O}_3$) films,” *Journal of the European Ceramic Society* 39 (4),
1263-1270, 2018.

Tesche, F. M., Barnes, P. R., & Meliopoulos, A. S. (1992). Magnetohydrodynamic
electromagnetic pulse (MHD-EMP) interaction with power transmission and distribution
systems (No. ORNL/Sub-90-SG828/1). Oak Ridge National Lab., TN (United States);
Georgia Inst. of Tech., Atlanta, GA (United States). Dept. of Electrical Engineering.

Thompson, G, Designing for The DMLS and SLS Processes, IMTS Conference Chicago,
Sep 2016, Protolab Inc.

Tsai, Y. L. (2017). Electroforming on ceramic.

Tumanski, Handbook of Magnetic Measurement, CRC press 2011, ISBN 978-1-4398-2951-6.

Vader, S., & Vader, Z. (2017). U.S. Patent No. 9,616,494. Washington, DC: U.S. Patent and Trademark Office.

Wang GX, Li N, Hu HL et al (2006) Process of direct copper plating on ABS plastics. Appl Surf Sci 253(2):480–484

Wang, P. J., Chang, C. Y., & Chang, M. L. (2004). Simulation of two-dimensional fully developed laminar flow for a magneto-hydrodynamic (MHD) pump. Biosensors and Bioelectronics, 20(1), 115-121.

Watanabe, N., Suda, M., Furuta, K., & Sakuhara, T. (2001, January). Fabrication of micro parts using only electrochemical process. In Technical Digest. MEMS 2001. 14th IEEE International Conference on Micro Electro Mechanical Systems (Cat. No. 01CH37090) (pp. 143-146). IEEE

Weber, E. H., Clingeman, M. L., and King, J. A., 2003, “ Thermally Conductive Vylom 6,6 and Polycarbonate Based Resins. I. Syneristic Effects of Carbon Fillers,” J. Appl. Polym. Sci., 88(1), pp. 112-122.

Weickhmann, M. NdFeB *Magnets Properties and Applications*, 2009, 1–10

Wojcik CC, Clark LT. Design, analysis, and testing of refractory metal heat pipes using lithium as the working fluid. AIAA-1991-1400. 1991:1–14.

Wu, J., and Azarm, S. "Metrics for Quality Assessment of a Multiobjective Design Optimization Solution Set ." ASME. J. Mech. Des.; 123(1): 18–25. (2001)

Wu, Zhaohui, et al. "Ceramic module for power semiconductor integrated packaging and preparation method thereof." U.S. Patent Application No. 16/208,572.

Wu, Zhaohui. "Method for preparing ceramic package substrate with copper-plated dam." U.S. Patent No. 10,297,498. 21 May 2019.

Xi, F, et al, Electromagnetic Field Enhancement and Its Application in Spin Rectification, Applied Physics Express 6(10):103002 , 2013

Xiao-Hu et al, Thermal Management of Li-ion Battery with Liquid Metal, Energy Conversion and Management, 117, 577-585 (2016)

I. Yadroitsev. A. Gusarov, I. Yadroitsava, I. Smurov, Single Track Formation in Selective Laser Melting of Metal Powders, Journal of Materials Processing Technology, Volume 210, Issue 12, Pages 1624-1631, (2010).

Yang, L., Eddins, R. A., & Grimes, D. L. (2019). “ Avionics cooling module”, U.S. Patent Application No. 15/941,932.

- Yang, S.Y.; Ma, C.C.M.; Teng, C.C.; Huang, Y.W.; Liao, S.H.; Huang, Y.L.; Tien, H.W.; Lee, T.M.; Chiou, K.C. Effect of functionalized carbon nanotubes on the thermal conductivity of epoxy composites. *Carbon* 2010, 48, 592–603.
- Yavari, F.; Fard, H.R.; Pashayi, K.; Rafiee, M.A.; Zamiri, A.; Yu, Z.; Ozisik, R.; Borcatasciuc, T.; Koratkar, N. Enhanced Thermal Conductivity in a Nanostructured Phase Change Composite due to Low Concentration Graphene Additives. *J. Phys. Chem. C* 2011, 115, 8753–8758.
- Yu, Q, Qi, L, Tsuru, T, Traylor, R, Rugg, D, Morris, JW Jr., Asta, M, Chrzan, CD, Minor, AM, “Origin of dramatic oxygen solute strengthening effect in titanium”, *Journal of science*, Vol. 347, Issue 6222, pp. 635-639 (Feb 2015)
- Zandrini, T., Taniguchi, S., & Maruo, S. (2017). Magnetically driven micromachines created by two-photon microfabrication and selective electroless magnetite plating for lab-on-a-chip applications. *Micromachines*, 8(2), 35.
- Zeigarnik, Y. A. (1996). Liquid metal Heat Transfer. *Intl. Encyclopedia of heat & mass transfer*, 673-675.
- Zhang, M., X. Liu, K. Biswas and J. Warner. 2019. A 3D Numerical Investigation of a Novel Shallow Bore Ground Heat Exchanger Integrated with Phase Change Material. *Applied Thermal Engineering* 162 (2019) 114297.
<https://doi.org/10.1016/j.applthermaleng.2019.114297>
- Zhao, D., Qian, X., Gu, X., Jajja, S. A., and Yang, R. (October 6, 2016). "Measurement Techniques for Thermal Conductivity and Interfacial Thermal Conductance of Bulk and Thin Film Materials." *ASME. J. Electron. Packag.* December 2016; 138(4): 040802.
<https://doi.org/10.1115/1.4034605>
- Zhong, J., Yi, M., & Bau, H. H. (2002). Magneto hydrodynamic (MHD) pump fabricated with ceramic tapes. *Sensors and Actuators A: Physical*, 96(1), 59-66.
- Zhou X W, Chen J Y. Overview on viscosity of liquid metals. *Journal of Shenyang Normal University (Natural Science Edition)*, 2003, 21(4): 255–259
- Zhu, J. Y., Tang, S. Y., Khoshmanesh, Khashayar, & Ghorbani, K. (2016). An integrated liquid cooling system based on Galinstan liquid metal droplets. *ACS applied materials & interfaces*, 8(3), 2173-2180.
- Zikanov, O., Krasnov, D., Boeck, T., Thess, A. & Rossi, M. (2014) Laminar-turbulent transition in magnetohydrodynamic duct, pipe, and channel flows. *Appl. Mech. Rev.* 66 (3), 030802.